

UvA-DARE (Digital Academic Repository)

Arterial network adaptation and endothelial shear stress

A tale of 3D imaging and hemodynamic modeling Schwarz, J.C.V.

Publication date 2021 Document Version Final published version

Link to publication

Citation for published version (APA):

Schwarz, J. C. V. (2021). Arterial network adaptation and endothelial shear stress: A tale of 3D imaging and hemodynamic modeling. [Thesis, fully internal, Universiteit van Amsterdam].

General rights

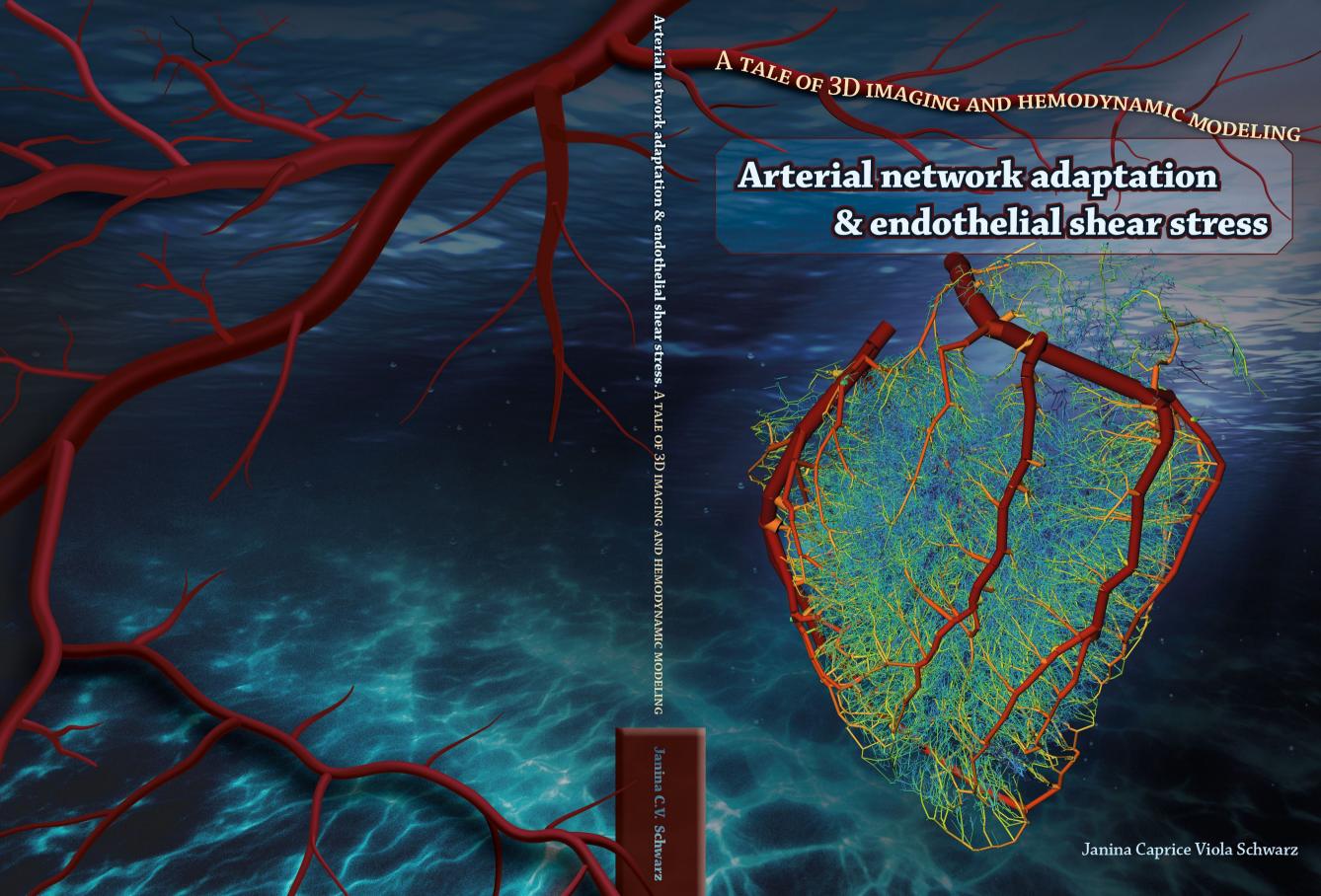
It is not permitted to download or to forward/distribute the text or part of it without the consent of the author(s) and/or copyright holder(s), other than for strictly personal, individual use, unless the work is under an open content license (like Creative Commons).

Disclaimer/Complaints regulations

If you believe that digital publication of certain material infringes any of your rights or (privacy) interests, please let the Library know, stating your reasons. In case of a legitimate complaint, the Library will make the material inaccessible and/or remove it from the website. Please Ask the Library: https://uba.uva.nl/en/contact, or a letter to: Library of the University of Amsterdam, Secretariat, Singel 425, 1012 WP Amsterdam, The Netherlands. You will be contacted as soon as possible.

UvA-DARE is a service provided by the library of the University of Amsterdam (https://dare.uva.nl)

Download date:10 Mar 2023



Arterial network adaptation and endothelial shear stress

A tale of 3D imaging and hemodynamic modeling

Janina Caprice Viola Schwarz

Cover: 3D reconstruction of a human heart; the colors indicate the modeled local blood flow. Background images by Tomislav Jakupec and by Jonathan Borba.

Arterial network adaptation and endothelial shear stress A tale of 3D imaging and hemodynamic modeling

Dissertation, University of Amsterdam, The Netherlands

Part of the research described in this thesis was performed within the framework of CTMM, the Center for Translational Molecular Medicine (www.ctmm.nl), project EMINENCE (grant 01C-204).

Author: Janina C. V. Schwarz

Cover design & layout: Janina C. V. Schwarz Printed by GVO drukkers & vormgevers B.V.

ISBN: 978-94-6332-782-4

Financial support by the Dutch Heart Foundation for the publication of this thesis is gratefully acknowledged.

Copyright © 2021 Janina C. V. Schwarz

All rights reserved. No part of this thesis may be reproduced, stored or transmitted in any form or by any means without prior written permission of the author or where appropriate the publisher.

Arterial network adaptation and endothelial shear stress

A tale of 3D imaging and hemodynamic modeling

ACADEMISCH PROEFSCHRIFT

ter verkrijging van de graad van doctor
aan de Universiteit van Amsterdam
op gezag van de Rector Magnificus
prof. dr. ir. K.I.J. Maex
ten overstaan van een door het College voor Promoties
ingestelde commissie,
in het openbaar te verdedigen in de Agnietenkapel
op woensdag 29 September 2021, te 16.00 uur

door

Janina Caprice Viola Schwarz geboren te Hamburg

Promotiecommissie

Ркомоток

prof. dr. E. T. van Bavel AMC-UvA

Copromotor

dr. ir. M. Siebes AMC-UvA

Overige Leden

prof. dr. D. Merkus Ludwig-Maximilians-Universität München

prof. dr. M. C. G. Aalders AMC-UvA dr. ir. J. J. Wentzel Erasmus MC prof. dr. J. J. Piek AMC-UvA

prof. dr. S. J. Payne University of Oxford

prof. dr. ir. A. G. Hoekstra Universiteit van Amsterdam

FACULTEIT DER GENEESKUNDE

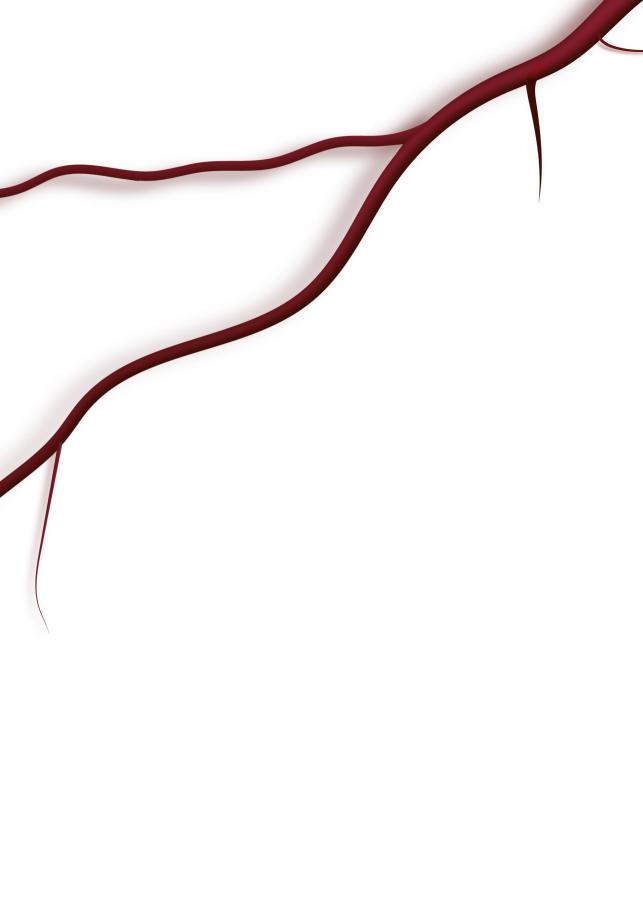
...I am strong, when I am on your shoulders; You raise me up to more than I can be.

(Brendan Graham)

Für meinen lieben Vater

Contents

1	Introduction	1
ı	Vascular Networks	39
2	3D Imaging of vascular networks for biophysical modeling of perfusion distribution within the heart	41
3	Optimization of Vascular Casting for Three-Dimensional Fluorescence Cryo-Imaging of Collateral Vessels in the Ischemic Rat Hindlimb	75
4	Topologic and Hemodynamic Characteristics of the Human Coronary Arterial Circulation	99
II	Wall Shear Stress	133
5	Endothelial shear stress estimation in the human carotid artery based on Womersley versus Poiseuille flow	135
6	The impact of scaled boundary conditions on wall shear stress computations in atherosclerotic human coronary bifurcations	157
Ш	Epilogue	179
7	General Discussion	181
8	Summary	207
Α	About the PhD Training	225



CHAPTER 1

Introduction

1.1 GENERAL INTRODUCTION

Cardiovascular disease (CVD) remains the leading cause of death worldwide in most middle- to high-income countries. Due to strong efforts over the past decades mortality could be reduced, particularly in high-income countries with a 19% decrease in mortality rate between 2000 and 2016 for 30- to 70-year-old and a decrease in the age-adjusted death rate. Nevertheless, CVD still accounts for 47% and 39% of all deaths in European females and males, respectively, and nearly 17.9 million deaths globally per year. In the member states of the European Society of Cardiology, 108.7 million patients were affected by CVD in 2017. It is not only a major contributor to years of life lost and of disability, but also effectuates a burden on the economy with annual direct and indirect costs of approximately \$351 billion in the United States as estimated for 2014/15. Page 10.10 for the past decades.

Atherosclerotic diseases dominate in CVD. Typically starting during early child-hood, lipids slowly begin to accumulate at the vessel walls. Simultaneously, pro-inflammatory cells are attracted to the site, where they migrate into the vessel wall, accompanied by proliferation of smooth muscle cells. These initially small atherosclerotic lesions grow with age, with risk factors such as high cholesterol levels and unhealthy nutrition accelerating the process. Progressive growth of the lesion eventually limits perfusion capacity, leading in the heart to myocardial ischemia during exercise or even in rest. Plaque rupture in coronary arteries can result in acute ischemia and tissue damage, culminating in myocardial infarction.

Reduced blood flow due to the presence of such a stenosis in the large arteries indirectly also affects the small vessels downstream. Slow chronic progression of such stenosis induces adaptation not only in the vessels themselves but also of the vascular network structure. This includes, for example, the recruitment and enlargement of alternate pathways but also maladaptive processes such as inward remodeling or even rarefaction of the microcirculation.^{5,6} The arterial bed also remodels in response to other long-term stimuli, such as hypertension, and myocardial diseases, such as hypertrophic cardiomyopathy.

There exists thus a strong interplay between arterial network structure on one side and organ function and perfusion on the other side, whereby both structural and functional alterations also influence remote locations. Comprehension of this complex interplay requires multi-scale approaches integrating different structural domains such as micro- and macrocirculation. The work leading to this thesis was directed to the investigation of this interplay by optimizing the multi-scale imaging of arterial networks at sites of active remodeling, which can then serve as input for

multi-scale hemodynamic simulations. Below, different types of vascular networks and adaptive mechanisms are described.

1.2 THE CARDIOVASCULAR SYSTEM

The cardiovascular system serves the distribution of oxygen from the lungs throughout the body. It also facilitates the exchange of nutrients, hormones, metabolites, and the response of the immune system as well as the clearance of waste products such as carbon dioxide in a double circular fashion. Oxygen-rich blood, returning from the lungs to the left atrium, is pumped by the left ventricle into the aorta (diameter approximately 3 cm), from where the blood is distributed to all organs and tissue along a tree-like structure that branches towards increasingly smaller vessels (Figure 1.1). The smallest vessels, the capillaries, with diameters ranging from 2 to 10 µm, reserve as exchange site with the local tissue. From there, the deoxygenated blood is returned via increasingly larger venules and veins to the right atrium, completing the systemic circulation. The pulmonary circulation equivalently transports the blood in a similar manner via pulmonary arteries and veins from the right ventricle to the lungs and back to the left atrium. The large arteries and veins are compliant with little pressure drop, thereby serving as reservoir, whereas the small arteries and arterioles act as flow resistance, slowing down the blood flow towards the exchange locations by virtue of the increasing total luminal cross-sectional area.

1.2.1 Vascular network structure

As described above, both the arterial and the venous system are hierarchically organized. Except for well-known connections between different branches, the so-called collateral vessels, the main vessels typically branch in a tree-like manner as indicated in Figure 1.1A. This predominantly tree-like structure can also be appreciated in the cerebral and coronary vasculature (Figure 1.1B, C). Prominent exceptions include the circle of Willis and the mesenteric circulation that form arterial arcades rather than trees (Figure 1.1D). Some arcades and collaterals are also found in the cerebral and coronary circulation, as can be seen in Figure 1.1B and 1.1C. Towards the microcirculation, the tree-like structure is more and more complemented, eventually becoming a mesh at the capillary level as depicted in Figure 1.1E.

This — in general tree-like — structure exhibits self-similar patterns, with branching characteristics statistically repeating at different spatial scales. This resemblance has led to a myriad of allometric models. Already more than 200 years ago, Keill,

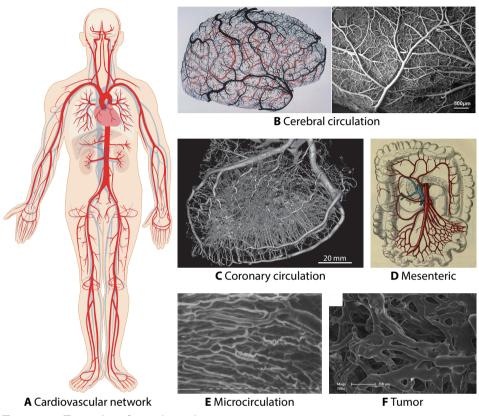


Figure 1.1: Examples of vascular architecture.

- (A) Illustration of the cardiovascular system with predominantly treelike structure. Adapted from [8].
- **(B)** Human pial vasculature (left) and detailed view of the murine anterior cortex (right). Reprinted from Duvernoy *et al.*⁹ with permission from Elsevier and from Meyer *et al.*, ¹⁰ Copyright (2008) National Academy of Sciences.
- **(C)** 3D-rendering of a human coronary circulation.
- (D) Sketch of the arcading superior mesenteric circulation. Reprinted from Gray & Lewis. 11
- (E) Scanning electon micrograph of the murine epicardial surface showing parallel capillary arcades. Bars are $10\,\mu m$. Reprinted from Potter & Groom⁷ with permission from Elsevier.
- **(F)** Murine tumor vasculature displaying heterogeneity and cast leakage (arrow). Reprinted from Pabst *et al.*¹² with permission from Elsevier.

Young, and Hales studied the branching of the arterial tree. ¹³ In his Croonian lecture in 1808, the polymath Thomas Young estimated from an idealized tree with 30 branch generations the total resistance of the arterial tree. Assuming a ratio of total cross-sectional area of 1:1.2586 across bifurcations, Young's estimates reasonably matched experiments. Thoma noticed that the flow through a vessel and its diameter are correlated. ¹⁴ He proposed a power-relation between the radii of parent (r_0) and daughter ($r_{1/2}$) vessels:

$$r_0^{\alpha} = r_1^{\alpha} + r_2^{\alpha} \,, \tag{1.1}$$

presenting data corroborating an exponent between 2 and 3 and reported $\alpha = 2$ for the branches of the human aorta. In his seminal article, Murray argued in 1926 that flow rate should be proportional to the cube of the corresponding vessel radius based on the minimization of the total cost of (laminar) blood flow and blood volume maintenance, which are competing factors as larger diameters pose less resistance but have higher costs for keeping up their volume. 15 Together with conservation of mass across branch points, this result implies a cubic relation between the radii of parent and daughter vessels, which has been coined Murray's law: $r_0^3 = r_1^3 + r_2^3$. It is noteworthy that for symmetric bifurcations this result remarkably matches Young's ratio (1:2^{1/3}=1:1.2599). Apparently unaware of Murray's work, Cohn rederived this finding for symmetric bifurcations, 16 while Uylings extended it to non-laminar flow.¹⁷ Uylings derived that the exponent can vary between 2.33 for turbulent flow and 3.0 for laminar flow constrained to the same optimal principle as postulated by Murray. In their highly influential but also controversial article, West, Brown, and Enquist proposed a new model as motivation for the ¾-allometric scaling law of metabolism. 18,19 Assuming a space-filling fractal-like structure with invariant terminal segments, their model minimized the energy needed for resource distribution. They proposed two regions, large vessels subject to pulsatile flow and small vessels with predominantly Poiseuille flow, with a step-like transition zone. Whereas the first region is dominated by minimization of wave reflections leading to area preservation and an exponent of 2, the latter is characterized by the cubic branching of Murray. The findings of Seiler et al. in the human epicardial arteries, ²⁰ which differed from Murray's model, initiated a refinement of Murray's theory by Kassab et al.²¹ In a series of articles, Kassab and coworkers applied the "minimum energy hypothesis" to subtrees — in contrast to Murray who considered a single bifurcation — in which they derived power-relationships between diameter, length, volume, flow, and mass. 21-26 With an exponent of 7/3, the Huo-Kassab model is closer to area-preservation (exponent 2) than to Murray's model.²³ They furthermore

devised a variable, y, to discriminate between fractal behaviors, where y = 0 implied space-filling, y = 1 area-filling, and y = 2 length-preservation. Based on a large number of morphometric data sets, they reported a mean y of 0.45 ± 0.49 , indicating mixed area–space-filling, and a mean Murray exponent $\alpha = 2.64 \pm 0.64$.

Even though real vascular trees clearly deviate from perfect symmetry, experiments corroborate the existence of a power-law relationship at least for parts of the arterial tree. The reported exponents typically varied between 2 and 3, with an exponent of 2 for large branches of the aorta²⁷ and exponents of 2.2 and 2.7 for the major arteries in porcine hearts. Also in a porcine model, VanBavel and Spaan found an exponent of 2.35 for coronary arteries larger than 200 μ m, whereas the exponent for diameters smaller than 40 μ m was higher (α = 2.82). For a historic overview, the reader is referred to the review of Sherman from 1981, which revived the scientific interest in this topic at that time.

Evidence for physiological principles underlying the scale-invariance comes from the similar fractal nature of myocardial perfusion³² and the deviations observed in disease. Power laws differ in case of coronary artery disease (CAD).²⁰ Also, Huo et al. showed a significant difference in patients with diffuse CAD in comparison with a matched control group.³³ Vice versa, Schoenenberger et al. found that deviation from Murray's law was associated with more substantial calcifications in human coronary bifurcations.³⁴

Nonetheless, despite the general principle of self-similarity, these models fall short of deterministically predicting individual bifurcations. Zamir in 1999 reported highly varying power-law exponents for the individual bifurcations, even exceeding the 2-3 range as measured in a cast of a human right coronary artery.³⁵ Yet, he noticed that the range of exponents was similar for most of the vasculature, which led him to the notion of "pseudo-fractal' properties, in the sense that vessels of different calibers displayed the same branching pattern but with a range of values of the branching parameter."³⁵, p. 517

Assessment of scaling behavior in large networks consisting of vessels of various scales and linking them to the physiological environment, e.g., local flow and pressure, can increase the insight into the underlying mechanisms that accomplish optimal network design and their malfunction in disease states.

1.3 HEMODYNAMICS

The work done by the heart provides the energy needed to move the blood around the vascular circulation. The pumping of the heart gives rise to pulsatile flow

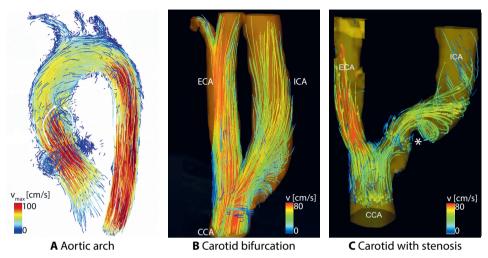


Figure 1.2: Typical examples of systolic blood flow as visualized by particle tracing. Colors represent flow velocity. **(A)** Regular flow in the descending aorta, whereas in the ascending aorta helices (white arrows) occur frequently. **(B)** Asymmetric, complex flow at the carotid bifurcation. Distal of the bifurcation, flow becomes more regular. **(C)** Accelerated flow at a stenosis (indicated by "*") with disturbed distal flow. ECA - external carotid artery, ICA - internal carotid artery, CCA - common carotid artery. Images adapted from Oechtering *et al.*, ³⁶ Harloff & Markl, ³⁷ and Markl *et al.* ³⁸ (left to right).

in arteries, where the pulsatility is damped until reaching steady flows in small arterioles, capillaries, and the venous part of the circulation. The hemodynamics depend on the vascular network, which in turn is influenced by hemodynamic forces as detailed in the subsequent sections. Figure 1.2 shows examples of typical flow patterns, with laminar flow in long straight segments. At valves, bifurcations, and sites of pathologic changes such as plaques and aneurysms flow becomes more complex (Figure 1.2C) and possibly even turbulent. For arteries and arterioles down to $100\,\mu m$, the Navier–Stokes equation is an excellent representation as blood can be considered a continuum here. The Navier–Stokes equation can be viewed as a balance of inertial, body, pressure, and viscous forces. In its general form it is described by

$$\rho \frac{D\mathbf{v}}{Dt} = \rho \left(\frac{\partial \mathbf{v}}{\partial t} + (\mathbf{v} \cdot \nabla)\mathbf{v} \right) = -\nabla p + \nabla \cdot \mathbf{T} + \mathbf{F}$$
 (1.2a)

where the deviatoric stress tensor T usually is taken as $T_{ij} = \mu \left(\frac{\partial v_i}{\partial x_j} + \frac{\partial v_j}{\partial x_i} \right) + \delta_{ij} \lambda \frac{\partial v_k}{\partial x_k}$ for Newtonian fluids. ρ is the density, v the flow velocity, t time, p pressure, μ shear

viscosity, and λ the second coefficient of viscosity ("volume viscosity"). δ_{ij} is the Kronecker delta, and F represents body forces, such as gravity. Together with the continuity equation,

$$\frac{\partial \rho}{\partial t} + \nabla \cdot (\rho \mathbf{v}) = 0, \qquad (1.2b)$$

this equation is the basis for computational fluid dynamics (CFD) simulations, that numerically model flow for specific boundary conditions in complex geometries, and also forms the foundation of simpler flow models based on further assumptions.

The most frequent assumptions are that blood is incompressible and has constant viscosity (Newtonian), reducing the equations to

$$\frac{\partial \mathbf{v}}{\partial t} + (\mathbf{v} \cdot \nabla) \mathbf{v} = -\frac{1}{\rho} \nabla p + \frac{\mu}{\rho} \nabla^2 \mathbf{v} + \frac{\mathbf{F}}{\rho}$$
 (1.2c)

$$\nabla \cdot \mathbf{v} = 0. \tag{1.2d}$$

As these equations cannot be solved analytically in general for blood vessels, numerical methods need to be employed. Numerical schemes including CFD simulations can yield detailed approximations, accounting for temporal and spatial variations. Yet, due to the high computational costs inherent to these methods, further simplifications are necessary for studying the behavior of the cardiovascular system.

Blood vessels are therefore frequently approximated as cylindrical tubes, much longer than wide, with rigid walls. External body forces, e.g., gravity, are neglected. Flow velocity is assumed to be axisymmetric along the cylinder axis and to be zero at the vessel wall (no-slip condition), which further reduces the Navier–Stokes equation to $\rho \frac{\partial v_z}{\partial t} = -\frac{\partial p}{\partial z} + \mu \left[\frac{1}{\varrho} \frac{\partial}{\partial \varrho} \left(\varrho \frac{\partial v_z}{\partial \varrho} \right) \right]$ with $\frac{\partial v_z}{\partial z} = 0$ in cylindrical coordinates (ϱ, φ, z) , where the cylinder axis is along the z-direction.

For a temporal oscillatory pressure gradient $\frac{\partial p}{\partial z} = \Re\{Pe^{i\omega t}\}$, Womersley solved this partial differential equation for the above stated boundary conditions (no-slip, axisymmetric, rigid wall) for a cylinder of radius r:⁴⁰

$$v(\varrho,t) = \Re\left\{\frac{P}{i\omega\rho}\left[1 - \frac{J_0(\alpha i^{\frac{3}{2}}\frac{\varrho}{r})}{J_0(\alpha i^{\frac{3}{2}})}\right]e^{i\omega t}\right\}$$
(1.3a)

with the Womersley number

$$\alpha = r\sqrt{\frac{\omega\rho}{\mu}}.$$
 (1.3b)

Fourier expansions yield approximate general periodic pressure gradients and flow in the large arteries as utilized in Chapter 5 for the carotid arteries.

The steady-state solution is given by:

$$v_{\rm HP}(\varrho) = \frac{1}{4\mu} \frac{\partial p}{\partial z} \left(\varrho^2 - r^2 \right) = v_{\varrho=0} \left(1 - \frac{\varrho^2}{r^2} \right). \tag{1.4a}$$

The subscript "HP" refers to Hagen and Poiseuille, who independently derived this equation experimentally in the nineteenth century. Mean velocity is half the axial velocity, and writing $\partial p/\partial z$ as $-\Delta p/l$ (l being the cylinder length), volume flow is

$$Q_{\rm HP} = \frac{\pi r^4}{8\mu l} \Delta p \,. \tag{1.4b}$$

This last equation is analogous to Ohm's law in electrical circuits I = V/R, with flow rate Q, pressure difference Δp , and hydrodynamic resistance $8\mu l/(\pi r^4)$ corresponding to current I, voltage V, and resistance R, respectively. Based on this analogy, simplified hydrodynamic networks can be analyzed according to the rules of electric circuits.

Due to the motion of the fluid, stresses exist between fluid layers moving at different velocities, as depicted by the stress tensor T in the general Navier–Stokes equation (Equation 1.2a). The law of Hagen–Poiseuille directly shows the effect of this internal viscous friction: The higher the viscosity of the fluid, the shallower will be the velocity profile.

For incompressible, Newtonian fluids there is a linear dependency between strain and shear stress:

$$\tau_{ij} = \mu \left(\frac{\partial v_i}{\partial x_j} + \frac{\partial v_j}{\partial x_i} \right). \tag{1.5a}$$

In the cylindrical pipe of Hagen–Poiseuille, shear stress increases linearly towards the outer cylindrical fluid layers:

$$\tau_{\rm HP}(\varrho) = -\mu \frac{4Q}{\pi r^4} \varrho. \tag{1.5b}$$

At the blood-wall interface, flowing blood exerts shear stress on the vessel wall. As discussed above, the vascular tree exhibits power-law behavior, where the Murray model ($Q \propto r^3$) implies constant wall shear stress throughout the tree. Even though real vasculature deviates from this model (but so does flow), wall shear stress still is

considered an integral biomechanical trigger for blood vessels to grow or regress. Endothelial cells respond to the strain or stress that they experience. An increase in wall shear stress causes muscular vessels to dilate as explained in more detail below, which in turn usually reduces shear stress, depending on the network configuration. As further detailed below, both in vitro experiments on isolated vessels as well as observations during in vivo vessel adaptation such as arteriogenesis are suggestive of a control mechanism driving the arterial network towards a preferred (range of) wall shear stress. Methods facilitating the estimation of wall shear stress in vivo may provide information on the distribution of wall shear stress in large cohorts, thereby improving the understanding of the underlying mechanistic principles and deviations in various (pathological) conditions, possibly in the same subjects.

1.4 HEMODYNAMIC REGULATION

Balanced integrative local and global responses of biological systems and respective hemodynamics to mechanical, neurohumoral, and metabolic stimuli are designed to maintain homeostatic conditions. The main central mechanisms controlling blood pressure and cardiac output are regulation of arterial resistance, modification of blood volume (or more generally, mean systemic filling pressure), and alteration of heart rate and cardiac contractility. Mechanoreceptors at specific locations in the arterial and atrial wall play key roles here. Examples are the baro- and chemoreceptors in the aortic arch and the carotid arteries whose sensing of blood pressure and arterial oxygen tension form the base of the central control system of blood pressure.⁴²

In addition, mechanoreceptors in probably all arteries and arterioles are involved in local regulation of smooth muscle contractile activity and vascular structure, rendering mechanosensing and -transduction key events also in the local regulation of blood flow and microvascular pressure. The focus for the remainder of this thesis will be on these local rather than the central mechanisms.

1.4.1 Local control of blood flow

Homeostatic maintenance of tissue oxygen supply without damaging the cardio-vascular system is crucial. Tissue oxygenation basically can be influenced by three means: 1) changing the oxygen carrying capacity of blood, 2) altering oxygen extraction efficiency, and 3) modifying blood flow.⁴³ Additionally, blood flow can be diverted to regions with higher demands by shifting of resistances, which limits overall conductance rise. While the first method can prominently contribute in some species, e.g., in dogs, by adapting hemoglobin concentrations, its role is limited

in humans. ⁴⁴ The second method is certainly relevant. Oxygen extraction of skeletal muscles, for example, can increase from a rest rate of about 30–40% up to 80–90% under exercise. ⁴⁴ Myocardial oxygen extraction also rises with exercise, yet with limited reserve as the heart has a high rest demand with a rest extraction rate of about 60 to 80%. ^{44–46} Higher myocardial oxygen demand is therefore primarily matched by augmenting coronary blood flow, which can increase to 4–5-fold above resting blood flow during exercise. ⁴⁴ This signifies the pivotal role of blood flow regulation.

In most organs, but most noticeable in the coronary, cerebral, and renal circulations, an autoregulatory mechanism controls blood flow to match oxygen consumption. ⁴⁷ This implies that 1) blood flow increases with higher oxygen consumption, but also that 2) blood flow at constant oxygen demand is rather independent of blood pressure over a large range (roughly 40–150 mmHg). ^{42,45,48–50} Within this pressure range, a sudden increase in blood pressure causes a transient rise of blood flow. After a few seconds, blood flow returns towards initial values as vascular resistance is increased by augmenting vasomotor tone independently of neurohumoral control. ⁴⁵ Outside the autoregulatory limits, the active mechanisms become exhausted such that there is nearly a linear relationship between pressure and flow, representing the passive and, respectively, maximum active resistance during maximal vasodilation and -constriction at low, respectively high, pressures.

1.4.2 Vasomotor tone control

Regulation of vascular resistance is an integral part of blood flow control, where total resistance is determined both by the network structure and the resistance of the individual vessels. For the latter, vascular smooth muscle cells are the effectors of the various stimuli of vasomotor control. Vasoactive substances secreted by the endothelial cells, nervous activation, circulating vasoactive substances, and electrochemical signaling can trigger a cascade of auto- and paracrine signaling. In general, these mechanisms modulate vascular smooth muscle function by either altering the concentration of free calcium in the cytosol of the vascular smooth muscle cells, e.g., by depolarization and voltage-dependent calcium channels, or by changing the sensitivity of the contractile elements to calcium. Potassium channels emerge as critical contributors to vascular smooth muscle cell regulation as they affect the membrane potential. Opening of K_{ATP} or K_{Ca} channels causes hyperpolarization, which leads to closing of voltage-gated calcium channels, reducing influx of calcium with consequential vasodilation. Stimuli known to act via K_{ATP} channels

include nitric oxide (NO), prostacyclin, adenosine, and β_2 -adrenoceptors. 43 K_{Ca} channels could also provide a negative feedback mechanism for vasoconstriction as they are affected by increased intracellular calcium levels. 43 Both vasoconstrictors (e.g., endothelin-1, angiotensin II) and vasodilators such as nitric oxide and other endothelium-derived factors, adenosine, norepinephrine, and hydrogen ions act via K_{Ca} channels. 43 Voltage-gated K_V channels are sensitive to β -adrenoceptor stimulation and reactive oxygen species. 43

1.4.3 Blood pressure and wall stress as modulators of vasomotor tone

An important mechanical modulator of vasomotor tone is microvascular blood pressure. Due to the difference between intravascular and tissue pressure, the vessel is subjected to axial, radial, and circumferential (hoop) stress. Axial or longitudinal stress acts along the vessel axis, whereas the hoop stress is azimuthal invariant, acting tangentially along the vessel circumference as indicated in Figure 1.3. Embedding of the vessel in tissue also contributes to the axial stress and strain in vivo. Isolated vessels typically retract in length in comparison to their native environment, which can be attributed to the reduced axial stress ex vivo. Data on the effect of axial stress are scarce, but maintenance of a normal level seems to be part of controlling vessel length. ^{54,55}

In order to neither collapse nor explode despite the transmural pressure difference, the vessel wall needs to withstand the associated hoop stress (σ_{hoop}). Even though Lamé's approach for thick-walled cylinders seems more appropriate for blood vessels, Laplace's solution for thin-walled cylinders, typically requiring a diameter-to-wall thickness ratio greater than 20, is frequently used to illustrate the basic determinants:

$$\sigma_{\text{hoop}} = \frac{\Delta pr}{h} \,. \tag{1.6}$$

From this relation, one immediately recognizes that the hoop stress increases with increasing transmural pressure difference (Δp) and radius (r) and decreases with wall thickness (h). Interestingly, after an immediate passive distension, vessels respond with active constriction in response to an increased transmural pressure difference. Similarly, a decrease in pressure causes the vessel to dilate after a transient diameter reduction.⁴⁷ This so-called myogenic response is facilitated by vascular smooth muscle cells that modify their tone by adjusted calcium signaling⁵⁵ independent of the endothelium.⁵⁶ It is this behavior that leads to the hypothesis that vessels strive to regulate the hoop stress by adjusting their tone in response to changes.⁴⁷

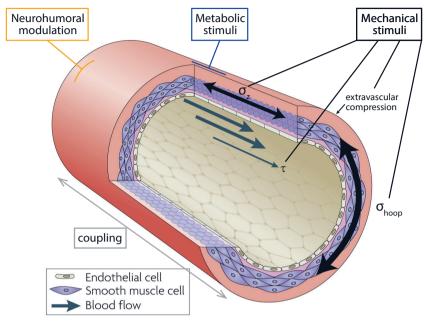


Figure 1.3: Sketch of an artery illustrating various stimuli. Blood exerts a shearing force (τ) on the endothelium along its flow direction. Blood pressure stresses the entire vessel wall $(\sigma_{\text{hoop}}, \sigma_z)$. The stimuli are transmitted and transduced to the vascular smooth muscles cells, which react by constriction or relaxation. Illustration adapted from Hahn & Schwartz⁵³ and Laughlin *et al.*⁴³

The radial stress is related to the hoop stress, but since it is much smaller, it is usually disregarded, and studies are lacking. It is important to note that even though vascular smooth muscle cells are the primary responders, these stresses act on all constituents of the vessel wall.

1.4.4 Blood flow and wall shear stress as modulators of vasomotor tone

Another important stimulus is local blood flow. Blood flowing along the inner surface of the vessel wall exerts a shearing force in the flow direction as described above, which results in stress and strain of the endothelium. Although the importance of shear stress for endothelial homeostasis is evident,⁵⁷ the exact mechanisms of shear stress sensing and mechanotransduction still need to be unraveled.⁵⁸ Absence of relaxation responses after removal of the endothelium⁵⁹ signifies that the endothelium is crucial for mechanosensing and signaling to the vascular smooth muscle cells.

As shear stress mainly acts as drag on the luminal surface of the endothelial cells, mechanosensors such as the glycocalyx and primary cilia are directly affected. But the forces are also transmitted throughout the cell as well as to attached structures giving rise to deformations and stresses. As such, the cytoskeleton along with cell junctions, gap junctions, and integrins are involved, as well as mechanosensing ion channels. An addition, mechanisms involving caveolar deformation the nucleus due to the hydrodynamic drag as it protrudes into the lumen have been suggested. By these means, an increase in shear stress triggers production of nitric oxide, prostacyclin, and — primarily in small vessels — endothelium-derived hyperpolarizing factors (EDHF), which relax the vascular smooth muscle cells via K_{ATP} and/or K_{Ca} channels.

1.4.5 Metabolic stimuli

Since an integral function of the circulation is to ensure the supply of all tissues with oxygen and nutrients, it is intuitive that a coupling between local metabolism and blood flow exists. The concept is that metabolites act on the vascular smooth muscle cells, in particular that an excess of metabolites causes vasodilation. The level of tissue oxygenation (pO₂) indeed is a very strong stimulus. In contrast, venous pO₂ seems to be less vital. A decrease in tissue pO₂ induces vasodilation by decreasing the cytosolic concentration of free calcium, with some support for an additional mechanism mediated by K_{ATP} channels. Yet, profound ischemia usually does not occur under normal physiological conditions. This mechanism becomes more relevant under pathophysiological conditions that induce ischemia. There is, for example, evidence for metabolic coronary vasodilation as myocardial pO₂ drops below a critical level. The evidence for metabolic coronary vasodilation as myocardial pO₂ drops below a critical level.

Also, an increase in carbon dioxide production evokes a rise of hydrogen ion concentration (H^+) and concomitant lowering of the pH, both of which have been proposed as initiator for the resulting vasodilation.⁶⁵

Adenosine, a product of adenosine triphosphate (ATP) usage, and reactive oxygen species are other potential metabolic vasodilators. The role of adenosine in controlling vasomotor tone has been highly debated and there exists a large amount of complex and contradictory literature.⁴³ Adenosine is a strong vasodilator, and myocardial adenosine secretion strongly increases with hypoxia severity,⁴⁷ particularly dilating the microcirculation.⁴⁴ The relevance of adenosine under rest conditions appears to be limited though.^{47,65} With respect to reactive oxygen species, direct relations between oxygen consumption and myocardial concentration of H₂O₂,

and between H_2O_2 and coronary blood flow have been shown.⁶⁵ Exogenously administered H_2O_2 produces vasodilation.⁴⁷ Together these findings suggest that H_2O_2 is a vasodilator acting in a feed forward manner.⁶⁵

Yet, the exact interactions of metabolic control remain unclear.⁶⁵ Experimental inhibition of one pathway does not per se compromise metabolic blood flow regulation,⁶ suggesting redundancy of synergistic mechanisms.⁴³

1.4.6 Neurohumoral modulation

Even though most vessels are innervated by the autonomic nervous system, this seems to contribute little to resting tone in the coronary circulation under physiological conditions. 6,46 It does, however, play a role during activation such as during exercise. The effect of sympathetic and parasympathetic activation is heterogeneous and appears to depend on transmitter concentration and distribution of receptors. Sympathetic activation of α -receptors of vascular smooth muscle cells elicits vasoconstriction, whereas stimulation of β -receptors causes vasodilation. The response is furthermore modulated by the endothelium, where adrenergic stimulation triggers vasodilatory mechanisms. Acetylcholine, acting via the muscarinic receptors, usually produces vasodilation in an endothelium-dependent fashion, but induces vasoconstriction after endothelial removal. 6,45,66 Other vasodilators include prostaglandins, which induce regional vasodilation. Quinines (e.g., bradykinin) and histamine also are arteriolar vasodilators that additionally increase vascular permeability. 42

At first view, existence of endogenous vasoconstrictors seems unnecessary. Yet, by counterbalancing vasodilatory mechanisms they do provide means to better finetune local responses in addition to satisfying global or regional needs. Endothelin-1 is a strong endogenous vasoconstrictor, probably abluminally released by the endothelium, thereby acting locally rather than in an endocrine, circulating fashion. 43 It can affect coronary resting tone, 46,67 but its overall effect appears to be modest under normal physiological conditions. 47,68

In addition to its renal action, angiotensin II is a potent vasoconstrictor as studies on isolated coronary arteries and arterioles and on in vivo administration have shown. ⁴⁷ Angiotensin II also stimulates production of vasopressin, another antidiuretic hormone. The vasomotor response to vasopressin is heterogeneous though, with microvascular constriction in arterioles smaller than 100 μm but vasodilation in larger arteries. 47,69

1.4.7 Sensitivity to these stimuli

While these fundamental mechanisms occur in all arterial vessels, their relative weight differs with vessel type and tissue as shown in Figure 1.4. Composition of the vessel wall, innervation, and the phenotypes of endothelial and vascular smooth muscle cells govern the relevance of the different mechanisms of vasomotor control.⁴³

The wall of large arteries contains large amounts of elastin, which decreases towards smaller vessels. Concomitantly, the number of smooth muscle cells in the media increases towards smaller vessels. ⁵⁵ The responsiveness to blood pressure reflects this difference in composition: the myogenic response is inherent to all vascular smooth muscle cells, yet the responsiveness increases with decreasing arteriolar diameter. ⁴³ In the coronaries, it is most effective in subepicardial arterioles smaller than 100 μm with subendocardial arterioles and arteries larger than 400 μm showing a modest reaction. ^{47,75}

Large arterioles of around 100 μm in diameter, on the other hand, are particularly sensitive to shear stress mediated dilation. This sensitivity decreases towards smaller arterioles but also in arteries. 5,43,76 Metabolic signals primarily act on the microcirculation, with greatest response in the smallest arterioles (smaller than 25 μm). Kuo et al. observed that the response to adenosine decreased with increasing diameter in coronary arterioles. 76

The responsiveness to sympathetic modulation is more divers. Most small arterioles are highly innervated and thus responsive to sympathetic modulation. Norepinephrine affects arteries and arterioles and to a small degree also venules and veins. Compared to the cerebral and coronary circulation, resting vasomotor tone is much higher in skeletal resistance arteries. This is partially due to the strong sympathetic stimulation in the latter as removal, e.g., by denervation, produces an increase in blood flow of 40-100%.

As can be appreciated by the marked pressure drop, most of the resistance resides in arterioles and small arteries.⁷⁸ These resistance vessels are therefore important controllers of blood flow. Additionally, downstream stimuli, such as metabolic factors, can lead to conducted vasomotor responses independent of flow.⁴³ Local regulation in response to a specific stimulus in addition induces up-stream changes. Vasodilation of the smallest arterioles due to hypoxia, for instance, lowers resistance, and the resulting augmented flow evokes upstream shear stress-mediated vasodilation.⁴³ Such mechanisms recruit the more upstream resistance vessels in regulation of blood flow.

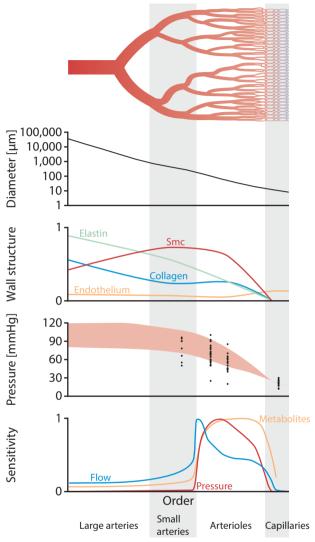


Figure 1.4: Paradigm of the structure and function of the arterial network. From the aorta, blood is distributed in a tree-like manner to the capillary mesh. The large arteries act as reservoir. The small arteries and arterioles, exhibiting the strongest pressure drop, control blood flow by adapting their diameters. Large arterioles are most sensitive to flow; the myogenic response is strongest in intermediate arterioles. Metabolites predominantly act on the smallest vessels. Smc = smooth muscle cells [The diameter curve and the wall content are based on data of [70] and [71], respectively. The pressure range (red area) is adapted from [72]; the individual data points are from [73]. The sensitivity curves are based on [74]].

Large arteries are less sensitive to changes in pressure or metabolism. They contribute little to overall resistance under normal physiological conditions, which is reflected by a small pressure drop.⁵

1.5 Adaptation of vascular structures

Sustained deviations induce physiological or pathological adaptations depending on the underlying cause as indicated in Figure 1.5. Wall stress and shear stress are important regulators of not only vasomotor tone but also of structural changes.

1.5.1 Role of wall stress in structural adaptation

It has been hypothesized that vessels strive towards a preferred range of either mechanical stress or strain both on the tissue as well as on the cell-matrix level. Large arteries indeed seem to seek a hoop stress of around 100 kPa.⁷⁹ Lamellar thickness is constant in the normotensive aorta, but in hypertension it is largest

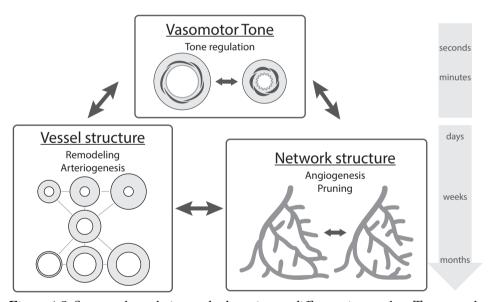


Figure 1.5: Structural regulation and adaptation at different time scales. Tone acutely regulates diameter, while long-lasting stimuli initiate structural adaptation of the vessel wall and network structure. These adaptations are strongly related. Sustained vasoconstriction, for example, causes inward remodeling, which eventually might result in pruning. Based on Pries *et al.*⁴⁶

in the sub-intimal region, where the hoop stress rises the strongest.⁸⁰ Also the nearly proportional relationship between aortic diameter and the number of elastic lamellae across various mammals suggests that development drives towards a nearly constant stress per lamella.⁸¹

So how can circumferential stress be controlled? The Laplace relation (Equation 1.6) indicates that a higher pressure requires either a thicker wall (hypertrophy) or a smaller lumen (inward remodeling) to normalize stress. Both responses are observed in hypertensive subjects and animal models. ⁸² Interestingly, the large arteries demonstrate hypertrophy, while inward remodeling is the dominant response in resistance vessels in most hypertensive models, with a varying contribution of wall hypertrophy, depending on the cause of hypertension. ^{83,84} The causes of this difference are not properly understood. These may relate to the weaker myogenic response and the higher elastic content in large vessels, resulting in increased distension. In resistance vessels, the myogenic response may maintain continuous vasoconstriction that provides a mold for inward remodeling. ⁸⁵ These responses are complicated by shear stress-dependent adaptation (below), which aims at maintaining inner diameter if flow was to remain constant in hypertension.

Control of axial stress seems subordinate. Circumferential and axial wall stress are coupled. Constant circumferential stress despite higher pressure would reduce axial stress unless the axial force changes as well,⁷⁹ matching observations in hypertensive arteries, which tend to retract less than normotensive ones when isolated from their tissue. ^{80,81}

1.5.2 Role of shear stress in structural adaptation

Endothelial cells respond to the experienced flow by changing their shape, orientation, polarization, and gene expression. Endothelial cells in static cultures have a polygonal shape with random orientation, whereas they align and elongate with laminar flow. Even though the precise response in cultured endothelial cells can differ with cell-line, endothelial cells in general become increasingly elongated with higher flow and thus shear stress levels, higher which goes hand in hand with a rearrangement of the intracellular stress fibers. These in vitro findings are corroborated by observations in arterial specimens, in which endothelial cells in "regular" flow regions (i.e., no large spatial or temporal variations) are aligned and elongated but exhibit random orientation with "cobblestone" shape in regions of "disturbed" flow, e.g., at bifurcations. Shear stress furthermore contributes to network stability. Endothelial cells migrate from regions with low flow to high-flow

regions, thereby enforcing pruning of low flow vessels and in turn stabilizing and assisting growth of vessels with high flow.^{58,86}

In addition, shear stress influences the transcriptional regulation of various processes, such as inflammation, cell cycle, cell apoptosis, and arterial/venous identity. In general, high (yet physiological, as extremely high levels are harmful) levels of shear stress promote atheroprotective gene expression, with antioxidant signaling and a quiescent phenotype, whereas low shear stress stimulates atherogenic gene expression. 91,94

Both prolonged decreased flow and hypertension are associated with inward remodeling. 95,96 Not only is there an inverse relationship between shear stress and lumen diameter, but there is also an inverse linear dependency of wall thickness and compliance on shear stress, 97 with regions of low shear stress having thicker vessel walls. 98 These adaptations are accompanied by cellular signaling, often including inflammatory processes. Low shear stress is thus not only promoting diameter reduction but also atherosclerotic processes. 99–104

It is important to note that neither wall stress nor shear stress is uniform. Both display temporal as well as spatial variations, in particular in arteries, where the pumping of the heart causes pulsations. The spatial variations imply that nearby segments encounter different stimuli. Temporal variations, on the other hand, affect endothelial cells individually, but are nonetheless relevant. Oscillatory shear stress, for example, also promotes proatherogenic gene expression similar to low steady shear stress. Palso, hoop stress returns to the normal range in distal vessels but not in the large conductive arteries, which are subjected to a much higher pulse pressure, indicating that pulsatility, i.e., cyclic stretching, modulates its set point.

1.5.3 Coupling between vasomotor tone and remodeling

It is striking that in resistance vessels many vasoconstrictors are also related to inward structural adaptation, while vasodilators are known to induce structural increases in diameter. Under prolonged elevated blood pressure levels, vessels sustain a smaller diameter even after return to baseline pressure. ^{55,106} In vitro, sustained vasoconstriction but not diameter reduction without tone provokes inward eutrophic remodeling of resistance arteries. ⁸⁵ This has generated the hypothesis that vascular tone itself is a major drive for structural adaptation. Under the so-called mold hypothesis, load is transferred away from the contractile elements during lasting vasoconstriction ⁵⁵ either by intracellular re-organization ¹⁰⁷ or by continuous addition of new components with length matching the current diameter. ¹⁰⁸ After

removal of the vasoconstrictive stimulus, this re-organization, respectively the new elements, limit relaxation with resulting reduced passive diameter, where such structural adaptions already begin within hours. 106

Altogether, structural adaptation of vascular diameter can thus be characterized by change of tone, lumen diameter, vascular wall mass or thickness as well as alteration of wall composition and arrangement.

1.6 ADAPTATION OF VASCULAR NETWORKS

Long-term increases in shear stress, such as under prolonged exercise training, lead to an increase in skeletal arteriolar density and size as well as capillary-to-fiber-ratio, ¹⁰⁹ indicating that not only the existing vessels remodel but that also the network structure adapts. In principle, one can discriminate between four types of such angioadaptation: vasculogenesis, angiogenesis, arteriogenesis, and vessel regression.

1.6.1 Vasculogenesis

Vasculogenesis describes the de novo formation of blood vessels from angiogenic progenitor cells. Originally, vasculogenesis denoted the differentiation of mesodermal cells into hemangioblasts, forming primitive blood islands with subsequent formation of the primary vascular plexus during embryogenesis. Recently, postnatal occurrence of vasculogenesis has been debated. Irrespective of the definition of vasculogenesis, there is evidence that endothelial progenitor cells contribute to angioadaptation also in the adult. 112

1.6.2 Angiogenesis

Closely related to vasculogenesis is angiogenesis, the sprouting of blood vessels from the existing vasculature. Angiogenesis is induced by hypoxia, which stimulates expression of angiogenic cytokines and growth factors such as vascular endothelial growth factor (VEGF) in a hypoxia-inducible factor 1 (HIF-1)-mediated manner. Some of these factors act locally on the vascular endothelial and smooth muscle cells. Circulating factors recruit various angiogenic cells, such as mesenchymal stem cells, from the bone marrow and from remote tissue. These cells home to the ischemic site, where they stimulate vascular remodeling. In the first type, intussusceptive angiogenesis, an existing vessel is longitudinally split by inward protrusion of endothelial cells from opposing sides, the sprouting of blood vessels are such as the proposition of endothelial cells from opposing sides, the sprouting of blood vessels are such as the proposition of blood vessels are such as the proposition of blood vessels are such as the proposition of blood vessels.

occur at regions of low wall shear stress. ⁸⁶ In sprouting angiogenesis, endothelial cells of capillaries protrude abluminally, whereas their apical membrane is subjected to inverse blebbing. ¹¹⁵ These so-called tip cells further elongate ("sprout") and divide until they make contact with another endothelial cell, merge, and re-align to form hollow tubes. ^{116,117} Rather than simple attraction to the angiogenic factors produced by the hypoxic cells, sprouting is directed by VEGF gradients, where positive gradients stimulate sprouting and negative ones dilation. ¹¹⁸ An additional cue comes from the pressure gradient. Interstitial flow seems to guide the sprouting towards vessels of higher pressure than at the sprout, ¹¹⁸ where the rate of sprouting is proportional to the pressure difference. ¹¹⁹ However, also mechanical stretch seems to be a cue as static stretching stimulated parallel vessel formation in contrast to a predominantly diagonal orientation under cyclic stretching. ¹²⁰

1.6.3 Arteriogenesis

Arteriogenesis can be viewed as a special case of structural regulation of the vascular diameter. It refers to the process during which arterioles or small arteries increase their lumen area and wall thickness, i.e., they outward remodel, usually in response to an increase in wall shear stress. ¹²¹ Elevated levels of wall shear stress activate molecular pathways initiating proliferation of endothelial and smooth muscle cells as well as augmentation of the vascular permeability. ¹²² This leads to increased monocyte attraction and adherence to the wall by chemoattractive proteins such as vascular cell adhesion molecule 1 (VCAM-1), intracellular adhesion molecule 1 (ICAM-1), monocyte chemoattractant protein 1 (MCP-1), and transforming growth factor beta (TGF- β). The monocytes migrate into the vessel wall, where they differentiate to macrophages secreting inflammatory cytokines as tumor necrosis factor-alpha (TNF- α), growth factors, e.g., fibroblast growth factor (FGF-2), and matrix metalloproteinases (MMP). ¹²³ Degradation of the vessel wall structure, re-organization, and reinforcement (maturation) of the new structure follow.

Arteriogenesis is most noticeable after occlusion (or experimental ligation) of an artery causing diversion of blood flow through pre-existing pathways that bypass the site of occlusion. These arterioles or small arteries typically carry little flow before the occlusion and experience a strong increase in wall shear stress after occlusion. Over the course of days to months, they can increase by up to a factor 20 in diameter. ¹²⁴ Initially, all pre-existing bypasses enlarge, but with time, most regress again such that only few large pathways remain. ^{125,126} There is evidence for innate existence of such bypasses, called collateral vessels, ¹²⁷ even though the prevalence and responsiveness

of these collaterals is highly variable^{128,129} and can be diminished in pathologic conditions such as diabetes¹³⁰ or with aging¹³¹. Well-developed collaterals can prevent myocardial ischemia during coronary occlusion and are associated with reduced mortality in patients with myocardial infarction.^{129,132}

1.6.4 Pruning

To ensure a functional network, the angiopromotive processes described above need to be counterbalanced by regressive mechanisms. Low wall shear stress promotes vasoconstriction and migration of endothelial cells, ⁸⁶ which stimulates inflammatory processes associated with wall remodeling in the most extreme case leading to apoptosis and collapse of the vessel. ⁹³ Without these balancing mechanisms, a dysfunctional microcirculation containing shunts is formed that is characterized by heterogeneous, maldistributed blood flow. ¹³³ Also pathologies, e.g., hypertension and diabetes, can cause aberrant networks by microvascular rarefaction. ¹³⁴

1.7 AIM AND OUTLINE OF THIS THESIS

Even though many mechanisms regulating vascular network design by local hemodynamic forces have been unraveled, they represent multiple tesserae that do not yet complete the overall picture. Inspired by the work of Murray, wall shear stress has long been thought to be the controlled variable. Shear stress, however, varies throughout the circulation, with typically much lower values in veins (0.1–0.6 Pa) than in arteries (1–2 Pa). The view of constant wall shear stress has accordingly been altered, by suggesting that wave reflections, en expression, or pressure modulate the set point. Circumferential wall stress, on the other hand, is also heterogeneous. The question thus remains how the various mechanisms interact and what variable(s) are eventually controlled.

The vascular network is not a static, a priori determined structure but rather dynamically adapting. Aging, exercise, dysfunctions as diabetes and hyperlipidemia, but also occlusive events dynamically affect not only selected local sites but also the network as whole. The vascular structural regulation outlined above is hence thought to direct the development of the vascular network structure. Studying the network design can thus help unraveling vascular regulation. Multi-scale three-dimensional quantitative data on vascular networks are scarce though. Modeling the hemodynamics and network adaptation can furthermore assist experimental studies in separating the effect of different mechanisms.

The aim of this thesis was to advance our understanding of vascular network design by further developing tools for collecting comprehensive anatomical data sets and generating detailed multi-scale representations of arterial networks with focus on adaptation of collateral vessels.

The first part of this thesis focuses on arterial networks. Understanding the dynamics of adapting networks provides a direct first insight into the course of remodeling. In addition, extensive experimental data serve as input for modeling studies to test what has driven this particular network design.

Chapter 2 provides an overview of current methods for imaging vascular networks and perfusion of organs, in particular the heart. This chapter also discusses modeling approaches to study structure—function relationships.

One of the presented tools, the imaging cryomicrotome, is utilized in Chapters 3 and 4 to obtain detailed reconstructions of arterial networks. A method to image and reconstruct the remodeling arterial network in a model of rat hindlimb ischemia is presented in Chapter 3, whereby several deep collateral pathways could be discerned that are missed with superficial imaging methods.

In Chapter 4, the coronary arterial tree of a human heart is reconstructed at great detail, and hemodynamic simulations are used to assess structure—function relationships. Network characteristics were found to be far from uniform and in fact changing with diameter.

The second part of this thesis focuses on one important stimulus of vascular regulation, wall shear stress. Two methods to estimate wall shear stress in vivo are presented, which may facilitate assessment in large clinical studies.

The first method (Chapter 5) expands simple Poiseuille-based wall shear stress estimation to pulsatile flow. In a cohort of 45 patients, this method better captured the oscillatory nature of shear stress and showed a good correlation with carotid mean wall thickness while maintaining good reproducibility.

Chapter 6 examines whether structure–function relations can replace invasive measurements for wall shear stress simulations in the human coronary arteries. Computational fluid dynamics (CFD) predictions based on scaling laws exhibited wall shear stress patterns comparable to those based on invasive flow measurements although the absolute magnitude differed.

The findings and conclusions of this thesis, including a discourse on the meaning of "collateral vessel", are discussed in Chapter 7.

REFERENCES

- 1. World health statistics 2020: monitoring health for the SDGs, sustainable development goals (World Health Organization, Geneva, 2020).
- 2. Virani, S. S. *et al.* Heart Disease and Stroke Statistics-2020 Update: A Report From the American Heart Association. *Circulation* **141**, e139–e596. doi:10.1161/CIR.0000000000000757 (2020).
- 3. Timmis, A. *et al.* European Society of Cardiology: Cardiovascular Disease Statistics 2019. *Eur Heart J* **41**, 12–85. doi:10.1093/eurheartj/ehz859 (2020).
- 4. Global Health Estimates 2016: Deaths by Cause, Age, Sex, by Country and by Region, 2000-2016 (World Health Organization, Geneva, 2018).
- 5. Camici, P. G. & Crea, F. Coronary microvascular dysfunction. *N Engl J Med* **356**, 830–840. doi:10.1056/NEJMra061889 (2007).
- 6. Duncker, D. J., Koller, A., Merkus, D. & Canty J. M., J. Regulation of coronary blood flow in health and ischemic heart disease. *Prog Cardiovasc Dis* 57, 409–422. doi:10.1016/j.pcad.2014.12.002 (2015).
- 7. Potter, R. F. & Groom, A. C. Capillary diameter and geometry in cardiac and skeletal muscle studied by means of corrosion casts. *Microvasc Res* **25**, 68–84. doi:10.1016/0026-2862(83)90044-4 (1983).
- 8. LadyofHats, Public domain, via Wikimedia Commons. https://commons.wikimedia.org/wiki/File:Circulatory_System_no_tags.svg (Oct. 3, 2020).
- 9. Duvernoy, H. M., Delon, S. & Vannson, J. L. Cortical blood vessels of the human brain. *Brain Res Bull* 7, 519–579. doi:10.1016/0361-9230(81)90007-1 (1981).
- Meyer, E. P., Ulmann-Schuler, A., Staufenbiel, M. & Krucker, T. Altered morphology and 3D architecture of brain vasculature in a mouse model for Alzheimer's disease. *Proc Natl Acad Sci U S A* 105, 3587–3592. doi:10.1073/pnas.0709788105 (2008).
- 11. Gray, H. & Lewis, W. H. *Anatomy of the human body* (Lea & Febiger, Philadelphia, 1918).
- 12. Pabst, A. M., Ackermann, M., Wagner, W., Haberthur, D., Ziebart, T. & Konerding, M. A. Imaging angiogenesis: Perspectives and opportunities in tumour research A method display. *J Craniomaxillofac Surg* **42**, 915–923. doi:10.1016/j.jcms.2014.01.010 (2014).
- 13. Young, T. The Croonian Lecture: On the Functions of the Heart and Arteries. *Philosophical Transactions of the Royal Society of London* **99**, 1–31. doi:10.1098/rstl. 1809.0001 (1809).

- 14. Thoma, R. Über den Verzweigungsmodus der Arterien. *Archiv für Entwicklungs-mechanik der Organismen* **12**, 352–413. doi:10.1007/BF02153043 (1901).
- 15. Murray, C. D. The Physiological Principle of Minimum Work: I. The Vascular System and the Cost of Blood Volume. *Proc Natl Acad Sci U S A* **12**, 207–214. doi:10.1073/pnas.12.3.207 (1926).
- Cohn, D. L. Optimal systems: I. The vascular system. Bull Math Biophys 16, 59–74. doi:10.1007/bf02481813 (1954).
- 17. Uylings, H. B. Optimization of diameters and bifurcation angles in lung and vascular tree structures. *Bull Math Biol* **39**, 509–520. doi:10.1007/bf02461198 (1977).
- 18. West, G. B., Brown, J. H. & Enquist, B. J. A general model for the origin of allometric scaling laws in biology. *Science* **276**, 122–126. doi:10.1126/science. 276.5309.122 (1997).
- 19. Kozłowski, J. & Konarzewski, M. Is West, Brown and Enquist's Model of Allometric Scaling Mathematically Correct and Biologically Relevant? *Funct Ecol* **18**, 283–289. doi:10.1111/j.0269-8463.2004.00830.x (2004).
- 20. Seiler, C., Kirkeeide, R. L. & Gould, K. L. Basic structure-function relations of the epicardial coronary vascular tree. Basis of quantitative coronary arteriography for diffuse coronary artery disease. *Circulation* **85**, 1987–2003. doi:10.1161/01.cir. 85.6.1987 (1992).
- 21. Huo, Y. & Kassab, G. S. Scaling laws of coronary circulation in health and disease. *J Biomech* **49**, 2531–2539. doi:10.1016/j.jbiomech.2016.01.044 (2016).
- 22. Kassab, G. S. Scaling laws of vascular trees: of form and function. *Am J Physiol Heart Circ Physiol* **290**, H894–H903. doi:10.1152/ajpheart.00579.2005 (2006).
- 23. Huo, Y. & Kassab, G. S. A scaling law of vascular volume. *Biophys J* **96**, 347–353. doi:10.1016/j.bpj.2008.09.039 (2009).
- 24. Zhou, Y., Kassab, G. S. & Molloi, S. On the design of the coronary arterial tree: a generalization of Murray's law. *Phys Med Biol* **44**, 2929–2945. doi:10.1088/0031–9155/44/12/306 (1999).
- 25. Huo, Y. & Kassab, G. S. The scaling of blood flow resistance: from a single vessel to the entire distal tree. *Biophys J* **96**, 339–346. doi:10.1016/j.bpj.2008.09.038 (2009).
- 26. Huo, Y. & Kassab, G. S. Intraspecific scaling laws of vascular trees. *J R Soc Interface* **9**, 190–200. doi:10.1098/rsif.2011.0270 (2012).
- 27. Zamir, M., Sinclair, P. & Wonnacott, T. H. Relation between diameter and flow in major branches of the arch of the aorta. *J Biomech* **25**, 1303–1310. doi:10.1016/0021-9290(92)90285-9 (1992).

- 28. Mittal, N. et al. Analysis of blood flow in the entire coronary arterial tree. Am J Physiol Heart Circ Physiol 289, H439-H446. doi:10.1152/ajpheart.00730.2004 (2005).
- 29. Zhou, Y., Kassab, G. S. & Molloi, S. In vivo validation of the design rules of the coronary arteries and their application in the assessment of diffuse disease. *Phys Med Biol* **47**, 977–993. doi:10.1088/0031-9155/47/6/309 (2002).
- 30. VanBavel, E. & Spaan, J. A. Branching patterns in the porcine coronary arterial tree. Estimation of flow heterogeneity. *Circ Res* **71**, 1200–1212. doi:10.1161/01.res.71.5.1200 (1992).
- 31. Sherman, T. F. On connecting large vessels to small. The meaning of Murray's law. *J Gen Physiol* **78**, 431–453. doi:10.1085/jgp.78.4.431 (1981).
- 32. Beard, D. A. & Bassingthwaighte, J. B. The fractal nature of myocardial blood flow emerges from a whole-organ model of arterial network. *J Vasc Res* **37**, 282–296. doi:10.1159/000025742 (2000).
- 33. Huo, Y. *et al.* CT-based diagnosis of diffuse coronary artery disease on the basis of scaling power laws. *Radiology* **268**, 694–701. doi:10.1148/radiol.13122181 (2013).
- 34. Schoenenberger, A. W. *et al.* Deviation from Murray's law is associated with a higher degree of calcification in coronary bifurcations. *Atherosclerosis* **221**, 124–130. doi:10.1016/j.atherosclerosis.2011.12.040 (2012).
- 35. Zamir, M. On fractal properties of arterial trees. *J Theor Biol* **197**, 517–526. doi:10. 1006/jtbi.1998.0892 (1999).
- 36. Oechtering, T. H. *et al.* Time-resolved 3-dimensional magnetic resonance phase contrast imaging (4D Flow MRI) reveals altered blood flow patterns in the ascending aorta of patients with valve-sparing aortic root replacement. *J Thorac Cardiovasc Surg* **159**, 798–810.e1. doi:10.1016/j.jtcvs.2019.02.127 (2020).
- 37. Harloff, A. & Markl, M. In vivo wall shear stress patterns in carotid bifurcations assessed by 4D MRI. *Perspectives in Medicine* 1, 137–138. doi:10.1016/j.permed. 2012.03.019 (2012).
- 38. Markl, M. *et al.* In vivo wall shear stress distribution in the carotid artery: effect of bifurcation geometry, internal carotid artery stenosis, and recanalization therapy. *Circ Cardiovasc Imaging* **3**, 647–655. doi:10.1161/CIRCIMAGING.110.958504 (2010).
- 39. Bessonov, N., Sequeira, A., Simakov, S., Vassilevskii, Y. & Volpert, V. Methods of blood flow modelling. *Math Model Nat Phenom* 11, 1–25. doi:10.1051/mmnp/201611101 (2016).

- 40. Womersley, J. R. Method for the calculation of velocity, rate of flow and viscous drag in arteries when the pressure gradient is known. *J Physiol* **127**, 553–563. doi:10.1113/jphysiol.1955.sp005276 (1955).
- 41. Davies, P. F. Flow-mediated endothelial mechanotransduction. *Physiol Rev* **75**, 519–560. doi:10.1152/physrev.1995.75.3.519 (1995).
- 42. Hick, C. & Hick, A. *Kurzlehrbuch Physiologie* 8th ed. (Urban & Fischer Verlag, München, 2017).
- 43. Laughlin, M. H. *et al.* Peripheral circulation. *Compr Physiol* **2**, 321–447. doi:10. 1002/cphy.c100048 (2012).
- 44. Duncker, D. J. & Bache, R. J. Regulation of coronary blood flow during exercise. *Physiol Rev* 88, 1009–1086. doi:10.1152/physrev.00045.2006 (2008).
- 45. Feigl, E. O. Coronary physiology. *Physiol Rev* **63**, 1–205. doi:10.1152/physrev. 1983.63.1.1 (1983).
- 46. Pries, A. R. *et al.* Coronary vascular regulation, remodelling, and collateralization: mechanisms and clinical implications on behalf of the working group on coronary pathophysiology and microcirculation. *Eur Heart J* **36**, 3134–3146. doi:10.1093/eurheartj/ehv100 (2015).
- 47. Goodwill, A. G., Dick, G. M., Kiel, A. M. & Tune, J. D. Regulation of Coronary Blood Flow. *Compr Physiol* 7, 321–382. doi:10.1002/cphy.c160016 (2017).
- 48. Mosher, P., Ross J., J., McFate, P. A. & Shaw, R. F. Control of Coronary Blood Flow by an Autoregulatory Mechanism. *Circ Res* 14, 250–259. doi:10.1161/01.res.14.3.250 (1964).
- 49. Rubio, R. & Berne, R. M. Regulation of coronary blood flow. *Prog Cardiovasc Dis* **18**, 105–122. doi:10.1016/0033-0620(75)90001-8 (1975).
- 50. Vergroesen, I., Noble, M. I., Wieringa, P. A. & Spaan, J. A. Quantification of O2 consumption and arterial pressure as independent determinants of coronary flow. *Am J Physiol Heart Circ Physiol* **252**, H545–H553. doi:10.1152/ajpheart.1987. 252.3.H545 (1987).
- 51. Tykocki, N. R., Boerman, E. M. & Jackson, W. F. Smooth Muscle Ion Channels and Regulation of Vascular Tone in Resistance Arteries and Arterioles. *Compr Physiol* 7, 485–581. doi:10.1002/cphy.c160011 (2017).
- 52. Fang, Y., Wu, D. & Birukov, K. G. Mechanosensing and Mechanoregulation of Endothelial Cell Functions. *Compr Physiol* **9**, 873–904. doi:10.1002/cphy.c180020 (2019).
- 53. Hahn, C. & Schwartz, M. A. Mechanotransduction in vascular physiology and atherogenesis. *Nat Rev Mol Cell Biol* **10**, 53–62. doi:10.1038/nrm2596 (2009).

- 54. Hoefer, I. E., den Adel, B. & Daemen, M. J. A. P. Biomechanical factors as triggers of vascular growth. *Cardiovasc Res* **99**, 276–283. doi:10.1093/cvr/cvt089 (2013).
- 55. Van den Akker, J., Schoorl, M. J., Bakker, E. N. & vanBavel, E. Small artery remodeling: current concepts and questions. *J Vasc Res* 47, 183–202. doi:10.1159/000255962 (2010).
- 56. Kuo, L., Chilian, W. M. & Davis, M. J. Coronary arteriolar myogenic response is independent of endothelium. *Circ Res* **66**, 860–866. doi:10.1161/01.res.66.3.860 (1990).
- 57. Chien, S., Li, S. & Shyy, Y. J. Effects of mechanical forces on signal transduction and gene expression in endothelial cells. *Hypertension* **31,** 162–169. doi:10.1161/01.hyp.31.1.162 (1998).
- 58. Roux, E., Bougaran, P., Dufourcq, P. & Couffinhal, T. Fluid Shear Stress Sensing by the Endothelial Layer. *Front Physiol* 11, 861. doi:10.3389/fphys.2020.00861 (2020).
- 59. Rubanyi, G. M., Romero, J. C. & Vanhoutte, P. M. Flow-induced release of endothelium-derived relaxing factor. *Am J Physiol Heart Circ Physiol* **250**, H1145–H1149. doi:10.1152/ajpheart.1986.250.6.H1145 (1986).
- 60. Reneman, R. S., Arts, T. & Hoeks, A. P. Wall shear stress—an important determinant of endothelial cell function and structure—in the arterial system in vivo. Discrepancies with theory. *J Vasc Res* **43**, 251–269. doi:10.1159/000091648 (2006).
- 61. Chistiakov, D. A., Orekhov, A. N. & Bobryshev, Y. V. Effects of shear stress on endothelial cells: go with the flow. *Acta Physiol* **219**, 382–408. doi:10.1111/apha.12725 (2017).
- 62. Shihata, W. A., Michell, D. L., Andrews, K. L. & Chin-Dusting, J. P. Caveolae: A Role in Endothelial Inflammation and Mechanotransduction? *Front Physiol* 7, 628. doi:10.3389/fphys.2016.00628 (2016).
- 63. Frangos, J. A., Eskin, S. G., McIntire, L. V. & Ives, C. L. Flow effects on prostacyclin production by cultured human endothelial cells. *Science* **227**, 1477–1479. doi:10.1126/science.3883488 (1985).
- 64. Qiu, Y., Myers, D. R. & Lam, W. A. The biophysics and mechanics of blood from a materials perspective. *Nat Rev Mater* **4,** 294–311. doi:10.1038/s41578-019-0099-y (2019).
- 65. Deussen, A., Ohanyan, V., Jannasch, A., Yin, L. & Chilian, W. Mechanisms of metabolic coronary flow regulation. *J Mol Cell Cardiol* **52**, 794–801. doi:10.1016/j.yjmcc.2011.10.001 (2012).

- Gericke, A. et al. Role of M₁, M₃, and M₅ muscarinic acetylcholine receptors in cholinergic dilation of small arteries studied with gene-targeted mice. Am J Physiol Heart Circ Physiol 300, H1602–H1608. doi:10.1152/ajpheart.00982.2010 (2011).
- 67. Merkus, D., Houweling, B., Mirza, A., Boomsma, F., van den Meiracker, A. H. & Duncker, D. J. Contribution of endothelin and its receptors to the regulation of vascular tone during exercise is different in the systemic, coronary and pulmonary circulation. *Cardiovasc Res* **59**, 745–754. doi:10.1016/s0008-6363(03)00479-6 (2003).
- 68. Rapoport, R. M. & Merkus, D. Endothelin-1 Regulation of Exercise-Induced Changes in Flow: Dynamic Regulation of Vascular Tone. *Front Pharmacol* **8**, 517. doi:10.3389/fphar.2017.00517 (2017).
- 69. Marcus, M. L., Chilian, W. M., Kanatsuka, H., Dellsperger, K. C., Eastham, C. L. & Lamping, K. G. Understanding the coronary circulation through studies at the microvascular level. *Circulation* 82, 1–7. doi:10.1161/01.cir.82.1.1 (1990).
- 70. Kassab, G. S., Rider, C. A., Tang, N. J. & Fung, Y. C. Morphometry of pig coronary arterial trees. *Am J Physiol Heart Circ Physiol* **265**, H350–H365. doi:10.1152/ajpheart.1993.265.1.H350 (1993).
- 71. Boron, W. F. & Boulpaep, E. L. Medical Physiology 3rd ed. (Elsevier, 2017).
- 72. Patton, K. T. Anatomy and physiology 9th ed. (Elsevier, St. Louis, Missouri, 2016).
- 73. Christensen, K. L. & Mulvany, M. J. Location of resistance arteries. *J Vasc Res* **38**, 1–12. doi:10.1159/000051024 (2001).
- 74. Kuo, L., Davis, M. J. & Chilian, W. M. Endothelial modulation of arteriolar tone. *Physiology* **7**, 5–9. doi:10.1152/physiologyonline.1992.7.1.5 (1992).
- 75. Kuo, L., Chilian, W. M. & Davis, M. J. Interaction of pressure- and flow-induced responses in porcine coronary resistance vessels. *Am J Physiol Heart Circ Physiol* **261**, H1706–H1715. doi:10.1152/ajpheart.1991.261.6.H1706 (1991).
- 76. Kuo, L., Davis, M. J. & Chilian, W. M. Longitudinal gradients for endothelium-dependent and -independent vascular responses in the coronary microcirculation. *Circulation* **92**, 518–525. doi:10.1161/01.cir.92.3.518 (1995).
- 77. Pi, X., Xie, L. & Patterson, C. Emerging Roles of Vascular Endothelium in Metabolic Homeostasis. *Circ Res* **123**, 477–494. doi:10.1161/CIRCRESAHA.118.313237 (2018).
- Chilian, W. M., Layne, S. M., Klausner, E. C., Eastham, C. L. & Marcus, M. L. Redistribution of coronary microvascular resistance produced by dipyridamole. *Am J Physiol Heart Circ Physiol* 256, H383–H390. doi:10.1152/ajpheart.1989.256.2.H383 (1989).

- 79. Humphrey, J. D. Mechanisms of arterial remodeling in hypertension: coupled roles of wall shear and intramural stress. *Hypertension* **52**, 195–200. doi:10.1161/HYPERTENSIONAHA.107.103440 (2008).
- 80. Hayashi, K. & Naiki, T. Adaptation and remodeling of vascular wall; biomechanical response to hypertension. *J Mech Behav Biomed Mater* **2**, 3–19. doi:10.1016/j.jmbbm.2008.05.002 (2009).
- 81. Humphrey, J. D. Vascular adaptation and mechanical homeostasis at tissue, cellular, and sub-cellular levels. *Cell Biochem Biophys* **50**, 53–78. doi:10.1007/s12013-007-9002-3 (2008).
- 82. Schiffrin, E. L. How Structure, Mechanics, and Function of the Vasculature Contribute to Blood Pressure Elevation in Hypertension. *Can J Cardiol* **36**, 648–658. doi:10.1016/j.cjca.2020.02.003 (2020).
- 83. Brown, I. A. M. *et al.* Vascular Smooth Muscle Remodeling in Conductive and Resistance Arteries in Hypertension. *Arterioscler Thromb Vasc Biol* **38**, 1969–1985. doi:10.1161/ATVBAHA.118.311229 (2018).
- 84. Laurent, S. & Boutouyrie, P. The structural factor of hypertension: large and small artery alterations. *Circ Res* **116**, 1007–1021. doi:10.1161/CIRCRESAHA.116.303596 (2015).
- 85. Bakker, E. N. T. P., van der Meulen, E. T., van den Berg, B. M., Everts, V., Spaan, J. A. & VanBavel, E. Inward remodeling follows chronic vasoconstriction in isolated resistance arteries. *J Vasc Res* **39**, 12–20. doi:10.1159/000048989 (2002).
- 86. Campinho, P., Vilfan, A. & Vermot, J. Blood Flow Forces in Shaping the Vascular System: A Focus on Endothelial Cell Behavior. *Front Physiol* 11, 552. doi:10.3389/fphys.2020.00552 (2020).
- 87. Topper, J. N. & Gimbrone M. A., J. Blood flow and vascular gene expression: fluid shear stress as a modulator of endothelial phenotype. *Mol Med Today* **5**, 40–46. doi:10.1016/s1357-4310(98)01372-0 (1999).
- 88. Jufri, N. F., Mohamedali, A., Avolio, A. & Baker, M. S. Mechanical stretch: physiological and pathological implications for human vascular endothelial cells. *Vasc Cell* 7, 8. doi:10.1186/s13221-015-0033-z (2015).
- 89. Barbee, K. A., Davies, P. F. & Lal, R. Shear stress-induced reorganization of the surface topography of living endothelial cells imaged by atomic force microscopy. *Circ Res* **74**, 163–171. doi:10.1161/01.res.74.1.163 (1994).
- 90. Levesque, M. J. & Nerem, R. M. The elongation and orientation of cultured endothelial cells in response to shear stress. *J Biomech Eng* **107**, 341–347. doi:10.1115/1.3138567 (1985).
- 91. Malek, A. M., Alper, S. L. & Izumo, S. Hemodynamic shear stress and its role in atherosclerosis. *JAMA* **282**, 2035–2042. doi:10.1001/jama.282.21.2035 (1999).

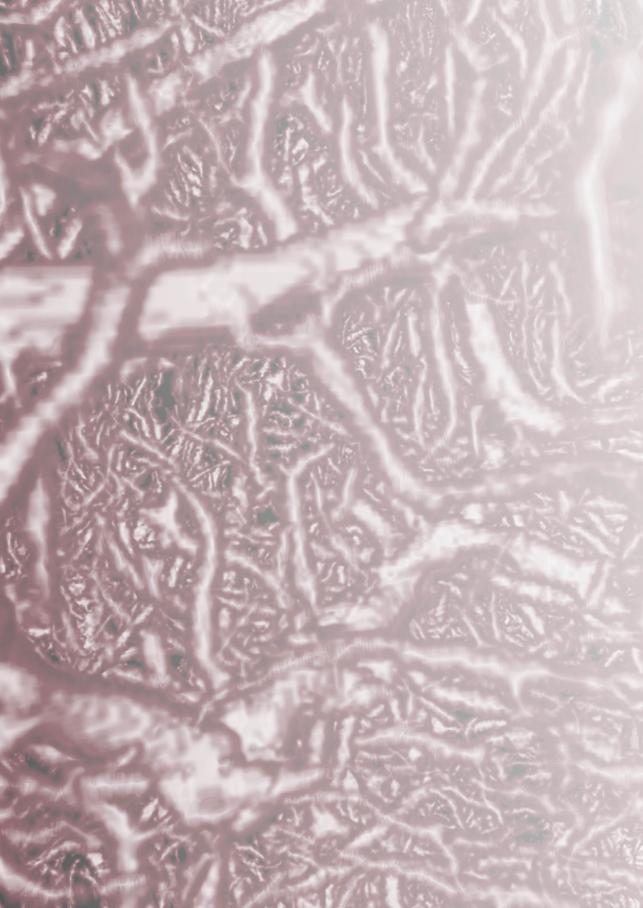
- 92. Chiu, J. J. & Chien, S. Effects of disturbed flow on vascular endothelium: pathophysiological basis and clinical perspectives. *Physiol Rev* **91**, 327–387. doi:10.1152/physrev.00047.2009 (2011).
- 93. Souilhol, C. *et al.* Endothelial responses to shear stress in atherosclerosis: a novel role for developmental genes. *Nat Rev Cardiol* **17**, 52–63. doi:10.1038/s41569-019-0239-5 (2020).
- 94. Baeyens, N., Bandyopadhyay, C., Coon, B. G., Yun, S. & Schwartz, M. A. Endothelial fluid shear stress sensing in vascular health and disease. *J Clin Invest* **126**, 821–828. doi:10.1172/JCI83083 (2016).
- 95. Langille, B. L. & O'Donnell, F. Reductions in arterial diameter produced by chronic decreases in blood flow are endothelium-dependent. *Science* **231**, 405–407. doi:10.1126/science.3941904 (1986).
- 96. Mulvany, M. J. Small artery remodelling in hypertension. *Basic Clin Pharmacol Toxicol* **110**, 49–55. doi:10.1111/j.1742-7843.2011.00758.x (2012).
- 97. Duivenvoorden, R. *et al.* Endothelial shear stress: a critical determinant of arterial remodeling and arterial stiffness in humans—a carotid 3.0-T MRI study. *Circ Cardiovasc Imaging* **3**, 578–585. doi:10.1161/CIRCIMAGING.109.916304 (2010).
- 98. Friedman, M. H., Hutchins, G. M., Brent Bargeron, C., Deters, O. J. & Mark, F. F. Correlation between intimal thickness and fluid shear in human arteries. *Atherosclerosis* **39**, 425–436. doi:10.1016/0021-9150(81)90027-7 (1981).
- 99. Caro, C. G., Fitz-Gerald, J. M. & Schroter, R. C. Arterial wall shear and distribution of early atheroma in man. *Nature* **223**, 1159–1160. doi:10.1038/2231159a0 (1969).
- 100. Cecchi, E. *et al.* Role of hemodynamic shear stress in cardiovascular disease. *Atheroscle-rosis* **214**, 249–256. doi:10.1016/j.atherosclerosis.2010.09.008 (2011).
- 101. Chatzizisis, Y. S., Coskun, A. U., Jonas, M., Edelman, E. R., Feldman, C. L. & Stone, P. H. Role of endothelial shear stress in the natural history of coronary atherosclerosis and vascular remodeling: molecular, cellular, and vascular behavior. *J Am Coll Cardiol* **49**, 2379–2393. doi:10.1016/j.jacc.2007.02.059 (2007).
- 102. Cunningham, K. S. & Gotlieb, A. I. The role of shear stress in the pathogenesis of atherosclerosis. *Lab Invest* **85**, 9–23. doi:10.1038/labinvest.3700215 (2005).
- 103. Ku, D. N., Giddens, D. P., Zarins, C. K. & Glagov, S. Pulsatile flow and atherosclerosis in the human carotid bifurcation. Positive correlation between plaque location and low oscillating shear stress. *Arterioscler Thromb Vasc Biol* 5, 293–302. doi:10.1161/01.ATV.5.3.293 (1985).
- 104. Wentzel, J. J., Chatzizisis, Y. S., Gijsen, F. J., Giannoglou, G. D., Feldman, C. L. & Stone, P. H. Endothelial shear stress in the evolution of coronary atherosclerotic plaque and vascular remodelling: current understanding and remaining questions. *Cardiovasc Res* **96**, 234–243. doi:10.1093/cvr/cvs217 (2012).

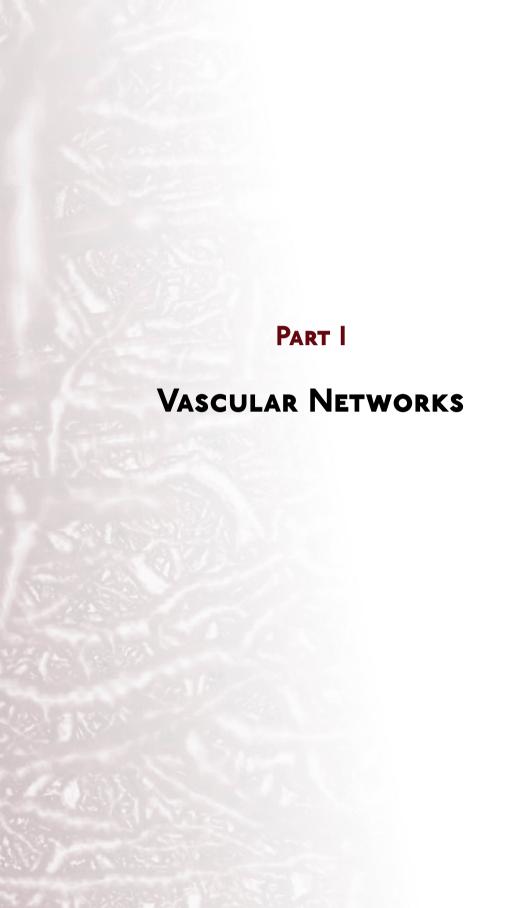
- 105. Brooks, A. R., Lelkes, P. I. & Rubanyi, G. M. Gene expression profiling of human aortic endothelial cells exposed to disturbed flow and steady laminar flow. *Physiol Genomics* **9**, 27–41. doi:10.1152/physiolgenomics.00075.2001 (2002).
- 106. Martinez-Lemus, L. A., Hill, M. A., Bolz, S. S., Pohl, U. & Meininger, G. A. Acute mechanoadaptation of vascular smooth muscle cells in response to continuous arteriolar vasoconstriction: implications for functional remodeling. *FASEB J* 18, 708–710. doi:10.1096/fj.03-0634fje (2004).
- 107. Martinez-Lemus, L. A., Hill, M. A. & Meininger, G. A. The plastic nature of the vascular wall: a continuum of remodeling events contributing to control of arteriolar diameter and structure. *Physiology* **24**, 45–57. doi:10.1152/physiol.00029.2008 (2009).
- 108. VanBavel, E., Bakker, E. N., Pistea, A., Sorop, O. & Spaan, J. A. Mechanics of microvascular remodeling. *Clin Hemorheol Microcirc* **34**, 35–41 (2006).
- 109. Hudlicka, O. & Brown, M. D. Adaptation of skeletal muscle microvasculature to increased or decreased blood flow: role of shear stress, nitric oxide and vascular endothelial growth factor. *J Vasc Res* **46**, 504–512. doi:10.1159/000226127 (2009).
- 110. Semenza, G. L. Vasculogenesis, angiogenesis, and arteriogenesis: mechanisms of blood vessel formation and remodeling. *J Cell Biochem* **102**, 840–847. doi:10.1002/jcb.21523 (2007).
- 111. Persson, A. B. & Buschmann, I. R. Vascular growth in health and disease. *Front Mol Neurosci* 4, 14. doi:10.3389/fnmol.2011.00014 (2011).
- 112. Carmeliet, P. Angiogenesis in health and disease. *Nat Med* **9**, 653–660. doi:10. 1038/nm0603-653 (2003).
- 113. Semenza, G. L. Vascular responses to hypoxia and ischemia. *Arterioscler Thromb Vasc Biol* **30**, 648–652. doi:10.1161/ATVBAHA.108.181644 (2010).
- 114. Burri, P. H., Hlushchuk, R. & Djonov, V. Intussusceptive angiogenesis: its emergence, its characteristics, and its significance. *Dev Dyn* **231**, 474–488. doi:10.1002/dvdy.20184 (2004).
- 115. Gebala, V., Collins, R., Geudens, I., Phng, L. K. & Gerhardt, H. Blood flow drives lumen formation by inverse membrane blebbing during angiogenesis in vivo. *Nat Cell Biol* **18**, 443–450. doi:10.1038/ncb3320 (2016).
- 116. Carmeliet, P. & Jain, R. Molecular mechanisms and clinical applications of angiogenesis. *Nature* **473**, 298–307. doi:10.1038/nature10144 (2011).
- 117. Risau, W. Mechanisms of angiogenesis. *Nature* **386**, 671–674. doi:10.1038/386671a0 (1997).
- 118. Song, J. W. & Munn, L. L. Fluid forces control endothelial sprouting. *Proc Natl Acad Sci U S A* **108**, 15342–15347. doi:10.1073/pnas.1105316108 (2011).

- 119. Ghaffari, S., Leask, R. L. & Jones, E. A. Flow dynamics control the location of sprouting and direct elongation during developmental angiogenesis. *Development* **142**, 4151–4157. doi:10.1242/dev.128058 (2015).
- 120. Rosenfeld, D. *et al.* Morphogenesis of 3D vascular networks is regulated by tensile forces. *Proc Natl Acad Sci U S A* **113**, 3215–3220. doi:10.1073/pnas.1522273113 (2016).
- 121. Faber, J. E., Chilian, W. M., Deindl, E., van Royen, N. & Simons, M. A brief etymology of the collateral circulation. *Arterioscler Thromb Vasc Biol* **34**, 1854–1859. doi:10.1161/ATVBAHA.114.303929 (2014).
- 122. Schaper, W. Collateral circulation: past and present. *Basic Res Cardiol* **104**, 5–21. doi:10.1007/s00395-008-0760-x (2009).
- 123. Allahwala, U. K. *et al.* Recruitment and Maturation of the Coronary Collateral Circulation: Current Understanding and Perspectives in Arteriogenesis. *Microvasc Res* **132**, 104058. doi:10.1016/j.mvr.2020.104058 (2020).
- 124. Buschmann, I., Heil, M., Jost, M. & Schaper, W. Influence of inflammatory cytokines on arteriogenesis. *Microcirculation* **10**, 371–379. doi:10.1038/sj.mn.7800199 (2003).
- 125. Hoefer, I. E., van Royen, N., Buschmann, I. R., Piek, J. J. & Schaper, W. Time course of arteriogenesis following femoral artery occlusion in the rabbit. *Cardiovasc Res* **49**, 609–617. doi:10.1016/s0008-6363(00)00243-1 (2001).
- 126. Scholz, D., Cai, W. J. & Schaper, W. Arteriogenesis, a new concept of vascular adaptation in occlusive disease. *Angiogenesis* **4**, 247–257. doi:10.1023/a:1016094004084 (2001).
- 127. Van den Wijngaard, J. P. H. M. *et al.* Porcine coronary collateral formation in the absence of a pressure gradient remote of the ischemic border zone. *Am J Physiol Heart Circ Physiol* **300**, H1930–H1937. doi:10.1152/ajpheart.00403.2010 (2011).
- 128. Helisch, A. & Schaper, W. Arteriogenesis The Development and Growth of Collateral Arteries. *Microcirculation* **10**, 83–97. doi:10.1038/sj.mn.7800173 (2003).
- 129. Seiler, C., Stoller, M., Pitt, B. & Meier, P. The human coronary collateral circulation: development and clinical importance. *Eur Heart J* **34**, 2674–2682. doi:10.1093/eurheartj/eht195 (2013).
- 130. DiStasi, M. R. et al. Impaired Compensation to Femoral Artery Ligation in Diet Induced Obese Mice Is Primarily Mediated via Suppression of Collateral Growth by Nox2 and p47^{phox}. Am J Physiol Heart Circ Physiol 309, H1207–H1217. doi:10.1152/ajpheart.00180.2015 (2015).

- 131. Faber, J. E. *et al.* Aging Causes Collateral Rarefaction and Increased Severity of Ischemic Injury in Multiple Tissues. *Arterioscler Thromb Vasc Biol* **31,** 1748–1756. doi:10.1161/ATVBAHA.111.227314 (2011).
- 132. Seiler, C. The human coronary collateral circulation. *Eur J Clin Invest* **40**, 465–476. doi:10.1111/j.1365-2362.2010.02282.x (2010).
- 133. Pries, A. R., Hopfner, M., le Noble, F., Dewhirst, M. W. & Secomb, T. W. The shunt problem: control of functional shunting in normal and tumour vasculature. *Nat Rev Cancer* **10**, 587–593. doi:10.1038/nrc2895 (2010).
- 134. Safar, M. E. & Struijker-Boudier, H. A. Cross-talk between macro- and microcirculation. *Acta Physiol* **198**, 417–430. doi:10.1111/j.1748-1716.2009.02073.x (2010).
- 135. Pries, A. R., Secomb, T. W. & Gaehtgens, P. Design principles of vascular beds. *Circ Res* 77, 1017–1023. doi:10.1161/01.res.77.5.1017 (1995).
- 136. Pries, A. R. & Secomb, T. W. Control of blood vessel structure: insights from theoretical models. *Am J Physiol Heart Circ Physiol* **288**, H1010–H1015. doi:10.1152/ajpheart.00752.2004 (2005).









CHAPTER 2

3D Imaging of vascular networks for biophysical modeling of perfusion distribution within the heart

Jeroen P. H. M. van den Wijngaard, Janina C. V. Schwarz, Pepijn van Horssen, Monique G. J. T. B. van Lier, Johannes G. G. Dobbe, Jos A. E. Spaan, and Maria Siebes

Department of Biomedical Engineering and Physics, Academic Medical Center, University of Amsterdam, Meibergdreef 9, 1105 AZ Amsterdam, The Netherlands

ABSTRACT

Background

One of the main determinants of perfusion distribution within an organ is the structure of its vascular network. Past studies were based on angiography or corrosion casting and lacked quantitative three dimensional, 3D, representation. Based on branching rules and other properties derived from such imaging, 3D vascular tree models were generated which were rather useful for generating and testing hypotheses on perfusion distribution in organs. Progress in advanced computational models for prediction of perfusion distribution has raised the need for more realistic representations of vascular trees with higher resolution.

Methods

This paper presents an overview of the different methods developed over time for imaging and modeling the structure of vascular networks and perfusion distribution, with a focus on the heart. The strengths and limitations of these different techniques are discussed.

Results

Episcopic fluorescent imaging using a cryomicrotome is presently being developed in different laboratories. This technique is discussed in more detail, since it provides high-resolution 3D structural information that is important for the development and validation of biophysical models but also for studying the adaptations of vascular networks to diseases. An added advantage of this method being is the ability to measure local tissue perfusion.

Conclusions

Clinically, indices for patient-specific coronary stenosis evaluation derived from vascular networks have been proposed and high-resolution noninvasive methods for perfusion distribution are in development. All these techniques depend on a proper representation of the relevant vascular network structures.

Keywords: Vascular network, Imaging cryomicrotome, Coronary blood flow, Myocardial perfusion, Personalized model

2.1 Introduction

Over the past 20 years, the technical advances in experimental physiology and imaging capabilities have vastly increased the quantity and quality of anatomical and physiological data. The concomitant steep rise in computational power and numerical techniques has enabled multi-scale biophysical modeling of organ function. Apart from integrative modeling of normal physiological function, these studies also aim to understand mechanisms in pathological conditions such as atherosclerosis, acardiac disease or tumor perfusion and to predict the effect of interventional treatment. Integrative modeling of the heart ranges from subcellular mechanisms and cardiomyocyte electrophysiology to whole heart mechanical and perfusion simulation.

Blood flow to the myocardium is distributed via the coronary arteries that comprise a densely branching network of blood vessels embedded in the contracting cardiac muscle. Myocardial perfusion is profoundly heterogeneous at multiple spatial scales due to heterogeneity in local oxygen consumption and the asymmetric branching of the intramural vascular tree. Normally, the coronary circulation is capable of matching blood flow to elevated metabolic demand by adjusting vascular tone. At maximal vasodilation, coronary flow becomes dependent on perfusion pressure and coronary resistance is essentially determined by microvascular structure (diameter and length) rather than function (tone). The impeding effect of cardiac contraction on blood flow in coronary resistance vessels results from a combination of mechanisms including local tissue pressure and time-varying muscle stiffness.^{8,9} A major consequence is that coronary blood flow occurs predominantly during diastole when the heart muscle relaxes. The dynamics of the contraction process also introduce a transmural gradient in tissue pressure, which is high at the subendocardium and declines toward the epicardium. ^{10–12} As a result, tissue closer to the left ventricular chamber is more susceptible to ischemia than the outer myocardial layers. The coronary vascular network is designed to compensate for this impediment by a larger number of subendocardial arterioles. 13 However, in conditions that lower perfusion pressure (epicardial stenosis) or shorten diastolic duration (elevated heart rate) the subendocardium will be jeopardized because its flow reserve is exhausted sooner.14,15

All modeling efforts of organ perfusion share the common need for a proper definition of the arterial vasculature within the tissue. Early models of vascular networks were based on generic topological properties rather than actual network reconstructions. In order to arrive at a realistic tree structure, the arterial system has to be visualized in three dimensions, 3D, so that arterial segments, their topology and geometry can be quantified. Validation of model-based prediction of perfusion requires methods to accurately measure tissue perfusion distribution in relation to vascular structure. This paper aims to give an overview of the challenges associated with collecting experimental data needed as foundation for model development on tissue perfusion in the heart and validation of these computational models. It is structured accordingly along the following outline; vascular tree visualization techniques, analysis and modeling, determination of tissue perfusion and flow model development for clinical applications.

2.2 VASCULAR TREE VISUALIZATION TECHNIQUES

As early as the second century, Galenius (129–200) described the existence of venous and arterial pools of blood and reasoned that blood was created in the liver and consumed by other organs. It was not until several centuries later that the existence of an actual blood circulation and perfusion of organs was postulated by Harvey (1578–1657) in his "De Motu Cordis". Harvey's conclusion was essentially based on a model interpretation of arterial and venous compartments and the communication between them, since it was not possible at that time to visualize capillaries. Precise vascular morphology in humans remains the realm of post-mortem investigation. Ruysch (1638–1731) conducted numerous studies using vascular infusions with colored liquid media so that at dissection, arteries could be traced throughout the body and organs. In 1857, Virchow succeeded in visualizing very fine details, including arterioles and capillaries of the kidney, by injecting a colored liquid which was subsequently cleared by gradual increase in alcohol concentration.¹⁶ Since then, different kinds of colored vascular casting have been used extensively in physiological research, with applications ranging from the detection of coronary collateral arteries¹⁷ to vascular anastomoses in placentas. ¹⁸

In this review we focus on studies aiming at visualization of vascular beds of organs allowing functional vascular network analysis. Imaging techniques with a rather limited field of view or superficial penetration such as intravital multiphoton laser scanning microscopy, optical coherence tomography, and orthogonal polarization spectral imaging have recently been reviewed elsewhere. ¹⁹ Systems combining noninvasive functional imaging information with structural information from computed tomography in small animals were also recently reviewed. ²⁰

2.2.1 X-ray angiography

The first x-ray angiograms demonstrating coronary collateral vessels were produced by Schlesinger in 1938 who filled ex vivo coronary vessels with a radiopaque contrast medium. ²¹ In the 1950s, Fulton used post-mortem stereo-angiography in preserved human hearts to visualize coronary arteries down to several tenths of millimeters in diameter. ^{22,23} He demonstrated extensive superficial and deep intercoronary anastomoses, which were particularly abundant in the interventricular septum and in the subendocardial plexus of the left ventricle. These images gave a good impression of the intricate course of the smaller coronary arteries and identified extensive intercoronary anastomoses (Figure 2.1). The technique was subsequently

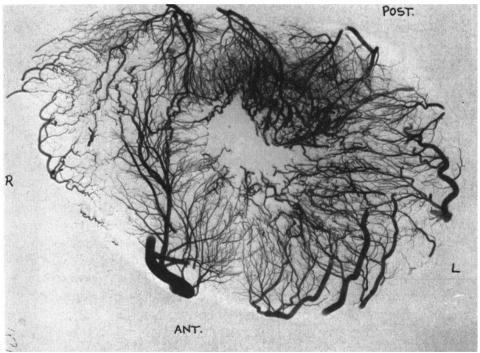


Figure 2.1: Ex vivo arteriogram of a short axis slice of a human heart, after filling the coronary arteries with bismuth-oxychloride-gelatin. Ischemia led to a strong increase in vascular density in the posterior wall of the left ventricle by formation of coronary collaterals, with enlargement of deep, subendocardial anastomoses. Branches of the unobstructed left circumflex artery can be seen on the right hand side of the illustration. Reproduced with permission from Fulton.²³

used by Schaper and co-workers to examine coronary collateral formation in the dog in response to timed coronary artery occlusion. These landmark studies identified the role of coronary collaterals in protecting myocardium against ischemia and the role of fluid shear stress in driving collateral vessel outward remodeling.^{24,25}

Although these angiographic techniques yielded important morphological information, the essentially two dimensional, 2D, images were not amenable to 3D modeling.

2.2.2 Vascular casting

Vascular casting opened the road to 3D visualization of the arterial tree. This technique involves the cannulation of the feeding artery of the vascular bed, the removal of blood by flushing with buffer solution and the infusion of a replica material that polymerizes over time. The intramural vessels of the cardiac muscle were studied in different ways. Bassingthwaighte et al. used a silicone elastomer to fill the coronary microcirculation of the dog heart and made the tissue transparent by prolonged immersion in ethanol and methyl salicylate at increasing concentrations. ²⁶ These authors demonstrated the continuity of the capillary bed over several centimeters with many interconnections between parallel running capillaries, resulting in unbranched capillary segments with an average length of $100 \, \mu m$. These replicas yielded an excellent overview of the capillary bed and its connection to arterioles and venules. However, the density of the capillary bed is so high that the depth of view was limited to less than 1 mm in most places.

Corrosion casting is a different technique to re-create the intra-organ vascular network, by which high-quality physical replicas of the vasculature are obtained after removal of the surrounding tissue by maceration with a concentrated base or acid.¹⁷ This technique revealed changes in capillary density between normal and hypertensive rat hearts,²⁷ but the high density of the microvascular network prevented measurements over large distances. Concurrently but independently, two research groups pruned sub-trees of porcine coronary corrosion casts down to the smallest arterioles and carefully measured individual segmental branching angles, diameters and lengths in order to arrive at branching information over many orders.^{28,29} The corrosion technique has delivered statistical descriptions of vascular networks that gave rise to sophisticated anatomical and flow simulations down to the capillary level (as discussed below). However, the true 3D structure was lost in this type of analysis as well as the information on the spatial relation between the myocardium and the embedded vessel segments.

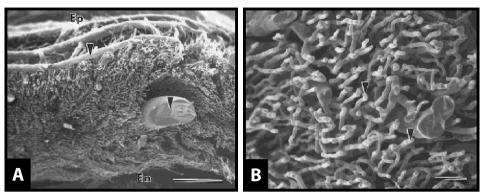


Figure 2.2: Vascular corrosion cast showing a transverse section of the ventricular wall of a rat heart. (**A**) Right ventricular free wall of an aged rat heart. Ep=epicardial surface, En=endocardial surface, arrowheads point at large coronary vasculature. Bar equals $500 \, \mu m$. (**B**) Left ventricular free wall of a rat heart. Arrowheads point at capillaries. Bar equals $50 \, \mu m$. Reproduced with permission from Hossler.³¹

Improvements in low viscosity resins have led to microvascular corrosion casts with ultrastructural detail that permit scanning electron microscopy (SEM). This technique was pioneered in the early $70s^{30}$ and applied to vascular casts of small animal hearts and lungs. As depicted in Figure 2.2, these SEM images clearly illustrate the dense organization of bundles of capillaries and permit the count of endothelial cells per unit area. The vascular architecture of many tissues has been analyzed using this technique, ranging from deviations in structure and wall porosity in brain vasculature in a mouse model for Alzheimer's disease to highly vascularized plexuses with varying diameters and even blind ends in tumors. Despite the attractive detail that can be obtained with SEM analysis, attempts to derive 3D information from casting combined with EM analysis have proven to be extremely cumbersome. As

Potential sources of error in casting techniques comprise non-physiological filling pressure, choice of polymer dilution to arrive at the desired viscosity for adequate filling of small vessels and the possible inclusion of air bubbles in the casting resin. In the case of coronary vessels in small hearts, the polymer is infused according to Langendorff via the aorta with the risk of unwillingly filling the left ventricle, which interferes with proper filling of the subendocardial microcirculation. Additional concerns are possible effects of energy dissipation in case of exothermic reaction and cast shrinkage upon polymerization.

2.2.3 Micro-computed tomography

Micro-computed tomography (micro-CT) is a relatively new modality that rapidly advanced high-resolution imaging of fine structures. 20,35,36 An important advantage of micro-CT is the ability to acquire in vivo images, which enables longitudinal studies of disease progression or vessel formation in single animals. However, given the radiation exposure, micro-CT with voxel resolution below 50 μm^3 is limited to a single scan in live animals. 36 Obviously, in the case of ex vivo imaging, radiation exposure does not pose such a constraint and resolutions of several microns can be achieved. Such high resolution 3D images have been obtained of mouse coronaries (Figure 2.3) and neovessel organization in a mouse model of hindlimb ischemia. 37 High-resolution datasets of small animal microcirculation with voxels <2 μm can be acquired with synchrotron radiation micro-CT. 38 In hierarchical microimaging a regular micro-CT is used to obtain whole organ anatomy and synchrotron radiation micro-CT to generate high resolution images in selected regions of interest. 39

Micro-CT angiography requires injection of a radiopaque contrast material with high x-ray absorption properties, such as iodinated compounds in case of in vivo animal imaging. For ex vivo application the vasculature can be filled with a suspension of lead chromate, barium sulfate or bismuth in silicone rubber or latex. Low viscosity microfil can overcome issues relating to high viscosity which prevents optimal penetration of the microvasculature. 40,41

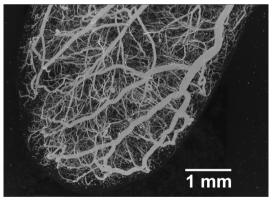


Figure 2.3: Maximum intensity projection of mouse coronary arteries obtained by micro-CT imaging with $4\,\mu m$ acquisition, downsampled twofold for display. Bar equals $1\,mm$. Image provided courtesy of Dr. Ghassan S. Kassab, Indiana University—Purdue University Indianapolis.

At present, possibilities for perfusion imaging with micro-CT are limited. Using advanced image reconstruction, ⁴² mean transit time determination from CT images is currently under investigation. Silver coated microspheres have been applied ⁴³ but this method does not allow for multiple measurements and control-intervention studies are not possible.

2.2.4 Episcopic (cryo-) microtome fluorescence imaging

The classical manner to arrive at a 3D reconstruction from microtomy is to separately image individual histological slices and subsequently re-align consecutive images using computer based 3D rendering. Episcopic 3D imaging, introduced about 15 years ago, overcomes the difficulty of dealing with unavoidable distortions, by creating digital volume data from images of the embedded tissue block surface after successive removal of imaged sections. Episcopic microtome techniques frequently employ high-resolution fluorescence imaging to result in a registered stack of 2D images containing detailed structural and/or functional information.

One of the first imaging cryomicrotomes using this principle (Barlow Scientific, Inc. Olympia WA) was developed for the purpose of automated detection of fluorescent microspheres in tissue (see Section 2.2.6) as tracers for spatial flow distribution. ^{47,48} Using filter wheels for excitation and emission light, 4 different fluorescent labels could be detected. In the original design, the reciprocal linear motion of the cutting blade was realized via a connecting rod attached to a rotating crank and wheel, which introduced sinusoidal variation in the cutting force and speed across the frozen tissue surface with each stroke and essentially prevented high quality reconstructions from the individual fluorescent images.

The group of Spaan designed a more robust imaging cryomicrotome in which the blade moves at a constant speed across the sample surface (Figure 2.4). ⁴⁹ In addition to microsphere detection, high quality vascular network visualization down to the arteriolar level (Figure 2.5) is achieved by prior injection of a fluorescent plastic replica material. ^{50,51} Through spectral unmixing, the number of fluorescent labels was increased to $6.^{52}$ A typical dataset of a porcine heart processed at an isotropic voxel resolution of 25 μ m may comprise close to 4000 slices. Depending on the number of fluorescent color channels, complete datasets may reach over 120 GB with images captured at 4096 × 4096 pixels and are acquired in 3–4 days of unattended continuous cutting and imaging.

A tradeoff exists between resolution and field of view. Since tissue perfusion is determined by the vascular architecture at multiple scales ranging from the relatively

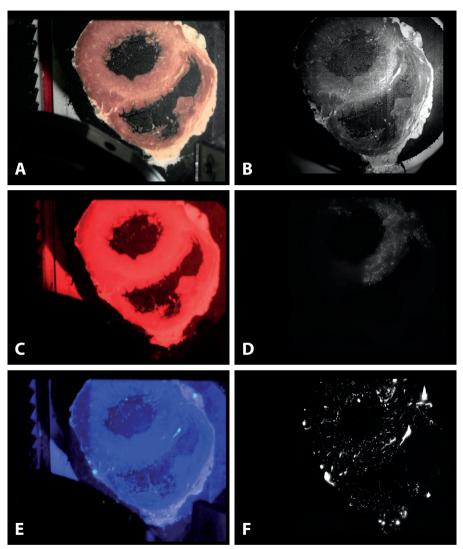


Figure 2.4: View of the cutting plane of the imaging cryomicrotome as developed by Spaan illustrating the image acquisition that yields co-registered vascular and microsphere data. ⁴⁹ Panels **(A)** through **(F)** show the same sample surface of a frozen human heart being cut in a short axis configuration, with illumination on the left and corresponding captured images on the right hand side. **(A)** Normal white light illumination; **(B)** gray scale outline image. **(C)** Excitation at 650 nm for scarlet fluorescent microsphere emission at 712 nm in panel **(D)**. **(E)** Illumination with 440 nm for emission of vascular replica material at 505 nm shown in Panel **(F)**.

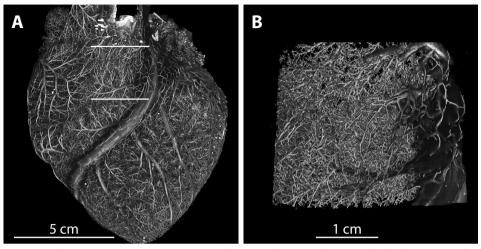


Figure 2.5: Intensity projection image of a normal porcine heart with high viscosity fluorescent replica material injected into the coronary arteries. The coronary vessels were reconstructed from 4080 slices, imaged with 4096×4096 pixels in-plane resolution, with voxel size $25 \times 25 \times 25 \ \mu m^3$. **(A)** Anterior view of the left anterior descending artery with major side branches (downsampled two-fold for display); **(B)** detail at higher resolution (between the white lines in panel **(A)**), showing the dense vasculature from a proximal LAD sidebranch and part of the vasa vasorum.

large conduit arteries to the small arterioles, systems with a larger field of view such as the Spaan or Barlow type cryomicrotome are best suited for whole organ vascular network reconstruction of larger mammals and humans. Other episcopic fluorescence imaging setups have been designed for whole mouse imaging by equipping commercially available cryostats with fluorescent imaging capabilities. S3,54 Systems based on paraffin embedding achieve ultra-high resolution of 0.5–2 μ m to visualize embryonic mouse hearts,55,56 by repetitive tissue staining, imaging and milling of the remaining tissue block or by employing two-photon imaging. Recent hybrid techniques combine micro-magnetic resonance imaging, μ -MRI, and subsequent high resolution tissue microtomy.

2.2.5 Image restoration and analysis for tree segmentation and microsphere detection

Extensive post-processing of the 3D image stack achieves detailed segmental reconstruction and quantitative analysis after image restoration. In case of episcopic fluorescence imaging with a cryomicrotome, blurring is introduced not only by lens distortions and inherent optical noise, but also by artifacts of subsurface fluorescence introduced by embedded microspheres or fluorescent cast material. Deblurring can be achieved by deconvolution with the system's 3D impulse response, or point spread function (PSF), ^{60,61} or by "next image out of plane fluorescence" correction. ^{52,62}

Segmentation of the vascular network, dependent on the outcome parameters, e.g. connecting nodes, vessel angles, vessel diameters, may require the determination of centerlines for all vessel segments. Several algorithms for this purpose have been described for larger vessels imaged by e.g. CT angiography or MRI.^{63,64} However, in terms of computational cost these techniques are not easily applicable to the much more extensive 3D whole-organ datasets produced by an imaging cryomicrotome. A computationally efficient method for skeletonization that can be implemented in parallel on multiple processor cores is based on a topology preserving thinning algorithm⁶⁵ results in a collection of points along the vascular center. This peeling procedure produces a segmented tree that serves as a topological representation of the vascular network (Figure 2.6) and connecting nodes, branch angles, as well as local segmental diameters can then be extracted for a complete anatomical characterization. Moreover, the image analysis software developed for

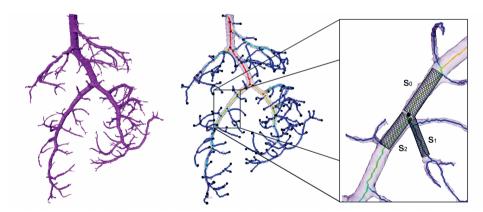


Figure 2.6: Illustration of vascular tree segmentation from cryomicrotome images. (**Left**) Main branches of left anterior descending artery. (**Middle**) Consecutive points indicate the centerline of the topological representative vascular tree. Color indicates local vascular diameter ranging from large (red) to small (dark blue) and black for endpoints. (**Right**) Detail of middle panel, where the mesh represents the average measured diameter of the segments, S_0 the mother segment and S_1 and S_2 being daughter segments.

this instrument allows co-registration of vessel structure and microsphere density as measure of local perfusion during various experimental conditions, or of other fluorophores as tracers of (patho-)physiological actions.

2.2.6 Tissue perfusion measurement with microspheres

Tissue perfusion is defined by the amount of blood per unit time that enters a tissue region of unit mass and passes through capillaries in that region. Perfusion distribution can be measured by addition of appropriately labeled microparticles or molecular tracers to the arterial bloodstream and quantifying the subsequent deposition per unit mass of tissue. 66,67 This method is based on the underlying assumption that particle deposition density represents the relative distribution of flow within the tissue region of interest. The use of differently labeled tracers allows the perfusion distribution measurement under different circumstances in the same experiment.

Historically, in most microsphere and molecular tracer studies, tissue was first cut into small pieces, which were weighed and the amount of tracer in the tissue sample was determined. For radioactive microspheres, automated gamma counters are used to determine radioactivity for different isotopes in the samples. For fluorescent microspheres, the tissue samples are homogenized and microspheres subsequently counted by a fluorescence activated cell sorter analyzer⁶⁸ or dissolved and fluorescence is measured in the solvent by a fluorescence spectrophotometer.⁶⁹ The spatial resolution of these methods is determined by the volume of the tissue samples and the accuracy of the perfusion distribution measurement is determined by the amount of microspheres in the samples. Assuming the deposition of microspheres follows a Poisson distribution, the accuracy relates to $1/\sqrt{N}$, N being the number of microspheres in the sample. Hence, an accuracy of 5% requires 400 microspheres in a sample.⁷⁰ However, detailed topological information of perfusion distribution is lost with this approach.

Epifluorescence images obtained with a cryomicrotome allow detecting the actual 3D position of each individual microsphere. ^{52,71} The great advantage is that this avoids the pitfalls of an a-priori tissue cutting scheme, whereby the resulting samples may contain tissues of diverse regions of interest, e.g. by crossing the boundary of an infarcted area. In the Spaan cryomicrotome, the original microsphere position is coregistered in 3D space with vascular structure and anatomical landmarks identifiable from the images. Since vascular structures can be visualized at high resolution, the flow distribution in these structures can be assessed with high spatial accuracy

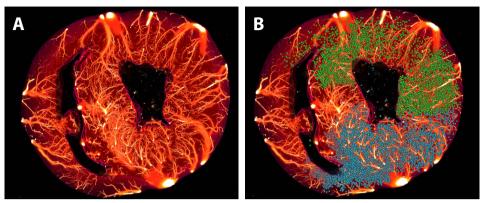


Figure 2.7: Example of the coronary vascular tree and perfusion territories obtained by processing cryomicrotome images of a dog heart. **(A)** Intensity projection image of a mid-LV transverse section. **(B)** Overlay of two microsphere populations (shown in green and blue) injected into different major left coronary arteries; microspheres are not represented to scale, width of the heart is 7.5 cm.

(Figure 2.7). Since also the segment diameter is known, shear stress distribution in the arterial tree can be estimated as well. Moreover, knowledge of all microsphere positions may allow for the development of new statistical techniques describing perfusion distribution.⁷²

Limitations associated with perfusion measurement by microsphere deposition relate to the number of issues ranging from the number of microspheres required for a volume sample and adequate mixing to rheological effects. To obtain a similar accuracy as in large animals, the number of microspheres per unit body mass needs to be higher in small animals, although flow disturbances have not been observed in small animals. Microspheres need to lodge in the tissue at first pass, which is accomplished by using microspheres of sufficient size, i.e. 15 µm. Preferential streaming of microspheres may occur at bifurcations. The effects of variations in particle density or particle dislodging have all shown to be negligible. Microsphere distribution measurement maintains its importance in studying perfusion distribution of perfusion distribution such as perfusion MRI.

2.3 VASCULAR TREE MODELING

The coronary vascular tree is the backbone for myocardial perfusion and a proper understanding of its structure and flow distribution capabilities is of great importance in unraveling the regional distribution of ischemia. At a global level and under normal physiological circumstances coronary flow is well matched to myocardial oxygen consumption. However, expressed per unit tissue, both oxygen consumption and perfusion are not homogeneously distributed and local microheterogeneity can result in patchy myocardial ischemia and necrosis, where areas of well-perfused myocardium are close to ischemic tissue units of only a few cubic mm, especially in the subendocardium. These regional and local differences are not only due to the spatial organization of the coronary vascular tree, but are strongly influenced by the compressive forces of the contracting myocardium on the embedded vessels. 8,78

Experimental findings and progress in tree visualization techniques have given rise to the development of structural and functional models of the coronary circulation. Moreover, such models have now reached the stage of clinical application, underlining their relevance.

2.3.1 Biophysical principles for vessel diameters and branching

Over more than a century, theories have been built for explaining the tree like characteristics of the arterial system. More than a century ago, Thoma reported a marked correlation between the diameter of a vessel and the flow conveyed by it.⁷⁹ Murray postulated that the relation between the flow and vascular diameter of a vessel results from a minimum energy hypothesis consisting out of a term related to producing blood to fill a particular vessel and one for transporting it.⁸⁰ A smaller diameter vessel requires less blood for the same length but will have a higher resistance according to Poiseuille's law. Accordingly, Murray's law describes the flow in the form of $Q = kr^3$, where Q is the flow, k is a constant and k is the vascular lumen radius. Since at a bifurcation the flow in the mother vessel must equal the sum of the flow rates in the daughter vessels, their sizes are related by $r_0^3 = r_1^3 + r_2^3$, where r_0 is the radius of the mother vessel and r_1 and r_2 are the radii of the daughter vessels.

Although some studies confirmed a third power relation between flow and radius, it is certainly not a general rule. An exponent of 2.3 has been reported for the human lung⁸¹ and 4 for the rabbit ear.⁸² For the heart, the exponent varied between 2 and 3 depending on vascular diameters.^{28,83,84} Especially within the coronary system, flow is pulsatile and energy is lost by wave reflection at branch points.

Hence, an additional optimization rule can be derived based on the principle of minimal wave reflections at branch points. For a symmetrical tree one arrives at $d_0^{2.55} = d_1^{2.55} + d_2^{2.55}$. Although the coronary vascular tree is highly asymmetric, this branching rule corresponded with a scaling law relating the number of distal segments with a diameter of 0.4 mm belonging to a branch to the diameter of the feeding vessel.

Note that these relationships do not take into account the dynamic nature of the vascular geometry. The diameter of arterial segments is not constant and changes due to adaptive tone of smooth muscle in their walls. This is especially the case in the small resistance arteries that are involved in control of blood flow. At relaxed smooth muscle tone, hyperemic coronary blood flow can be four times higher than at rest. Moreover, local adaptation in reaction to reduced tissue perfusion stimulates angiogenic and arteriogenic compensatory processes in a patient- and disease-specific way.⁸⁶ Adaptation of wall structure and diameter takes place in vessels with tone and isolated vessel studies indeed showed that tone is even a prerequisite for remodeling. 87 Wall shear stress has a predominant role in remodeling of vessels and thereby on re-structuring the arterial tree. A reduction in wall shear stress induces a decrease in diameter and vice versa via an endothelium-dependent process. 88 Mathematically, Murray's law corresponds with the constant shear stress hypothesis. 89,90 However, the relation between shear stress and vessel diameter is not fixed and depends on vessel type and species. 91,92 This needs to be taken into account when relating tree properties, often measured at maximal dilatation, to biophysical quantities such as pressure, flow and wall shear rate.

2.3.2 Vascular tree generation

Network models have been developed to understand the heterogeneous flow distribution in the cardiac muscle, which was experimentally shown to be fractal in nature, implying that the relative dispersion of flow distribution has a power law relation with sample volume for perfusion measurement. Similarly, a vascular network is considered fractal when branching patterns recur over multiple spatial scales. A relation has been suggested between the fractal flow distribution and the fractal nature of the coronary network. Optimized constraint models in fact suggest a duality between heterogeneity in flow and shear stress and found that uniform shear and homogeneous perfusion cannot be obtained simultaneously.

From the corrosion cast studies discussed above, coronary networks have been generated based on measured scaling relationships at branch points, not necessarily

fractal.^{28,29} Vanbavel and Spaan reported asymmetry and expansion ratios as the two most mutually independent parameters obtained from their morphological dataset, where asymmetry, S, is the ratio between the diameters of the smallest and the largest daughter vessel as $S = d_s/d_l$ and expansion, A, is the ratio between the sum of the daughter radii squared and radius squared of the mother vessel as $A = (d_1^2 + d_2^2)/d_m^2$. Using Strahler ordering starting at the pre-capillary level, networks were created applying statistical information on the relationship between asymmetry and expansion ratios as function of diameter as well as the segmental length-diameter relation. Models based on several combinations of asymmetry and expansion ratios demonstrated that the experimentally reported pressure-segment diameter relation could only be obtained in trees with high asymmetry. 98 Kassab and coworkers reported their experimental data according to a modified, diameterbased Strahler ordering which facilitated calculations of flow distribution in the network.²⁹ This work was extended to include the capillary bed and venous vascular network. 99 Network studies based on these corrosion cast data resulted in fractal flow distribution as described above. 100

2.4 PREDICTIVE BIOPHYSICAL BASED MODELING

2.4.1 Structure-function relationships

A class of models based on scaling laws has evolved to relate simulated tree structure to physiology. In these models stochastic tree growing algorithms based on morphometric branching rules serve as the basis for the extension to power law relations of a stem–crown system that can be mapped onto the myocardium. ^{101–104} A stem can be any segment that feeds a crown formed by the subtree distal to the stem. These models are essentially a generalization of Murray's law to a subtree level and describe relationships of diameter, length, and volume between the feeding segment and its corresponding crown. ⁸³ Note that length and volume are cumulative quantities and refer to the sum of segmental lengths and volumes in the crown under consideration.

Flow simulations across these tree designs yielded hemodynamic relations between crown resistance and its volume and length, and between stem blood flow and stem diameter and crown length, respectively, which were consistent with experimental observations 105,106 and measurements in patients. 107,108 Choy and Kassab found that $V \propto m^1$, $L \propto m^{34}$, $D \propto m^{36}$, and $Q \propto m^{34}$, where V and L correspond to cumulative arterial volume and length, respectively, D is arterial diameter, Q the volumetric flow, and M the myocardial mass. 109 Additional structure—function

scaling relations have been formulated on the basis of a volume–scaling relation (HK model) that is based on a $\frac{7}{3}$ exponent, slightly less than Murray's exponent of $3.^{105}$ The resulting scaling laws included the diameter–length, volume–length, flow–diameter, and volume–diameter relations, with exponent values of $\frac{3}{7}$, $\frac{7}{9}$, and $\frac{3}{9}$, respectively. The $\frac{3}{4}$ power law relation between total crown lumen volume V and flow Q was extended to a resistance scaling law for a vascular tree, i.e. the resistance of a vessel segment scales with the equivalent resistance of the corresponding distal tree. This relation can be expressed as $(R_s/R_c \propto L_s/L_c)$, where R_s and L_s are the resistance and length of a vessel segment, respectively, and R_c and L_c are the equivalent resistance and total length of the corresponding distal tree, respectively. Morphology derived scaling laws have made it possible to relate geometric information obtained from vascular images to functional properties of the coronary circulation.

2.4.2 Image-based modeling of coronary blood flow for patient-specific diagnosis

Although the above relationships assume generalized design principles underlying the structure-function relationship of the coronary arterial tree, they provided a rationale for clinical applications, whereby (partial) trees obtained from digital angiography, CT, or magnetic resonance imaging are used to predict flow and pressure distribution for diagnostic purposes. The applicability of these methods for clinical diagnosis remains to be established. Flow calculations in simulated trees demonstrated a remarkable consistency of the ³/₄ power relation between maximal coronary blood flow and the perfusion bed size expressed as the sum of the perfused arterial volume at maximal vasodilation. These findings were confirmed in vivo and allowed prediction of hyperemic blood flow in a swine animal model by estimating the crown volume from angiographic images of the coronary arteries.¹¹¹ Fractional flow reserve (FFR) is a clinical index defined as the ratio between the maximal coronary flow through a stenotic vessel and the theoretical maximal coronary flow through the same vessel without a stenosis. 112 The above method can be employed to derive FFR based on angiographic data alone, in conjunction with videodensitometrically measured hyperemic blood flow in the presence of an epicardial stenosis. It should be noted however that these methods implicitly rely on the translation of relations that were established in healthy animals and volunteers.

Sophisticated numerical models have been developed that combine computational fluid dynamics (CFD) and finite element models (FEM) in order to derive patient-specific diagnostic information, based on extraction of anatomical as well as hemodynamic or functional information from medical images. ^{113,114} One of the most important challenges is to apply realistic boundary conditions in order to simulate dynamic blood flow in the extracted (truncated) geometry of the imaged vascular system. For the coronary circulation, the periodic deformation and compression of the vasculature are a must to consider. ^{8,115} Myocardial–vascular interaction has been incorporated by a lumped parameter coronary vascular bed model including the intramyocardial pump action for discrete coronary outlets to represent the impedance of downstream coronary vascular networks. ^{116–118} Others have used 1D models to prescribe the distributed outlet pressure and flow ^{101,119,120} or integrated the microvascular domain in terms of a multi-compartment coupled porous–mechanical model of the cardiac left ventricle. ¹²¹

Depending on the desired predictive power of integrated heart models, interactions between the blood, deformable vessel wall and surrounding tissue need to be taken into account by incorporating fluid-structure interaction (FSI) and coupling with a myocardial mechanical model. 122 In order to keep the computational demands on a feasible level, flow rate and pressure on the outflow (or inflow) of an image-based, 3D numerical domain can be coupled to the inflow (or outflow) of a reduced-order model, i.e. a one-dimensional network or zero-dimensional (lumped) model. 123 This multi-scale approach was adopted by Kim et al. to compute physiologically realistic pressure and flow waveforms in coronary vessels at baseline conditions using a FEM model of the upper aorta and major coronary arteries constructed from CT images. 124 3D CFD simulations, including FSI with elastic boundary conditions for the image-based domain, were coupled with an analytical 1D model of the circulation and a lumped-parameter coronary resistance model. This model is now being applied clinically to compute mean pressure fields along stenotic coronary vessels at simulated maximal hyperemia to predict FFR noninvasively from cardiac-gated CT images in patients. ¹²⁵ Despite the initial success of this application, some underlying assumptions give rise to potential limitations: baseline flow is related to LV mass, but flow depends on the amount of viable myocardium and oxygen consumption; hyperemic flow is simulated assuming a fully functional microcirculation, although the effects of obstructive epicardial disease extend into the microcirculation, perfusion pressure is not linear with flow and microvascular resistance in relaxed vessels is pressure-dependent; 112 vascular remodeling and collateral flow are not considered, and uniform vessel wall properties are assumed. Finally, the coronary arteries are fixed to the surface of the heart which is frozen in space and time, i.e. the motion of cardiac contraction is not modeled and transmural mapping of coronary arteries is not incorporated.

Advanced integrated models of coronary perfusion using CFD-FEM simulations include active cardiac–coronary mechanical coupling and several generations of coronary vessels embedded within the ventricular wall in a multi-scale multi-physics approach. ^{6,126} Conversely, models directed at excitation–contraction coupling and cardiac wall mechanics based on myocyte force generation and tissue deformation need incorporation of perfusion since it places an upper limit on metabolism and affects contraction. ^{127,128}

2.5 Discussion

This paper provides an overview of the different techniques that have evolved in the past decades for the visualization and analysis of vascular structures and organ perfusion. The discussion focused on the heart since it is not only one of the most vital but also one of the most complex organs in terms of understanding and modeling of blood flow. The principal aspects, however, apply to organ perfusion in general.

Morphology derived scaling laws have made it possible to relate image-based vascular structure to functional properties of the coronary circulation. A proper characterization of the intramural vascular network is at the basis of such a modeling effort. Knowledge of structure alone, however, is often not sufficient, since local perfusion also depends on organ function. Control and regulation of adequate tissue perfusion is realized by adaptation of vessel diameters via a process termed autoregulation. In case of the myocardium, the recurrent compression of the embedded blood vessels and the time-varying stiffening of the heart muscle itself add another level of complexity to assess local tissue perfusion. Since perfusion determines the metabolic substrate availability for cardiomyocyte contraction, significant "cross-talk" exists between the perfusion and the pumping of the heart.8 Numerous physiological and patho-physiological processes modify this interaction through short-term and long-term adaptation of both vascular and fiber structure of the cardiac muscle. Most CFD studies cover a duration of a few seconds, but diseases develop over years. Mathematical models and numerical methods are needed that span the diverse spatial and temporal scales in clinically relevant problems.

Simulation of flow in arteries and organ perfusion forms an important opportunity in computational physiology and medicine. The possibility to noninvasively

determine the functional severity of coronary occlusions or derive estimates of the theoretical maximal coronary flow carries promising clinical implications. 129 At the heart of integrative models of organ perfusion in health and disease is the concept of 'intelligent' imaging, i.e. the derivation of diagnostic information from non-invasive image data to improve early diagnosis and optimize treatment planning on a patient-specific basis. Prominent examples of current research in pursuit of this goal are the EU-wide ICT-based projects for modeling and simulation of human physiology under the umbrella of the Virtual Physiological Human (VPH) initiative (www.vph-noe.eu). Among these, the euHeart project (http://www.euHeart.eu) focuses on the translational aspects of multi-scale multi-physics cardiovascular modeling and the suitability of these models for use in clinical environments, based on realistic 3D information on vascular branching, fiber sheet information and perfusion. The envisioned benefits of this approach are improved diagnosis with better selection of patients for treatment, and enhanced personalized care that is based upon the interpretation of the individual patient data and medical history rather than population derived averages.¹³¹

Many challenges remain associated with image-based modeling for patientspecific diagnosis. A key challenge in realizing the goal of clinical application of personalized modeling is to establish a practical, reliable, efficient tool for in vivo detailed perfusion predictions from noninvasive imaging data that is not only adequately verified, but also easy to use and fast. Other issues relate to the definition of reliable and predictive branching rules and the proper assessment of the patient-specific parameters. The step from a generic to a patient-specific model of organ perfusion involves matching the model predictions to clinical data by appropriately tuning model parameters. To this end, integrative patient-specific model development has benefited tremendously from the increase in available clinical observations for validation, ranging from cardiac wall motion and chamber flow patterns to coronary pressure and flow waveforms and from the sequence of electrical activation to mechanical contraction and local tissue perfusion. The question is whether clinical observations contain enough detail to unambiguously determine the unknown model properties. Application of fluorescent cryomicrotome imaging for this purpose may offer a valid strategy to obtain the necessary data, since it allows the detailed quantitative analysis of structural as well as functional information of the arterial tree that supplies the heart muscle with blood.

In conclusion, the development of integrated multi-scale and multi-physics models of the heart has the potential to make a real impact on medical practice. Such an endeavor needs strengthening the collaboration between biomedical engineers developing image-based modeling tools and basic scientists and clinicians focused on understanding and treating vascular disease. The promising outlook of patient-specific modeling is that the beneficial outcome may well be more than the sum of its parts.

Acknowledgments

The authors would like to acknowledge funding from the European Commission (FP7-ICT-2007/2013 no. 224495: euHeart). This work was performed within the framework of CTMM, the Center for Translational Molecular Medicine (www.ctmm.nl), project EMINENCE (grant 01C-204) and was further supported by grants from the Netherlands Heart Foundation (NHS 2006B186 and 2006B226) and the Netherlands Organization for Health Research and Development (ZonMw 91105008 and 91112030). Jeroen P.H.M. van den Wijngaard is funded by a Veni grant from the Netherlands Organization for Scientific Research (NWO/ZonMw 91611171).

Conflict of interest statement

None of the authors has a conflict of interest to disclose.

REFERENCES

- 1. Hunter, P. J. & Borg, T. K. Integration from proteins to organs: the Physiome Project. *Nat Rev Mol Cell Biol* **4**, 237–243. doi:10.1038/nrm1054 (2003).
- 2. Bassingthwaighte, J. B. & Chizeck, H. J. The Physiome Projects and Multiscale Modeling. *IEEE Signal Process Mag* **25**, 121–144. doi:10.1109/MSP.2007.914723 (2008).
- 3. Krams, R. *et al.* Evaluation of endothelial shear stress and 3D geometry as factors determining the development of atherosclerosis and remodeling in human coronary arteries in vivo. Combining 3D reconstruction from angiography and IVUS (ANGUS) with computational fluid dynamics. *Arterioscler Thromb Vasc Biol* **17**, 2061–2065. doi:10.1161/01.atv.17.10.2061 (1997).
- 4. Noble, D. Modeling the heart-from genes to cells to the whole organ. *Science* **295**, 1678–1682. doi:10.1126/science.1069881 (2002).
- 5. Bassingthwaighte, J. B. & Vinnakota, K. C. The computational integrated myocyte: a view into the virtual heart. *Ann NY Acad Sci* **1015**, 391–404. doi:10.1196/annals.1302.034 (2004).

- 6. Smith, N. *et al.* euHeart: personalized and integrated cardiac care using patient-specific cardiovascular modelling. *Interface Focus* **1**, 349–364. doi:10.1098/rsfs. 2010.0048 (2011).
- 7. Chilian, W. M. Microvascular pressures and resistances in the left ventricular subepicardium and subendocardium. *Circ Res* **69**, 561–570. doi:10.1161/01.res.69.3.561 (1991).
- 8. Westerhof, N., Boer, C., Lamberts, R. R. & Sipkema, P. Cross-talk between cardiac muscle and coronary vasculature. *Physiol Rev* **86**, 1263–1308. doi:10.1152/physrev.00029.2005 (2006).
- 9. Spaan, J. *et al.* Coronary structure and perfusion in health and disease. *Phil Trans R Soc A* **366**, 3137–3153. doi:10.1098/rsta.2008.0075 (2008).
- 10. Hoffman, J. I. & Buckberg, G. D. Pathophysiology of subendocardial ischaemia. *Br Med J* 1, 76–79. doi:10.1136/bmj.1.5949.76 (1975).
- 11. Hoffman, J. I. & Spaan, J. A. Pressure-flow relations in coronary circulation. *Physiol Rev* **70**, 331–390. doi:10.1152/physrev.1990.70.2.331 (1990).
- 12. Camici, P. G. & Crea, F. Coronary microvascular dysfunction. *N Engl J Med* **356**, 830–840. doi:10.1056/NEJMra061889 (2007).
- 13. Wüsten, B., Buss, D. D., Deist, H. & Schaper, W. Dilatory capacity of the coronary circulation and its correlation to the arterial vasculature in the canine left ventricle. *Basic Res Cardiol* **72**, 636–650. doi:10.1007/BF01907044 (1977).
- 14. Merkus, D. *et al.* Stenosis differentially affects subendocardial and subepicardial arterioles in vivo. *Am J Physiol Heart Circ Physiol* **280**, H1674–H1682. doi:10.1152/ajpheart.2001.280.4.H1674 (2001).
- 15. Fokkema, D. S., VanTeeffelen, J. W., Dekker, S., Vergroesen, I., Reitsma, J. B. & Spaan, J. A. Diastolic time fraction as a determinant of subendocardial perfusion. *Am J Physiol Heart Circ Physiol* **288**, H2450–H2456. doi:10.1152/ajpheart.00790. 2004 (2005).
- 16. Virchow, R. Einige Bemerkungen über die Circulationsverhältnisse in den Nieren. *Archiv f pathol Anat* **12**, 310–325. doi:10.1007/BF01940148 (1857).
- 17. Baroldi, G., Mantero, O. & Scomazzoni, G. The collaterals of the coronary arteries in normal and pathologic hearts. *Circ Res* 4, 223–229. doi:10.1161/01.res.4.2.223 (1956).
- 18. Van den Wijngaard, J. P. *et al.* Deep-hidden anastomoses in monochorionic twin placentae are harmless. *Prenat Diagn* **27**, 233–239. doi:10.1002/pd.1652 (2007).
- 19. Kiessling, F., Razansky, D. & Alves, F. Anatomical and microstructural imaging of angiogenesis. *Eur J Nucl Med Mol Imaging* **37**, 4–19. doi:10.1007/s00259-010-1450-0 (2010).

- 20. De Kemp, R. A., Epstein, F. H., Catana, C., Tsui, B. M. & Ritman, E. L. Small-animal molecular imaging methods. *J Nucl Med* 51, 18S–32S. doi:10.2967/jnumed. 109.068148 (2010).
- 21. Schlesinger, M. J. An injection plus dissection study of coronary artery occlusions and anastomoses. *Am Heart J* **15**, 528–568. doi:10.1016/S0002-8703(38)90559-9 (1938).
- 22. Fulton, W. F. Chronic generalized myocardial ischaemia with advanced coronary artery disease. *Br Heart J* **18**, 341–354. doi:10.1136/hrt.18.3.341 (1956).
- 23. Fulton, W. F. The Dynamic Factor in Enlargement of Coronary Arterial Anastomoses, and Paradoxical Changes in the Subendocardial Plexus. *Br Heart J* **26**, 39–50. doi:10.1136/hrt.26.1.39 (1964).
- 24. Schaper, W., Frenzel, H. & Hort, W. Experimental coronary artery occlusion. I. Measurement of infarct size. *Basic Res Cardiol* **74**, 46–53. doi:10.1007/BF01907684 (1979).
- 25. Schaper, W., Frenzel, H., Hort, W. & Winkler, B. Experimental coronary artery occlusion. II. Spatial and temporal evolution of infarcts in the dog heart. *Basic Res Cardiol* **74**, 233–239. doi:10.1007/BF01907740 (1979).
- 26. Bassingthwaighte, J. B., Yipintsoi, T. & Harvey, R. B. Microvasculature of the dog left ventricular myocardium. *Microvasc Res* 7, 229–249. doi:10.1016/0026-2862(74)90008-9 (1974).
- 27. Tomanek, R. J., Searls, J. C. & Lachenbruch, P. A. Quantitative changes in the capillary bed during developing, peak, and stabilized cardiac hypertrophy in the spontaneously hypertensive rat. *Circ Res* **51**, 295–304. doi:10.1161/01.res.51.3. 295 (1982).
- 28. VanBavel, E. & Spaan, J. A. Branching patterns in the porcine coronary arterial tree. Estimation of flow heterogeneity. *Circ Res* **71**, 1200–1212. doi:10.1161/01.res.71.5.1200 (1992).
- 29. Kassab, G. S., Rider, C. A., Tang, N. J. & Fung, Y. C. Morphometry of pig coronary arterial trees. *Am J Physiol Heart Circ Physiol* **265**, H350–H365. doi:10.1152/ajpheart.1993.265.1.H350 (1993).
- 30. Murakami, T. Application of the scanning electron microscope to the study of the fine distribution of the blood vessels. *Arch Histol Jpn* **32**, 445–454. doi:10.1679/aohc1950.32.445 (1971).
- 31. Hossler, F. E. & Douglas, J. E. Vascular corrosion casting: Review of advantages and limitations in the application of some simple quantitative methods. *Microsc Microanal* 7, 253–264. doi:10.1017/S1431927601010261 (2001).

- 32. Meyer, E. P., Ulmann-Schuler, A., Staufenbiel, M. & Krucker, T. Altered morphology and 3D architecture of brain vasculature in a mouse model for Alzheimer's disease. *Proc Natl Acad Sci U S A* **105**, 3587–3592. doi:10.1073/pnas.0709788105 (2008).
- 33. Stuker, F. *et al.* Hybrid small animal imaging system combining magnetic resonance imaging with fluorescence tomography using single photon avalanche diode detectors. *IEEE Trans Med Imaging* **30**, 1265–1273. doi:10.1109/TMI.2011.2112669 (2011).
- 34. Minnich, B. & Lametschwandtner, A. Lengths measurements in microvascular corrosion castings: two-dimensional versus three-dimensional morphometry. *Scanning* **22**, 173–177. doi:10.1002/sca.4950220305 (2000).
- 35. Jorgensen, S. M., Demirkaya, O. & Ritman, E. L. Three-dimensional imaging of vasculature and parenchyma in intact rodent organs with X-ray micro-CT. *Am J Physiol Heart Circ Physiol* **275**, H1103–H1114. doi:10.1152/ajpheart.1998.275.3.H1103 (1998).
- 36. Ritman, E. L. Current status of developments and applications of micro-CT. *Annu Rev Biomed Eng* **13**, 531–552. doi:10.1146/annurev-bioeng-071910-124717 (2011).
- 37. Oses, P. *et al.* Mapping 3-dimensional neovessel organization steps using microcomputed tomography in a murine model of hindlimb ischemia-brief report. *Arterioscler Thromb Vasc Biol* **29**, 2090–2092. doi:10.1161/ATVBAHA.109.192732 (2009).
- 38. Liu, P. *et al.* Microvascular imaging using synchrotron radiation. *J Synchrotron Radiat* **17,** 517–521. doi:10.1107/S0909049510018832 (2010).
- 39. Heinzer, S. *et al.* Hierarchical microimaging for multiscale analysis of large vascular networks. *Neuroimage* **32**, 626–636. doi:10.1016/j.neuroimage.2006.03.043 (2006).
- 40. Marxen, M. *et al.* MicroCT scanner performance and considerations for vascular specimen imaging. *Med Phys* **31**, 305–313. doi:10.1118/1.1637971 (2004).
- 41. Vasquez, S. X. *et al.* Optimization of microCT imaging and blood vessel diameter quantitation of preclinical specimen vasculature with radiopaque polymer injection medium. *PLoS One* **6**, e19099. doi:10.1371/journal.pone.0019099 (2011).
- 42. Lauzier, P. T. & Chen, G. H. Characterization of statistical prior image constrained compressed sensing. I. Applications to time-resolved contrast-enhanced CT. *Med Phys* **39**, 5930–5948. doi:10.1118/1.4748323 (2012).
- 43. Marxen, M., Paget, C., Yu, L. X. & Henkelman, R. M. Estimating perfusion using microCT to locate microspheres. *Phys Med Biol* **51**, N9–N16. doi:10.1088/0031-9155/51/1/N02 (2006).

- 44. Aanhaanen, W. T. J. *et al.* Developmental origin, growth, and three-dimensional architecture of the atrioventricular conduction axis of the mouse heart. *Circ Res* **107**, 728–736. doi:10.1161/CIRCRESAHA.110.222992 (2010).
- 45. Weninger, W. J., Meng, S., Streicher, J. & Muller, G. B. A new episcopic method for rapid 3-D reconstruction: applications in anatomy and embryology. *Anat Embryol* **197**, 341–348. doi:10.1007/s004290050144 (1998).
- 46. Ewald, A. J., McBride, H., Reddington, M., Fraser, S. E. & Kerschmann, R. Surface imaging microscopy, an automated method for visualizing whole embryo samples in three dimensions at high resolution. *Dev Dyn* **225**, 369–375. doi:10.1002/dvdy.10169 (2002).
- 47. Kelly, J. J., Ewen, J. R., Bernard, S. L., Glenny, R. W. & Barlow, C. H. Regional blood flow measurements from fluorescent microsphere images using an Imaging CryoMicrotome. *Rev Sci Instrum* **71**, 228–234. doi:10.1063/1.1150188 (2000).
- 48. Bernard, S. L. *et al.* High spatial resolution measurements of organ blood flow in small laboratory animals. *Am J Physiol Heart Circ Physiol* **279**, H2043–H2052. doi:10.1152/ajpheart.2000.279.5.H2043 (2000).
- 49. Spaan, J. A. E. *et al.* Visualisation of intramural coronary vasculature by an imaging cryomicrotome suggests compartmentalisation of myocardial perfusion areas. *Med Biol Eng Comput* **43**, 431–435. doi:10.1007/BF02344722 (2005).
- Van den Wijngaard, J. P. H. M. et al. Organization and collateralization of a subendocardial plexus in end-stage human heart failure. Am J Physiol Heart Circ Physiol 298, H158–H162. doi:10.1152/ajpheart.00654.2009 (2010).
- 51. Van den Wijngaard, J. P. H. M. *et al.* Porcine coronary collateral formation in the absence of a pressure gradient remote of the ischemic border zone. *Am J Physiol Heart Circ Physiol* **300**, H1930–H1937. doi:10.1152/ajpheart.00403.2010 (2011).
- 52. Van Horssen, P., Siebes, M., Hoefer, I., Spaan, J. A. E. & van den Wijngaard, J. P. H. M. Improved detection of fluorescently labeled microspheres and vessel architecture with an imaging cryomicrotome. *Med Biol Eng Comput* **48**, 735–744. doi:10.1007/s11517-010-0652-8 (2010).
- 53. Roy, D., Steyer, G. J., Gargesha, M., Stone, M. E. & Wilson, D. L. 3D cryoimaging: a very high-resolution view of the whole mouse. *Anat Rec* **292**, 342–351. doi:10.1002/ar.20849 (2009).
- 54. Sarantopoulos, A., Themelis, G. & Ntziachristos, V. Imaging the bio-distribution of fluorescent probes using multispectral epi-illumination cryoslicing imaging. *Mol Imaging Biol* 13, 874–885. doi:10.1007/s11307-010-0416-8 (2011).

- 55. Rosenthal, J., Mangal, V., Walker, D., Bennett, M., Mohun, T. J. & Lo, C. W. Rapid high resolution three dimensional reconstruction of embryos with episcopic fluorescence image capture. *Birth Defects Res C Embryo Today* **72**, 213–223. doi:10.1002/bdrc.20023 (2004).
- 56. Mohun, T. J. & Weninger, W. J. Imaging heart development using high-resolution episcopic microscopy. *Curr Opin Genet Dev* **21**, 573–578. doi:10.1016/j.gde. 2011.07.004 (2011).
- 57. Sands, G. B., Smaill, B. H. & LeGrice, I. J. Virtual sectioning of cardiac tissue relative to fiber orientation in 2008 30th Annual International Conference of the IEEE Engineering in Medicine and Biology Society (2008), 226–229. doi:10.1109/IEMBS. 2008.4649131.
- 58. Huang, H. *et al.* Three-dimensional cardiac architecture determined by two-photon microtomy. *J Biomed Opt* **14**, 044029. doi:10.1117/1.3200939 (2009).
- Pieles, G. et al. μMRI-HREM pipeline for high-throughput, high-resolution phenotyping of murine embryos. J Anat 211, 132–137. doi:10.1111/j.1469-7580. 2007.00746.x (2007).
- 60. Rolf, M. P., ter Wee, R., van Leeuwen, T. G., Spaan, J. A. & Streekstra, G. J. Diameter measurement from images of fluorescent cylinders embedded in tissue. *Med Biol Eng Comput* **46**, 589–596. doi:10.1007/s11517-008-0328-9 (2008).
- 61. Krishnamurthi, G., Wang, C. Y., Steyer, G. & Wilson, D. L. Removal of subsurface fluorescence in cryo-imaging using deconvolution. *Opt Express* **18**, 22324–22338. doi:10.1364/0E.18.022324 (2010).
- 62. Steyer, G. J., Roy, D., Salvado, O., Stone, M. E. & Wilson, D. L. Removal of out-of-plane fluorescence for single cell visualization and quantification in cryo-imaging. *Ann Biomed Eng* **37**, 1613–1628. doi:10.1007/s10439-009-9726-x (2009).
- 63. Flasque, N., Desvignes, M., Constans, J. M. & Revenu, M. Acquisition, segmentation and tracking of the cerebral vascular tree on 3D magnetic resonance angiography images. *Med Image Anal* 5, 173–183. doi:10.1016/s1361-8415(01)00038-x (2001).
- 64. Lee, J., Beighley, P., Ritman, E. & Smith, N. Automatic segmentation of 3D micro-CT coronary vascular images. *Med Image Anal* 11, 630–647. doi:10.1016/j.media. 2007.06.012 (2007).
- 65. Palágyi, K. & Kuba, A. A 3D 6-subiteration thinning algorithm for extracting medial lines. *Pattern Recognition Letters* **19**, 613–627. doi:10.1016/s0167-8655(98)00031-2 (1998).
- 66. Rudolph, A. M. & Heymann, M. A. The circulation of the fetus in utero. Methods for studying distribution of blood flow, cardiac output and organ blood flow. *Circ Res* **21**, 163–184. doi:10.1161/01.res.21.2.163 (1967).

- 67. Heymann, M. A., Payne, B. D., Hoffman, J. I. & Rudolph, A. M. Blood flow measurements with radionuclide-labeled particles. *Prog Cardiovasc Dis* **20**, 55–79. doi:10.1016/s0033-0620(77)80005-4 (1977).
- 68. Hoefer, I. E., van Royen, N., Buschmann, I. R., Piek, J. J. & Schaper, W. Time course of arteriogenesis following femoral artery occlusion in the rabbit. *Cardiovasc Res* **49**, 609–617. doi:10.1016/s0008-6363(00)00243-1 (2001).
- Van Oosterhout, M. F., Willigers, H. M., Reneman, R. S. & Prinzen, F. W. Fluorescent microspheres to measure organ perfusion: validation of a simplified sample processing technique. *Am J Physiol Heart Circ Physiol* 269, H725–H733. doi:10.1152/ajpheart.1995.269.2.H725 (1995).
- Buckberg, G. D., Luck, J. C., Payne, D. B., Hoffman, J. I., Archie, J. P. & Fixler, D. E. Some sources of error in measuring regional blood flow with radioactive microspheres. *J Appl Physiol* 31, 598–604. doi:10.1152/jappl.1971.31.4.598 (1971).
- 71. Robertson, H. T., Krueger, M. A., Lamm, W. J. & Glenny, R. W. High-resolution spatial measurements of ventilation-perfusion heterogeneity in rats. *J Appl Physiol* **108**, 1395–1401. doi:10.1152/japplphysiol.01161.2009 (2010).
- 72. Huo, Y. & Kassab, G. S. Intraspecific scaling laws of vascular trees. *J R Soc Interface* **9**, 190–200. doi:10.1098/rsif.2011.0270 (2012).
- 73. Prinzen, F. W. & Bassingthwaighte, J. B. Blood flow distributions by microsphere deposition methods. *Cardiovasc Res* **45**, 13–21. doi:10.1016/s0008-6363(99) 00252-7 (2000).
- 74. Decking, U. K. *et al.* High-resolution imaging reveals a limit in spatial resolution of blood flow measurements by microspheres. *Am J Physiol Heart Circ Physiol* **287**, H1132–H1140. doi:10.1152/ajpheart.00119.2004 (2004).
- 75. Hsu, L. Y., Groves, D. W., Aletras, A. H., Kellman, P. & Arai, A. E. A Quantitative Pixel-Wise Measurement of Myocardial Blood Flow by Contrast-Enhanced First-Pass CMR Perfusion Imaging: Microsphere Validation in Dogs and Feasibility Study in Humans. *JACC Cardiovasc Imaging* 5, 154–166. doi:10.1016/j.jcmg. 2011.07.013 (2012).
- 76. Hoffman, J. I. Heterogeneity of myocardial blood flow. *Basic Res Cardiol* **90**, 103–111. doi:10.1007/BF00789440 (1995).
- 77. Kaneko, N., Matsuda, R., Toda, M. & Shimamoto, K. Three-dimensional reconstruction of the human capillary network and the intramyocardial micronecrosis. *Am J Physiol Heart Circ Physiol* **300**, H754–H761. doi:10.1152/ajpheart.00486.2010 (2011).

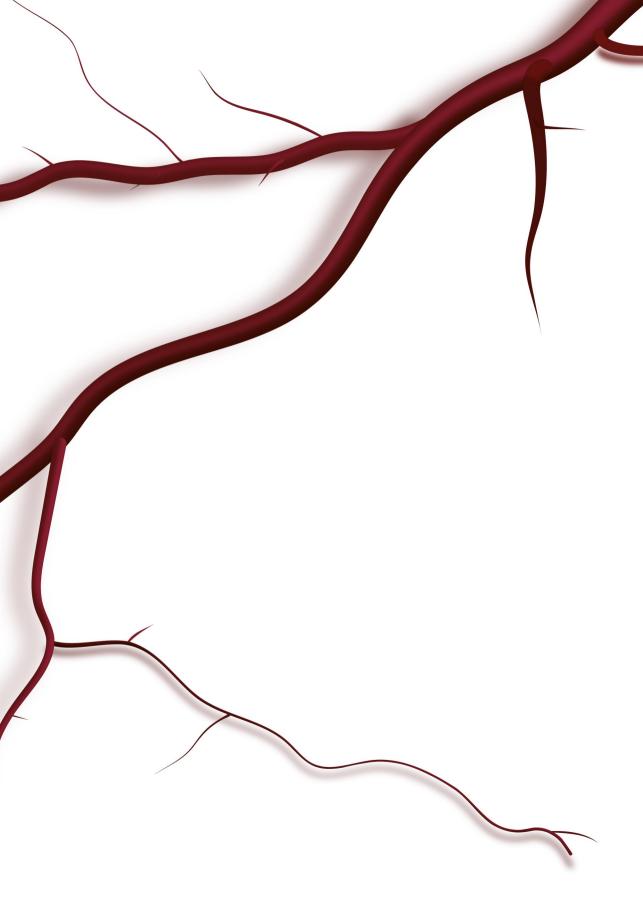
- 78. Komaru, T., Kanatsuka, H. & Shirato, K. Coronary microcirculation: physiology and pharmacology. *Pharmacol Ther* **86**, 217–261. doi:10.1016/s0163-7258(00)00057-7 (2000).
- 79. Thoma, R. Untersuchungen über die Histogenese und Histomechanik des Gefässsystems (Enke, Stuttgart, 1893).
- 80. Murray, C. D. The Physiological Principle of Minimum Work: I. The Vascular System and the Cost of Blood Volume. *Proc Natl Acad Sci U S A* **12**, 207–214. doi:10.1073/pnas.12.3.207 (1926).
- 81. Horsfield, K. & Woldenberg, M. J. Diameters and cross-sectional areas of branches in the human pulmonary arterial tree. *Anat Rec* **223**, 245–251. doi:10.1002/ar.1092230302 (1989).
- 82. Griffith, T. M. & Edwards, D. H. EDRF in intact vascular networks. *Blood Vessels* **27**, 230–237. doi:10.1159/000158814 (1990).
- 83. Zhou, Y., Kassab, G. S. & Molloi, S. On the design of the coronary arterial tree: a generalization of Murray's law. *Phys Med Biol* **44**, 2929–2945. doi:10.1088/0031-9155/44/12/306 (1999).
- 84. Kassab, G. S. Scaling laws of vascular trees: of form and function. *Am J Physiol Heart Circ Physiol* **290**, H894–H903. doi:10.1152/ajpheart.00579.2005 (2006).
- 85. Arts, T., Kruger, R. T., van Gerven, W., Lambregts, J. A. & Reneman, R. S. Propagation velocity and reflection of pressure waves in the canine coronary artery. *Am J Physiol Heart Circ Physiol* **237**, H469–H474. doi:10.1152/ajpheart.1979.237.4.H469 (1979).
- 86. Schaper, W. Collateral circulation: past and present. *Basic Res Cardiol* **104**, 5–21. doi:10.1007/s00395-008-0760-x (2009).
- 87. Van den Akker, J., Schoorl, M. J., Bakker, E. N. & vanBavel, E. Small artery remodeling: current concepts and questions. *J Vasc Res* 47, 183–202. doi:10.1159/000255962 (2010).
- 88. Langille, B. L. & O'Donnell, F. Reductions in arterial diameter produced by chronic decreases in blood flow are endothelium-dependent. *Science* **231**, 405–407. doi:10.1126/science.3941904 (1986).
- 89. Hacking, W. J., VanBavel, E. & Spaan, J. A. Shear stress is not sufficient to control growth of vascular networks: a model study. *Am J Physiol Heart Circ Physiol* **270**, H364–H375. doi:10.1152/ajpheart.1996.270.1.H364 (1996).
- 90. Liu, Y. & Kassab, G. S. Vascular metabolic dissipation in Murray's law. *Am J Physiol Heart Circ Physiol* **292**, H1336–H1339. doi:10.1152/ajpheart.00906.2006 (2007).

- 91. Cheng, C. *et al.* Large variations in absolute wall shear stress levels within one species and between species. *Atherosclerosis* **195**, 225–235. doi:10.1016/j.atherosclerosis. 2006.11.019 (2007).
- 92. Reneman, R. S. & Hoeks, A. P. Wall shear stress as measured in vivo: consequences for the design of the arterial system. *Med Biol Eng Comput* **46**, 499–507. doi:10.1007/s11517-008-0330-2 (2008).
- 93. Bassingthwaighte, J. B., King, R. B. & Roger, S. A. Fractal nature of regional myocardial blood flow heterogeneity. *Circ Res* **65**, 578–590. doi:10.1161/01.res. 65.3.578 (1989).
- 94. Zamir, M. On fractal properties of arterial trees. *J Theor Biol* **197**, 517–526. doi:10. 1006/jtbi.1998.0892 (1999).
- 95. Van Beek, J. H., Roger, S. A. & Bassingthwaighte, J. B. Regional myocardial flow heterogeneity explained with fractal networks. *Am J Physiol Heart Circ Physiol* **257**, H1670–H1680. doi:10.1152/ajpheart.1989.257.5.H1670 (1989).
- 96. Schreiner, W., Karch, R., Neumann, M., Neumann, F., Roedler, S. M. & Heinze, G. Heterogeneous perfusion is a consequence of uniform shear stress in optimized arterial tree models. *J Theor Biol* **220**, 285–301. doi:10.1006/jtbi.2003.3136 (2003).
- 97. Strahler, A. N. Hypsometric (Area-Altitude) Analysis of Erosional Topography. *Geol Soc Am Bull* **63**, 1117–1142. doi:10.1130/0016-7606(1952)63[1117:Haaoet]2.0.Co;2 (1952).
- 98. Dankelman, J., Cornelissen, A. J. M., Lagro, J., VanBavel, E. & Spaan, J. A. E. Relation between branching patterns and perfusion in stochastic generated coronary arterial trees. *Med Biol Eng Comput* **45**, 25–34. doi:10.1007/s11517-006-0139-9 (2007).
- 99. Kaimovitz, B., Lanir, Y. & Kassab, G. S. A full 3-D reconstruction of the entire porcine coronary vasculature. *Am J Physiol Heart Circ Physiol* **299**, H1064–H1076. doi:10.1152/ajpheart.00151.2010 (2010).
- 100. Huo, Y., Kaimovitz, B., Lanir, Y., Wischgoll, T., Hoffman, J. I. & Kassab, G. S. Biophysical model of the spatial heterogeneity of myocardial flow. *Biophys J* **96**, 4035–4043. doi:10.1016/j.bpj.2009.02.047 (2009).
- 101. Smith, N. P., Pullan, A. J. & Hunter, P. J. Generation of an anatomically based geometric coronary model. *Ann Biomed Eng* **28**, 14–25. doi:10.1114/1.250 (2000).
- 102. Smith, N. P. & Kassab, G. S. Analysis of coronary blood flow interaction with myocardial mechanics based on anatomical models. *Phil Trans R Soc A* **359**, 1251–1262. doi:10.1098/rsta.2001.0829 (2001).

- 103. Mittal, N., Zhou, Y., Ung, S., Linares, C., Molloi, S. & Kassab, G. S. A computer reconstruction of the entire coronary arterial tree based on detailed morphometric data. *Ann Biomed Eng* **33**, 1015–1026. doi:10.1007/s10439-005-5758-z (2005).
- 104. Schreiner, W., Karch, R., Neumann, M., Neumann, F., Szawlowski, P. & Roedler, S. Optimized arterial trees supplying hollow organs. *Med Eng Phys* **28**, 416–429. doi:10.1016/j.medengphy.2005.07.019 (2006).
- 105. Huo, Y. & Kassab, G. S. A scaling law of vascular volume. *Biophys J* **96**, 347–353. doi:10.1016/j.bpj.2008.09.039 (2009).
- 106. Huo, Y. & Kassab, G. S. The scaling of blood flow resistance: from a single vessel to the entire distal tree. *Biophys J* **96**, 339–346. doi:10.1016/j.bpj.2008.09.038 (2009).
- 107. Seiler, C., Kirkeeide, R. L. & Gould, K. L. Basic structure-function relations of the epicardial coronary vascular tree. Basis of quantitative coronary arteriography for diffuse coronary artery disease. *Circulation* **85**, 1987–2003. doi:10.1161/01.cir. 85.6.1987 (1992).
- 108. Seiler, C., Kirkeeide, R. L. & Gould, K. L. Measurement from arteriograms of regional myocardial bed size distal to any point in the coronary vascular tree for assessing anatomic area at risk. *J Am Coll Cardiol* 21, 783–797. doi:10.1016/0735– 1097 (93) 90113-f (1993).
- 109. Choy, J. S. & Kassab, G. S. Scaling of myocardial mass to flow and morphometry of coronary arteries. *J Appl Physiol* **104**, 1281–1286. doi:10.1152/japplphysiol.01261.2007 (2008).
- 110. Molloi, S. & Wong, J. T. Regional blood flow analysis and its relationship with arterial branch lengths and lumen volume in the coronary arterial tree. *Phys Med Biol* **52**, 1495–1503. doi:10.1088/0031-9155/52/5/018 (2007).
- 111. Molloi, S., Chalyan, D., Le, H. & Wong, J. T. Estimation of coronary artery hyperemic blood flow based on arterial lumen volume using angiographic images. *Int J Cardiovasc Imaging* **28**, 1–11. doi:10.1007/s10554-010-9766-1 (2012).
- 112. Van de Hoef, T. P. *et al.* Coronary pressure-flow relations as basis for the understanding of coronary physiology. *J Mol Cell Cardiol* **52**, 786–793. doi:10.1016/j.yjmcc.2011.07.025 (2012).
- 113. Taylor, C. A. & Steinman, D. A. Image-Based Modeling of Blood Flow and Vessel Wall Dynamics: Applications, Methods and Future Directions. *Ann Biomed Eng* **38**, 1188–1203. doi:10.1007/s10439-010-9901-0 (2010).
- 114. Siebes, M. & Ventikos, Y. The Role of Biofluid Mechanics in the Assessment of Clinical and Pathological Observations. *Ann Biomed Eng* **38**, 1216–1224. doi:10.1007/s10439-010-9903-y (2010).

- 115. Kajiya, F., Yada, T., Hiramatsu, O., Ogasawara, Y., Inai, Y. & Kajiya, M. Coronary microcirculation in the beating heart. *Med Biol Eng Comput* **46**, 411–419. doi:10.1007/s11517-008-0335-x (2008).
- 116. Van den Wijngaard, J. P. *et al.* Model prediction of subendocardial perfusion of the coronary circulation in the presence of an epicardial coronary artery stenosis. *Med Biol Eng Comput* **46**, 421–432. doi:10.1007/s11517-008-0314-2 (2008).
- 117. Garcia, D. *et al.* Impairment of coronary flow reserve in aortic stenosis. *J Appl Physiol* **106**, 113–121. doi:10.1152/japplphysiol.00049.2008 (2009).
- 118. Algranati, D., Kassab, G. S. & Lanir, Y. Mechanisms of myocardium-coronary vessel interaction. *Am J Physiol Heart Circ Physiol* **298**, H861–H873. doi:10.1152/ajpheart.00925.2009 (2010).
- 119. Smith, N. P. A computational study of the interaction between coronary blood flow and myocardial mechanics. *Physiol Meas* **25**, 863–877. doi:10.1088/0967-3334/25/4/007 (2004).
- 120. Huo, Y. & Kassab, G. S. A hybrid one-dimensional/Womersley model of pulsatile blood flow in the entire coronary arterial tree. *Am J Physiol Heart Circ Physiol* **292**, H2623–H2633. doi:10.1152/ajpheart.00987.2006 (2007).
- 121. Cookson, A. N. *et al.* A novel porous mechanical framework for modelling the interaction between coronary perfusion and myocardial mechanics. *J Biomech* **45**, 850–855. doi:10.1016/j.jbiomech.2011.11.026 (2012).
- 122. Waters, S. L. *et al.* Theoretical models for coronary vascular biomechanics: progress & challenges. *Prog Biophys Mol Biol* **104**, 49–76. doi:10.1016/j.pbiomolbio.2010.10.001 (2011).
- 123. Formaggia, L., Nobile, F., Quarteroni, A. & Veneziani, A. Multiscale modelling of the circulatory system: a preliminary analysis. *Comput Visual Sci* **2**, 75–83. doi:10.1007/s007910050030 (1999).
- 124. Kim, H. J., Vignon-Clementel, I. E., Coogan, J. S., Figueroa, C. A., Jansen, K. E. & Taylor, C. A. Patient-specific modeling of blood flow and pressure in human coronary arteries. *Ann Biomed Eng* **38**, 3195–3209. doi:10.1007/s10439-010-0083-6 (2010).
- 125. Koo, B.-K. et al. Diagnosis of ischemia-causing coronary stenoses by noninvasive fractional flow reserve computed from coronary computed tomographic angiograms. Results from the prospective multicenter DISCOVER-FLOW (Diagnosis of Ischemia-Causing Stenoses Obtained Via Noninvasive Fractional Flow Reserve) study. J Am Coll Cardiol 58, 1989–1997. doi:10.1016/j.jacc.2011.06.066 (2011).
- 126. Lee, J. & Smith, N. P. The multi-scale modelling of coronary blood flow. *Ann Biomed Eng* **40**, 2399–2413. doi:10.1007/s10439-012-0583-7 (2012).

- 127. Lee, J. *et al.* Coupling contraction, excitation, ventricular and coronary blood flow across scale and physics in the heart. *Philos Trans A Math Phys Eng Sci* **367**, 2311–2331. doi:10.1098/rsta.2008.0311 (2009).
- 128. Nordsletten, D. A., Niederer, S. A., Nash, M. P., Hunter, P. J. & Smith, N. P. Coupling multi-physics models to cardiac mechanics. *Prog Biophys Mol Biol* **104**, 77–88. doi:10.1016/j.pbiomolbio.2009.11.001 (2011).
- 129. Ricotta, J. J., Pagan, J., Xenos, M., Alemu, Y., Einav, S. & Bluestein, D. Cardiovas-cular disease management: the need for better diagnostics. *Med Biol Eng Comput* **46**, 1059–1068. doi:10.1007/s11517-008-0416-x (2008).
- 130. Hunter, P. J. & Viceconti, M. The VPH-Physiome Project: Standards and Tools for Multiscale Modeling in Clinical Applications. *IEEE Reviews in Biomedical Engineering* **2**, 40–53. doi:10.1109/RBME.2009.2036204 (2009).
- 131. Niederer, S. A. & Smith, N. P. At the heart of computational modelling. *J Physiol* **590**, 1331–1338. doi:10.1113/jphysiol.2011.225045 (2012).





CHAPTER 3

Optimization of Vascular Casting for Three-Dimensional Fluorescence Cryo-Imaging of Collateral Vessels in the Ischemic Rat Hindlimb

Janina C. V. Schwarz, Monique G. J. T. B. van Lier, Erik N. T. P. Bakker, Judith de Vos, Jos A. E. Spaan, Ed van Bavel, and Maria Siebes

Department of Biomedical Engineering and Physics, Academic Medical Center, University of Amsterdam, Meibergdreef 9, 1105 AZ Amsterdam, The Netherlands

ABSTRACT

Background

Development of collateral vessels, arteriogenesis, may protect against tissue ischemia, however, quantitative data on this process remain scarce.

Methods

We have developed a technique for replicating the entire arterial network of ischemic rat hindlimbs in three dimensions (3D) based on vascular casting and automated sequential cryo-imaging. Various dilutions of Batson's No. 17 with methyl methacrylate were evaluated in healthy rats, with further protocol optimization in ischemic rats.

Results

Penetration of the resin into the vascular network greatly depended on dilution; the total length of casted vessels below 75 μm was 13-fold higher at 50% dilution compared with the 10% dilution. Dilutions of 25–30%, with transient clamping of the healthy iliac artery, were optimal for imaging the arterial network in unilateral ischemia. This protocol completely filled the lumina of small arterioles and collateral vessels. These appeared as thin anastomoses in healthy legs and increasingly larger vessels during ligation (median diameter 1 week: 63 μm , 4 weeks: 127 μm).

Conclusions

The presented combination of quality casts with high-resolution cryo-imaging enables automated, detailed 3D analysis of collateral adaptation, which furthermore can be combined with co-registered 3D distributions of fluorescent molecular imaging markers reflecting biological activity or perfusion.

Keywords: 3D imaging, vascular imaging, vascular casting, hindlimb ischemia, collateral vessels

3.1 Introduction

Remodeling of the arterial network, including enlargement of preexisting anastomoses, may protect against chronically developing tissue ischemia. The rodent hindlimb ischemia model is frequently employed to unravel mechanisms of such angio-adaptation¹⁻³ and to determine the effect of pro-angiogenic and pro-arteriogenic therapies. 4-6 The changes in vascular anatomy in this model are typically assessed with X-ray or magnetic resonance angiography, 7,8 however, these methods have limited spatial resolution. Contrast-enhanced micro-computed tomography (micro-CT) and optical techniques provide alternatives. 9-11 Of these, optical techniques provide the advantage of molecular imaging possibilities. Such techniques, in combination with anatomical imaging, are needed for monitoring expression of relevant markers in among others endothelial and inflammatory cells. Histological techniques provide excellent resolution for immunohistochemical and other molecular markers. However, imaging over large tissue volumes or in three dimensions (3D) is generally not feasible. Alternative molecular imaging methods include nuclear imaging methodologies, such as single photon emission CT or positron emission tomography. These allow high sensitivity probing of expression and also of regional perfusion in vivo, 12 yet these modalities have very limited resolution and do not provide details on individual vessels beyond the major arteries.

The recent surge in the development of fluorescent markers presents opportunities for 3D optical imaging technologies that can track the remodeling process of the involved vascular networks in response to an ischemic insult or therapeutic intervention in combination with the distribution of fluorescent biomarkers that report on local molecular activity. Such combined acquisition is feasible with an imaging cryomicrotome, which performs sequential cutting and high-resolution episcopic imaging, discriminating up to six distinct fluorescent labels in frozen organs. Complete vascular networks can be visualized in 3D with this technique, based on classical vascular casting techniques using a fluorescently labeled replica material. He

High-resolution imaging of angio-adaptation covering a wide range of vessel sizes over a larger volume requires balanced filling by the casting material. Obviously, collateral vessels should be reliably casted. Filling of capillaries, however, should be prevented as the large volume of interest can only be imaged at supra-capillary resolution and at such resolution, filled capillaries would appear as increased background fluorescence that diminishes image contrast. Therefore, the aim of this study was to optimize vascular specimen preparation for detailed 3D fluorescence cryo-

imaging and quantification of the entire arterial network, especially all collateral anastomoses, in the ischemic rat thigh. We tested the outcome of different cast materials, resin compositions as well as infusion methods both in healthy hindlimbs and at different time points after inducing vascular remodeling by selective artery ligation and provide an optimized protocol for this method.

3.2 MATERIALS AND METHODS

In an initial series of experiments, the effect of resin composition on small artery penetration was investigated in 34 healthy hindlimbs of 23 rats obtained immediately post mortem after completion of other in-house studies. Optimized filling of collateral arteries was subsequently tested in 12 rats (male Sprague-Dawley rats, 9–12 weeks old; Charles River, Germany) in which arteriogenesis was stimulated by unilateral hindlimb ischemia, as described below. The animals had access to food and water ad libitum. The protocol was approved by the Institutional Animal Care and Use Committee of the Academic Medical Center of the University of Amsterdam.

3.2.1 Hindlimb Ischemia Model

After receiving a subcutaneous injection of buprenorphine (temgesic, 0.03 mg/kg) and carprofen as analgesics (15 mg/kg), the animals were anesthetized in an induction box with isoflurane (3%). Throughout the procedure, anesthesia was maintained by inhalation of 2.5% isoflurane mixed with oxygen through a nose mask and the animal was kept on a heating pad to maintain body temperature. The right thigh was shaved and disinfected with iodine solution. Moderate hindlimb ischemia was induced by ligating three arteries with 7-0 silk sutures: the epigastric artery, the proximal saphenous artery, and the femoral artery just proximal to its division into the saphenous and popliteal artery. The skin was closed with a sterile 5-0 suture, and the animal was allowed to recover.

3.2.2 Replica Materials

The cast was formed by polymerization of a base solution with a catalyst. Three components were utilized for the base solutions: Batson's No. 17 monomer solution (Polysciences, Warrington, PA, USA), Mercox (Ladd Research Industries, Williston, VT, USA) and methyl methacrylate (MMA; Polysciences, Warrington, PA, USA), where Batson's monomer solution is more viscous than Mercox and MMA acts as

a diluent. Different base solutions were created by varied combinations of these components: Batson's diluted 10–50% with MMA, Batson's-Mercox mixtures, and undiluted Mercox. Fluorescent dye (UV blue; VasQTec, Zurich, Switzerland) was added to the base solutions. Polymerization was initiated either with Mercox catalyst or with Batson's promoter and catalyst based on the main component.

3.2.3 Vascular Casting

In the healthy rats, the abdominal cavity was opened immediately post mortem and either the abdominal aorta or one or both of the iliac arteries were dissected free and cannulated (short tubing of 0.3–0.6 mm inner diameter attached to a longer tubing of larger diameter).

In the ischemic animals, anesthesia was induced 1 (n = 6) or 4 (n = 6) weeks after surgery with isoflurane, which was hereafter maintained using an intraperitoneal injection of ketamine (75 mg/kg) and dexdomitor (0.5 mg/kg). Heparin (250 U) was injected for anticoagulation. Then, both hindlimbs were shaved, the legs were fixated in a spread position, and the abdomen was opened. The abdominal aorta was dissected free and cannulated distal to the renal arteries in the direction of flow. For this purpose, a custom-built cannula was made by connecting a 2.5 cm tip of a rat femoral catheter (1.02 mm outer diameter; 0.61 mm inner diameter; Alzet, Charles River Laboratories, L'Arbresle Cedex, France) to an extension tube (2.5 mm inner diameter; Vygon, Valkenswaard, The Netherlands). Subsequently, the rats were euthanized by an injection of pentobarbital into the vena cava.

After cannulating the arterial access vessel, the vena cava was severed to provide outflow. To prevent thrombus formation and to ensure maximum and reproducible vasodilation, the hindlimb vasculature was flushed with heparinized calcium-free buffer solution (composed of 8.474 g/l sodium chloride, 0.628 g/l 3-(N-morpholino)propanesulfonic acid (MOPS), 0.351 g/l potassium chloride, 0.288 g/l magnesium sulphate, and 0.166 g/l monosodium phosphate, pH = 7.35) prewarmed to 37 °C. First, the buffer was infused manually using a syringe. When sanguineous efflux from the vena cava was noticed, the cannula was connected to a pressure-controlled system kept at 100 mmHg. After the hindlimb(s) became pale, perfusion was switched to the replica material at the same pressure. Great care was taken to not introduce any air bubbles to the perfusate, and observed bubbles were removed via a T-junction.

For the ischemic rats, the filling protocol was additionally modified to improve collateral penetration. The left iliac artery and vein (healthy side) were clamped during flushing once the efflux was clear of blood. These clamps were released during vascular casting as soon as arrival of the fluorescent resin was noted in the right, ischemic foot (typically within a few minutes) to complete arterial filling of the healthy leg.

The onset of polymerization could be noted by a temperature rise as well as by a color change from light yellow to orange. The resin was allowed to cure at ambient temperature for several hours, after which the specimen was frozen at -20 °C. In preparation for episcopic cryo-imaging, the frozen rat hindlimbs were embedded in a gel containing carboxymethylcellulose sodium solvent (Brunschwig Chemie, Amsterdam, The Netherlands) mixed with Indian ink (Royal Talens, Apeldoorn, The Netherlands). The embedded sample was frozen and stored at -20 °C.

3.2.4 Episcopic Cryomicrotome Imaging

Co-registered stacks of sequential 2D images were acquired for each specimen with an automated imaging cryomicrotome. ^{14,15} The sample surface was illuminated by light emitting diodes (Luxeon emitters; Philips Lumileds Lighting, San Jose, CA, USA). The camera lens (AF-D Zoom Micro-Nikkor 70–180 mm; Nikon, Tokyo, Japan) and the slice thickness were set to yield an isotropic voxel resolution of $24 \,\mu\text{m}$ over a field of view of $9.8 \times 9.8 \,\text{cm}^2$. After each slice was cut, two 12-bit images of the bulk surface were acquired with a 4096 × 4096 pixel charge-coupled device camera (Alta U-16; Apogee Imaging Systems Inc., Roseville, CA, USA). The first image was of vascular cast fluorescence with peak excitation at 361 nm and emission at 435 nm (bandwidth 25 nm) or 505 nm (bandwidth 30 nm) using interference filters (Chroma Technology, Bellows Falls, VT, USA). To optimize the image quality for segmentation, the emission filter, the camera aperture, and exposure time were slightly varied during the initial stage (f/8-f/22, time 10-20 s). The improved lens performance at 505 nm outweighed the weaker fluorescent signal such that the 505 nm filter (f/8, exposure time 10 s) was subsequently used. The second (brightfield) image was acquired in order to obtain structural information using excitation at 440 nm and emission at 435 nm.

3.2.5 Image Analysis and Quantification

The detailed 3D vascular architecture of the entire hindlimbs was reconstructed from the co-registered image stacks. Preprocessing included correction of pixels suffering from dark current noise and Richardson-Lucy deconvolution¹⁶ of the raw cast images with a system-specific point-spread function established by blind

deconvolution (Matlab; The MathWorks Inc., Natick, MA, USA). Visualization and segmentation of the vascular structures was done in Amira 5.6 (FEI Visualization Sciences Group, Mérignac Cedex, France). First, a coarse binary mask to select the regions containing fluorescent structures was created by morphological growth (hole filling, dilation) of the union of the 0.5% voxels with highest intensity and the connected components (minimum size 1000 voxels) of the 1% voxels with highest intensity. As vascular trees are connected and the morphological operations accounted for possible artifacts such as broken cast segments, this mask was then restricted to connected components with a minimum size of 10 000 voxels. The segmented vasculature was obtained by thresholding the masked de-blurred image stack. Finally, the segmented vasculature was skeletonized and represented as a graph consisting of segments with associated length and mean diameter using Amira's Auto Skeleton module. Graphs were visualized with continuous pseudo-coloring of the local diameter.

In order to evaluate the effect of resin dilution, a region of interest of $10 \times 15 \times 15$ mm³ was defined around the distal femoral artery for the healthy animals. The segments in this region were grouped according to their diameter, counted, and the average segment length as well as the cumulative length per tissue volume was computed per diameter class. The segmented vasculature within this region normalized to the tissue volume was defined as the vascular volume fraction. In the ischemic hindlimbs, the gracilis collaterals, which form superficial anastomoses between the muscular branch of the femoral artery and the saphenous artery, are frequently used to assess arteriogenesis and were identified in Amira and segmented for two representative cases as described in Figure 3.1.

In addition, the vasculature of one ischemic hindlimb was segmented, the vessels were represented by their centerlines, and collateral candidates were automatically detected as previously described. Collaterals were selected from the candidates bridging the femoral occlusion, followed by manual verification of their pathways against the raw data. Collateral length was computed as the sum of the distances between adjacent centerline points. The ratio of collateral length to the distance between the end points of the collateral was taken as a measure of tortuosity, where unity represents straight vessels and higher values reflect increasing tortuosity.

Kruskal–Wallis tests with Dunn's post-hoc analysis were employed to compare segment lengths and collateral diameters. Differences in segment characteristics per diameter class between dilutions were assessed using Friedman's test. A *p*-value of 0.05 was considered significant. All analyses were performed using SPSS version 20.0 (IBM Corporation, Armonk, NY, USA).

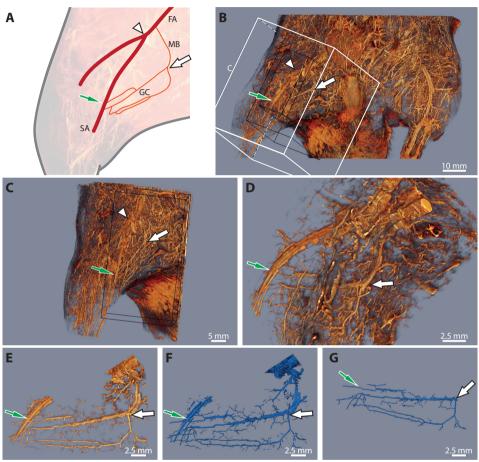


Figure 3.1: Identification of the gracilis collaterals (GC) based on anatomic landmarks as depicted in **(A)**. First, the femoral artery (FA) and the saphenous artery (SA) were identified in a three-dimensional volume rendering of the entire raw data set **(B)**. Then, the field of view was iteratively increasingly restricted as indicated by the boxes **(C,D)** up to a final, manually selected region of interest **(E)**. For the final region, a binary mask was created by thresholding **(F)**. Segmentation of the GC was obtained by restriction of this mask with subsequent manual inspection **(G)**. MB = muscular branch of femoral artery.

3.3 RESULTS

All specimens were successfully casted and cryo-imaged in continuous sessions lasting between 25 h for part of a leg and 165 h for the entire lower body of a rat. Typical data sets ranged from 60 GB (1500 slices) for part of the thigh to 220 GB (5500 slices) for the lower body.

3.3.1 Vessel Filling in Healthy Rats

Penetration into the vascular bed and polymerization of the resin were achieved with all resin combinations. The degree of filling varied with dilution of the base solution. The most viscous resin (10% dilution) only reached arteries and main arterioles (Figure 3.2). With increasing dilution, more detailed arterial structures were penetrated by the resin as reflected in the segmented vascular network (middle and bottom panels of Figure 3.2). These graphs comprised 755, 9300, and 18129 segments for the 10%, the 20%, and the 50% dilution, respectively. Figures 3.3A and 3.3B illustrate that the total length of filled vessels strongly increased with dilution in the region of interest (as indicated by boxes in Figure 3.2, p < 0.001) and in the thigh in general (p < 0.001). The cumulative normalized length of small vessels (mean diameter <75 µm) rose fivefold and 13-fold in the region of interest for the moderate and the strong dilution, respectively. Also the summed length of mediumsized (75–300 µm) vessels increased with dilution, yet to a smaller degree (inserts in Figure 3.3). This was paralleled by a rise in casted vascular volume fraction from 0.1% to 0.4% and 1.8%. Figure 3.3C shows that the increase in length was mainly due to a larger number of segments (p = 0.002) rather than an increase in individual segment length (Figure 3.3D). The normalized number of small segments increased by factors of 6 and 13, respectively, whereas there was no significant difference in median segment length between the low and the moderate dilution with a moderate increase for the strongest dilution (respectively 184, 176, and 236 µm).

Venous filling was generally observed with low viscosity resins, such as Mercox or high dilutions of Batson's, as reflected by the presence of vessels >600 μm for the 50% diluted resin. Such large segments were absent in the other resins (Figure 3.3). Overall, a mixture of Batson's with 25–30% MMA produced optimal casts of arteries and arterioles for cryo-imaging with little venous filling. This dilution was selected for casting of the ischemic hindlimbs.

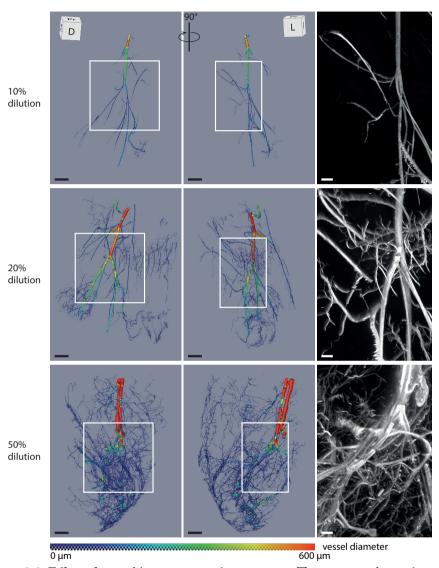


Figure 3.2: Effect of resin dilution on vessel penetration. The segmented vasculature in the hindlimbs of healthy rats is shown by volume renderings pseudo-colored by diameter (left and center panels, orthogonal views) and by maximum intensity projections of the raw data in a region of interest (right panels). Diluted Batson's penetrated smaller vessels: limited penetration at 10% dilution **(top)**, 20% dilution **(middle)**, and filling of veins at 50% dilution **(bottom)**. D, dorsal; L, lateral; M, medial; Pr, proximal; V, ventral. Scale bar: **(left and center)** 3 mm and **(right)** panels 1 mm.

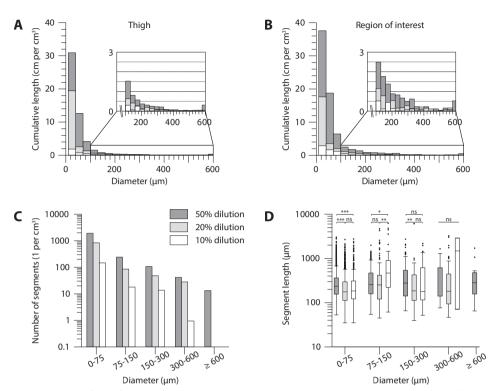


Figure 3.3: Effect of resin dilution on cumulative vessel length versus diameter in hindlimbs of healthy rats for the thigh **(A)** and a region of interest around the distal femoral artery **(B)**. Inserts show expanded length scale for diameters $\geq 100 \, \mu m$. Both the number of segments **(C)** and, to a smaller degree, the individual segment lengths **(D)** contributed to the difference in cumulative length. * p < 0.05, ** p < 0.01, *** p < 0.001.

3.3.2 Vessel Filling in Unilateral Hindlimb Ischemia

Simultaneous perfusion of both the healthy and ischemic hindlimb with the optimal resin mixture established for healthy legs resulted in an imbalanced filling (Figure 3.4A). Although the resin reached the toes of the healthy left leg, no vessel distal to the femoral ligation was penetrated. Modification of the protocol by initial clamping of the iliac artery of the unligated side during infusion of the replica material yielded more complete vascular casts (Figures 3.4B, 3.4C). Main vessels of all regions in the leg such as the femoral, saphenous, and tibial arteries were consistently visible in both hindlimbs. Casts replicated the arterial network with a great level of detail. Histology confirmed successful penetration of the selected

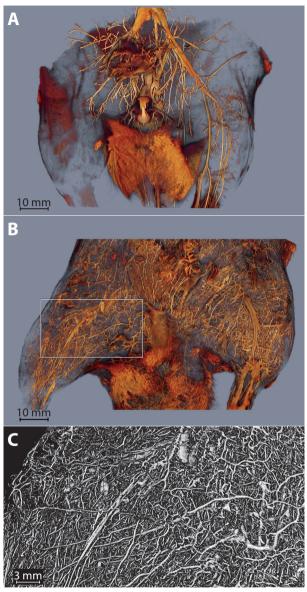


Figure 3.4: Three-dimensional visualization of hindlimb vasculature 1 week post unilateral ligation using the optimized resin dilution. In contrast to unbalanced filling of the healthy left and ischemic right hindlimb with simultaneous filling **(A)**, collaterals and vessels distal to the femoral obstruction were adequately penetrated when sequential perfusion was applied by initial clamping of the left iliac artery **[(B)** raw data, **(C)** segmented vasculature].

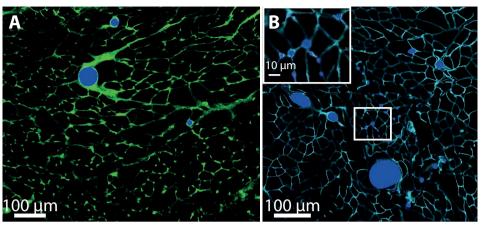


Figure 3.5: Representative histological sections of a healthy rat thigh perfused with resin according to the optimized protocol (blue) and stained with lectin [green, (**A**)] and against laminin α -1 as basement membrane marker [cyan, (**B**)]. Cast material demonstrates complete filling of the lumina including small vessels. The inset of (**B**) demonstrates occasional filling of capillaries close to major vessels.

resin into small vessels (diameter in the order of $15\,\mu m$) with complete filling of the vascular lumen (Figures 3.5A, 3.5B). The capillary bed remained unfilled in most of the hindlimb (Figure 3.5A), with occasional filling of capillaries that were located close to much larger arteries (Figure 3.5B and inset).

Importantly, the collateral vessels of the ischemic leg were reliably replicated as assessed by macroscopic inspection of the commonly described preexisting anastomoses. Figure 3.6 and Supplementary Movie 1 (Figure 3.S1) show the 12 collateral pathways bypassing the ligation that were found in an exemplary hindlimb 1 week post ligation. The deep pathways tended to be more tortuous, with the collaterals re-entering into the popliteal artery exhibiting the longest paths (Table 3.1). The gracilis collateral pathways appeared as thin anastomoses in healthy legs and early

Table 3.1: Collateral characteristics

Re-entry location	n	Length (mm)	Tortuosity
Saphenous artery Popliteal artery Geniculate artery	4 4 4	28.2 ± 2.6 39.9 ± 8.9 25.8 ± 2.3	1.5 ± 0.1 2.0 ± 0.4 1.9 ± 0.3

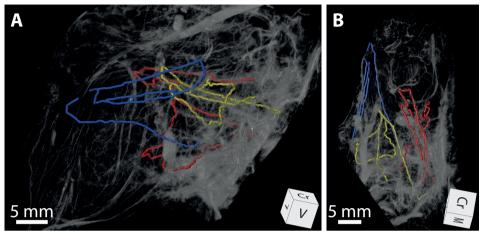


Figure 3.6: Collateral pathways in a hindlimb 1 week post ligation. Multiple deep pathways feed the popliteal artery (red) and the geniculate artery (yellow); the saphenous artery is supplied by one deep pathway as well as by the superficial gracilis collaterals (blue). Cr, cranial; L, lateral; M, medial; V, ventral.

after femoral artery ligation, whereas they became increasingly prominent 1 and 4 weeks post ligation. Figure 3.7 illustrates segmentation and diameter estimation of the gracilis collaterals with a representative case shown for each time point. Four weeks post ligation (Figure 3.7B), the collateral network was more developed than in the hindlimb 1 week post ligation (Figure 3.7A). This was reflected by an increase in both the number of vessels and the diameter of the main collateral vessels. The total length and volume of the collateral vasculature increased threefold and sevenfold, respectively. The median diameter of the main collateral vessels enlarged from 63 μ m 1 week post ligation to 127 μ m after 4 weeks of ligation (p < 0.001).

3.4 Discussion

We presented an optimized vascular casting method of the ischemic rat hindlimb for episcopic fluorescence imaging with an automated cryomicrotome. The resulting image stacks yielded detailed 3D reconstructions of the entire arterial network in the lower body, with vessels ranging from 24 μ m to 1.5 mm, enabling quantification of collateral vessel remodeling with prolonged ischemia.

Figure 3.S1: Supplementary Movie 1 visualizing the collaterals in a hindlimb 1 week post ligation. The movie can be found online at https://static.cambridge.org/content/id/urn:cambridge.org:id:article:S1431927617000095/resource/name/S1431927617000095sup001.mp4



3.4.1 Factors Influencing the Quality of Arterial Vascular Filling

The completeness of a vascular cast greatly depends on the material and infusion protocol. Choice of preparatory steps, material as well as infusion pressure has been a matter of controversy^{18–20} and depends on the experimental objective. In order to quantify collateral growth, it is paramount that the cast includes all arterial vessels, with minor filling of capillaries that would otherwise elevate the background fluorescence level.

We optimized the composition of the replica material with the goal to visualize small collateral vessels in the rat hindlimb with cryomicrotome imaging. Filling could be restricted to the main arteries and large arterioles by selection of a viscous resin such as undiluted Batson's. The degree of arterial filling was associated with the amount of dilution of the base solution. Partial venous filling was already noted with moderately diluted resins. We speculate that in the absence of capillary penetration over most of the tissue, arterio-venous shunts caused such locally confined venous filling. The nature and location of such shunts, however, remains to be established. We also tested Mercox as casting material, but observed substantial

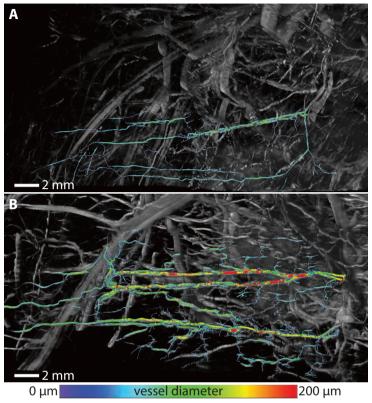


Figure 3.7: Representative examples showing three-dimensional renderings of the vascular cast in the ischemic rat hindlimb with segmented collaterals color-coded by diameter. The superficial gracilis collaterals are notably smaller 1 week post ligation **(A)** compared with 4 weeks post ligation **(B)**.

filling of the capillaries. In addition, for low viscosity resins, such as Mercox and Microfil, extravasation has been reported.^{21,22} Such resins should therefore be used cautiously.

The degree of filling further depends on the pressure gradients throughout the vascular bed, which can be controlled by either using a constant flow rate or by applying a constant pressure at the infusion site.²³ The latter is usually controlled upstream of the cannulation site such that pressure losses along the infusion catheter must be taken into account. Control of the flow rate has been reported to provide more complete casts. However, local pressures may become very high, causing

vascular distension.²³ Perfusion fixation before vascular casting can reduce such distension,²⁴ but at the risk of shrinking the vasculature or resulting in less complete casts.²⁵ We therefore chose to infuse the resin under pressure-controlled conditions, maintaining the input pressure at physiological levels. Also the outflow pressure at the severed vena cava was comparable with the in vivo pressure. Under controlled inflow and outflow pressure, the flow rate depends on the vascular resistance as well as on the viscosity of the fluid. The resulting pressure distribution for a specific vasculature, however, is independent of the viscosity of the material. In order to allow for a deep penetration of the resin, we induced a slow polymerization. We speculate that in the short filling phase of the moderately to strongly diluted resins, polymerization was minimal, such that large differences in viscosity remained absent and local pressures therefore approached physiological levels. In 90% Batson's, flow was much slower and ceased before reaching the small vessels. Apart from poor filling, this may have resulted in more variation in local pressures, depending on the sites where polymerization starts.

Shrinkage of the cast material while curing also influences the accuracy of replicated dimensions. High monomer content causes 5–20% shrinkage. Shrinkage is even more pronounced in samples that undergo maceration or clearing. An average diameter reduction of 65% has been reported for Microfil after methylsalicylate clearing. Modified Batson's mixtures are less prone to shrinkage, and we did not observe any partially filled lumen by histological examination, whereas incomplete luminal filling has been observed with Microfil casts. Our fluorescent cast cryo-imaging does not require any tissue clearing or maceration steps in order to obtain sufficient contrast to visualize small vessels. Therefore, we are confident that shrinkage did not greatly affect our quantitative results.

3.4.2 Optimized Filling of Collateral Vessels in Ischemic Hindlimbs

The challenges to reliably fill collateral vessels in the rodent hindlimb, especially in unilateral hindlimb ischemia, have been acknowledged previously. ^{33,34} Our method of transiently clamping the iliac artery on the unligated side produced successful sequential filling of the ischemic and the healthy hindlimb, whereas only requiring a single cannulation of a large vessel. Slow onset of polymerization ensured that both legs were filled under similar conditions. In some cases, the preexisting collateral vessels on the healthy side were less reliably filled than on the ischemic side, with a cleft void of cast appearing between two filled aligned segments on either side. Flow in the preexisting collateral vessels in the healthy leg is bidirectional with low

flow rates in the mid portion³² which could explain incomplete penetration of the resin in these collateral segments.

3.4.3 3D Fluorescence Cryo-Imaging of Vascular Networks

Collateral vessels have been suggested to develop from preexisting small arterioles, by arteriolization of connecting capillaries, or even by de-novo formation of blood vessels.³⁵ With the proposed filling technique, the vascular architecture of the rat hindlimb could be reliably filled to reflect dimensional changes of collateral growth. Sequential stacks of 2D images, obtained by automated episcopic cryomicrotome imaging, allowed reconstruction of the entire network at a resolution comparable with ex vivo micro-CT. Such detailed 3D vascular networks of the entire leg are a first step toward a detailed analysis of vascular adaptation in response to an ischemic insult, as, for example, reflected by an increase in diameter, length, and tortuosity, and can serve as rigorous input for modeling studies on blood flow and shear stress distribution, vascular remodeling, and oxygen transport to tissue. 14 Unlike micro-CT, joint 3D fluorescence cryo-imaging of vascular cast and molecular and cellular tracers permits co-registered high-resolution reconstruction of fluorescently labeled markers of biological activity and perfusion. 36,37 Together these facilitate future integrative studies on arteriogenesis that combine local activity and shear stress with adaptation of vascular morphology and perfusion.

Our 3D imaging covers a very large tissue volume, but simultaneously imaging resolution is limited. Voxel size was $24\,\mu m$, and based on the ability to detect calibration spheres we estimate that vessels of 15 μm in diameter are reliably detected due to the very strong fluorescence signal. Diameters of these vessels, however, cannot be estimated. Based on these limitations, the current technique would allow the detection of preexisting arteriolar connections of 15 μm or larger in diameter, but would not allow discrimination between outgrowth of still smaller vessels or the other modes of collateral artery formation. Inclusion of molecular markers or combination with high-resolution confocal microscopy would be required to address these issues.

3.4.4 Study Limitations

As vascular casting techniques only permit investigations at a single time point and do not allow longitudinal follow up of individual rats, we compared the influence of resin viscosity and femoral artery ligation across animals. To limit the resulting variability, we assessed the level of filling of similarly sized vessels in a region of

interest based on anatomic landmarks. Some variation was unavoidable as, for example, the size of the femoral artery of the 10% dilution was notably smaller than for the other resins. This could have been either due to intraspecies variability (despite similar age and same strain as the rat with 20% dilution) or due to the filling procedure.

The parameters influencing a vascular cast have been previously studied in the context of corrosion casting,²³ and cast quality has frequently been assessed by the quality of the endothelial imprints.²⁷ The objective of casting for 3D vascular imaging of entire organs or vascular regions differs, in that the cast should be a facsimile of vessels ranging from the highest imaging resolution of a few micrometers to large arteries. The goal of this study was to optimize the filling protocol for fluorescence imaging of the ischemic rat hindlimb arterial vasculature in sectioned frozen tissue. As such, our study was restricted to methacrylate resins which are suitable for cryomicrotome cutting, in contrast to more elastic materials such as Microfil, neoprene, or latex that are commonly used for micro-CT.

3.5 Conclusions

We developed a casting protocol with material and infusion pressure of 100 mmHg optimized for reliably replicating the arterial and collateral network in ischemic rat hindlimbs. Together with episcopic cryomicrotome imaging, this method allowed 3D reconstruction of the entire rat hindlimb vasculature with great level of detail. In future work, this method can be combined with fluorescent markers reflecting biological activity or perfusion.

Acknowledgments

This work was supported by the Center for Translational Molecular Medicine (CTMM EMINENCE project, 01C-204).

REFERENCES

- 1. Limbourg, A., Korff, T., Napp, L. C., Schaper, W., Drexler, H. & Limbourg, F. P. Evaluation of postnatal arteriogenesis and angiogenesis in a mouse model of hind-limb ischemia. *Nat Protoc* **4**, 1737–1746. doi:10.1038/nprot.2009.185 (2009).
- 2. Schaper, W. Collateral circulation: past and present. *Basic Res Cardiol* **104,** 5–21. doi:10.1007/s00395-008-0760-x (2009).

- 3. Ziegler, M. A. *et al.* Marvels, mysteries, and misconceptions of vascular compensation to peripheral artery occlusion. *Microcirculation* **17**, 3–20. doi:10.1111/j.1549-8719.2010.00008.x (2010).
- 4. Schirmer, S. H., van Nooijen, F. C., Piek, J. J. & van Royen, N. Stimulation of collateral artery growth: travelling further down the road to clinical application. *Heart* **95**, 191–197. doi:10.1136/hrt.2007.136119 (2009).
- 5. Lotfi, S., Patel, A. S., Mattock, K., Egginton, S., Smith, A. & Modarai, B. Towards a more relevant hind limb model of muscle ischaemia. *Atherosclerosis* 227, 1–8. doi:10.1016/j.atherosclerosis.2012.10.060 (2013).
- 6. Welten, S. M. *et al.* Inhibition of 14q32 MicroRNAs miR-329, miR-487b, miR-494 and miR-495 increases neovascularization and blood flow recovery after ischemia. *Circ Res* **115**, 696–708. doi:10.1161/CIRCRESAHA.114.304747 (2014).
- 7. Madeddu, P. *et al.* Murine models of myocardial and limb ischemia: diagnostic end-points and relevance to clinical problems. *Vascul Pharmacol* **45**, 281–301. doi:10.1016/j.vph.2006.08.008 (2006).
- 8. Jacoby, C. *et al.* Dynamic changes in murine vessel geometry assessed by high-resolution magnetic resonance angiography: a 9.4T study. *J Magn Reson Imaging* **28**, 637–645. doi:10.1002/jmri.21482 (2008).
- 9. Oses, P. *et al.* Mapping 3-dimensional neovessel organization steps using microcomputed tomography in a murine model of hindlimb ischemia-brief report. *Arterioscler Thromb Vasc Biol* **29**, 2090–2092. doi:10.1161/ATVBAHA.109.192732 (2009).
- 10. Zhang, Z. *et al.* Enhanced collateral growth by double transplantation of genenucleofected fibroblasts in ischemic hindlimb of rats. *PLoS One* **6**, e19192. doi:10.1371/journal.pone.0019192 (2011).
- 11. Poole, K. M., Tucker-Schwartz, J. M., Sit, W., Walsh, A. J., Duvall, C. L. & Skala, M. C. Quantitative Optical Imaging of Vascular Response in vivo in a Model of Peripheral Arterial Disease. *Am J Physiol Heart Circ Physiol* **305**, H1168–H1180. doi:10.1152/ajpheart.00362.2013 (2013).
- 12. Stacy, M. R., Paeng, J. C. & Sinusas, A. J. The role of molecular imaging in the evaluation of myocardial and peripheral angiogenesis. *Ann Nucl Med* **29**, 217–223. doi:10.1007/s12149-015-0961-y (2015).
- 13. Van Horssen, P., Siebes, M., Hoefer, I., Spaan, J. A. E. & van den Wijngaard, J. P. H. M. Improved detection of fluorescently labeled microspheres and vessel architecture with an imaging cryomicrotome. *Med Biol Eng Comput* 48, 735–744. doi:10.1007/s11517-010-0652-8 (2010).

- 14. Van den Wijngaard, J. P. H. M. *et al.* 3D Imaging of vascular networks for biophysical modeling of perfusion distribution within the heart. *J Biomech* **46**, 229–239. doi:10. 1016/j.jbiomech.2012.11.027 (2013).
- 15. Spaan, J. A. E. *et al.* Visualisation of intramural coronary vasculature by an imaging cryomicrotome suggests compartmentalisation of myocardial perfusion areas. *Med Biol Eng Comput* **43**, 431–435. doi:10.1007/BF02344722 (2005).
- 16. Biggs, D. S. & Andrews, M. Acceleration of iterative image restoration algorithms. *Appl Opt* **36**, 1766–1775. doi:10.1364/ao.36.001766 (1997).
- 17. Van den Wijngaard, J. P. H. M. *et al.* Porcine coronary collateral formation in the absence of a pressure gradient remote of the ischemic border zone. *Am J Physiol Heart Circ Physiol* **300**, H1930–H1937. doi:10.1152/ajpheart.00403.2010 (2011).
- 18. Lametschwandtner, A., Lametschwandtner, U. & Weiger, T. Scanning electron microscopy of vascular corrosion casts—technique and applications. *Scan Electron Microsc*, 663–695 (1984).
- Grabherr, S., Djonov, V., Yen, K., Thali, M. & Dirnhofer, R. Postmortem Angiography: Review of Former and Current Methods. *Am J Roentgenol* 188, 832–838. doi:10.2214/AJR.06.0787 (2007).
- 20. Haenssgen, K., Makanya, A. N. & Djonov, V. Casting materials and their application in research and teaching. *Microsc Microanal* **20**, 493–513. doi:10.1017/S1431927613014050 (2014).
- 21. Krucker, T., Lang, A. & Meyer, E. P. New polyurethane-based material for vascular corrosion casting with improved physical and imaging characteristics. *Microsc Res Tech* **69**, 138–147. doi:10.1002/jemt.20263 (2006).
- Mondy, W. L., Casteleyn, C., Loo, D. V., Raja, M., Singleton, C. & Jacot, J. G. Osmium tetroxide labeling of (poly)methyl methacrylate corrosion casts for enhancement of micro-CT microvascular imaging. *Microsc Microanal* 19, 1416–1427. doi:10.1017/S1431927613013421 (2013).
- 23. Hodde, K. C. & Nowell, J. A. SEM of micro-corrosion casts. *Scan Electron Microsc*, 89–106 (1980).
- 24. Kratky, R. G., Lo, D. K. & Roach, M. R. Quantitative measurement of fixation rate and dimension changes in the aldehyde/pressure-fixed canine carotid artery. *Blood Vessels* **28**, 386–395. doi:10.1159/000158885 (1991).
- 25. Reddy, P. A., Douglas, J. E., Schulte, M. & Hossler, F. E. The effect of prefixation on the quality of vascular corrosion casts of rat heart. *Cardiovasc Pathol* **4,** 133–140. doi:10.1016/1054-8807(94)00047-U (1995).

- Weiger, T., Lametschwandtner, A. & Stockmayer, P. Technical parameters of plastics (Mercox CL-2B and various methylmethacrylates) used in scanning electron microscopy of vascular corrosion casts. Scan Electron Microsc, 243–252 (1986).
- 27. Hossler, F. E. & Douglas, J. E. Vascular corrosion casting: Review of advantages and limitations in the application of some simple quantitative methods. *Microsc Microanal* 7, 253–264. doi:10.1017/S1431927601010261 (2001).
- 28. Bassingthwaighte, J. B., Yipintsoi, T. & Harvey, R. B. Microvasculature of the dog left ventricular myocardium. *Microvasc Res* **7**, 229–249. doi:10.1016/0026-2862(74)90008-9 (1974).
- 29. Levesque, M. J., Cornhill, J. F. & Nerem, R. M. Vascular casting. A new method for the study of the arterial endothelium. *Atherosclerosis* **34**, 457–467. doi:10.1016/0021-9150(79)90070-4 (1979).
- 30. Potter, R. F. & Groom, A. C. Capillary diameter and geometry in cardiac and skeletal muscle studied by means of corrosion casts. *Microvasc Res* **25**, 68–84. doi:10.1016/0026-2862(83)90044-4 (1983).
- 31. Distasi, M. R. *et al.* Suppressed hindlimb perfusion in Rac2^{-/-} and Nox2^{-/-} mice does not result from impaired collateral growth. *Am J Physiol Heart Circ Physiol* **296**, H877–H886. doi:10.1152/ajpheart.00772.2008 (2009).
- 32. Heuslein, J. L. *et al.* Mechanisms of amplified arteriogenesis in collateral artery segments exposed to reversed flow direction. *Arterioscler Thromb Vasc Biol* **35**, 2354–2365. doi:10.1161/ATVBAHA.115.305775 (2015).
- 33. Shireman, P. K. & Quinones, M. P. Differential necrosis despite similar perfusion in mouse strains after ischemia. *J Surg Res* **129**, 242–250. doi:10.1016/j.jss.2005.06.013 (2005).
- 34. Westerweel, P. E., Rookmaaker, M. B., van Zonneveld, A. J., Bleys, R. L. A. W., Rabelink, T. J. & Verhaar, M. C. A study of neovascularization in the rat ischemic hindlimb using Araldite casting and Spalteholtz tissue clearing. *Cardiovasc Pathol* 14, 294–297. doi:10.1016/j.carpath.2005.07.007 (2005).
- 35. Faber, J. E., Chilian, W. M., Deindl, E., van Royen, N. & Simons, M. A brief etymology of the collateral circulation. *Arterioscler Thromb Vasc Biol* **34**, 1854–1859. doi:10.1161/ATVBAHA.114.303929 (2014).
- 36. Lagerveld, B. W. *et al.* Gradient changes in porcine renal arterial vascular anatomy and blood flow after cryoablation. *J Urol* **186**, 681–686. doi:10.1016/j.juro.2011.03.146 (2011).
- 37. Hakimzadeh, N. *et al.* Detection and quantification methods of monocyte homing in coronary vasculature with an imaging cryomicrotome. *J Mol Cell Cardiol* **76**, 196–204. doi:10.1016/j.yjmcc.2014.08.019 (2014).







Topologic and Hemodynamic Characteristics of the Human Coronary Arterial Circulation

Janina C. V. Schwarz, Monique G. J. T. B. van Lier, Jeroen P. H. M. van den Wijngaard, Maria Siebes, and Ed van Bavel

Department of Biomedical Engineering and Physics, Amsterdam UMC, University of Amsterdam, Amsterdam, The Netherlands

ABSTRACT

Background

Many processes contributing to the functional and structural regulation of the coronary circulation have been identified. A proper understanding of the complex interplay of these processes requires a quantitative systems approach that includes the complexity of the coronary network. The purpose of this study was to provide a detailed quantification of the branching characteristics and local hemodynamics of the human coronary circulation.

Methods

The coronary arteries of a human heart were filled post-mortem with fluorescent replica material. The frozen heart was alternately cut and block-face imaged using a high-resolution imaging cryomicrotome. From the resulting 3D reconstruction of the left coronary circulation, topological (node and loop characteristics), topographic (diameters and length of segments), and geometric (position) properties were analyzed, along with predictions of local hemodynamics (pressure and flow).

Results

The reconstructed left coronary tree consisted of 202 184 segments with diameters ranging from 30 μ m to 4 mm. Most segments were between 100 μ m and 1 mm long. The median segment length was similar for diameters ranging between 75 and 200 μ m. 91% of the nodes were bifurcations. These bifurcations were more symmetric and less variable in smaller vessels. Most of the pressure drop occurred in vessels between 200 μ m and 1 mm in diameter. Downstream conductance variability affected neither local pressure nor median local flow and added limited extra variation of local flow. The left coronary circulation perfused 358 cm³ of myocardium. Median perfused volume at a truncation level of 100 to 200 μ m was 20 mm³ with a median perfusion of 5.6 ml/(min g) and a high local heterogeneity.

Conclusion

This study provides the branching characteristics and hemodynamic analysis of the left coronary arterial circulation of a human heart. The resulting model can be deployed for further hemodynamic studies at the whole organ and local level.

Keywords: human, coronary circulation, hemodynamics, myocardial perfusion, modeling, branching patterns, scaling laws

4.1 Introduction

The coronary arterial circulation consists of a myriad of vessel segments, starting at the main stem and right coronary artery and repeatedly branching toward the smallest arterioles that connect to the capillary bed. This system, covering around a 500-fold range in diameters in humans, normally allows for adequate matching of local perfusion to the oxygen needs. Thus, coronary autoregulation ensures by adjusting vasomotor tone that local perfusion at rest increases with, among others, oxygen demand, and is relatively insensitive to changes in systemic pressure. ^{1,2} It is generally believed that also the coronary artery structure adapts to allow for optimal perfusion capacity, although the concepts and mechanisms here are far less clear. ^{3,4} This system is challenged in coronary artery disease (CAD), where proximal stenoses cause flow impairment. In addition, downstream coronary arteries and arterioles may also be affected by CAD, resulting in endothelial dysfunction and, consequently, impaired regulatory capacity and reduced ability for structural adaptation.

Many processes have been identified that contribute to functional and structural regulation in the coronary circulation. For acute autoregulation, these include effects of local metabolites released from the cardiomyocytes, the myogenic response to changes in local pressure, and flow-dependent dilation.⁵ In addition, conducted vasomotor responses may further integrate the local responses.⁶ Structural adaption may include hypoxia-driven angiogenesis, flow-dependent remodeling, and pressure-induced changes in wall-to-lumen ratio.^{7–9} We also demonstrated in a range of in vitro and in vivo settings that vasomotor tone itself is a drive for structural changes in arterial caliber.^{10,11}

It has long been realized that proper understanding of the interplay of all of these processes requires a quantitative systems approach that includes the complexity of the coronary network. Accordingly, several previous studies provided detailed descriptions of such networks, based mostly on porcine coronary arterial casts. ^{12–15} Yet, data on human coronary branching patterns are extremely scarce. ^{16–18}

The purpose of the current study therefore was to provide a detailed quantification of the branching characteristics of the human coronary circulation. These data were obtained from a human heart in which coronary arteries were filled with casting material, followed by sectioning in a 3D imaging cryomicrotome, 3D reconstruction, and post hoc image processing. Our analysis included topological (e.g., node and loop characteristics), topographic (diameters and length of segments) and geometric (position) data along with predictions of local hemodynamics (pressure and flow).

These data allow evaluation of the relevance of previous animal studies and provide a base for a systems analysis of human coronary flow regulation.

4.2 MATERIALS AND METHODS

4.2.1 Human Heart

The data in this study were derived from a post-mortem human heart obtained at the Department of Pathology of the Academic Medical Center, University of Amsterdam, Netherlands. Heart weight was 330 gram. The patient was an 84-year-old female suffering from amyotrophic lateral sclerosis (ALS). Cause of death was listed as euthanasia. The patient history included atrial tachycardia, mitral stenosis, abdominal aortic aneurysm, atherosclerosis, and hypertension. However, the patient had never suffered any major cardiovascular events, and the heart had a normal appearance, without evidence of contracture. The patient's relatives gave written consent to use this heart for research.

4.2.2 Vascular Cast and Imaging

A 3D-representation of the coronary vasculature was obtained utilizing the cryomicrotome imaging procedure described previously. 19,20 In brief, after removing the heart, the left circumflex, left anterior descending artery, and right coronary artery were cannulated, flushed with calcium-free buffer and thereafter filled with fluorescent vascular cast material (UV-Blue, VasQtec, Switzerland, suspended in Batson's no. 17, Polysciences, United States; infusion pressure 90 mmHg). The vascular filling protocol was optimized to fill down to arterioles of around 15 µm in diameter to avoid background fluorescence via capillary filling. After the cast material had hardened, the heart was suspended in a carboxymethylcellulose sodium solvent (Brunschwig Chemie, Netherlands) blackened with 5% Indian ink (Royal Talens, Netherlands) and frozen at -20 °C. To acquire a 3D digital reproduction, the frozen sample was sectioned with a slice thickness of 30 µm, matching the in-plane image resolution. After every slice, the remaining block surface, rather than the slice itself, was imaged twice for two optical settings. This automated procedure thereby yielded two co-registered image stacks, each containing 4200 4096 × 4096 16-bit images: a stack with reflection images and a stack of fluorescent images optimized for the vascular cast (excitation, 365 nm and emission, 505 nm) (Figure 4.1A).

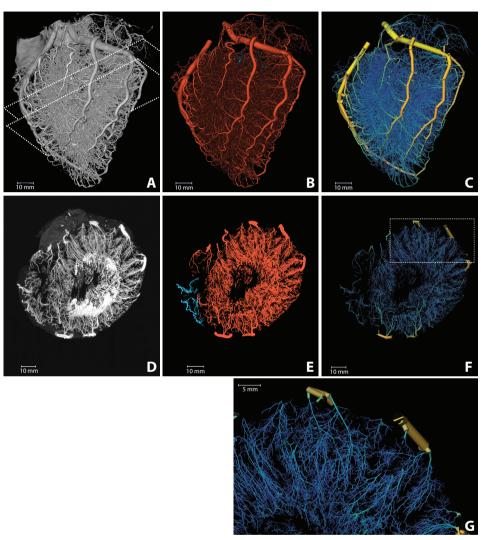


Figure 4.1: Reconstruction of the coronary vasculature. **(A)** Raw data. Dashed lines indicate the 1 cm slab (transversal, parallel to the cutting plane) used for the MIP. **(B)** Segmented vasculature. **(C)** Reconstructed tree with color coded diameter (yellow = 4 mm, blue = $50 \mu m$). **(D)** 1 cm MIP of raw data. **(E)** 1 cm MIP of segmented data (red, left; blue, right circulation). **(F)** 3D visualization of a 1 cm slab parallel to the cutting plane. **(G)** Magnification of the reconstructed vasculature (area indicated in F).

4.2.3 Vessel Segmentation and Quantification

As a next step, the topological tree was extracted from the digital reproduction of the fluorescent vascular cast. For this, dark current artifacts were eliminated and optical blurring was corrected by deconvolving the images with a system-specific point-spread function (Matlab; The MathWorks Inc., Natick, MA, United States).²¹ Subsequently, the vessels were segmented (Figure 4.1B) in three steps. First, the major coronary arteries were manually segmented in Amira (FEI Visualization Sciences Group, France) using a fourfold down-sampled image stack. Secondly, arterioles and arteries were enhanced by multi-scale vesselness filtering. For vessels smaller than 300 µm the original resolution was used; larger vessels were enhanced at half the original resolution. Thirdly, the centerline representation of the entire arterial vasculature was obtained by thresholding the result of the second step and subsequent merging with the skeleton of the manually segmented large vessels from step 1. The resulting image stack was up-sampled to full resolution, after which the centerlines were obtained by 3D-skeletonization. 22 We visually inspected the results and compared these with the original image data. Obvious artifacts resulting from cast interruption or cutting debris were corrected.

Every point on a centerline was classified according to the number of neighboring points. Points with a single neighbor were classified as terminal node. Points with two neighbors were considered to be mid-segmental points. Points with three or more neighbors in the skeleton reflected internal nodes connecting multiple segments.

The diameter at each point was estimated using a full width at half maximum algorithm on the normal plane. Segments were defined as the centerline path between two nodes. Internal segments connect two internal nodes, while terminal segments connect an internal and terminal node. Segment diameters were determined as the mean of the diameters of the segment's mid-segment points. Spurious terminal segments and triangular loops were eliminated based on quality measures for the diameter, including the condition that the segment length should be larger than the segment diameter. Diameters of internal segments that were underestimated, e.g., due to cast artifacts, were corrected by interpolation from diameters of neighboring segments. The results were stored in graph notation, a means to study relations and processes in networks, representing the vasculature as a set of nodes and cylindrical segments with associated information on its characteristics and its neighboring nodes and segments. For every node, the proximity to its coronary root was calcu-

lated. Segment description included their path length, mean diameter, as well as myocardial region (Figure 4.1C).

In order to study vessel branching, bifurcations were identified. For every bifurcation, the three connected segments were classified into mother and daughter segments based on flow direction.

The symmetry (S) of the daughters was defined as the ratio of the smaller (d_S) to the larger (d_L) diameter.

$$S = d_S/d_L \tag{4.1}$$

As a second parameter, the relation between mother (*M*) and her daughters was represented by the increase in total cross-sectional area:

$$A = \frac{d_L^2 + d_S^2}{d_M^2} \tag{4.2}$$

For analysis, segments and bifurcations were grouped into ten classes based on (mother) diameter (d_M) .

4.2.4 Extension of the Measured Tree Toward the Terminal Microcirculation

The extracted coronary vascular network terminates at 30 µm segments, since this was the resolution of the imaging technique, or at larger diameters where cast material had insufficiently filled the arterial bed. In order to estimate hemodynamic properties of the human coronary circulation, extrapolation toward the terminal arterioles is required. Notably, distributions of downstream conductances distal to the extracted end segments are needed. These were obtained by simulating segments smaller than 30 µm based on interpolation and extrapolation of the extracted vascular network. These in silico trees were generated as follows. Starting with an initial segment with a diameter between 300 and 400 μm, two daughter segments were created with symmetry stochastically drawn from the symmetry distribution observed in this human heart coronary network for segments of the same diameter class. Their diameters were set to match the area growth for their symmetry and mother diameter as expected from the data. Segment lengths were randomly assigned based on the segment-length-to-diameter distribution of their diameter class. For diameters below 30 µm, extrapolated branching characteristics were used. This procedure was iterated until the capillary domain (5.0–7.5 μm) was reached. For every segment, the total conductance of its distal network was calculated. Fifty trees in total were generated for this purpose, resulting in a distribution

of downstream conductances for segments in the range between 30 μm and 400 μm . These predictions were then imputed to the recorded tree. Finally, hemodynamics in the extracted coronary tree was determined for 1000 simulations of the stochastic terminal conductances.

4.2.5 Computational Hemodynamic Modeling

Blood was modeled as an incompressible, isotropic homogeneous fluid. To account for the Fåhræus-Lindqvist effect, an empirical diameter-dependent relationship derived by Pries et al.^{23,24} was used to model blood viscosity (μ), assuming a constant hematocrit $H_d = 0.4$:

$$\mu = \left[1 + (\mu_{0.45}^* - 1) \frac{(1 - H_d)^C - 1}{(1 - 0.45)^C - 1} \left(\frac{d}{d - 1.1}\right)^2\right] \left(\frac{d}{d - 1.1}\right)^2 \tag{4.3}$$

with

$$\mu_{0.45}^* = 6e^{-0.085d} + 3.2 - 2.44e^{-0.06d^{0.645}}$$

$$C = \left(0.8 + e^{-0.075d}\right) \left(-1 + \frac{1}{1 + 10^{-11}d^{12}}\right) + \frac{1}{1 + 10^{-11}d^{12}}$$

The fully developed, laminar axisymmetric steady-state flow through a segment was modeled based on Poiseuille's law including the above Fåhræus-Lindqvist effect. For a segment with nodes i and j, the flow $(Q_{i\rightarrow j})$ through and the conductance (G_{ij}) of the segment are:

$$Q_{i \to j} = G_{ij} \left(P_i - P_j \right) \tag{4.4}$$

$$G_{ij} = \frac{\pi d_{ij}^4}{128\mu_{ij}l_{ij}} \tag{4.5}$$

where P_i is the pressure at node i, μ_{ij} is the blood viscosity, d_{ij} is the diameter and l_{ij} the length of the segment between nodes i and j. Applying Kirchhoff's current law, i.e., conservation of mass at every junction,

$$\sum_{i\in N_j}Q_{i\to j}=0,$$

where N_j is the set of neighbor nodes, yields a system of linear equations that can be solved via matrix inversion for a given set of flow or pressure boundary conditions.

We used a coronary inlet pressure of 90 mmHg and capillary pressure of 20 mmHg. Wall shear stress was estimated under the premise of non-accelerating flow such that the frictional forces with the wall balance the force from the pressure gradient in every segment.²⁵

$$\tau_{ij} = \frac{\left(P_i - P_j\right) d_{ij}}{4l_{ij}} \tag{4.6}$$

Perfusion was derived by relating the flow through $100-200\,\mu m$ segments to the weight of their perfusion territory. The perfusion territories were determined in 3D by Voronoi tessellation. Voxels within the heart belong to the Voronoi cell of the closest terminal node. The union of all Voronoi cells perfused by a single $100-200\,\mu m$ segment was taken as its perfusion territory.

4.2.6 Statistical Analysis

The difference between two daughter symmetry classes was tested using a Mann–Whitney U-test. Differences between multiple diameter classes and myocardial regions were tested using a one-way Kruskal–Wallis analysis followed by a Dunn's multiple comparison test. A two-way ANOVA followed by Bonferroni's correction for multiple comparisons was employed to assess differences in area growth. Statistical analyses were performed using GraphPad Prism (GraphPad Software, Inc., La Jolla, CA, United States). Least-squares regression in Matlab was used for testing the agreement between hemodynamic results, for analyzing the relation between diameter, symmetry, and area growth (linear fit) and for determining the power laws (non-linear fit). A p < 0.05 was considered statistically significant.

4.3 RESULTS

4.3.1 Coronary Arterial Topology

Figure 4.1A provides a 3D visualization of the coronary arterial cast (raw data), as acquired with the imaging cryomicrotome, while Figures 4.1B,C show the results of the segmentation in single color and diameter-encoded color, respectively. Figures 4.1D–G provide maximum intensity projections of a transversal section and a magnification. Visual inspection of the raw data revealed nearly complete filling of the arterial tree down to 30 μm , covering the expected perfusion territory. Vascular density appeared highest in the subendocardium and lowest in the subepicardium. While Figure 4.1 depicts both the left and right coronary circulation, the remainder of the study focused on the left coronary circulation.

Table 4.1: Segment distribution

	A11		Terminal		Subepi- cardium		Midmyo- cardium		Subendo- cardium	
Diameter class	Number of segments (n, %)				LV density of terminal segments (n/cm³, %)					
30–45 μm	8 047	(4.0)	6 6 9 5	(6.6)	12.2	(7.2)	20.9	(5.8)	34.9	(7.3)
45–60 μm	22 204	(11.0)	20 760	(20.6)	37.4	(22.2)	65.5	(18.3)	104.2	(21.9)
60–75 μm	32 500	(16.1)	27 545	(27.3)	46.2	(27.4)	90.3	(25.2)	136.3	(28.6)
75–90 µm	33 605	(16.6)	22 872	(22.7)	38.0	(22.6)	83.0	(23.2)	106.8	(22.4)
90–105 μm	27 816	(13.8)	12860	(12.7)	21.9	(13.0)	52.0	(14.5)	50.2	(10.5)
105–120 μm	19 444	(9.6)	5 428	(5.4)	7.9	(4.7)	23.9	(6.7)	21.6	(4.5)
120–150 μm	24 598	(12.2)	3 2 7 4	(3.2)	3.4	(2.0)	15.3	(4.3)	14.8	(3.1)
150–200 μm	19718	(9.8)	1 204	(1.2)	1.1	(0.7)	5.5	(1.5)	6.2	(1.3)
200–400 μm	12 665	(6.3)	321	(0.3)	0.3	(0.2)	1.5	(0.4)	1.6	(0.3)
≥400 µm	1 587	(0.8)	2	(0.0)	0.0	(0.0)	0.0	(0.0)	0.0	(0.0)
Total	202 184	(100.0)	100 961	(100.0)	168.4	(100.0)	357.8	(100.0)	476.6	(100.0)
Diameter, median (μm)	92.3		72.4		71.2		75.4		70.6	
Diameter, interdecile range (µm)	54.3–178		47.8–105		47.4–100		48.9–110		46.7–103	
Length, median (µm)	441		443		473		453		391	

The reconstructed left coronary tree consisted of 202 184 segments with diameters ranging from 30 μ m in small arterioles to 4 mm for the epicardial arteries. Table 4.1 gives an overview of distribution of these segments over diameter classes and myocardial regions. Taking the class sizes into account, the data show increased density of smaller segments, as expected, which levels off below 60 μ m diameter. We attribute this to incomplete filling of vessels smaller than 60 μ m. Terminal segment density increased strongly from subepicardium to subendocardium, in accordance with visual inspection of the transversal sections of Figure 4.1. The distributions of

terminal segment diameters in the three myocardial regions were very comparable, indicating that the increased subendocardial density is not a result of better filling of the distal vessels in this region.

The reconstructed coronary network was not a simple tree with only bifurcations. Rather, 91% of the nodes were bifurcations, 8% were trifurcations (connecting four segments) and less than 1% connected more than four segments. The network also contained arcades or loops: an analysis based on graph theory revealed 3202 such loops.

As shown in Figure 4.2A, segment length exhibited a large range, from 60 μm for distal vessels to around 2 mm for the main coronaries, with a strongly skewed distribution. Most segments were between 100 μm and 1 mm long. While the segments with smallest diameter were also the shortest, median segment length was remarkably similar in the diameter range between 75 and 200 μm (Figure 4.2B). Subepicardial terminal segments were longer than midmyocardial and subendocardial ones (Table 4.1, p<0.001).

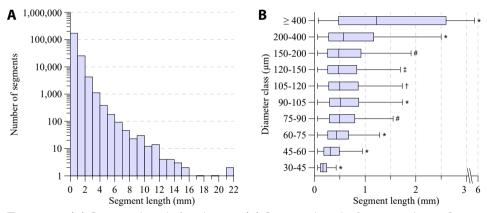


Figure 4.2: (A) Segment length distribution. **(B)** Segment length–diameter relation for ten diameter classes. Boxplot indicates median (black line); the left and right edges of the box indicate the 25th and 75th percentiles. Whiskers indicate 1.5 IQR. Outliers are not shown. * Significant different from all (p < 0.001).

[#] Significant different from 30–45, 45–60, 60–75, 90–105, 200–400, ≥400 (p < 0.001).

[†] Significant different from 30–45, 45–60, 60–75, 90–105, 120–150, 200–400, \geq 400 (p < 0.001).

 $^{^{\}ddagger}$ Significant different from 30–45, 45–60, 60–75, 90–105, 105–120, 200–400, ≥400 (p < 0.001).

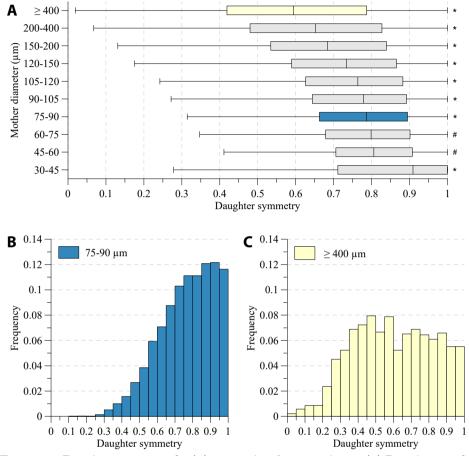


Figure 4.3: Daughter symmetry for **(A)** ten mother diameter classes. **(B)** Distributions for mother diameter 75–90 μ m (blue) and **(C)** \geq 400 μ m (yellow).

Figure 4.3A depicts the symmetry of the bifurcations, reflected by the ratio of daughter segment diameters, in the various mother diameter classes. Very asymmetric branches generally reflected consecutive segments of large vessels having small side branches. Here, d_L is expected to be close to d_M and indeed, the d_L/d_M -ratio was significantly larger for such asymmetric nodes (p < 0.001). For all diameter classes, in particular for segments larger than 150 µm, node symmetry was highly

^{*} Significant different from all (p < 0.05).

[#] Significant different from 30–45, 75–90, 90–105, 105–120, 120–150, 150–200, 200–400, \geq 400 (p < 0.05).

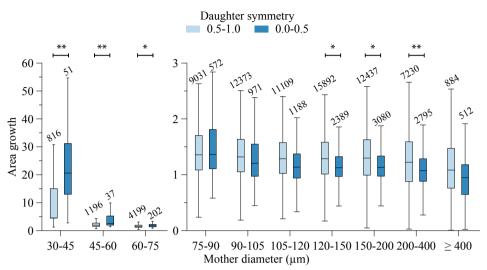


Figure 4.4: Area growth and mother diameter relation. Per mother diameter class, data are grouped in two daughter symmetry classes. Numbers above the bars indicate group size. Significant difference: ** p < 0.001, * p < 0.01.

variable. With decreasing diameter, the nodes became more symmetric, and the dispersion in symmetry decreased slightly, as illustrated by the histograms in Figures 4.3B,C.

The area growth at bifurcations was also highly variable. For segments larger than 400 µm, on average the cross-sectional area remained stable (median area growth: 1.02). For most other bifurcations, the total cross-sectional area of the daughters was larger than the cross-sectional area of their mother segment. Linear regression showed that area growth (*A*) increased with decreasing mother diameter (d_M) and increasing symmetry (*S*): ($A = -0.66d_M + 0.34S + 1.13$, $d_M \in [75,600] \times 10^{-6}$ m). Even though all coefficients in the fit were highly significant (p < 0.001), the low $r^2 = 0.047$ indicates that mother diameter and daughter asymmetry account only little (4.7%) for the encountered variability. Figure 4.4 shows this relationship, where the data are grouped in order to comprehensively visualize the effect of both mother diameter as well as symmetry.

4.3.2 Prediction of Distal Arterial Conductance

The fifty in silico trees, generated from the above described relationships for segment length, daughter symmetry and area growth, on average consisted of 1.22 ± 0.05 mil-

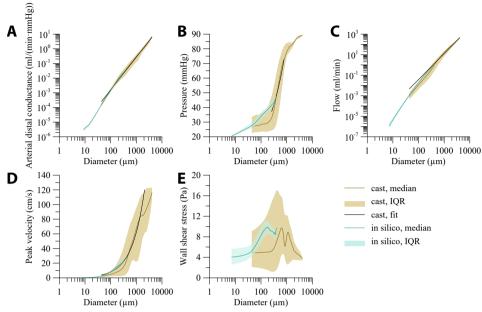


Figure 4.5: Dependency of hemodynamic parameters on segment diameter for the trees stochastically generated based on the branching characteristics of the human vasculature (in silico) and the reconstructed human coronary circulation with extrapolated microcirculation (cast). **(A)** Arterial distal conductance—diameter relation, **(B)** pressure—diameter relation, **(C)** flow—diameter relation, and **(D)** centerline velocity—diameter relation. **(E)** Wall shear stress—diameter relation. Lines indicate the median; areas indicate the interquartile range.

lion segments. For all trees, there was a linear relation between the log-transformed segment diameter and distal arterial conductance. As the linear regressions were very similar for all trees (coefficient of variation for both coefficients below 0.5%), all in silico data were pooled (Figure 4.5A, turquoise area). For the smallest segments with diameter less than 12 μ m, the distal arterial conductance was more variable than for larger segments. Moreover, distal conductance became less dependent on diameter. The increase in distal arterial conductance (in m³/Pa/s) for larger vessels was well predicted by the allometric relation $G_{is} = 1.64 \times 10^{-3} \cdot d^{2.49}$ (d in m; $r^2 = 0.98$, p < 0.001).

4.3.3 Pressure and Flow Distributions

Hemodynamics in the reconstructed arterial network with stochastically extended downstream conductances were determined in 1000 simulations of this whole net-

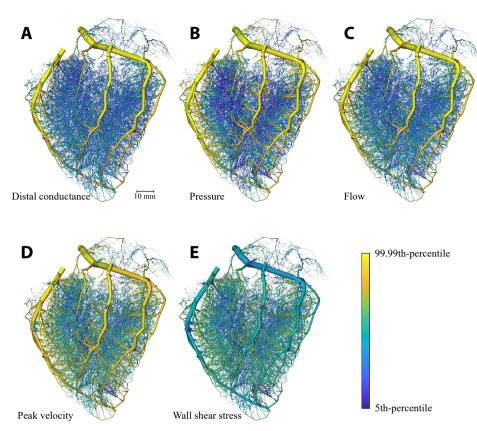


Figure 4.S1: 3D-renderings of the reproduced coronary vasculature visualizing the hemodynamics for imputed median distal arterial conductances. Segments are colored according to their log-transformed values.

work. Supplementary Figure 4.S1 provides a 3D rendering of the median parameter values derived from the hemodynamic simulations across the segmented vascular segments.

The coefficient of variation of the conductance downstream of a specific end segment over these simulations was 0.11 (median over all end segments). We questioned to what extent this variation in chosen downstream conductances affects the calculated pressure and flow in the complete left coronary network. Table 4.2 summarizes this analysis. In the stochastic model, pressure in individual segments varied marginally between the simulations, whereas the median coefficient of varia-

Variability Agreement with median CV MAD Power fit Median G P95 P95 Median Median **PCC** В **PCC** β Pressure 0.004 0.10 1.000 0.997 1.000 0.011 0.36 1.000 (mmHg) Flow (ml/min) 0.999 0.074 0.104 < 0.001 < 0.01 1.000 1.008 1.000 Wall shear stress 0.074 0.104 0.21 1.13 0.999 0.994 1.000 1.000

Table 4.2: Stochastic variation

Variability of outcome over the 1000 simulations (Variability) and agreement with deterministic models (Agreement with median). CV, coefficient of variation over the 1000 simulations; MAD, mean absolute deviation over the 1000 simulations; P95, 95-percentile; power fit, comparison to a deterministic model based on a power fit of distal conductance on end segment diameter. Median G, comparison to a deterministic model taking the median distal conductances in 2.5% diameter classes; PCC, Pearson's correlation coefficient; β , unstandardized coefficient.

tion for flow was 7.4%. Hemodynamic simulations with deterministically assigned distal arterial conductances yielded flow and pressure values that fully agreed with the median values of all stochastic simulations. This was the case for two choices for downstream conductance in each measured end segment: based on the power fit above or based on the median value of downstream conductance for similar-sized segments (diameter within 2.5%) in the in silico data. This analysis thus reveals that downstream conductance variability affects neither local pressure or its variability, nor median local flow, and adds limited extra variation of local flow in the various diameter classes. For these reasons, further analysis was based on the deterministic model for distal conductance, using the median values in the 2.5% diameter intervals.

The brown line in Figure 4.5A represents the median distal arterial conductance for the reconstructed human left coronary tree with extrapolated microcirculation. This line closely matches the in silico results by design for small diameters, mostly reflecting terminal segments, yet also agrees well for larger segments ($G = 1.58 \times 10^{-4} \cdot d^{-2.22}$, d in m, G in m³/Pa/s, $r^2 = 0.81$; for internal segments the exponent was: 2.18).

(Pa)

Figure 4.5B shows the pressure as a function of segment diameter. Most of the pressure drop occurred in vessels between 200 µm and 1 mm in diameter whereas only little pressure drop was seen in larger arteries. Despite this trend, the pressure differed greatly between segments of similar diameter. The pressure–diameter relation was $P = 5.40 \times 10^3 \cdot d^{0.60}$ ($d \in [250, 800] \times 10^{-6}$ m, P = 0.14).

Blood flow varied with diameter by about a fivefold interquartile range as indicated by the brown area in Figure 4.5C. Arteries larger than 1 mm carried a median of 36.6 ml/min, about 3000-times as much blood per vessel as 100 μ m segments. An allometric fit of flow ($Q = ad^{\gamma}$) over the whole diameter range predicts an exponent γ of 2.53 ($Q = 5.07 \times 10^8 \cdot d^{2.53}$, d in m, Q in ml/min, $r^2 = 0.83$).

As shown in Figure 4.5D, centerline velocity followed the same trend as blood flow and increased with increasing diameter. The diameter velocity relation was: $v = 3.00 \times 10^4 \cdot d^{0.89}$ (d in m, v in cm/s, $r^2 = 0.21$). Centerline velocity along the epicardial arteries decreased with branching.

The brown area in Figure 4.5E visualizes the high variability of wall shear stress, particularly for segments between $100\,\mu m$ and $1\,mm$. For larger segments, the variation decreased. For segments smaller than $300\,\mu m$, median wall shear stress leveled off around $5\,Pa$.

4.3.4 Local Myocardial Perfusion

The left coronary circulation perfused in total $358\,\mathrm{cm^3}$ of myocardium. Truncating the measured tree in the range of $100\text{--}200\,\mu\mathrm{m}$ resulted in 4954 segments perfusing as many territories. The median perfused volume of these truncated segments was $20.2\,\mathrm{mm^3}$ (interquartile range: $7.2\text{--}56.5\,\mathrm{mm^3}$) with a median perfusion of $5.6\,\mathrm{ml/(min\,g)}$ (flow per weight of the perfusion territory), yet with high local heterogeneity (interquartile range: $2.6\text{--}10.8\,\mathrm{ml/(min\,g)}$, Figure 4.6). Despite the higher vascular density, subendocardial perfusion in the left ventricle free wall was lower than midmyocardial and subepicardial perfusion. Septal perfusion from the left coronaries tended to drop from the left toward the right ventricular layer.

4.4 Discussion

In this study, we extensively quantified the branching characteristics of the human coronary circulation, and used these data to predict local hemodynamics, including pressure, flow and wall shear stress, and their variation along the vascular network. These data add to previous work on various animal species and provide a base for a systems analysis of human coronary flow distribution and regulation.

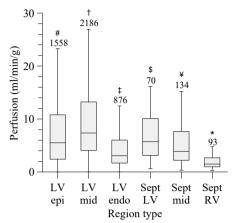


Figure 4.6: Perfusion distribution per myocardial region. LV, left ventricular free wall; RV, right ventricular free wall; Sept, septum; epi, subepicardium; mid, midmyocardium; endo, subendocardium. Outliers are not shown. Numbers above the bars indicate group size.

* Sept RV: significant different from all (p < 0.001);

4.4.1 Previous Data

To the best of our knowledge, no extensive studies have been made on branching patterns and related hemodynamics in the human coronary circulation. Available anatomical studies address specific research questions and provide only limited data that do not allow a translation toward global coronary hemodynamics. This includes the vascularization of the anterior papillary muscle, perfused by the LCA versus RCA, ²⁶ the impact of branching on wave propagation, ²⁷ the effect of side branches on coronary flow, ²⁸ and branching patterns of only the large coronary arteries. ^{3,29–35} In an initial study, we analyzed the presence of collateral connections within and between the perfusion territories in the human heart. ¹⁸

While human data are rare, several animal studies do provide quantitative data on coronary artery and microvascular branching patterns. Thus, VanBavel and Spaan analyzed the branching patterns in corrosion casts of porcine hearts, covering the major arteries down to precapillary arterioles.¹² In that work, "branching rules"

[#]LV epi: significant different from LV mid, LV endo, Sept RV (p < 0.001);

[†]LV mid: significant different from LV epi, LV endo, Sept mid, Sept RV (p < 0.001);

[‡]LV endo: significant different from LV epi, LV mid, Sept RV (p < 0.001), and Sept LV (p < 0.01);

^{\$} Sept LV: significant different from Sept RV (p < 0.001) and LV endo (p < 0.01);

[¥] Sept mid: significant different from LV mid, Sept RV (p < 0.001).

were derived that relate diameter and length of individual segments, as well as the diameters of mother and daughter segments in nodes. A combination of actual data for the larger vessels and computer-generated distal branches was then used for the assessment of local pressures, flows and their dispersion. A shortcoming in that work was the limitation to topology, ignoring the 3D distribution over the myocardium. More extensive work came from the group of Kassab, who in a series of studies described these characteristics in the arterial, capillary, and venous coronary bed of pigs, also based on corrosion casts, followed by extensive modeling and hemodynamic analyses. ^{4,13,14,36–41} Following initial work on manual segmentation of the coronary vasculature based on corrosion casts, our lab has developed an imaging cryomicrotome that allows for extensive 3D recording of branching structures ¹⁹ and applied this technique for the study of network characteristics in several species and organs, ^{20,21,42–46} culminating in the current work on the human heart.

4.4.2 Topology

The branching characteristics were described in terms of segmental diameter-length relations in addition to symmetry and area growth at branch points, as was previously done in porcine hearts. 12 Segmental length was intrinsically variable, reflecting the stochastic nature of the network. There was no clear correlation between segment length and diameter as already has been previously noted for the human right coronary artery.¹⁷ Our previous porcine data predict a mean length of 275 and 619 µm in, respectively, the 90–105 and 200–400 µm diameter class, as compared to the currently observed mean values of 675 and 908 µm. However, in the same animal model Kassab et al.¹³ observed values that are closer to our findings in the current study. The differences between the porcine data may be explained by differences in filling by the casting material. Since very asymmetric nodes occur regularly, the exclusion of very small unfilled side branches would affect a substantial part of the diameter-length relation. Also symmetry was intrinsically variable. Yet, branching was more symmetric and very asymmetric nodes occurred far less in the current human heart as compared to porcine hearts. For example, for large mother diameters (>500 µm) the median observed symmetry ratio was 0.59, in contrast to values below 0.40 for porcine data. 12,27,37 Despite the same trend of increasing symmetry with decreasing diameter, this difference was found for all diameter classes, and at least for the larger diameter classes this cannot be attributed to the 30 µm resolution in the current study.

The absence of growth of cross-sectional area in the largest diameter class (mother diameter \geq 400 µm) is in accordance with previous observations on human¹⁷ and porcine data, ^{12,40} as well as observations from angiographic imaging of the epicardial arteries. ^{3,29,31,35} Nodes originating from smaller vessels did show growth of cross-sectional area, implying a decreasing flow velocity toward the microcirculation, as was to be expected. If the diameters of a node would adhere to a scaling law (Equation 4.7), area growth (*A*) at that node would be directly related to the daughter symmetry *S* by

$$d_M^{\gamma} = d_L^{\gamma} + d_S^{\gamma} \tag{4.7}$$

$$A = \frac{1 + S^2}{(1 + S^{\gamma})^{2/\gamma}} \tag{4.8}$$

implying that growth in cross-sectional area increases with increasing daughter symmetry for $\gamma > 2$ ($\frac{\partial A}{\partial S} = f(S, \gamma)(S^2 - S^\gamma)$, $f(S, \gamma) > 0$, $S \le 1$). In our study, symmetric bifurcations indeed tended to show a larger area growth than asymmetric nodes, agreeing with previous observations in the human¹⁶ and in the porcine heart.²⁷ A comparison with prior findings reveals that area growth tends to be higher in the present human heart as compared with similar sized arteries in the porcine hearts,¹² rat and human hearts,¹⁶ while the variability in area growth was less in the human hearts. Area growth, however, tended to be smaller in the human heart in comparison to values observed in the human cerebral vasculature⁴⁷ and in mice hearts⁴⁸ while following the same general trend of increasing area growth for smaller segments. Estimates of area growth are intrinsically sensitive to precision of diameter measurements, with random errors causing a strong upward bias in the estimate. This holds even more strongly for misclassification of mother versus daughter segments in nodes, and such bias may underlie the high growth in the smallest diameter classes.

4.4.3 Hemodynamic Predictions

We initially aimed to derive hemodynamic parameters throughout the network by solving the Poiseuille and Kirchhoff equations with assumptions on distal boundary conditions, such as diameter-defined flow or back pressure. Such attempts resulted in highly variable estimates for local pressure and flow that were at variance with the assumed boundary conditions. A better strategy therefore was to assume a diameter-dependent downstream conductance for each outflow segment in the casted vasculature. The generation of this relation by constructing and imputing

simulated networks, based on observed and extrapolated branching characteristics and taking variability into account, allowed the hemodynamic analysis of the full, hybrid network.

A comparison of the recorded and imputed part of these networks (brown and blue lines and areas in Figure 4.5) reveals that the imputed data demonstrated less variability. We conclude from this that we did not fully cover the properties of the recorded data. Aspects that were not included in the simulated parts of the network include arcading segments, trifurcations, and possible deeper correlations in the data, such as correlations between area growth in successive nodes. Such deeper correlations are difficult to discern and quantitate, and we do not expect that including them would strongly affect the predictions of the hemodynamic profiles.

It is now commonly accepted that the major part of the pressure drop occurs over the arterial system, with substantial contribution of arterioles and small arteries. Direct recordings of this pressure distribution are very limited and do not include human hearts. In a classical study in the porcine heart at diastolic arrest and vasodilation, Chilian et al. demonstrated that pressure in 80–120 μm vessels has dropped to 60% and 80% of the perfusion pressure in the subendocardium and subepicardium, respectively. VanBavel and Spaan indeed predicted this range of pressures in their network analysis. However, the current human study predicts a median pressure in 100 μm vessels around 32% of systemic pressure, suggesting that far more of the pressure dissipation occurs in vessels much larger than 100 μm (mainly between 200 μm and 1 mm). This could have been caused by arcades and trifurcations in the data. Also, the presence of daughter segments with a larger diameter compared to their mother could have contributed to this finding. The in silico data, with a more standardized vascular pattern, suggest that most of the pressure drop occurs in the range of 30 μm to 300 μm .

The hemodynamic parameters reported in this study for a vasodilated arterial network were slightly higher than measurements in human subjects during hyperemia. Flow velocities in the range of 10–30 cm/s are reported in angiographically normal epicardial coronary arteries at rest and 60–100 cm/s at hyperemia and are highly variable between individuals.^{50,51} Flow velocities tend to be lower in the left anterior descending and left circumflex coronary artery compared with the left main coronary artery.⁵⁰ The high flow velocities found in our study were associated with high levels of perfusion (median: 5.6 ml/(min g)). Perfusion as measured with positron emission tomography typically increases from 0.6–1.2 ml/(min g) at rest to values between 1.9 and 5.0 ml/(min g) during hyperemia, with higher values found in females.^{52,53} In animal models, regional differences in perfusion were reported

with generally equal or higher perfusion at the subendocardium compared to the subepicardium. For the human heart in the present study we found the opposite. Since the simulations were based on data obtained in a diastolic heart, the results resemble hemodynamics in a diastolically arrested heart. Furthermore, the influence of cardiac contraction and myocardial tone were not taken into account in our hemodynamic model. In the beating heart, systolic flow in notably the subendocardium is impaired by the contracting surrounding myocardium. In a model study, Namani et al. showed that not only is flow higher under passive conditions than under autoregulation, but that ignoring the interaction between vessels and the surrounding myocardium indeed results in increased flow and thus perfusion estimates. Bache et al. found an increase in the subendocardium/subepicardium perfusion ratio with decreasing heart rate at maximal vasodilation. This together with topology artifacts, ignoring extra resistance in bifurcations or possibly a comparatively low prescribed capillary pressure could have influenced our hemodynamic calculations.

4.4.4 Allometric Description of Topology and Hemodynamics

Allometric (power law) relations have regularly been used to describe relations between physiological and anatomical parameters,⁵⁷ including the coronary circulation. ^{4,58–62} The arguably best known relation is "Murray's law" that, based on cost minimization principles, relates flow in a blood vessel to the cube of its diameter. In Poiseuille flow, this relates to wall shear stress being constant along the vasculature. Murray's law certainly is not universally valid, and alternative allometric relations have been derived from various optimality principles, including space-filling requirements, ^{64,65} relating properties of stems to corresponding crowns, ⁶¹ optimization of total conductance, ⁶⁶ and application of constructional laws. ⁶⁷ The postulated scaling exponent typically ranges between 2 and 3.

Our observation of constant cross-sectional area in the larger coronaries is in accordance with several other studies, 12,39 suggesting an exponent close to 2 rather than 3 for large coronaries. The scaling exponent γ can be derived from area growth by fitting Equation 4.8 or alternatively by fitting any reformulation of Equation 4.7. There are various possible optimization strategies, resulting in different estimates for γ , which are furthermore strongly influenced by extreme values. It was therefore difficult to thoroughly quantitate γ based on branching. In general, the scaling exponent increased with decreasing diameters, typically from a value close to 2 for the large segments toward values larger than 3 for small segments. Rivolo et al. also

observed the same trend in the porcine heart, with a y increasing from approximately 2.25 for large vessels to values around 4 for vessels smaller than $100 \, \mu m.^{27}$ For the human heart in the present study, the scaling exponent in the diameter-flow relation decreased from 3.21 in the smallest vessels to 2.55 in the major vessels, and shear stress depended biphasically on diameter, having its peak at 630 µm. Van der Giessen et al. found an exponent of 2.55 based on biplanar angiography of human epicardial arteries for the flow-diameter relation, ⁶⁸ which matches our results. The exponents in the human heart appear to be higher than the ones observed in porcine hearts. VanBavel and Spaan also described non-constant exponents, increasing from 2.35 for segments larger than 200 µm to 2.82 for diameters smaller than 40 µm. 12 Mittal et al. used morphometric data of the entire porcine coronary arterial tree down to the first capillary branch to conduct hemodynamic analysis and determined a flow-diameter power law relation with exponent 2.2.38 Despite these deviations from Murray's and other invariant scaling laws, downstream conductance scaled with diameter to the power 2.22 over a large range. Common to all invariant allometric relations is that they postulate a general optimality principle. However, as derived by Uylings, different exponents are ideal for different flow types (ranging between 2.33 for turbulent to 3.0 for laminar flow). ⁶⁹ Similar effects have been shown for rheological variation⁶⁷ and flow pulsatility.²⁷ Flow in the coronaries is pulsatile and near-Newtonian whereas laminar, non-pulsatile flow subject to shearrate dependent viscosity is characteristic for the small vasculature. These differences together with other influences mainly affecting the larger vessels such as areas of low or oscillating wall shear stress³¹ and wave reflections^{27,70} may lead to shifting optimal branch relations as we have observed. Altogether, while it is tempting to use allometric descriptors, reality seems a bit more complex and the deviations may lead to substantial differences in physiological parameters such as shear stress and local pressure.

4.4.5 Limitations

A series of image processing steps was required to translate the image stack to a network representation. These included segmentation of the arterial bed, 3D skeletonization, and diameter estimation. This was a major challenge, due to the large difference in vascular diameter between the major branches and the 30 μm smallest vessels that were included. Manual and automated correction was needed. The choices here were based on comparison of the original images to the vascular network representations as well as on common sense. Thus, a few interruptions in

cast filling of the major vessels needed to be corrected manually. Very short triangular loops were clearly the result of errors in skeletonization and were pruned to simple paths. Likewise, spurious side branches were removed and some regularization of diameter along vascular paths was included. Since as many as 202 184 segments were included in the final representation, some level of error in the topology and diameters remains unavoidable. However, while it remains necessary to further test and improve the procedures, we do believe that the current work provides an adequate translation from the image stack to the graph representation.

The heart was imaged at 30 µm resolution. Moreover, care was taken not to fill the vessels toward the capillary bed, as this would have resulted in strong background fluorescence. Meanwhile, data on the more distal arterioles were needed for the hemodynamics analysis. We therefore extrapolated branching characteristics when simulating the network toward 5.0–7.5 µm segments. Future work should provide branching characteristics of also the smallest arterioles. While it will not be feasible to fully cover such branching in the whole heart, microscopic data from much smaller tissue samples could be imputed into the simulated networks, improving reliability of the hemodynamic analysis.

The current study is based on a single heart from an elderly patient having atherosclerosis and may not be representative for a normal heart from a person in the same age category or for a healthy young heart. Even though Chen et al. showed in a mice model that the scaling exponent is not affected by aging, ⁷¹ we acknowledge that this may limit the current work. Yet, human hearts rarely become available for this purpose and the whole procedure from filling to graph representation is extremely labor- and computer-intensive. While it will not be feasible to perform studies such as the present one on large numbers of human hearts, inclusion of more hearts is needed to draw conclusions on reproducibility and dependence on age, sex and morbidities. The current study provides a pipeline for doing this work, and with further optimization, automation of the procedures, and improved computer power the inclusion of more samples should become feasible in the near future.

Further limitations of the work include the assumption of Poiseuille flow, the exclusion of the capillary and venous bed in the hemodynamics calculations, and the exclusion of the wave transformation effect. We presume that these assumptions have not substantially altered our main findings. We also were not able to analyze the right coronary artery perfusion territory due to insufficient quality of the vascular filling and subsequent segmentation.

4.4.6 Future Work and Application of the Current Data

An important next step will be the direct quantification of also the most distal vessels, as well as improved routines for image processing and imputation strategies based on a deeper analysis of the data, in addition to extension of the data set.

It has become clear over the years that CAD is not limited to the epicardial vessels. Rather, intra-myocardial arteries and arterioles are also affected, as evidenced by impaired endothelial responsiveness and alterations in vascular structure, caliber and resistance. 72 Moreover, the vasculature adapts, for better or worse, to the presence of a proximal stenosis and the associated reduced pressure, vascular tone, and hyperemic flow. 73–75 Local perfusion and perfusion reserve are known to be heterogeneous in animal models and healthy humans, ^{76–78} with heterogeneity increasing at smaller length scales. Depending on the adaptation of the coronary bed, developing CAD and its effects on the microcirculation may well affect such dispersion of local perfusion and reserve, leading to local ischemic zones. A framework such as presented here could help understanding the relation between microvascular structure and function and the local perfusion and perfusion reserve. We therefore foresee application of the current data and analyses in systems approaches of the coronary circulation, leading to new experimentally testable hypotheses on microvascular adaptation in CAD. In addition, the current study may add to the modeling required in silico clinical trials on new drugs and devices, in extension to the current in silico work on drug-eluting stents⁷⁹ and in analogy to work currently done in acute ischemic stroke.80

4.5 Conclusion

We have presented a processing pipeline and extensive data on branching characteristics and predicted hemodynamics of the human coronary circulation. Our findings provide a base for further modeling, including incorporation of vasomotor responsiveness, structural adaptation and their effects on the balance between oxygen demand and supply in health and CAD.

Data Availability Statement

The datasets generated for this study are available on request to the corresponding author.

Conflict of Interest

The authors declare that the research was conducted in the absence of any commercial or financial relationships that could be construed as a potential conflict of interest.

REFERENCES

- 1. Mosher, P., Ross J., J., McFate, P. A. & Shaw, R. F. Control of Coronary Blood Flow by an Autoregulatory Mechanism. *Circ Res* 14, 250–259. doi:10.1161/01.res.14.3.250 (1964).
- 2. Goodwill, A. G., Dick, G. M., Kiel, A. M. & Tune, J. D. Regulation of Coronary Blood Flow. *Compr Physiol* 7, 321–382. doi:10.1002/cphy.c160016 (2017).
- 3. Seiler, C., Kirkeeide, R. L. & Gould, K. L. Basic structure-function relations of the epicardial coronary vascular tree. Basis of quantitative coronary arteriography for diffuse coronary artery disease. *Circulation* **85**, 1987–2003. doi:10.1161/01.cir.85.6.1987 (1992).
- 4. Kassab, G. S. Functional hierarchy of coronary circulation: direct evidence of a structure-function relation. *Am J Physiol Heart Circ Physiol* **289**, H2559–H2565. doi:10.1152/ajpheart.00561.2005 (2005).
- 5. Dole, W. P. Autoregulation of the coronary circulation. *Prog Cardiovasc Dis* **29**, 293–323. doi:10.1016/s0033-0620(87)80005-1(1987).
- 6. Palao, T., van Weert, A., de Leeuw, A., de Vos, J., Bakker, E. N. T. P. & van Bavel, E. Sustained conduction of vasomotor responses in rat mesenteric arteries in a two-compartment in vitro set-up. *Acta Physiol* **224**, e13099. doi:10.1111/apha.13099 (2018).
- Hoefer, I. E., den Adel, B. & Daemen, M. J. A. P. Biomechanical factors as triggers of vascular growth. *Cardiovasc Res* 99, 276–283. doi:10.1093/cvr/cvt089 (2013).
- 8. Silvestre, J. S., Smadja, D. M. & Levy, B. I. Postischemic revascularization: from cellular and molecular mechanisms to clinical applications. *Physiol Rev* **93**, 1743–1802. doi:10.1152/physrev.00006.2013 (2013).
- 9. Zimarino, M., D'Andreamatteo, M., Waksman, R., Epstein, S. E. & De Caterina, R. The dynamics of the coronary collateral circulation. *Nat Rev Cardiol* 11, 191–197. doi:10.1038/nrcardio.2013.207 (2014).
- 10. Bakker, E. N. T. P., van der Meulen, E. T., van den Berg, B. M., Everts, V., Spaan, J. A. & VanBavel, E. Inward remodeling follows chronic vasoconstriction in isolated resistance arteries. *J Vasc Res* **39**, 12–20. doi:10.1159/000048989 (2002).
- 11. VanBavel, E., Bakker, E. N., Pistea, A., Sorop, O. & Spaan, J. A. Mechanics of microvascular remodeling. *Clin Hemorheol Microcirc* **34**, 35–41 (2006).

- 12. VanBavel, E. & Spaan, J. A. Branching patterns in the porcine coronary arterial tree. Estimation of flow heterogeneity. *Circ Res* **71**, 1200–1212. doi:10.1161/01.res.71.5.1200 (1992).
- 13. Kassab, G. S., Rider, C. A., Tang, N. J. & Fung, Y. C. Morphometry of pig coronary arterial trees. *Am J Physiol Heart Circ Physiol* **265**, H350–H365. doi:10.1152/ajpheart.1993.265.1.H350 (1993).
- 14. Kassab, G. S. & Fung, Y. C. Topology and dimensions of pig coronary capillary network. *Am J Physiol Heart Circ Physiol* **267**, H319–H325. doi:10.1152/ajpheart.1994.267.1.H319 (1994).
- 15. Kaimovitz, B., Lanir, Y. & Kassab, G. S. A full 3-D reconstruction of the entire porcine coronary vasculature. *Am J Physiol Heart Circ Physiol* **299**, H1064–H1076. doi:10.1152/ajpheart.00151.2010 (2010).
- Zamir, M. & Chee, H. Branching characteristics of human coronary arteries. Can J Physiol Pharmacol 64, 661–668. doi:10.1139/y86-109 (1986).
- 17. Zamir, M. On fractal properties of arterial trees. *J Theor Biol* **197,** 517–526. doi:10. 1006/jtbi.1998.0892 (1999).
- 18. Van Lier, M. G. J. T. B. *et al.* Transmural distribution and connectivity of coronary collaterals within the human heart. *Cardiovasc Pathol* **25**, 405–412. doi:10.1016/j.carpath.2016.06.004 (2016).
- 19. Spaan, J. A. E. *et al.* Visualisation of intramural coronary vasculature by an imaging cryomicrotome suggests compartmentalisation of myocardial perfusion areas. *Med Biol Eng Comput* **43**, 431–435. doi:10.1007/BF02344722 (2005).
- 20. Van Horssen, P., van den Wijngaard, J. P. H. M., Brandt, M. J., Hoefer, I. E., Spaan, J. A. E. & Siebes, M. Perfusion territories subtended by penetrating coronary arteries increase in size and decrease in number toward the subendocardium. *Am J Physiol Heart Circ Physiol* **306**, H496–H504. doi:10.1152/ajpheart.00584.2013 (2014).
- 21. Schwarz, J. C. V. *et al.* Optimization of Vascular Casting for Three-Dimensional Fluorescence Cryo-Imaging of Collateral Vessels in the Ischemic Rat Hindlimb. *Microsc Microanal* **23,** 77–87. doi:10.1017/S1431927617000095 (2017).
- 22. Lee, T. C., Kashyap, R. L. & Chu, C. N. Building Skeleton Models Via 3-D Medial Surface Axis Thinning Algorithms. *CVGIP: Graphical Models and Image Processing* **56**, 462–478. doi:10.1006/cgip.1994.1042 (1994).
- 23. Pries, A. R., Secomb, T. W., Gessner, T., Sperandio, M. B., Gross, J. F. & Gaehtgens, P. Resistance to blood flow in microvessels in vivo. *Circ Res* **75**, 904–915. doi:10.1161/01.res.75.5.904 (1994).
- 24. Secomb, T. W. & Pries, A. R. Blood viscosity in microvessels: experiment and theory. *C R Phys* **14**, 470–478. doi:10.1016/j.crhy.2013.04.002 (2013).

- 25. Munson, B. R., Okiishi, T. H., Huebsch, W. W. & Rothmayer, A. P. Fundamentals of fluid mechanics 7th ed. (J. Wiley & Sons, Hoboken, NJ, 2013).
- 26. Zajaczkowski, M. A. *et al.* Individual variability of vascularization of the anterior papillary muscle within the right ventricle of human heart. *PLoS One* **13**, e0205786. doi:10.1371/journal.pone.0205786 (2018).
- 27. Rivolo, S. *et al.* Impact of Coronary Bifurcation Morphology on Wave Propagation. *Am J Physiol Heart Circ Physiol* **311**, H855–H870. doi:10.1152/ajpheart.00130.2016 (2016).
- 28. Wiwatanapataphee, B., Wu, Y. H., Siriapisith, T. & Nuntadilok, B. Effect of branchings on blood flow in the system of human coronary arteries. *Math Biosci Eng* **9**, 199–214. doi:10.3934/mbe.2012.9.199 (2012).
- 29. Hutchins, G. M., Miner, M. M. & Boitnott, J. K. Vessel caliber and branch-angle of human coronary artery branch-points. *Circ Res* **38**, 572–576. doi:10.1161/01.res.38.6.572 (1976).
- 30. Van der Waal, E. C. *et al.* Intravascular ultrasound and 3D angle measurements of coronary bifurcations. *Catheter Cardiovasc Interv* **73**, 910–916. doi:10.1002/ccd. 21965 (2009).
- 31. Schoenenberger, A. W. *et al.* Deviation from Murray's law is associated with a higher degree of calcification in coronary bifurcations. *Atherosclerosis* **221**, 124–130. doi:10.1016/j.atherosclerosis.2011.12.040 (2012).
- 32. Cardenes, R., Diez, J. L., Duchateau, N., Pashaei, A. & Frangi, A. F. Model generation of coronary artery bifurcations from CTA and single plane angiography. *Med Phys* **40**, 013701. doi:10.1118/1.4769118 (2013).
- 33. Gupta, T., Saini, A. & Sahni, D. Terminal branching pattern of the right coronary artery in left-dominant hearts: a cadaveric study. *Cardiovasc Pathol* **22**, 179–182. doi:10.1016/j.carpath.2012.08.001 (2013).
- 34. Medrano-Gracia, P. et al. A Study of Coronary Bifurcation Shape in a Normal Population. J Cardiovasc Transl Res 10, 82–90. doi:10.1007/s12265-016-9720-2 (2017).
- 35. Ormiston, J. A. *et al.* Bench testing and coronary artery bifurcations: a consensus document from the European Bifurcation Club. *EuroIntervention* **13**, e1794–e1803. doi:10.4244/EIJ-D-17-00270 (2018).
- 36. Kassab, G. S., Le, K. N. & Fung, Y. C. A hemodynamic analysis of coronary capillary blood flow based on anatomic and distensibility data. *Am J Physiol Heart Circ Physiol* **277**, H2158–H2166. doi:10.1152/ajpheart.1999.277.6.H2158 (1999).
- 37. Kalsho, G. & Kassab, G. S. Bifurcation asymmetry of the porcine coronary vasculature and its implications on coronary flow heterogeneity. *Am J Physiol Heart Circ Physiol* **287**, H2493–H2500. doi:10.1152/ajpheart.00371.2004 (2004).

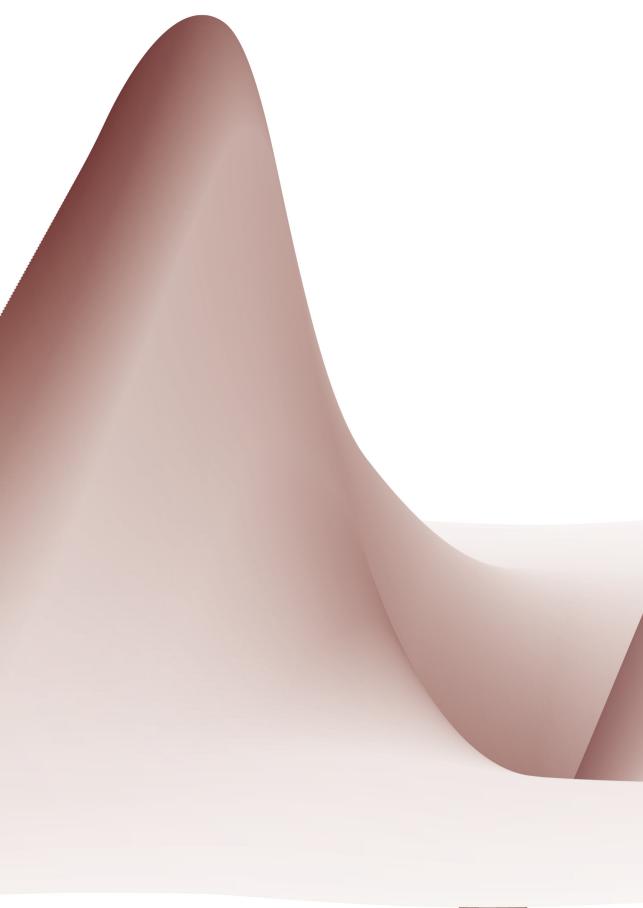
- 38. Mittal, N. et al. Analysis of blood flow in the entire coronary arterial tree. Am J Physiol Heart Circ Physiol 289, H439-H446. doi:10.1152/ajpheart.00730.2004 (2005).
- 39. Mittal, N., Zhou, Y., Ung, S., Linares, C., Molloi, S. & Kassab, G. S. A computer reconstruction of the entire coronary arterial tree based on detailed morphometric data. *Ann Biomed Eng* **33**, 1015–1026. doi:10.1007/s10439-005-5758-z (2005).
- 40. Kaimovitz, B., Huo, Y., Lanir, Y. & Kassab, G. S. Diameter asymmetry of porcine coronary arterial trees: structural and functional implications. *Am J Physiol Heart Circ Physiol* **294**, H714–H723. doi:10.1152/ajpheart.00818.2007 (2008).
- 41. Namani, R., Kassab, G. S. & Lanir, Y. Integrative model of coronary flow in anatomically based vasculature under myogenic, shear, and metabolic regulation. *J Gen Physiol* **150**, 145–168. doi:10.1085/jgp.201711795 (2018).
- 42. Van Horssen, P., Siebes, M., Hoefer, I., Spaan, J. A. E. & van den Wijngaard, J. P. H. M. Improved detection of fluorescently labeled microspheres and vessel architecture with an imaging cryomicrotome. *Med Biol Eng Comput* 48, 735–744. doi:10.1007/s11517-010-0652-8 (2010).
- 43. Van Horssen, P. *et al.* Influence of segmented vessel size due to limited imaging resolution on coronary hyperemic flow prediction from arterial crown volume. *Am J Physiol Heart Circ Physiol* **310**, H839–H846. doi:10.1152/ajpheart.00728.2015 (2016).
- 44. Van den Wijngaard, J. P. H. M. *et al.* Porcine coronary collateral formation in the absence of a pressure gradient remote of the ischemic border zone. *Am J Physiol Heart Circ Physiol* **300**, H1930–H1937. doi:10.1152/ajpheart.00403.2010 (2011).
- 45. Hakimzadeh, N. *et al.* Detection and quantification methods of monocyte homing in coronary vasculature with an imaging cryomicrotome. *J Mol Cell Cardiol* **76**, 196–204. doi:10.1016/j.yjmcc.2014.08.019 (2014).
- 46. Bedussi, B. *et al.* Clearance from the mouse brain by convection of interstitial fluid towards the ventricular system. *Fluids Barriers CNS* **12**, 23. doi:10.1186/s12987-015-0019-5 (2015).
- 47. Cassot, F., Lauwers, F., Lorthois, S., Puwanarajah, P., Cances-Lauwers, V. & Duvernoy, H. Branching patterns for arterioles and venules of the human cerebral cortex. *Brain Res* **1313**, 62–78. doi:10.1016/j.brainres.2009.12.007 (2010).
- 48. Feng, Y. *et al.* Bifurcation Asymmetry of Small Coronary Arteries in Juvenile and Adult Mice. *Front Physiol* **9**, 519. doi:10.3389/fphys.2018.00519 (2018).
- 49. Chilian, W. M. Microvascular pressures and resistances in the left ventricular subepicardium and subendocardium. *Circ Res* **69**, 561–570. doi:10.1161/01.res.69.3.561 (1991).

- 50. Kern, M. J. *et al.* Regional coronary blood flow velocity and vasodilator reserve in patients with angiographically normal coronary arteries. *Coron Artery Dis* **1,** 579–590. doi:10.1097/00019501-199009000-00010 (1990).
- 51. Ofili, E. O. *et al.* Differential characterization of blood flow, velocity, and vascular resistance between proximal and distal normal epicardial human coronary arteries: analysis by intracoronary Doppler spectral flow velocity. *Am Heart J* **130**, 37–46. doi:10.1016/0002-8703(95)90233-3 (1995).
- 52. Sdringola, S., Johnson, N. P., Kirkeeide, R. L., Cid, E. & Gould, K. L. Impact of unexpected factors on quantitative myocardial perfusion and coronary flow reserve in young, asymptomatic volunteers. *JACC Cardiovasc Imaging* **4**, 402–412. doi:10.1016/j.jcmg.2011.02.008 (2011).
- 53. Murthy, V. L. *et al.* Clinical Quantification of Myocardial Blood Flow Using PET: Joint Position Paper of the SNMMI Cardiovascular Council and the ASNC. *J Nucl Med* **59**, 273–293. doi:10.2967/jnumed.117.201368 (2018).
- 54. Feigl, E. O. Coronary physiology. *Physiol Rev* **63**, 1–205. doi:10.1152/physrev. 1983.63.1.1 (1983).
- 55. Hoffman, J. I. & Spaan, J. A. Pressure-flow relations in coronary circulation. *Physiol Rev* **70**, 331–390. doi:10.1152/physrev.1990.70.2.331 (1990).
- 56. Bache, R. J. & Cobb, F. R. Effect of maximal coronary vasodilation on transmural myocardial perfusion during tachycardia in the awake dog. *Circ Res* **41**, 648–653. doi:10.1161/01.res.41.5.648 (1977).
- 57. Thompson, D. On growth and form 2nd ed. doi:10.2307/3619729 (Cambridge University Press, Cambridge, 1942).
- 58. Molloi, S. & Wong, J. T. Regional blood flow analysis and its relationship with arterial branch lengths and lumen volume in the coronary arterial tree. *Phys Med Biol* **52**, 1495–1503. doi:10.1088/0031-9155/52/5/018 (2007).
- 59. Le, H. Q., Wong, J. T. & Molloi, S. Allometric scaling in the coronary arterial system. *Int J Cardiovasc Imaging* **24,** 771–781. doi:10.1007/s10554-008-9303-7 (2008).
- 60. Huo, Y. & Kassab, G. S. The scaling of blood flow resistance: from a single vessel to the entire distal tree. *Biophys J* **96**, 339–346. doi:10.1016/j.bpj.2008.09.038 (2009).
- 61. Huo, Y. & Kassab, G. S. A scaling law of vascular volume. *Biophys J* **96**, 347–353. doi:10.1016/j.bpj.2008.09.039 (2009).
- 62. Huo, Y. & Kassab, G. S. Scaling laws of coronary circulation in health and disease. *J Biomech* 49, 2531–2539. doi:10.1016/j.jbiomech.2016.01.044 (2016).

- 63. Murray, C. D. The Physiological Principle of Minimum Work: I. The Vascular System and the Cost of Blood Volume. *Proc Natl Acad Sci U S A* **12**, 207–214. doi:10.1073/pnas.12.3.207 (1926).
- 64. Cohn, D. L. Optimal systems: I. The vascular system. *Bull Math Biophys* **16**, 59–74. doi:10.1007/bf02481813 (1954).
- 65. West, G. B., Brown, J. H. & Enquist, B. J. A general model for the origin of allometric scaling laws in biology. *Science* 276, 122–126. doi:10.1126/science. 276.5309.122 (1997).
- 66. Razavi, M. S., Shirani, E., Salimpour, M. R. & Kassab, G. S. Constructal law of vascular trees for facilitation of flow. *PLoS One* **9**, e116260. doi:10.1371/journal.pone.0116260 (2014).
- 67. Miguel, A. F. Toward an optimal design principle in symmetric and asymmetric tree flow networks. *J Theor Biol* **389**, 101–109. doi:10.1016/j.jtbi.2015.10.027 (2016).
- 68. Van der Giessen, A. G. *et al.* The influence of boundary conditions on wall shear stress distribution in patients specific coronary trees. *J Biomech* **44**, 1089–1095. doi:10.1016/j.jbiomech.2011.01.036 (2011).
- 69. Uylings, H. B. Optimization of diameters and bifurcation angles in lung and vascular tree structures. *Bull Math Biol* **39**, 509–520. doi:10.1007/bf02461198 (1977).
- 70. Reneman, R. S., Arts, T. & Hoeks, A. P. Wall shear stress—an important determinant of endothelial cell function and structure—in the arterial system in vivo. Discrepancies with theory. *J Vasc Res* **43**, 251–269. doi:10.1159/000091648 (2006).
- 71. Chen, X. *et al.* Growth, ageing and scaling laws of coronary arterial trees. *J R Soc Interface* **12**, 20150830. doi:10.1098/rsif.2015.0830 (2015).
- 72. Crea, F., Camici, P. G. & Bairey Merz, C. N. Coronary microvascular dysfunction: an update. *Eur Heart J* **35**, 1101–1111. doi:10.1093/eurheartj/eht513 (2014).
- 73. Siebes, M., Verhoeff, B.-J., Meuwissen, M., de Winter, R. J., Spaan, J. A. & Piek, J. J. Single-Wire Pressure and Flow Velocity Measurement to Quantify Coronary Stenosis Hemodynamics and Effects of Percutaneous Interventions. *Circulation* 109, 756–762. doi:10.1161/01.cir.0000112571.06979.b2 (2004).
- 74. Verhoeff, B. J. *et al.* Influence of percutaneous coronary intervention on coronary microvascular resistance index. *Circulation* **111,** 76–82. doi:10.1161/01.CIR.0000151610.98409.2F (2005).
- 75. Sorop, O. *et al.* Functional and structural adaptations of coronary microvessels distal to a chronic coronary artery stenosis. *Circ Res* **102**, 795–803. doi:10.1161/CIRCRESAHA.108.172528 (2008).

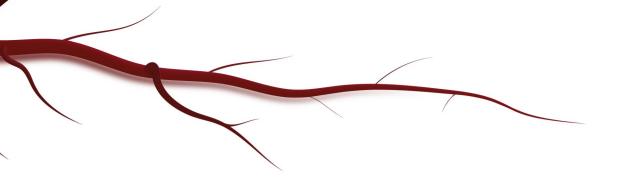
- 76. Bassingthwaighte, J. B., King, R. B. & Roger, S. A. Fractal nature of regional myocardial blood flow heterogeneity. *Circ Res* **65**, 578–590. doi:10.1161/01.res. 65.3.578 (1989).
- 77. Austin, R. E., Aldea, G. S., Coggins, D. L., Flynn, A. E. & Hoffman, J. I. Profound spatial heterogeneity of coronary reserve. Discordance between patterns of resting and maximal myocardial blood flow. *Circ Res* 67, 319–331. doi:10.1161/01.res. 67.2.319 (1990).
- 78. Chareonthaitawee, P., Kaufmann, P. A., Rimoldi, O. & Camici, P. G. Heterogeneity of resting and hyperemic myocardial blood flow in healthy humans. *Cardiovasc Res* **50**, 151–161. doi:10.1016/s0008-6363(01)00202-4 (2001).
- 79. Karanasiou, G. et al. In Silico analysis of stent deployment- effect of stent design in 2018 40th Annual International Conference of the IEEE Engineering in Medicine and Biology Society (EMBC) (2018), 4567–4570. doi:10.1109/EMBC.2018.8513205.
- 80. Konduri, P. et al. Risk factors for infarct growth in patients with acute ischemic stroke in 4th European Stroke Organisation Conference 3 (European Stroke Journal, 2018), 403. doi:10.1177/2396987318770127.





PART II WALL SHEAR STRESS





CHAPTER 5

Endothelial shear stress estimation in the human carotid artery based on Womersley versus Poiseuille flow

Janina C. V. Schwarz¹, Raphaël Duivenvoorden², Aart J. Nederveen³, Erik S. G. Stroes², and Ed van Bavel¹

Janina C. V. Schwarz and Raphaël Duivenvoorden have contributed equally.

Department of Biomedical Engineering and Physics, Academic Medical Center, University of Amsterdam, Amsterdam, The Netherlands

² Department of Vascular Medicine, Academic Medical Center, University of Amsterdam, Amsterdam, The Netherlands

³ Department of Radiology, Academic Medical Center, University of Amsterdam, Amsterdam, The Netherlands

ABSTRACT

Background

Endothelial shear stress (ESS) dynamics are a major determinant of atherosclerosis development. The frequently used Poiseuille method to estimate ESS dynamics has important limitations. Therefore, we investigated whether Womersley flow may provide a better alternative for estimation of ESS while requiring equally simple hemodynamic parameters.

Methods

Common carotid blood flow, centerline velocity, lumen diameter and mean wall thickness (MWT) were measured with 3T-MRI in 45 subjects at three different occasions. Mean ESS and two measures of pulsatility [shear pulsatility index (SPI) and oscillatory shear index (OSI)] were estimated based on Poiseuille and Womersley flow and compared to the more complex velocity gradient modelling method. The association between ESS and MWT was tested with multiple linear regression analysis; interscan reproducibility was assessed using intraclass correlation coefficients (ICC).

Results

Mean ESS and pulsatility indices based on Womersley flow (ESS_{wq} β = -0.18, p = 0.04; SPI_{wq} β = 0.24, p = 0.02; OSI_{wq} β = 0.18, p = 0.045) showed equally good correlations with carotid MWT as the velocity gradient method (ESS_{vg} β = -0.23, p = 0.01; SPI_{vg} β = 0.21, p = 0.02; OSI_{vg} β = 0.07, p = 0.47). This was in contrast to the Poiseuille flow method that only showed a good correlation for mean ESS (ESS_{pq} β = -0.18, p = 0.04; SPI_{pq} β = 0.14, p = 0.14; OSI_{pq} β = 0.04, p = 0.69). Womersley and Poiseuille methods had high intraclass correlation coefficients indicating good interscan reproducibility (both ICC = 0.84, 95% confidence interval 0.75–0.90).

Conclusions

Estimation of ESS dynamics based on Womersley flow modelling is superior to Poiseuille flow modelling and has good interscan reproducibility.

Keywords: Endothelial shear stress, Cardiovascular magnetic resonance, Common carotid artery, Intima media thickness

5.1 Introduction

Endothelial shear stress (ESS) is the hemodynamic force that flowing blood exerts on the vessel wall. This force is continuously sensed by mechanoreceptors that are attached to the cytoskeleton of endothelial cells. Processes involved in endothelial cell turnover, inflammation, coagulation, extracellular matrix degradation, and production of vasoactive substances such as nitric oxide are all tightly regulated by ESS. In vitro and animal studies showed that protracted decrease in ESS and high variation of ESS during the cardiac cycle cause endothelial receptor and gene expression to switch to an atherogenic phenotype. Vascular imaging studies corroborate these findings, showing a causal relationship between ESS and atherosclerosis development. Set when the set of the set

Assessing ESS in vivo is technically challenging, which is the reason why human studies on ESS remain scarce, and are typical performed in small sample sizes. Various methods are used, including computational fluid dynamics, velocity gradient modelling, and methods assuming Poiseuille flow. 9 Computational fluid dynamics can solve the Navier-Stokes equations of fluid flow, while velocity gradient modelling is based on the spatial gradient of the velocities close to the artery wall using second-order curve fitting of the velocity profile.^{5,9,10} Although accurate methods, their downsides pertain to the fact that high resolution information is needed on the local velocity vector throughout the cycle, respectively as boundary condition for the Navier-Stokes equations and as base for the accurate fitting of the velocity gradient perpendicular to the wall. Obtaining such data is labor intensive and dedicated software is needed for the complex data analysis, which is not freely available. In contrast, Poiseuille based methods are simpler as they merely require measurement of artery diameter and flow rate or centerline velocity followed by a simple calculation. Estimations of ESS dynamics are then based on the instantaneous hemodynamics during the cycle. However, Poiseuille flow requires among others steady flow in straight rigid tubes. These conditions are violated in vivo in human arteries, resulting in deviation from the assumed parabolic velocity profile. 9,11 Despite the inherent inadequacy of Poiseuille based methods, the majority of current literature relies on this approach due to its simplicity and availability.6-8,12,13

Therefore, we investigated whether an equally simple method based on similar parameters (diameter and flow rate or centerline velocity) provides a better alternative to the Poiseuille based method. This method is based on Womersley flow, which in contrast to Poiseuille covers pulsatile flow components. We compared the

Womersley method to the Poiseuille based method as well as to velocity gradient modelling from high resolution phase contrast (PC)-MRI. We correlated ESS of each method with carotid artery wall thickness, assuming that higher correlations are obtained with more accurate ESS estimations. ¹⁵ We also compared reproducibility of each of the methods. All measurements were performed in the common carotid arteries by 3T-MRI.

5.2 Methods

5.2.1 Subject population

Forty-five subjects (age range 19–79 years) were enrolled prospectively. The population consisted of 30 volunteers and 15 patients with cardiovascular disease who were selected from the outpatient clinic of the Department of Vascular Medicine of the Academic Medical Center, Amsterdam, The Netherlands. In all subjects repeat 3T-MRI scans were acquired on three separate occasions, 1–3 weeks apart. All image analyses were done off-line. Prior to the studies, approval was obtained from the institutional review board of the Academic Medical Center, Amsterdam, The Netherlands. All subjects gave written informed consent.

5.2.2 Image acquisition

Magnetic resonance imaging scans were obtained bilaterally on a 3T-MRI scanner (Intera, Philips Medical Systems, Best, The Netherlands) using a single-element microcoil (Philips, Hamburg, Germany) with a diameter of 5 cm. Axial magnetic resonance angiography images were acquired using a time of flight sequence to localize the left and right common carotid artery and position the scan planes perpendicular to the vessel.

For hemodynamic assessments, axial gradient echo phase-contrast images were acquired with a temporal resolution of 17 ms, and temporal interpolation was performed by the scanner software to 60 phases per heartbeat (retrospective electrocardiography gating). The scan plane was positioned 27 mm proximal to the carotid flow divider. Sequence parameters were: slice thickness 3 mm, non-interpolated pixel size $0.65 \times 0.65 \, \text{mm}^2$, field of view $60 \times 60 \, \text{mm}^2$, velocity encoding 150 cm/s (unidirectional), repetition time 8.1 ms, echo time 5 ms, flip angle 10°, number of signal averages 2, total scan time 3–4 min. Both magnitude images and velocity encoded phase images were reconstructed.

To assess carotid wall thickness, axial T1-weighted Turbo Spin Echo image stacks were acquired at end-diastole using double inversion recovery black blood preparation applying active fat suppression (spectral attenuated inversion recovery technique) as described previously. Sequence parameters were: slice thickness 3 mm, imaging matrix size 240, field of view of $60 \times 60 \text{ mm}^2$, non-interpolated pixel size $0.25 \times 0.25 \text{ mm}^2$, echo time 9 ms, repetition time according to the subjects' heart rate (approximately 900 ms), echo train length 7, echo train duration 63 ms. All imaging was performed with cardiac gating.

5.2.3 Image analysis

For assessment of hemodynamic parameters in the carotid arteries, off-line semiautomated qualitative and quantitative image analysis was performed using software written in Matlab developed at the Academic Medical Center, Amsterdam, The Netherlands. The lumen area (LA, mm²) of all 60 phases per cardiac cycle was assessed by automated tracing of the lumen-wall boundaries on the gradient echo images. 16 The velocity at each pixel in the artery lumen was measured, which enabled the calculation of the volumetric flow rate $(Q, \text{cm}^3/\text{s})$ and centerline velocity $(v, \text{cm}^3/\text{s})$ cm/s) of each phase in the cardiac cycle. The measured lumen area, flow rate, and centerline velocity were used to calculate the Poiseuille and Womersley based endothelial shear rate (ESR, 1/s). The calculations are shown in the Supplementary Methods. While Poiseuille and Womersley should predict identical mean ESS, a very minor difference exists in the data due to taking respectively an actual and a time-averaged diameter for the calculations. For the assessment of ESR based on the velocity gradient modelling method, we used dedicated software written in Matlab developed at the Academic Medical Center, Amsterdam, The Netherlands. We have described the method in detail previously.⁵ Firstly, the lumen area (LA, mm²) of all 60 phases per cardiac cycle was assessed as described above. Secondly, for each pixel the shortest distance to the artery wall was calculated. The lumenwall boundaries were projected on the velocity encoded images. The ESR was assessed by determining the spatial gradient of the velocities close to the artery wall using second order curve fitting of the velocity profile. The pixels located from 0.31 to 1.56 mm from the wall were included for the analysis. The fit was forced to include the position of the artery wall with a velocity of zero to conform to the zero-slip condition.

For all methods (Poiseuille, Womersley and velocity gradient modelling), ESR was multiplied with the blood viscosity to calculate the ESS throughout the cardiac cycle. Blood viscosity was assumed to be $3.2 \, \text{cP.}^{17}$ Poiseuille and Womersley methods were either based on flow rate (ESS_{pq}, ESS_{wq}) or centerline velocity (ESS_{pv}, ESS_{wv}).

From these dynamics, we calculated the mean ESS of all phases in the cardiac cycle as well as the shear pulsatility index (SPI) and the oscillatory shear index (OSI). SPI was defined as difference between the maximum and minimum ESS in the cardiac cycle divided by their sum. The oscillatory shear index represents the proportion of shear stress deviating from its predominant direction during the cardiac cycle.¹⁸

For the carotid wall thickness quantification, semiautomated image analysis was performed using VesselMass software (Leiden University Medical Center, Leiden, The Netherlands). VesselMass performed automated tracing of the lumen-wall boundaries and the outer wall boundaries. The software algorithm for boundary detection and analysis methods are described elsewhere. ^{19,20}

5.2.4 Statistical analysis

Continuous variables are expressed as means ± standard deviations (SD). We used multiple linear regression analysis to assess the association between the ESS values and MWT with MWT as the response variable and ESS as the explanatory variable. We determined by stepwise analysis with backward elimination that age and systolic blood pressure were the only significant confounders among all measured cardio-vascular risk factors (patient characteristics and biochemistry as listed in Table 5.1). We therefore adjusted for these confounders. The agreement between successive ESS estimations was assessed using intraclass correlation coefficients (ICC) and the 95% confidence intervals of the ICCs. For all statistical analyses Statistical Package for the Social Sciences version 20.0 for Windows was used.

5.3 RESULTS

Three MRI scans were performed in all 45 subjects. The population consisted of 20 females and 25 males. Their characteristics are shown in Table 5.1. Figure 5.1 shows two examples of wall thickness (Figure 5.1A,D), measured peak systolic flow velocity (color scales in Figure 5.1B,C,E,F), and estimations of peak systolic flow velocity based on Poiseuille (Figure 5.1B,E) and Womersley (Figure 5.1C,F) with flow rate as input. As can be seen, both vessels were approximately circular and measured flow velocity was relatively axisymmetric in both examples. The Womersley-based prediction far more closely matched the measured profile as compared to the Poiseuille-based estimate. The Womersley but not the Poiseuille model predicted flow reversal at the wall (OSI > 0), while in these cases the thicker wall was associated with a larger OSI_{wq}. Average data for common carotid lumen area,

Table 5.1: Volunteer characteristics, hemodynamics and ESS estimates

	(N = 45)		
Patient characteristics			
Age (years)	48.9 (17.6)		
Male gender $(n, \%)$	26 (58)		
Body Mass Index (kg/m ²)	24 (22–26)		
Smokers $(n, \%)$	5 (11)		
Cardiovascular disease $(n, \%)$	15 (33)		
Biochemistry	15 (66)		
Total Cholesterol (mmol/l)	4.7 (3.9–5.5)		
Low density lipoprotein cholesterol (mmol/l)	2.5 (1.9–3.5)		
High density lipoprotein cholesterol (mmol/l)	1.6 (0.4)		
Triglycerides (mmol/l)	0.8 (0.6–1.1)		
Fasting glucose (mmol/l)	5.2 (0.7)		
Carotid wall and lumen	, ,		
Carotid lumen area (mm²)	34.0 (8.4)		
Carotid wall thickness (mm)	0.72 (0.23)		
Hemodynamic parameters	,		
Heart rate (1/min)	64 (10)		
Systolic blood pressure (mmHg)	127 (15)		
Diastolic blood pressure (mmHg)	73 (7)		
Mean carotid flow (cm ³ /s)	6.27 (1.14)		
Peak carotid centerline velocity (cm/s)	71.14 (14.42)		
Velocity gradient modelling	,		
Mean ESS _{vg} (N/m ²)	0.87 (0.25)		
SPI_{vg} (–)	0.82 (0.12)		
OSI_{vg} (-)	0.001 (0.004)		
Womersley, centerline velocity			
Mean ESS _{wv} (N/m ²)	0.63 (0.15)		
SPI _{wv} (–)	1.67 (0.41)		
OSI_{wv} (–)	0.083 (0.055)		
Womersley, flow			
Mean ESS _{wq} (N/m ²)	0.76 (0.19)		
SPI _{wq} (–)	1.30 (0.21)		
OSI_{wq} (-)	0.026 (0.021)		
Poiseuille, centerline velocity			
Mean ESS _{pv} (N/m ²)	0.63 (0.15)		
SPI _{pv} (–)	0.60 (0.08)		
OSI_{pv} (–)	0.000 (0.000)		
Poiseuille, flow			
Mean ESS _{pq} (N/m ²)	0.73 (0.18)		
SPI_{pq} (–)	0.67 (0.08)		
OSI_{pq}^{rq} (-)	0.000 (0.001)		

Mean (\pm SD) values or median (interquartile range) values for non-normal distributions for volunteer characteristics, biochemistry, hemodynamic parameters, and carotid wall and lumen parameters measured by 3T-MRI (reported previously). ESS is endothelial shear stress, SPI is shear pulsatility index and OSI is oscillatory shear index

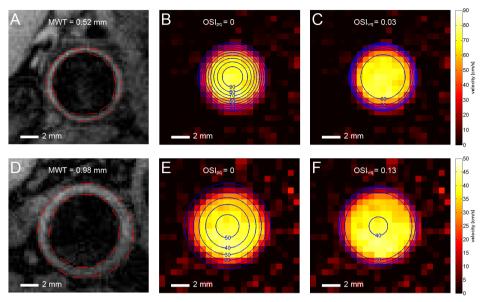


Figure 5.1: Two examples of measured mean wall thickness (MWT, (**A,D**)) and peak systolic flow velocity profiles with their Poiseuille- and Womersley-based estimates. The phase contrast MRI-based velocity profiles are shown as color-coded image (**B,C,E,F**). Estimated profiles are indicated as contour plots. (**B,E**) Poiseuille-based with flow rate as input, (**C,F**) Womersley-based with flow rate as input. OSI: estimated oscillatory shear index

mean wall thickness (MWT, mm), hemodynamic parameters, and ESS parameters are shown in Table 5.1. Mean ESS is by definition equal when based on Poiseuille or Womersley flow, and these estimates were comparable to the estimate from velocity gradient modelling. SPI for the Womersley based methods was around twice as high as that for the other methods. The amount of negative shear stress as assessed with OSI was low for all methods with Womersley based methods exhibiting the highest values (Table 5.1). In particular, the OSI_{pv} was constantly zero such that its reproducibility and correlation with MWT could not be assessed. Figure 5.2 shows the different ESS estimates throughout the cardiac cycle averaged for all subjects.

Partial regression coefficients between ESS, SPI and OSI values and MWT, adjusted for the potential confounders age and systolic blood pressure, are shown in Table 5.2. The mean ESS and SPI of the velocity gradient modelling and Womersley flow rate based modelling methods correlated equally well with MWT, while only the mean ESS of the Poiseuille flow rate based method correlated with MWT. The

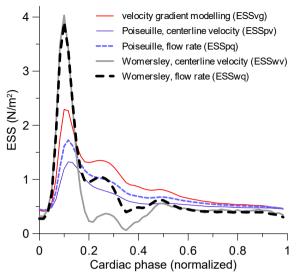


Figure 5.2: Common Carotid Endothelial Shear Stress (ESS, N/m²) during the cardiac cycle averaged for all subjects for all estimation methods (*red* velocity gradient modelling method, *blue* Poiseuille flow modelling based on centerline velocity, *interrupted blue* Poiseuille flow modelling based on flow rate, *grey* Womersley flow modelling based on centerline velocity, *interrupted black* Womersley flow modelling based on flow rate). Per cardiac cycle, 60 image frames were made where the first frame coincided with the R wave of electrocardiogram. ESS was quantified for all 60 frames per heartbeat

OSI of both Womersley methods (either based on flow rate or centerline velocity) correlated with MWT. The Poiseuille centerline velocity based method did not show any good correlations with MWT. The interscan variabilities of the different methods are shown in Table 5.3. Womersley and Poiseuille based methods tended to have higher intraclass correlation coefficients than the velocity gradient modelling methods, indicating better interscan reproducibility.

5.4 DISCUSSION

In the present study we show that for estimation of dynamic ESS from flow rate or centerline velocity in the common carotid artery, methods based on Womersley outperform Poiseuille based methods. Furthermore we show that flow rate-based methods perform better than centerline velocity-based methods. We base these conclusions on the correlation of predicted ESS with the mean wall thickness of the

Table 5.2: Relation between endothelial shear stress and carotid wall thickness

	Beta coefficient	95% CI	р
Velocity gradient modelling			
Mean ESS _{vg}	-0.23	-0.35 to -0.05	0.01
$\mathrm{SPI}_{\mathrm{vg}}$	0.21	0.06 to 0.66	0.02
OSI_{vg}°	0.07	-6.64 to 14.23	0.47
Womersley, centerline velocity			
Mean ESS _{wv}	-0.13	-0.45 to 0.09	0.19
$\mathrm{SPI}_{\mathrm{wv}}$	0.23	0.02 to 0.23	0.02
$\mathrm{OSI}_{\mathrm{wv}}$	0.19	0.03 to 1.41	0.04
Womersley, flow			
Mean ESS _{wq}	-0.18	-0.42 to -0.01	0.04
$\mathrm{SPI}_{\mathrm{wq}}$	0.24	0.04 to 0.47	0.02
OSI_{wq}	0.18	0.04 to 3.61	0.045
Poiseuille, centerline velocity			
Mean ESS _{pv}	-0.13	-0.45 to 0.09	0.19
$\mathrm{SPI}_{\mathrm{pv}}$	0.12	-0.16 to 0.77	0.19
$OS\dot{I}_{ m pv}$	_	-	-
Poiseuille, flow			
Mean ESS _{pq}	-0.18	-0.42 to -0.01	0.04
$\mathrm{SPI}_{\mathrm{pq}}$	0.14	-0.12 to 0.81	0.14
OSI_{pq}	0.04	-373.49 to 556.56	0.69

Linear regression analysis to assess the association between endothelial shear stress (ESS) values and mean wall thickness (MWT) adjusted for age and systolic blood pressure are shown (beta coefficients and 95% confidence intervals of the unstandardized coefficients). SPI is shear pulsatility index, OSI is oscillatory shear index

vessel. A third method, based on the velocity gradient near the wall, also predicted ESS that correlates with MWT, but this method requires detailed information on the flow pattern, which is not commonly available. All methods had good interscan reproducibility. Our findings implicate that the easily applicable Womersley based method enables better ESS, SPI and OSI estimation in future clinical studies and can replace the currently frequently used Poiseuille based methods.

Womersley theory is far from new.^{14,21} Yet, it is not commonly applied for estimation of ESS parameters²² with few in vivo applications,^{23–26} and studies on the correlation with MWT in the common carotid arteries were lacking. The fundamental difference between Poiseuille and Womersley flow is that the latter takes the inertia of blood into account. This effect of inertia depends on the flow dynamics

Table 5.3: Interscan measurement variability of endothelial shear stress estimations

	ICC	95% CI	p
Velocity gradient modelling			
Mean ESS _{vg}	0.78	0.67-0.86	< 0.001
$\mathrm{SPI}_{\mathrm{vg}}$	0.74	0.61-0.84	< 0.001
${ m OSI}_{ m vg}^{\circ}$	0.66	0.51-0.78	< 0.001
Womersley, centerline velocity			
Mean ESS _{wv}	0.86	0.78 - 0.92	< 0.001
$\mathrm{SPI}_{\mathrm{wv}}$	0.62	0.47 - 0.76	< 0.001
$\mathrm{OSI}_{\mathrm{wv}}$	0.75	0.62-0.84	< 0.001
Womersley, flow			
Mean ESS _{wq}	0.84	0.75-0.90	< 0.001
$\mathrm{SPI}_{\mathrm{wq}}$	0.80	0.70-0.88	< 0.001
$\mathrm{OSI}_{\mathrm{wq}}^{-1}$	0.73	0.60-0.83	< 0.001
Poiseuille, centerline velocity			
Mean ESS _{pv}	0.86	0.78 - 0.92	< 0.001
$\mathrm{SPI}_{\mathrm{pv}}$	0.66	0.51-0.78	< 0.001
$OS\dot{I}_{pv}$	_	_	_
Poiseuille, flow			
Mean ESS _{pq}	0.84	0.75-0.90	< 0.001
$\mathrm{SPI}_{\mathrm{pq}}$	0.69	0.55-0.80	< 0.001
OSI_{pq}	-0.01	-0.16 to 0.18	n.s.

Intraclass correlation coefficients (ICC, 95% confidence interval) for all estimation methods are shown. ESS is endothelial shear stress, SPI is shear pulsatility index and OSI is oscillatory shear index

and the geometry and is known to be substantial for common carotid arteries.²⁷ For the mean ESS, inertia is not relevant and Poiseuille and Womersley provide identical estimates.

A low time-averaged ESS is considered to be atherogenic.^{3,6–8,28–30} We indeed observed that low mean ESS, when using the flow rate as input, or based on the velocity gradient method, correlated with a thicker wall. We did find differences in estimates for mean ESS between the methods. In particular, using centerline velocity as input predicted lower values, which also were no longer correlated with MWT. This may be caused by more inherent noise in centerline velocity as compared to the flow rate, as well as by systematic deviations of the time-averaged velocity field from an axisymmetric parabolic profile, towards a flatter profile. For flow rate as input, the difference between the Womersley-based prediction and the velocity

gradient method was limited to ≈13%. Such systematic deviation would not affect the relevance for clinical studies, as demonstrated by the significant correlation of mean ESS with MWT. Taken together, the data suggest that flow rate should be preferred over centerline velocity as input for estimation of mean ESS.

Temporal variations in ESS and notably a change in direction during part of the cycle have strong effects on endothelial biology towards a pro-atherogenic phenotype. 1,3,28,29 The more than twofold difference in estimated SPI between Poiseuille and Womersley flow and the lack of correlation between Poiseuille-based SPI and OSI estimation and MWT demonstrate the necessity to account for blood inertia in pulsatility assessment. This is notably the case in peak systole, where a major deviation from a parabolic flow profile occurred. The supplementary material analysis shows the consistency of flow profiles under Womersley and Poiseuille.

Importantly, in Womersley flow, phases of negative ESS can co-exist with continuous forward flow and forward centerline velocity. In Poiseuille flow, this is not possible. Indeed, Womersley flow predicted a non-zero OSI in part of the cases, while for Poiseuille flow OSI was zero, in concordance with the absence of flow reversal in the studied non-stenotic common carotid arteries. The occurrence of a non-zero OSI in the Womersley predictions depends primarily on the balance of mean flow and the amplitude of the pulsatile components. Also, the SPI was defined as this balance. The correlations of the Womersley-predicted OSI and SPI with MWT strongly suggest that this balance is clinically relevant. Vascular stiffening and increased pulse pressure are conditions that would increase the pulsatile flow components and cause a non-zero OSI. A high mean flow would reduce the likelihood of a non-zero OSI. It remains to be established whether the correlation of low mean flow with thicker walls that we observed is in fact the consequence of reversal of ESS during the heart cycle.

A substantial difference remained between Womersley-based and gradient-based estimates of ESS pulsation. Extensive work on software phantoms has evaluated the accuracy and precision of a comparable velocity gradient technique as a function of scanning and resolution parameters, ³¹ providing arguments for the accuracy of this method. However, in the absence of a golden truth in the current data, there is no straightforward way of quantitating accuracy of any of the methods. We suspect that the bias is also in the gradient method. ESR is defined as the velocity gradient in an infinitesimal small space above the endothelial cells. This gradient quickly falls further away from the endothelium in notably dynamic flow. The gradient method, having a finite resolution, might thus underestimate ESS pulsatility and also miss local reversal of the direction. Womersley provides a continuous solution for velocity

as function of distance from the endothelium, which under the assumption of no-slip should give an inherently better estimate of ESS pulsatility. The Womersley-based and gradient-based SPI correlated equally well with MWT, indicating that these differences do not affect the usefulness of either SPI estimate in clinical studies. However, the OSI, which relies on subtle changes of the flow in the boundary layer, only correlated with MWT for Womersley-based methods.

5.4.1 Applicability

The current approach uses vascular diameter and either centerline velocity or flow rate as input, without requirement for more detailed data on the spatial velocity profile. Techniques that can provide such data include Echo-Doppler scanning and phase contrast MRI. The ability to estimate ESS from Echo-Doppler scanning allows implementation as pseudo-endpoint in large clinical studies. MRI methods based on direct measurement of local velocity vectors in 3D, such as 3D PC-MRI, may form a good approach for dedicated studies in complex geometries.³² Yet, the current findings suggest that a much simpler implementation of Womersley-based estimation of shear parameters with consequently much shorter scanning times is a good alternative strategy in clinical studies on common carotid arteries.

All applied methods had good reproducibility. Reproducibility of the flow-based Womersley estimates for mean ESS and pulsatility exceeded that of the gradient modelling. While flow rate should be preferred over centerline velocity for mean ESS, for pulsatility (SPI and OSI) centerline velocity also provides a good correlation with MWT and good reproducibility, supporting the use of ultrasound or simple MRI protocols for pulsatility quantification.

5.4.2 Limitations of the study

It is clear that the requirements for Womersley flow were violated to some degree. Recently, Mynard et al.³³ evaluated the consequences of carotid curvature on Poiseuille- and Womersley-based estimates for mean and peak ESS. In that study, computational fluid dynamics based on the Navier–Stokes equations were used as the gold standard. Their results indicate that even a slight curvature causes substantial bias and circumferential heterogeneity of these estimates. The effect of curvature on SPI or OSI was not tested. In the current study, we did not apply computational fluid dynamics, and it remains to be established to what extent deviations from a straight tube influence the pulsatile ESS parameters and their correlation with MWT. Computational fluid dynamics methods are, apart from

being time-consuming, affected by errors in boundary conditions and geometry definitions, as well as by assumptions on wall rigidity and blood rheology, precluding their general use in large clinical studies.

In the absence of a gold standard for ESS in large clinical studies, evidence for usefulness of any ESS method comes from correlation with wall biology and thickening, and it seems reasonable to evaluate the accuracy of the ESS estimates from the correlation with MWT. The current correlation of Womersley-based mean ESS, SPI and OSI with MWT as a marker for atherosclerotic burden is not necessarily causal; longitudinal studies on predictive value of shear parameters for cardiovascular events should allow evaluating their usefulness as pseudo-endpoints in clinical studies.

5.5 CONCLUSIONS

In the present study we developed a reproducible and accurate Womersley flow based method to estimate the endothelial shear stress dynamics in the common carotid arteries. We showed that this method is equally good as the more complex velocity gradient modelling method and superior to the simpler Poiseuille flow based method to estimate ESS. The Womersley based method we present solely requires the measurement of flow rate or centerline velocity and carotid artery diameter. This renders the method applicable for large clinical studies without the need for complex analyses and computations. While having its limitations, the Womersley based method should therefore replace the frequently used Poiseuille based method, enabling better assessment of the relationship between ESS, atherosclerosis and cardiovascular disease in future clinical studies.

Acknowledgments

We would like to thank A.M. van den Berg for assisting in the data acquisition. JCVS was supported by Grant 01C-204 (EMINENCE project) from the Center for Translational Molecular Medicine.

Conflict of interest

The authors declare that they have no conflict of interest.

SUPPLEMENTARY MATERIAL

Computations and models

The endothelial shear stress (ESS) was predicted by assuming Poiseuille or Womersley flow. Both models carry several assumptions that are not necessarily met in the common carotid artery: Most notably, they both describe (axisymmetric) flow through a rigid cylindrical tube; less stringent limitations include ignorance of entrance effects and assuming laminar flow as well as blood being a Newtonian fluid.³⁴ Contrary to Poiseuille flow, Womersley profiles account for the pulsatile nature of the pressure gradient in blood vessels. Both models were used to predict the wall shear stress based on either centerline velocity or blood flow. For (quasi-static) Poiseuille flow, the predictions were:

$$ESS_{pv}(t) = \frac{2\mu}{R(t)} \cdot \nu(0, t)$$
 (5.1)

$$ESS_{pq}(t) = \frac{4\mu}{\pi R^3(t)} \cdot Q(t)$$
 (5.2)

where μ is the blood viscosity (taken as 3.2×10^{-3} Pa s), R the radius of the vessel, $\nu(0,t)$ the centerline velocity, and Q(t) the flow rate. The (time-dependent) radius R was estimated from lumen area assuming a circular cross-section of the vessel.

Womersley described flow caused by a pulsatile pressure gradient:¹⁴

$$v(y,t) = \frac{A}{i\omega\rho} \left(1 - \frac{J_0(\alpha y i^{3/2})}{J_0(\alpha i^{3/2})} \right) e^{i\omega t}$$
 (5.3)

$$Q(t) = \frac{\pi R^2 A}{i\omega\rho} \left(1 - \frac{2\alpha i^{3/2} J_1(\alpha i^{3/2})}{i^3\alpha^2 J_0(\alpha i^{3/2})} \right) e^{i\omega t}$$
 (5.4)

A is the (complex) amplitude and ω is the angular frequency of the driving pressure gradient. R is the radius of the tube, y the fractional radial position $y = \frac{r}{R}$, ρ is the fluid density, J_n is a Bessel function of order n, and α is a dimensionless number describing the relation of inertial to viscous forces: $\alpha = R\sqrt{\frac{\omega \rho}{\mu}}$.

For calculating Womersley flow, we decomposed both the measured centerline velocity and the flow rate into their Fourier components. Harmonics of the heart rate (HR, beats/min), i.e. frequencies of approximately 1 Hz, 2 Hz, etc. up to the

order of 30 were included:

$$v(0,t) = \sum_{n=-30}^{30} v_n(t)$$
 (5.5)

$$Q(t) = \sum_{n=-30}^{30} Q_n(t)$$
 (5.6)

where $v_n(t)$ and $Q_n(t)$ are the *n*-th Fourier component of the centerline velocity and the flow rate respectively, e.g. $v_n(t) = a_n e^{in\omega t}$, with ω the base angular frequency, which in this case equals $2\pi HR/60$, and a_n being the complex amplitude. Each component has its own Womersley number α_n :

$$\alpha_n = R\sqrt{\frac{|n|\omega\rho}{\mu}} \tag{5.7}$$

with ρ the density of blood (1.05 g/ml) and R being the time averaged radius. The ESS was derived by describing the derivative of Equation 5.3 at the vessel wall (r = R) in terms of either the centerline velocity v(t) or the flow rate Q(t) and a subsequent summation over the harmonics:

$$ESS_{wv}(t) = \frac{2\mu}{R} v_0(t) - \frac{\mu}{R} \sum_{\substack{n=-30\\n\neq 0}}^{30} \Re\left(\frac{J_1(b_n)}{J_0(b_n) - 1} v_n(t)\right)$$
 (5.8)

$$ESS_{wq}(t) = \frac{4\mu}{\pi R^3} Q_0(t) + \frac{\mu}{\pi R^3} \sum_{\substack{n=-30\\n\neq 0}}^{30} \Re\left(\frac{b_n J_1(b_n)}{J_2(b_n)} Q_n(t)\right)$$
(5.9)

where $b_n := \alpha_n i^{\frac{3}{2}}$ and \Re denotes that only the real part is taken. Thus, based on the equations above we predicted ESS based on four different models: Poiseuille with flow rate or centerline velocity as input as well as Womersley with flow rate or centerline velocity as input.

Consistency of centerline velocity and flow

Maximum velocity as predicted by the flow models was compared to measured maximum velocity to assess the applicability of the Poiseuille and the Womersley model. There was good agreement for both models in diastole (see Figure 5.S1). In systole, the centerline velocity predicted by Womersley flow matched well whereas

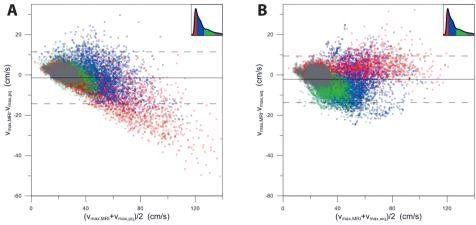


Figure 5.S1: Bland–Altman-plot comparing measured maximum velocity to maximum velocity predicted from total flow rate based on **(A)** Poiseuille flow and **(B)** Womersley flow (all frames for all acquisitions ignoring the correlated nature of the data points). The solid lines indicate the mean difference; the dashed lines demark the mean \pm 1.96 SD. Four phases of the cardiac cycle are discriminated as indicated by the inset: in red the accelerating systole, in blue late-systole, in green and in grey are early and late diastole respectively.

Poiseuille flow predicted a higher maximum velocity. The variability in prediction was higher during the decelerating phase for both models with Womersley tending towards a higher maximum velocity than measured.

The bias in the Poiseuille estimation during systole can be attributed to the blunt flow in the common carotid, ³⁵ which implies an improper pulsatility description of the Poiseuille model. In contrast, for Womersley the extreme velocities are in good agreement.

REFERENCES

- Davies, P. F. Hemodynamic shear stress and the endothelium in cardiovascular pathophysiology. Nat Clin Pract Cardiovasc Med 6, 16–26. doi:10.1038/ncpcardio1397 (2009).
- Tzima, E. et al. A mechanosensory complex that mediates the endothelial cell response to fluid shear stress. Nature 437, 426–431. doi:10.1038/nature03952 (2005).

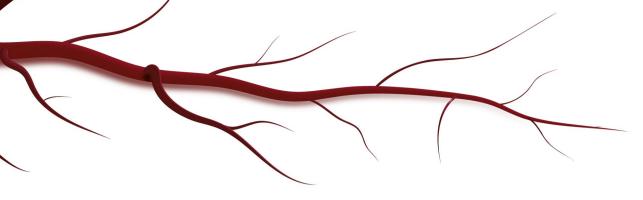
- 3. Dai, G. *et al.* Distinct endothelial phenotypes evoked by arterial waveforms derived from atherosclerosis-susceptible and -resistant regions of human vasculature. *Proc Natl Acad Sci U S A* **101**, 14871–14876. doi:10.1073/pnas.0406073101 (2004).
- 4. Langille, B. L. & O'Donnell, F. Reductions in arterial diameter produced by chronic decreases in blood flow are endothelium-dependent. *Science* **231**, 405–407. doi:10.1126/science.3941904 (1986).
- 5. Duivenvoorden, R. et al. Endothelial shear stress: a critical determinant of arterial remodeling and arterial stiffness in humans—a carotid 3.0-T MRI study. Circ Cardiovasc Imaging 3, 578–585. doi:10.1161/CIRCIMAGING.109.916304 (2010).
- 6. Gnasso, A. *et al.* Association between intima-media thickness and wall shear stress in common carotid arteries in healthy male subjects. *Circulation* **94**, 3257–3262. doi:10.1161/01.CIR.94.12.3257 (1996).
- 7. Irace, C. *et al.* Human common carotid wall shear stress as a function of age and gender: a 12-year follow-up study. *Age* **34**, 1553–1562. doi:10.1007/s11357-011-9318-1 (2012).
- 8. Irace, C., Cortese, C., Fiaschi, E., Carallo, C., Farinaro, E. & Gnasso, A. Wall shear stress is associated with intima-media thickness and carotid atherosclerosis in subjects at low coronary heart disease risk. *Stroke* **35**, 464–468. doi:10.1161/01. STR.0000111597.34179.47 (2004).
- 9. Katritsis, D., Kaiktsis, L., Chaniotis, A., Pantos, J., Efstathopoulos, E. P. & Marmarelis, V. Wall shear stress: theoretical considerations and methods of measurement. *Prog Cardiovasc Dis* 49, 307–329. doi:10.1016/j.pcad.2006.11.001 (2007).
- 10. Oyre, S. *et al.* Accurate noninvasive quantitation of blood flow, cross-sectional lumen vessel area and wall shear stress by three-dimensional paraboloid modeling of magnetic resonance imaging velocity data. *J Am Coll Cardiol* **32**, 128–134. doi:10.1016/s0735-1097(98)00207-1 (1998).
- 11. Ford, M. D., Xie, Y. J., Wasserman, B. A. & Steinman, D. A. Is flow in the common carotid artery fully developed? *Physiol Meas* **29**, 1335–1349. doi:10.1088/0967-3334/29/11/008 (2008).
- Box, F. M. et al. Reproducibility of wall shear stress assessment with the paraboloid method in the internal carotid artery with velocity encoded MRI in healthy young individuals. J Magn Reson Imaging 26, 598–605. doi:10.1002/jmri.21086 (2007).
- 13. Box, F. M. *et al.* Pravastatin decreases wall shear stress and blood velocity in the internal carotid artery without affecting flow volume: results from the PROSPER MRI study. *Stroke* **38**, 1374–1376. doi:10.1161/01.STR.0000260206.56774.aa (2007).

- 14. Womersley, J. R. Method for the calculation of velocity, rate of flow and viscous drag in arteries when the pressure gradient is known. *J Physiol* **127**, 553–563. doi:10.1113/jphysiol.1955.sp005276 (1955).
- 15. Friedman, M. H., Hutchins, G. M., Brent Bargeron, C., Deters, O. J. & Mark, F. F. Correlation between intimal thickness and fluid shear in human arteries. *Atherosclerosis* **39**, 425–436. doi:10.1016/0021-9150(81)90027-7 (1981).
- Li, C., Kao, C.-Y., Gore, J. C. & Ding, Z. Implicit Active Contours Driven by Local Binary Fitting Energy in 2007 IEEE Conference on Computer Vision and Pattern Recognition (2007), 1–7. doi:10.1109/CVPR.2007.383014.
- 17. Reneman, R. S., Arts, T. & Hoeks, A. P. Wall shear stress—an important determinant of endothelial cell function and structure—in the arterial system in vivo. Discrepancies with theory. *J Vasc Res* **43**, 251–269. doi:10.1159/000091648 (2006).
- 18. Ku, D. N., Giddens, D. P., Zarins, C. K. & Glagov, S. Pulsatile flow and atherosclerosis in the human carotid bifurcation. Positive correlation between plaque location and low oscillating shear stress. *Arterioscler Thromb Vasc Biol* 5, 293–302. doi:10.1161/01.ATV.5.3.293 (1985).
- 19. Adame, I. M., van der Geest, R. J., Bluemke, D. A., Lima, J. A., Reiber, J. H. & Lelieveldt, B. P. Automatic vessel wall contour detection and quantification of wall thickness in in-vivo MR images of the human aorta. *J Magn Reson Imaging* **24**, 595–602. doi:10.1002/jmri.20662 (2006).
- 20. Duivenvoorden, R. *et al.* In vivo quantification of carotid artery wall dimensions: 3.0-Tesla MRI versus B-mode ultrasound imaging. *Circ Cardiovasc Imaging* **2**, 235–242. doi:10.1161/CIRCIMAGING.108.788059 (2009).
- 21. Ugron, Á. & Paál, G. On the boundary conditions of cerebral aneurysm simulations. *Periodica Polytechnica Mech Eng* **58**, 37–45. doi:10.3311/PPme.7392 (2014).
- 22. Taylor, C. A. & Steinman, D. A. Image-Based Modeling of Blood Flow and Vessel Wall Dynamics: Applications, Methods and Future Directions. *Ann Biomed Eng* **38**, 1188–1203. doi:10.1007/s10439-010-9901-0 (2010).
- 23. Remuzzi, A. *et al.* Radial artery wall shear stress evaluation in patients with arteriovenous fistula for hemodialysis access. *Biorheology* **40**, 423–430 (2003).
- 24. Simon, A. C., Levenson, J. & Flaud, P. Pulsatile flow and oscillating wall shear stress in the brachial artery of normotensive and hypertensive subjects. *Cardiovasc Res* **24**, 129–136. doi:10.1093/cvr/24.2.129 (1990).
- 25. Stroev, P. V., Hoskins, P. R. & Easson, W. J. Distribution of wall shear rate throughout the arterial tree: a case study. *Atherosclerosis* **191**, 276–280. doi:10.1016/j.atherosclerosis.2006.05.029 (2007).

- 26. Struijk, P. C. *et al.* Wall shear stress and related hemodynamic parameters in the fetal descending aorta derived from color Doppler velocity profiles. *Ultrasound Med Biol* **31**, 1441–1450. doi:10.1016/j.ultrasmedbio.2005.07.006 (2005).
- 27. Holdsworth, D. W., Norley, C. J., Frayne, R., Steinman, D. A. & Rutt, B. K. Characterization of common carotid artery blood-flow waveforms in normal human subjects. *Physiol Meas* **20**, 219–240. doi:10.1088/0967-3334/20/3/301 (1999).
- 28. Brooks, A. R., Lelkes, P. I. & Rubanyi, G. M. Gene expression profiling of human aortic endothelial cells exposed to disturbed flow and steady laminar flow. *Physiol Genomics* **9**, 27–41. doi:10.1152/physiolgenomics.00075.2001 (2002).
- 29. Malek, A. M., Alper, S. L. & Izumo, S. Hemodynamic shear stress and its role in atherosclerosis. *JAMA* **282**, 2035–2042. doi:10.1001/jama.282.21.2035 (1999).
- 30. Chatzizisis, Y. S., Coskun, A. U., Jonas, M., Edelman, E. R., Feldman, C. L. & Stone, P. H. Role of endothelial shear stress in the natural history of coronary atherosclerosis and vascular remodeling: molecular, cellular, and vascular behavior. *J Am Coll Cardiol* 49, 2379–2393. doi:10.1016/j.jacc.2007.02.059 (2007).
- 31. Potters, W. V., van Ooij, P., Marquering, H., vanBavel, E. & Nederveen, A. J. Volumetric arterial wall shear stress calculation based on cine phase contrast MRI. *J Magn Reson Imaging* **41**, 505–516. doi:10.1002/jmri.24560 (2015).
- 32. Van Ooij, P. *et al.* Wall shear stress estimated with phase contrast MRI in an in vitro and in vivo intracranial aneurysm: WSS in Intracranial Aneurysms. *J Magn Reson Imaging* **38**, 876–884. doi:10.1002/jmri.24051 (2013).
- 33. Mynard, J. P., Wasserman, B. A. & Steinman, D. A. Errors in the estimation of wall shear stress by maximum Doppler velocity. *Atherosclerosis* **227**, 259–266. doi:10.1016/j.atherosclerosis.2013.01.026 (2013).
- 34. Vlachopoulos, C., O'Rourke, M. & Nichols, W. W. McDonald's Blood Flow in Arteries: Theoretical, Experimental and Clinical Principles 6th ed., 768. doi:10.1201/b13568 (CRC Press, 2011).
- 35. Reneman, R. S., van Merode, T., Hick, P. & Hoeks, A. P. Flow velocity patterns in and distensibility of the carotid artery bulb in subjects of various ages. *Circulation* **71**, 500–509. doi:10.1161/01.CIR.71.3.500 (1985).







CHAPTER 6

The impact of scaled boundary conditions on wall shear stress computations in atherosclerotic human coronary bifurcations

Jelle T.C. Schrauwen¹, Janina C.V. Schwarz², Jolanda J. Wentzel¹, Antonius F.W. van der Steen^{1,3}, Maria Siebes², and Frank J. H. Gijsen¹

Department of Biomedical Engineering, Thorax Center, Erasmus Medical Center, Rotterdam, The Netherlands

Department of Biomedical Engineering and Physics, Academic Medical Center, Amsterdam, The Netherlands

³ Department of Imaging Physics, Delft University of Technology, Delft, The Netherlands

ABSTRACT

Aim

The aim of this study was to determine if reliable patient-specific wall shear stress (WSS) can be computed when diameter-based scaling laws are used to impose the boundary conditions for computational fluid dynamics. This study focused on mildly diseased human coronary bifurcations since they are predilection sites for atherosclerosis.

Methods

Eight patients scheduled for percutaneous coronary intervention were imaged with angiography. The velocity proximal and distal of a bifurcation was acquired with intravascular Doppler measurements. These measurements were used for inflow and outflow boundary conditions for the first set of WSS computations. For the second set of computations, absolute inflow and outflow ratios were derived from geometry-based scaling laws based on angiography data. Normalized WSS maps per segment were obtained by dividing the absolute WSS by the mean WSS value. Absolute and normalized WSS maps from the measured-approach and the scaled-approach were compared.

Results

A reasonable agreement was found between the measured and scaled inflows, with a median difference of 0.08 ml/s [-0.01; 0.20]. The measured and the scaled outflow ratios showed a good agreement: 1.5 percentage points [-19.0; 4.5]. Absolute WSS maps were sensitive to the inflow and outflow variations, and relatively large differences between the two approaches were observed. For normalized WSS maps, the results for the two approaches were equivalent.

Conclusions

This study showed that normalized WSS can be obtained from angiography data alone by applying diameter-based scaling laws to define the boundary conditions. Caution should be taken when absolute WSS is assessed from computations using scaled boundary conditions.

Keywords: coronary bifurcation, CFD, boundary conditions, scaling laws, shear stress

6.1 Introduction

Plaque development in coronary arteries is the underlying cause of stable angina and acute myocardial events. Predilection sites for plaque development are regions near bifurcations, which are exposed to low time-averaged wall shear stress (WSS). When a plaque grows and subsequently protrudes into the lumen, it will be exposed to different WSS patterns. At the location of the narrowing and proximal to that narrowing, the plaque is subjected to relatively high WSS. Evidence suggests that prolonged high WSS initiates processes that promote plaque destabilization. To study these processes in large patient groups, a tool that can compute WSS in a clinical setting would be valuable.

WSS can be obtained by performing flow simulations with computational fluid dynamics (CFD). The first requirement to perform CFD in coronary arteries is to obtain an accurate representation of the lumen geometry. During coronary interventions, angiography is the preferred imaging technique and thus routinely available. Recent advancements in the field of image reconstruction led to online techniques for the reconstruction of lumen geometry. Angiography-based reconstruction techniques are therefore an attractive possibility to generate three-dimensional (3D) lumen surfaces for WSS computations. ¹¹

The second requirement for CFD in coronary bifurcations is imposing appropriate boundary conditions at the inlet and outlets. Boundary conditions can be determined based on flow measurements. In previous studies the inflow boundary conditions were set using quantitative velocity measurements that were performed with catheter-based Doppler technique.^{7,8,12}

While Doppler velocity measurements provide absolute velocity data, they do require insertion of an additional catheter. It is also possible to use image-based modeling techniques to estimate flow boundary conditions. Diameter-based scaling laws directly relate flow to the diameter at specific locations. The scaling laws were first formulated by Murray¹³ who postulated that blood flow is proportional to the diameter to the power 3 based on the assumption of energy efficiency. Later studies found that the value of the power for the coronary vasculature ranged between 2 and 3 for the coronary system. ^{14–19} In the study by van der Giessen et al., ²⁰ empirical relations were found specifically for mildly diseased coronary bifurcations. These models are relatively simple and could prove to be effective alternative for invasive measurements in setting boundary conditions.

Whether these scaling laws are accurate enough to serve as boundary conditions, even in healthy arteries, is largely unknown. Application of these scaling laws in

diseased vessels is further compromised by the fact that changes in the resistance of the distal vascular bed due to atherosclerosis are not accounted for. Nonetheless, these models are frequently used as to determine boundary conditions in diseased coronary arteries. ^{21–25} Therefore, this study investigates whether diameter-based scaling laws can be applied to impose boundary conditions to accurately compute patient-specific WSS maps. We performed CFD simulations in mildly diseased human coronary bifurcations following two different methodologies: one with boundary conditions based on invasive velocity measurements and the other with boundary conditions derived from geometry-based scaling laws. This allowed for a direct comparison of the WSS resulting from the two approaches, and we determined whether angiography data alone is sufficient to obtain WSS data in mildly diseased human coronary bifurcations.

6.2 METHODS

6.2.1 Patient selection

The patient population used in this study was previously described in Nolte et al.²⁶ Briefly, patients with stable angina pectoris scheduled for percutaneous coronary intervention were included. From this population, patients were retrospectively selected when three requirements were met: first, adequate image quality of the angiographic data and the angular projections needed to generate a 3D reconstruction of a coronary bifurcation. Second, two locations of velocity measurement had to be proximal and distal of that bifurcation, without any side branches visible other than the bifurcation (Figure 6.1). Third, the velocity measurements were performed in an angiographically healthy segment. Ultimately, eight eligible cases were selected.

6.2.2 Geometry reconstruction

Angiography images were recorded with a Philips Integris H system (Philips Health-care, Best, The Netherlands). Two projections were selected that optimally visualized the region of interest with minimal foreshortening and at least 30° between the imaging angles. On the basis of those angiographic images 3D volumes of the coronary bifurcations were constructed using commercially available software (CAAS v3.11; Pie Medical Imaging, Maastricht, The Netherlands).

6.2.3 Velocity measurements

The velocity in the coronary arteries was measured by a catheter-based Doppler technique (Combowire XT, model 9500; Volcano, San Diego, CA). The wire was

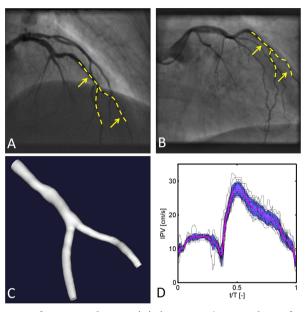


Figure 6.1: Overview of a patient dataset. **(A)** Angiography recording of a coronary bifurcation in the left anterior descending artery. The dashed lines indicate the region of interest. The 2 arrows point to the location where the velocity was measured. **(B)** 2nd angiography recording from a different angle allowing for a 3-dimensional (3D) reconstruction. **(C)** 3D reconstruction of the luminal surface of the coronary bifurcation. **(D)** Intravascular velocity measurement at the proximal location. The recordings of multiple consecutive heartbeats are normalized to the length of their cardiac cycle (T) and superimposed (black lines). The purple line is the average of the recordings per time point in the cardiac cycle, with the blue area around it indicating the standard deviation.

advanced into the coronary artery where it was manipulated to obtain optimal signals. Phasic recordings of maximal cross-sectional velocity were obtained at stable positions proximal and distal to a bifurcation. From these recordings, multiple consecutive heartbeats during rest with a stable signal were selected (Figure 6.1D); on average a period of 23 ± 14 heartbeats was used. From that period, the time-averaged velocity was calculated. Velocity data were combined with diameter measurements to obtain the flow rate. The local diameter was measured with conventional two-dimensional (2D) QCA at the location of the Doppler-wire tip in the same two projections as used for the 3D reconstruction. From the mean diameter of the two projections the cross-sectional area was determined, and by assuming a parabolic

velocity distribution the flow was computed. This methodology was followed to determine the flow in the mother branch $(\overline{q}_{\rm in})$ and in one daughter branch $(\overline{q}_{\rm out1})$. The flow through the second daughter branch $(\overline{q}_{\rm out2})$ was not measured but followed from conservation of mass.

6.2.4 Scaling laws

The flow through the inlet and daughter branches can be estimated with scaling laws. Van der Giessen et al.²⁰ derived two diameter-based scaling laws from a patient population with mild coronary artery disease. With the first scaling law the inflow was estimated and the second scaling law was used to estimate the outflow ratio. The first scaling law is defined as:

$$q_{\rm in} = 1.43 d_{\rm in}^{2.55},$$
 (6.1)

resulting in a flow (q) for the inlet. The diameter (d) and the velocity was measured at the same location in the mother branch. The second scaling law for the outflow ratio was defined as:

$$\frac{q_{\text{out2}}}{q_{\text{out1}}} = \left(\frac{d_{\text{out2}}}{d_{\text{out1}}}\right)^{2.27}.$$
(6.2)

The diameter d_{out1} was measured in the largest daughter branch and d_{out2} in the other daughter branch. The diameter of the daughter branch with the Doppler wire was determined at the location where the velocity was measured. In the other daughter branch the diameter was measured at an angiographically healthy section distal to the bifurcation near the ostium.

6.2.5 Computational fluid dynamics

Before the mesh generation, flow extensions were added to the 3D volumes (VMTK; Orbix, Bergamo, Italy). To ensure a smooth inlet profile for the CFD computations the inlet was extended with five times the radius. An outlet extension of five times the radius was added to exclude upstream effects due to the imposed boundary conditions. ²⁷ Meshes were built with commercially available software (ICEM v14.5; Ansys, Canonsburg, PA). A typical cell size of 0.1 mm was used and five prism layers at the wall were constructed. This resulted in a typical mesh size of 2×10^6 cells. Blood was modeled as a non-Newtonian fluid by applying a Carreau model with the parameters taken from Cho and Kensey. ²⁸ The density was set to 1060 kg/m^3 . The wall was modeled as rigid and a no-slip condition was imposed at the wall.

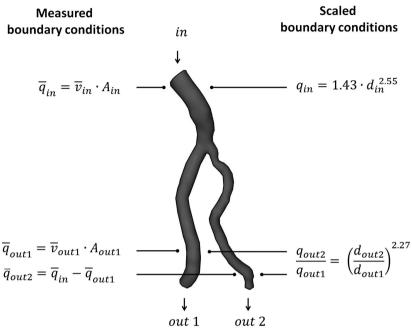


Figure 6.2: Cartoon illustrating the study setup. The inflow and outflow boundary conditions for wall shear stress (WSS) computations in mildly diseased coronary plaques were set by 2 different approaches. First, the measured boundary conditions were used, for which the flow is measured in the mother branch and in 1 daughter branch. The overbars indicate that a time-averaged value was used. Second, the scaled-approach was used, which sets the inflow and outflow conditions using diameter-based scaling laws.

A Poiseuille profile was prescribed at the inlet based on either the measured or the scaled flow rate (Equation 6.1, Figure 6.2). At the outlets of the two daughter branches either the measured or the scaled outflow ratio (Equation 6.2) was defined. Since the association of WSS with enhanced plaque vulnerability is based on time-averaged data we focused on steady flow simulations. ^{29–32} A finite volume solver was used to perform steady-state simulations using standard numerical techniques (Fluent v14.5; Ansys).

We performed two CFD simulations in 3D lumen reconstructions of all eight geometries. First, intravascular velocity measurements were imposed as boundary conditions at both the inlet and outlets. Subsequently, the boundary conditions for the same cases were assigned using diameter-based scaling laws based on geometry (Figure 6.2).

6.2.6 Data analysis

The WSS magnitude was extracted from the CFD results and mapped to a 2D coordinate system for further analysis. First the centerline was traced (VMTK; Orobix, Bergamo, Italy). Next, cross sections were defined at 0.45-mm intervals perpendicular to the centerline. The cross sections were partitioned in sectors of 22.5°, resulting in 16 bins between 2 sequential cross sections.²⁷ The mean WSS of each bin was used to construct the 2D map. The 2D maps of the mother and daughter branches were analyzed separately. The mean WSS in the axial and circumferential direction was calculated per branch. Next, a point-to-point comparison was performed with the data from the 2D WSS maps of the two approaches. A correlation plot was generated, with a linear fit going through the origin. By forcing the fit through zero, the correlation was characterized by a single quantity, coefficient k, the slope of the fit. A k-value equal to 1 indicates that the WSS results of both methodologies were similar. Complementary to that, the value of |1 - k| is used as a measure for the difference between the methods.

Normalized WSS was also investigated in addition to the absolute WSS. For the normalization procedure each 2D WSS map was normalized by its 50th percentile value.

6.2.7 Statistics

Summarized data are presented as the median and the 25th and 75th percentiles. A Spearman correlation test was used as a measure of agreement between the WSS resulting from the two methods. The outflow ratio over the outlet of the bifurcation is given in percentage of the total flow. The difference in outflow through a branch due to the different methods is therefore expressed in percentage points.

A noninferiority test was employed to find statistical evidence whether the two models provide outcome that can be regarded as equivalent.³³ In this test the null-hypothesis states that the absolute WSS difference between the two models is larger than a chosen margin, which was rejected at a significance level of $\alpha = 0.05$. In a previous report by Schrauwen et al.³⁴ the margin to test for differences was set to 0.25 Pa. This value was based on the resolution limitation of angiography and its effect on the precision of the computed absolute WSS. The margin for normalized WSS was set using the previously reported 1.3-Pa baseline value for WSS in coronary arteries.³⁵ By taking the ratio of 0.25 and 1.3 Pa, a margin of 0.2 was established for normalized WSS.

6.3 RESULTS

Figure 6.3A shows the measured diameter–flow relation for the mother branch and the daughter branch. The black line is the diameter–flow relationship derived by van der Giessen et al. 20 A similar behavior was found with a median inflow difference of 0.08 ml/s [-0.01; 0.20], although the measured flow in the mother branch tended to be higher than the scaled value. In the daughter branch, the difference between the measured and scaled flow was -0.01 ml/s [-0.04; 0.07]. The measured flow ratio is plotted as a function of the diameter ratio of the daughter branches in Figure 6.3B, with the black line representing the relationship found by van der Giessen et al. In six out of the eight cases, a good agreement was found: The median of the difference for all cases was 1.5 percentage points [-19.0; 4.5]. In two cases the measured flow ratio was above 1. Since $d_{\rm out1}$ was defined to be larger than $d_{\rm out2}$, this indicates that in these two cases more flow was going through the smaller daughter branch.

Figure 6.4 illustrates the WSS results for one case (arrow in Figure 6.3). In this case the measured and scaled inflow differed, with a measured flow of 0.55 ml/s and

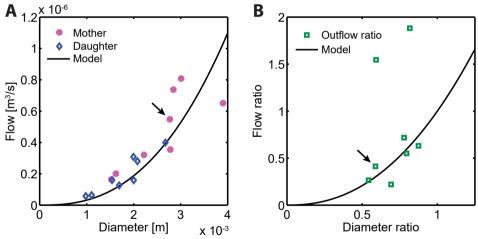


Figure 6.3: Hemodynamic data from the patient populations. **(A)** Measured diameter–flow relation in the mother branch (dots) and daughter branch (diamonds) of 8 patients. **(B)** Measured diameter ratio of the daughter branches vs. the measured flow ratio in those branches. On the x-axis the diameter ratio is defined as the smaller over the larger diameter of the daughter branches. The black lines in both panels plot the relationships derived by van der Giessen et al. The arrow indicates the measurement associated with the case described in Results and Figure 6.4.

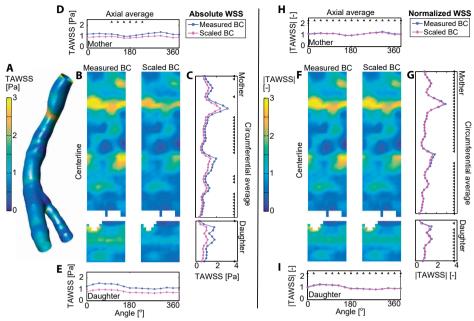


Figure 6.4: Overview of results for one case. The inflow was underestimated by the scaled approach, while the outflow ratios were similar. (A) 3D reconstruction of the geometry with color map indicating the WSS computed with measured boundary conditions (BC); TA, time averaged. (B) 2D maps of the computed absolute WSS with the 2 approaches. The maps of the mother branch and the daughter where the flow was measured are plotted. (C) Circumferential average of the absolute WSS in the two segments for the measured-approach (circles) and scaled-approach (diamonds). (D) Axial average in the mother branch of both methods. (E) Axial average of the daughter branch of both methods. (F) Normalized 2-dimensional (2D) WSS maps computed with the 2 methods. (G) Circumferential averages of the normalized WSS in the mother branch. (II) Axial average of the normalized WSS in the daughter branch.

a scaled flow of 0.43 ml/s. The outflow ratios for both approaches agreed nicely: 29%/71% with the measured approach and 23%/77% with the scaled approach. In Figure 6.4A the WSS computed with the measured-approach is plotted in 3D. Just distal of the inlet, the mother branch shows a lumen-intruding plaque, causing a region of high WSS. Halfway down the mother branch, a local widening of the lumen induces low WSS, immediately followed by a high WSS spot. As expected, higher WSS was found at the flow divider of the main daughter branch. The curvature of the segment is not very strong, leading to only minor asymmetries

Table 6.1: Overview of the percentage of area where the WSS outcome of the 2 models in axial and circumferential direction can be regarded as equal according to the noninferiority test

	Absolute WSS			Normalized WSS				
	Circun	nferential	A	xial	Circumferential		Axial	
Case	Mother	Daughter	Mother	Daughter	Mother	Daughter	Mother	Daughter
1	0	0	0	0	92	93	100	100
2	0	30	0	13	78	83	94	94
3	0	2	0	0	80	72	81	50
4	100	88	100	94	100	100	100	100
5	4	0	0	0	91	90	100	100
6	20	18	0	0	100	94	100	100
7	45	0	0	0	91	91	100	100
8	57	14	38	0	94	93	100	94
Median	12	8	0	0	92	92	100	100
IQR	[0;48]	[0; 21]	[0; 10]	[0;3]	[88; 96]	[88; 93]	[99; 100]	[94; 100]

The percentages are reported for both absolute and normalized wall shear stress (WSS). IQR, interquartile range.

in WSS distributions. The 2D representations of the WSS computed with both approaches are plotted in Figure 6.4B. In these maps the focal high WSS are clearly distinguishable. In both the mother and the daughter branch, the WSS from the scaled approach is lower than the WSS from the measured approach, due to the lower inflow but similar outflow ratio. The averaged WSS in Figure 6.4, C–E, confirmed these observations, with more pronounced differences at high WSS regions. The triangles indicate equal WSS values for both models based on the noninferiority test. Most sections show that the WSS was not equivalent.

In Figure 6.4, F–I, the results of the same cases are given after normalization to the 50th percentile of each branch. The 2D maps in Figure 6.4F show that the results were in good agreement. Also the circumferential and axial averaged normalized WSS values showed an excellent agreement between the results for the different boundary conditions. This was confirmed by the results of the noninferiority test.

Table 6.1 gives the percentage of area per branch where the WSS from both models was equal. The absolute WSS showed little agreement in nearly all the

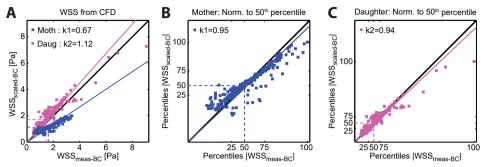


Figure 6.5: Quantitative comparison of the 2D WSS maps from the case in Figure 6.4. **(A)** Absolute WSS from the measured approach vs. the absolute WSS from the scaled approach. The WSS in the mother segment (blue) and daughter (pink) are plotted separately. The lines represent the linear fit through the data points and the origin. The coefficient k indicates the slope of the fit. CFD, computational fluid dynamics (CFD). **(B)** Normalized WSS in the mother branch from both methods ($r^2 = 0.88$). **(C)** Normalized WSS in the daughter branch from both methods ($r^2 = 0.92$). The black solid lines represent the line of identity and the dashed lines represent the 50th percentile values.

cases. In *case 4* the boundary conditions of the models matched exceptionally well, resulting in a high agreement. The normalized WSS shows that in all the cases a high agreement was found between the models.

The WSS data from the 2D maps of *case* 2 from Table 6.2 are plotted in Figure 6.5A. The linear fit through the WSS data in the mother branch resulted in a coefficient k = 0.67 for the slope, which indicates that the scaled approach underestimated the absolute WSS. In the daughter branch this was k = 1.12, demonstrating general overestimation of the WSS. The result after normalization in the mother branch is plotted in Figure 6.5B. A high agreement between the results was seen, as indicated by k = 0.95. Similarly, a high agreement (k = 0.94) was found in the daughter branch (Figure 6.5C). The median values of the coefficients (and [1st; 3rd quartile]) of the fits for all cases are given in Table 6.2. The much smaller interquartile range of k for the normalized WSS in the daughter vessel indicated that the agreement between the two approaches improved. Moreover, the median of the absolute difference of |1 - k| decreased from 0.35 [0.23; 0.40] to 0.04 [0.01; 0.05] for the mother vessel and from 0.31 [0.21; 0.43] to 0.05 [0.02; 0.06] for the daughter vessel. This decrease of |1 - k| indicates that the normalized WSS results were in much better agreement than the absolute WSS.

Table 6.2: Overview of k for all 8 cases

	Absolu	te WSS	Normalized WSS		
Case	Mother	Daughter	Mother	Daughter	
1	0.57	0.59	0.96	0.93	
2	0.67	1.12	0.95	0.94	
3	0.64	0.50	0.93	0.86	
4	1.20	1.25	1.01	1.01	
5	0.61	1.11	0.99	0.98	
6	0.77	1.24	0.99	1.00	
7	1.49	1.54	1.05	1.04	
8	0.78	0.63	0.96	0.95	
Median	0.72	1.12	0.98	0.97	
Quartiles	[0.63; 0.89]	[0.62; 1.24]	[0.96; 1.00]	[0.94; 1.00]	

This coefficient is indicative for the agreement between the WSS results from the 2 methods; when k equals 1, there is high agreement in the results.

With the Pearson correlation a high agreement was found for the mother and daughter branch in Figure 6.4: $r^2 = 0.88$ and $r^2 = 0.92$, respectively. In the other seven cases, the r^2 ranged between 0.90 and 1.00. These values did not change after normalization.

6.4 Discussion

We studied the WSS distribution in mildly diseased human coronary bifurcations using CFD. We applied boundary conditions for both the inlet and outlet derived from catheter-based invasive measurements. Additionally, the inflow and outflow boundary conditions were determined by combining diameter-based scaling laws with diameter measurements from angiographic images. Although in general a reasonable agreement was found for the inflow and a good agreement for the outflow ratio, the differences between the two approaches were considerable in some cases. These differences in the boundary conditions in turn led to differences in the computed absolute WSS values. However, after normalization to the 50th percentile an excellent agreement was found between the normalized WSS maps from the two approaches.

The diameter–flow relationship used in this study was derived by van der Giessen et al. For their derivation they used the measurements reported by Doriot et al.³⁶ In the study by Doriot et al., the velocity of the blood was measured in the mother and the two daughter branches of angiographically normal coronary bifurcations of patients suffering from coronary artery disease. These measurements showed a consistent behavior and a simple diameter-based scaling law could describe the diameter-flow relation.²⁰ We previously derived the outflow ratio of mildly diseased coronary bifurcations from computed tomography perfusion measurements and found a high agreement between the measured and the scaled outflow ratio.²⁷ The results in that study showed a homogeneous perfusion of the myocardium associated with the daughter branches of the bifurcations. In this study, the scaling laws generally worked well for the outflow ratio, but in some cases it led to relatively large discrepancies in the flow estimation. The deviations between the measured and scaled flow were most likely caused by differences in the resistance of the distal vascular bed. However, we could not identify these cases based on the angiography data, for instance, by using the area stenosis. As long as these cases cannot be identified with angiography, caution should be taken when employing diameterbased scaling laws to estimate boundary conditions, especially for the inflow in more diseased cases.

Many studies tried to correlate absolute WSS to a marker of atherosclerosis. 3,8,32 To compute WSS in geometries with multiple outlets, several studies rely on a form of scaling for setting the boundary conditions. ^{22,37–41} Van der Giessen et al. ²⁰ investigated how different outflow boundary conditions affect computed WSS values but could not incorporate patient-specific measurements to compare their results. Alternatively, Molony et al. 42 studied the effect of imposing patient-specific or scaled inflow boundary conditions on computed WSS. In a previous study, we investigated the effect of scaled outflow conditions on WSS computations at hyperemic conditions.²⁷ In our current study patient-specific measurements were available for both the inlet and outlet boundary conditions. The studies by van der Giessen et al.²⁰ and Molony et al.⁴² showed that the difference between measured and scaled boundary conditions can give rise to large difference in absolute WSS. In our study this was particularly striking at focal spots of high WSS, but areas exposed to decreased WSS can be misinterpreted as well. This could frustrate the search for a correlation between absolute WSS and an atherosclerotic marker. 43 On these grounds geometric scaling does not seem to be appropriate to accurately determine absolute WSS values in mildly diseased coronary bifurcations. The pointby-point comparison confirms these findings: a considerable difference between

the two approaches was shown, and although axial and circumferential averaging led to smaller differences, the noninferiority test demonstrated that they were not negligible.

The normalized WSS on the other hand was unaffected by the difference between the measured and scaled boundary conditions. It has been hypothesized that, instead of absolute WSS levels, the endothelium is sensitive to deviations from normal WSS values at baseline flow. 44 These deviations from the baseline WSS values might thus be a potential marker for the onset and progression of atherosclerosis and could be detected with normalized WSS maps. For instance, in a study by Gijsen et al. 7 normalized WSS levels were correlated to strain levels within plaques. The highest strains were found in regions exposed to high normalized WSS, which suggests that high WSS might be associated with plaque destabilization. The study by Eshtehardi et al. 45 found a relation between the lowest 25% of WSS and plaque phenotype development. Further studies are warranted to explore the effect of normalized WSS on markers of atherosclerosis in larger patient groups.

Our study showed that normalized WSS proved to be a robust measure, even in cases where the difference in outflow ratio was relatively large. This was also found by Marzo et al. 46 for cerebral aneurysms, but only qualitative results for normalized WSS were reported. This implies that, despite the nonlinear nature of flow phenomena, the flow in these cases was within a range that normalization still yielded similar results. This means that it would be possible to compute normalized WSS distributions from angiography data alone without the need for intravascular velocity measurements.

The hemodynamic significance of a coronary stenosis can be determined with fractional flow reserve (FFR), which is derived at hyperemic conditions. Several studies focused on computing FFR to replace invasive measurements. In a previous report we investigated the influence of scaled outflow conditions on the pressure drop and FFR during hyperemia. That study showed that the FFR was not influenced by the variation in outflow ratio. However, the absolute inflow is expected to have a greater effect on the overall pressure drop than the outflow ratio. Therefore the variations in inflow conditions could influence the computed FFR. In this study, baseline conditions were evaluated only, and it would be interesting to investigate in a subsequent study how scaled inflow affects FFR.

6.4.1 Limitations

For this study only a small number of patients were selected. Future studies with a larger patient population should confirm that diameter-based scaling laws in combination with angiography images are sufficient to determine normalized WSS distribution. It would be particularly interesting to include patients at a later stage of the disease that suffer from lumen intruding plaques. The intravascular Doppler measurements could not individually be verified and it is possible that the outcome differs at various time points. However, the intracoronary Doppler measurements were obtained by an experienced operator using state-of-the art technology during stable heart rate. A large body of evidence attests to the reliability and accuracy of this method, which has been extensively validated. 49,50

For the geometry reconstruction elliptical cross sections derived from two angiography images were used. Although this resulted in representative geometries, improvements can be made to acquire a more precise lumen representation, for instance by using rotational angiography. The goal of this study was to compare the influence of different boundary conditions. Since the same geometry was used to compute WSS with two different sets of boundary conditions, the use of angiography-based reconstructions should not affect the findings of this study.

The locations where the diameters were measured were selected by a trained reader. Nonetheless, Valen-Sendstad et al.⁵¹ showed that this choice can influence the computed absolute WSS. Based on angiography alone it remains difficult to select a healthy and representative section that can be used for the geometric scaling laws. However, this study demonstrates that normalized WSS will probably be more robust to the small deviations in diameters.

Finally, other parameters besides WSS are associated with atherosclerosis, such as the oscillatory shear index or the relative residence time, which depend on transient flow computations.⁵² Although the diameter-based outflow models proved effective in this study, more advanced outflow models are likely better suited for transient computations.

6.5 Conclusion

In conclusion, normalized WSS was shown to be unaffected by the variation in boundary conditions obtained either from invasive flow measurements or by applying diameter-based scaling laws. Caution should be taken when absolute WSS values are assessed from computations based on scaled boundary conditions.

Grants

This research was performed within a framework of the CARISMA Program of the technology foundation "Stichting Technische Wetenschappen." This research was funded by CARISMA Program Stichting Technische Wetenschappen (STW) Grant 11635.

Disclosures

No conflicts of interest, financial or otherwise, are declared by the author(s).

REFERENCES

- 1. Falk, E., Shah, P. K. & Fuster, V. Coronary plaque disruption. *Circulation* **92**, 657–671. doi:10.1161/01.cir.92.3.657 (1995).
- Nakazawa, G., Yazdani, S. K., Finn, A. V., Vorpahl, M., Kolodgie, F. D. & Virmani, R. Pathological findings at bifurcation lesions: the impact of flow distribution on atherosclerosis and arterial healing after stent implantation. *J Am Coll Cardiol* 55, 1679–1687. doi:10.1016/j.jacc.2010.01.021 (2010).
- 3. Wentzel, J. J., Chatzizisis, Y. S., Gijsen, F. J., Giannoglou, G. D., Feldman, C. L. & Stone, P. H. Endothelial shear stress in the evolution of coronary atherosclerotic plaque and vascular remodelling: current understanding and remaining questions. *Cardiovasc Res* **96**, 234–243. doi:10.1093/cvr/cvs217 (2012).
- 4. Slager, C. J. *et al.* The role of shear stress in the generation of rupture-prone vulnerable plaques. *Nat Clin Pract Cardiovasc Med* **2**, 401–407. doi:10.1038/ncpcardio0274 (2005).
- 5. Fujii, K. *et al.* Intravascular ultrasound profile analysis of ruptured coronary plaques. *Am J Cardiol* **98**, 429–435. doi:10.1016/j.amjcard.2006.03.020 (2006).
- 6. Gijsen, F. J., van der Giessen, A., van der Steen, A. & Wentzel, J. Shear stress and advanced atherosclerosis in human coronary arteries. *J Biomech* **46**, 240–247. doi:10.1016/j.jbiomech.2012.11.006 (2013).
- 7. Gijsen, F. J. *et al.* Strain distribution over plaques in human coronary arteries relates to shear stress. *Am J Physiol Heart Circ Physiol* **295**, H1608–H1614. doi:10.1152/ajpheart.01081.2007 (2008).
- 8. Samady, H. *et al.* Coronary artery wall shear stress is associated with progression and transformation of atherosclerotic plaque and arterial remodeling in patients with coronary artery disease. *Circulation* **124**, 779–788. doi:10.1161/CIRCULATIONAHA. 111.021824 (2011).

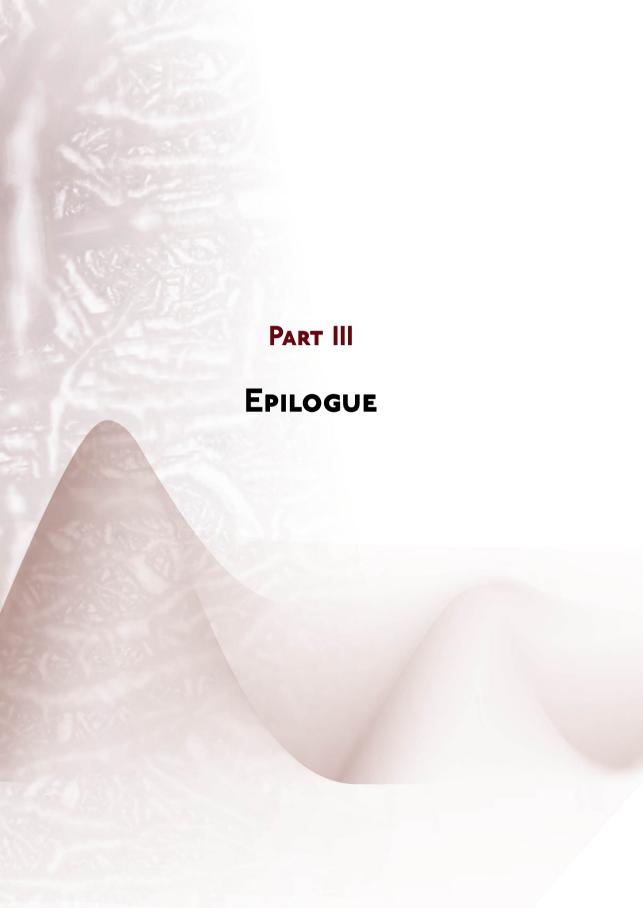
- 9. Girasis, C. *et al.* Advanced three-dimensional quantitative coronary angiographic assessment of bifurcation lesions: methodology and phantom validation. *EuroIntervention* **8**, 1451–1460. doi:10.4244/EIJV8I12A219 (2013).
- 10. Tu, S. *et al.* In vivo assessment of bifurcation optimal viewing angles and bifurcation angles by three-dimensional (3D) quantitative coronary angiography. *Int J Cardiovasc Imaging* **28**, 1617–1625. doi:10.1007/s10554-011-9996-x (2012).
- 11. Goubergrits, L., Wellnhofer, E., Kertzscher, U., Affeld, K., Petz, C. & Hege, H. C. Coronary artery WSS profiling using a geometry reconstruction based on biplane angiography. *Ann Biomed Eng* **37**, 682–691. doi:10.1007/s10439-009-9656-7 (2009).
- 12. Timmins, L. H. *et al.* Focal association between wall shear stress and clinical coronary artery disease progression. *Ann Biomed Eng* **43**, 94–106. doi:10.1007/s10439-014-1155-9 (2015).
- 13. Murray, C. D. The Physiological Principle of Minimum Work: I. The Vascular System and the Cost of Blood Volume. *Proc Natl Acad Sci U S A* **12**, 207–214. doi:10.1073/pnas.12.3.207 (1926).
- 14. VanBavel, E. & Spaan, J. A. Branching patterns in the porcine coronary arterial tree. Estimation of flow heterogeneity. *Circ Res* **71**, 1200–1212. doi:10.1161/01.res.71.5.1200 (1992).
- 15. Huo, Y. & Kassab, G. S. Intraspecific scaling laws of vascular trees. *J R Soc Interface* **9**, 190–200. doi:10.1098/rsif.2011.0270 (2012).
- 16. Kassab, G. S. Scaling laws of vascular trees: of form and function. *Am J Physiol Heart Circ Physiol* **290**, H894–H903. doi:10.1152/ajpheart.00579.2005 (2006).
- 17. LaBarbera, M. Principles of design of fluid transport systems in zoology. *Science* **249**, 992–1000. doi:10.1126/science.2396104 (1990).
- 18. Mittal, N. et al. Analysis of blood flow in the entire coronary arterial tree. Am J Physiol Heart Circ Physiol 289, H439-H446. doi:10.1152/ajpheart.00730.2004 (2005).
- 19. Molloi, S. & Wong, J. T. Regional blood flow analysis and its relationship with arterial branch lengths and lumen volume in the coronary arterial tree. *Phys Med Biol* **52**, 1495–1503. doi:10.1088/0031-9155/52/5/018 (2007).
- 20. Van der Giessen, A. G. *et al.* The influence of boundary conditions on wall shear stress distribution in patients specific coronary trees. *J Biomech* **44**, 1089–1095. doi:10.1016/j.jbiomech.2011.01.036 (2011).
- 21. Chaichana, T., Sun, Z. & Jewkes, J. Hemodynamic impacts of various types of stenosis in the left coronary artery bifurcation: a patient-specific analysis. *Phys Med* **29**, 447–452. doi:10.1016/j.ejmp.2013.02.001 (2013).

- 22. Joshi, A. K., Leask, R. L., Myers, J. G., Ojha, M., Butany, J. & Ethier, C. R. Intimal thickness is not associated with wall shear stress patterns in the human right coronary artery. *Arterioscler Thromb Vasc Biol* **24**, 2408–2413. doi:10.1161/01.ATV.0000147118.97474.4b (2004).
- 23. Rikhtegar, F., Wyss, C., Stok, K. S., Poulikakos, D., Muller, R. & Kurtcuoglu, V. Hemodynamics in coronary arteries with overlapping stents. *J Biomech* 47, 505–511. doi:10.1016/j.jbiomech.2013.10.048 (2014).
- 24. Soulis, J. V., Farmakis, T. M., Giannoglou, G. D. & Louridas, G. E. Wall shear stress in normal left coronary artery tree. *J Biomech* **39**, 742–749. doi:10.1016/j.jbiomech.2004.12.026 (2006).
- 25. Zhang, J. M. *et al.* Numerical simulation and clinical implications of stenosis in coronary blood flow. *Biomed Res Int* **2014**, 514729. doi:10.1155/2014/514729 (2014).
- 26. Nolte, F. *et al.* Functional coronary stenosis severity assessed from the mean pressure gradient-velocity relationship obtained by contrast medium-induced submaximal hyperaemia. *EuroIntervention* **10**, 320–328. doi:10.4244/EIJV10I3A55 (2014).
- 27. Schrauwen, J. T. C. *et al.* Functional and anatomical measures for outflow boundary conditions in atherosclerotic coronary bifurcations. *J Biomech* **49**, 2127–2134. doi:10.1016/j.jbiomech.2015.11.036 (2016).
- 28. Cho, Y. I. & Kensey, K. R. Effects of the non-Newtonian viscosity of blood on flows in a diseased arterial vessel. Part 1: Steady flows. *Biorheology* **28**, 241–262. doi:10.3233/bir-1991-283-415 (1991).
- 29. Feldman, C. L., Ilegbusi, O. J., Hu, Z., Nesto, R., Waxman, S. & Stone, P. H. Determination of in vivo velocity and endothelial shear stress patterns with phasic flow in human coronary arteries: A methodology to predict progression of coronary atherosclerosis. *Am Heart J* **143**, 931–939. doi:10.1067/mhj.2002.123118 (2002).
- 30. Johnston, B. M., Johnston, P. R., Corney, S. & Kilpatrick, D. Non-Newtonian blood flow in human right coronary arteries: transient simulations. *J Biomech* **39**, 1116–1128. doi:10.1016/j.jbiomech.2005.01.034 (2006).
- 31. Myers, J. G., Moore, J. A., Ojha, M., Johnston, K. W. & Ethier, C. R. Factors influencing blood flow patterns in the human right coronary artery. *Ann Biomed Eng* **29**, 109–120. doi:10.1114/1.1349703 (2001).
- 32. Stone, P. H. *et al.* Prediction of progression of coronary artery disease and clinical outcomes using vascular profiling of endothelial shear stress and arterial plaque characteristics: the PREDICTION Study. *Circulation* **126**, 172–181. doi:10.1161/CIRCULATIONAHA.112.096438 (2012).
- 33. Walker, E. & Nowacki, A. S. Understanding equivalence and noninferiority testing. *J Gen Intern Med* **26**, 192–196. doi:10.1007/s11606-010-1513-8 (2011).

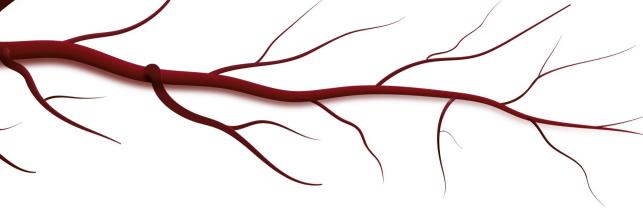
- 34. Schrauwen, J. T. *et al.* Influence of the Accuracy of Angiography-Based Reconstructions on Velocity and Wall Shear Stress Computations in Coronary Bifurcations: A Phantom Study. *PLoS One* **10**, e0145114. doi:10.1371/journal.pone.0145114 (2015).
- 35. Wentzel, J. J. *et al.* In vivo assessment of the relationship between shear stress and necrotic core in early and advanced coronary artery disease. *EuroIntervention* **9**, 989–995. doi:10.4244/EIJV9I8A165 (2013).
- 36. Doriot, P. A., Dorsaz, P. A., Dorsaz, L., De Benedetti, E., Chatelain, P. & Delafontaine, P. In-vivo measurements of wall shear stress in human coronary arteries. *Coron Artery Dis* **11**, 495–502. doi:10.1097/00019501-200009000-00008 (2000).
- 37. Gijsen, F. J., Schuurbiers, J. C., van de Giessen, A. G., Schaap, M., van der Steen, A. F. & Wentzel, J. J. 3D reconstruction techniques of human coronary bifurcations for shear stress computations. *J Biomech* 47, 39–43. doi:10.1016/j.jbiomech. 2013.10.021 (2014).
- 38. Li, Y. *et al.* Impact of Side Branch Modeling on Computation of Endothelial Shear Stress in Coronary Artery Disease: Coronary Tree Reconstruction by Fusion of 3D Angiography and OCT. *J Am Coll Cardiol* **66**, 125–135. doi:10.1016/j.jacc. 2015.05.008 (2015).
- 39. Malve, M. *et al.* Tortuosity of coronary bifurcation as a potential local risk factor for atherosclerosis: CFD steady state study based on in vivo dynamic CT measurements. *Ann Biomed Eng* **43**, 82–93. doi:10.1007/s10439-014-1056-y (2015).
- 40. Sommer, K., Schmidt, R., Graafen, D., Breit, H. C. & Schreiber, L. M. Contrast agent bolus dispersion in a realistic coronary artery geometry: influence of outlet boundary conditions. *Ann Biomed Eng* **42**, 787–796. doi:10.1007/s10439-013-0950-z (2014).
- 41. Wellnhofer, E., Osman, J., Kertzscher, U., Affeld, K., Fleck, E. & Goubergrits, L. Flow simulation studies in coronary arteries—impact of side-branches. *Atherosclerosis* 213, 475–481. doi:10.1016/j.atherosclerosis.2010.09.007 (2010).
- 42. Molony, D. S., Timmins, L. H., Hung, O. Y., Rasoul-Arzrumly, E., Samady, H. & Giddens, D. P. An assessment of intra-patient variability on observed relationships between wall shear stress and plaque progression in coronary arteries. *Biomed Eng Online* 14, S2. doi:10.1186/1475-925X-14-S1-S2 (2015).
- 43. Peiffer, V., Sherwin, S. J. & Weinberg, P. D. Does low and oscillatory wall shear stress correlate spatially with early atherosclerosis? A systematic review. *Cardiovasc Res* **99**, 242–250. doi:10.1093/cvr/cvt044 (2013).

- 44. Cheng, C. *et al.* Large variations in absolute wall shear stress levels within one species and between species. *Atherosclerosis* **195**, 225–235. doi:10.1016/j.atherosclerosis. 2006.11.019 (2007).
- 45. Eshtehardi, P. *et al.* Association of coronary wall shear stress with atherosclerotic plaque burden, composition, and distribution in patients with coronary artery disease. *J Am Heart Assoc* **1**, e002543. doi:10.1161/JAHA.112.002543 (2012).
- 46. Marzo, A. *et al.* Computational hemodynamics in cerebral aneurysms: the effects of modeled versus measured boundary conditions. *Ann Biomed Eng* **39**, 884–896. doi:10.1007/s10439-010-0187-z (2011).
- 47. Morris, P. D., van de Vosse, F. N., Lawford, P. V., Hose, D. R. & Gunn, J. P. "Virtual" (Computed) Fractional Flow Reserve: Current Challenges and Limitations. *JACC Cardiovasc Interv* 8, 1009–1017. doi:10.1016/j.jcin.2015.04.006 (2015).
- 48. Taylor, C. A., Fonte, T. A. & Min, J. K. Computational fluid dynamics applied to cardiac computed tomography for noninvasive quantification of fractional flow reserve: scientific basis. *J Am Coll Cardiol* **61**, 2233–2241. doi:10.1016/j.jacc. 2012.11.083 (2013).
- 49. Doucette, J. W. *et al.* Validation of a Doppler guide wire for intravascular measurement of coronary artery flow velocity. *Circulation* **85**, 1899–1911. doi:10.1161/01.cir.85.5.1899 (1992).
- 50. Siebes, M., Verhoeff, B.-J., Meuwissen, M., de Winter, R. J., Spaan, J. A. & Piek, J. J. Single-Wire Pressure and Flow Velocity Measurement to Quantify Coronary Stenosis Hemodynamics and Effects of Percutaneous Interventions. *Circulation* 109, 756–762. doi:10.1161/01.cir.0000112571.06979.b2 (2004).
- 51. Valen-Sendstad, K., Piccinelli, M., KrishnankuttyRema, R. & Steinman, D. A. Estimation of inlet flow rates for image-based aneurysm CFD models: where and how to begin? *Ann Biomed Eng* **43**, 1422–1431. doi:10.1007/s10439-015-1288-5 (2015).
- 52. Lee, S. W., Antiga, L. & Steinman, D. A. Correlations among indicators of disturbed flow at the normal carotid bifurcation. *J Biomech Eng* **131**, 061013. doi:10.1115/1.3127252 (2009).









CHAPTER 7

General Discussion

Over the past decades, the importance of the vasculature beyond the large arteries for cardiovascular pathologies became more evident. Aside from atherosclerosis of the large coronary arteries with concomitant typical complaints such as chest pain, some patients with visible lesions are complaint-free. Others without any visible atherosclerosis, on the other hand, do experience complaints, highlighting the complexity of cardiovascular disease. Local malfunctioning can affect remote locations; the network structure affects the hemodynamics and vice versa. The overall objective of this thesis was to advance the understanding of the role of hemodynamic factors in arterial network design. Our findings on reconstructing arterial networks over multiple scales are discussed below, where the highly dynamic environment of (remodeling) collateral vessels will be considered in more detail. Future directions and conclusions conclude this chapter.

7.1 EXPERIMENTAL DATA FOR ARTERIAL NETWORK RECONSTRUCTION

Chapter 1 explains how arterial network design determines hemodynamic variables such as local pressure, flow, and shear stress. It also indicates how such local factors in turn are thought to influence the network design. Since comprehension of this interplay by means of modeling requires sound data, several possibilities for acquiring such data are described in Chapter 2. Importantly, predicting hemodynamics at any specific scale (no matter whether large vessels or microcirculation) requires a model for network morphology over the full range of arterial diameters. While this consequence of Ohm's and Kirchhoff's laws (Chapter 1) may seem obvious to most engineers, we have experienced that clinicians in the cardiovascular field quite frequently find this concept difficult to grasp.

As was pointed out in Chapter 2, in vivo imaging of arterial structures lacks sufficient resolution for reconstruction of the full arterial network and subsequent modeling of hemodynamics based on such reconstructions. Microscopic techniques, on the other hand, do provide sufficient resolution but only over a limited sampling volume, with additional concerns for in vivo imaging. We evaluated the imaging cryomicrotome as a modality for obtaining whole-organ data at a resolution well beyond the clinical modalities. By alternating cutting and taking images of the surface of the remaining bulk, the imaging cryomicrotome provides image stacks of 4096×4096 pixel at resolutions ranging from 5 to 40 μ m. The applications described in various chapters demonstrate the large potential but also make clear that many pitfalls exist, including a still limited resolution and sampling volume. This raises the

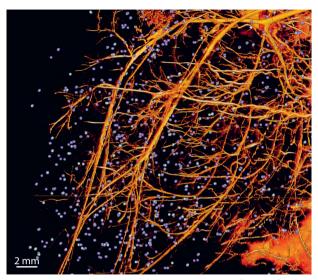


Figure 7.1: Three-dimensional rendering of the vascular cast (orange) of a rat hindlimb and two colors of microspheres (glacier, purple), demonstrating the feasibility of the imaging cyromicrotome to concurrently image the arterial network together with markers of perfusion.

question whether other modalities could have been chosen for the current studies. With generated volumes of typically 500³ to 2000³ voxels, micro-CT also allows imaging over fairly large sampling volumes with a resolution of 50 μm. 1,2 Such resolution allows imaging of human atria.³ Stephenson et al. imaged whole human hearts ex vivo at a resolution of 73 µm, 4 about half the resolution we obtained with the imaging cryomicrotome (Chapter 4). For both the imaging cryomicrotome and micro-CT, resolution can be increased at the cost of a smaller sampling volume, achieving spatial resolutions of 1 to 10 µm for sample volumes of approximately 1 cm³. While micro-CT provides a similar resolution and leaves the tissue intact, the imaging cryomicrotome allows imaging of larger volumes and at multiple wavelengths. We used this advantage to combine structural data with microsphere deposition for local perfusion estimation (Chapter 2 and Figure 7.1) and molecular imaging. One possibility that remains to be explored is the combination of the cryomicrotome data with high resolution (confocal or multiphoton) microscopic data. Such an approach would require very extensive microscopic imaging and a thorough a priori understanding of local differences but would have allowed a better evidence-based generation of the distal networks in Chapter 4.

7.1.1 Vascular casting for fluorescence cryomicrotome imaging

The strength of the imaging cryomicrotome, generation of high-resolution 3D structural information, was demonstrated in Chapter 4, where the entire arterial network of a human heart could be reconstructed with a voxel size of $(30 \, \mu m)^3$. Filling the vessels with casting material prior to image acquisition proved challenging. Cryomicrotome imaging relies critically on proper filling, similar to ex vivo micro-CT. While this seems a mere technical issue, the dominant role of this methodology in the work described in this thesis calls for some discussion here.

Vascular casting with Batson's no. 17 yielded good results in large organs, e.g., canine, porcine, and human hearts, ^{7,8} but we encountered difficulties with filling small animal vasculature. This point was addressed in Chapter 3, where our objective was filling as needed for a replication of the in vivo morphology with accurate diameters, lengths, and branch angles. Based on this goal, the ideal filling compound would have fulfilled the following criteria: ^{9,10}

- 1. It fills all vessels of interest including small connections.
- 2. Filling of vessels smaller than the spatial resolution is minimal.
- 3. It hardens evenly and timely.
- 4. It does not extravasate.
- 5. Shrinkage after solidification is minimal. It does not alter the quantitative morphology of the vessels from in vivo dimensions.
- 6. It is visible at a wavelength used by the imaging methodology (and different from wavelengths used by other compounds)
- 7. It provides sufficient fluorescence signal for all vessels of interest.

While no material was found that satisfied all these requirements, perfusion with a substance that subsequently polymerizes into a solid (vascular casting) was chosen as our preferred method among the various filling techniques, as cryomicrotome imaging inherently relies on cutting a solid, non-elastic sample. Vascular casting moreover has a long history in studying the geometry of arterial networks and endothelial morphology.¹¹

In addition to the degree of wanted and unwanted (e.g., capillary and venous) filling, we would like to reiterate the importance of faithfully replicating the in vivo architecture for hemodynamic modeling and studies on network design. Since the vessel diameters strongly depend on local pressure, we aimed to replicate the in vivo pressure distribution. Controlled injection at physiological pressure (taking into consideration the pressure drop over narrow cannulas) theoretically provides the best approximation of the in vivo pressure distribution independent of the viscosity of

the perfusate, but causes slow flow rates of the commonly viscous cast materials. In Chapter 3, we encountered problems with injection of Batson's compound no. 17 at physiological pressure, which resulted in incomplete filling of the microcirculation. This can be explained by the high viscosity of Batson's no. 17 (about 260 cP $^{12-14}$), resulting in a theoretically 65-to-90-times lower flow rate than blood. With progressing polymerization and concomitantly rising viscosity, flow progressively slows down during the course of filling. We have even encountered premature flow cessation. Although polymerization could be delayed by reducing the amount of added promoter and catalyst or by cooling, gradual onset of polymerization typically began within minutes after start of injection. Similar to findings reported by Levesque et al. 11, we have observed a quicker polymerization of small than of large volumes, which likely further impeded the filling of the microcirculation. Casting of the microcirculation is feasible using high injection pressures but at the cost of skewing the pressure distribution with high intravascular pressures possibly rupturing vessels or amplifying extravasation of the compound. High injection pressures should thus be avoided for faithful reconstruction of entire networks. Similarly, flow-controlled injection would bias the morphometry. By lowering the viscosity, either by diluting Batson's no. 17 with methyl methacrylate (MMA) or by using Mercox (viscosity 20–30 cP¹⁵), we could fill small vessels while maintaining a physiological injection pressure. We avoided strong (>50%) dilutions as less pre-polymerized mixtures exhibit more shrinkage and the resulting capillary and venous filling complicates the subsequent image analysis.

Some of the studies described in this thesis addressed the development of collaterals after experimental flow blockage. Flow in innate collaterals is usually very low and bidirectional and thus poses a particular challenge for filling. The low flow conditions necessitate filling with a compound of low viscosity. However, even when using materials of low viscosity, some collateral vessels in our experiments filled from either side with a void region in the middle, which was not or only sparingly reached by the cast material (Figure 7.2). When the objective is to investigate collateral vessels, filling with materials of low viscosity and with slow polymerization is thus advisable.

7.1.2 Image reconstruction

The imaging and image analysis procedures form an essential part of the work underlying this thesis. Cryomicrotome imaging suffers from various imaging artifacts such as optical blurring, camera noise, and stuck cutting debris. Since these

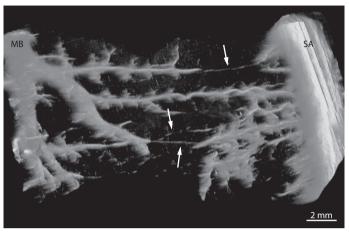


Figure 7.2: Uneven filling of the gracilis network of a healthy rat hindlimb, where regions of low flow are characterized by only marginal filling (arrows). Please note that the signal was amplified in order to visualize this filling. MB = muscular branch, SA = saphenous artery.

challenges formed an integral part of the research work, some of these aspects warrant a discussion here. Image blurring originates from two sources: the response of the optical system and scattering and attenuation of light within the sample. In order to quantify the blurring, we imaged microspheres smaller than the resolution under various conditions (different colors, spatial resolution, surrounding material). This revealed that the largest contribution comes from the scattering within the sample rather than the blurring due to the optical system. The microspheres were already visible several slices before they appeared at the cutting surface, such that they were visualized as comets with long halos over several slices in 3D. We have also noted some variation with tissue type and wavelength. For simplification, we established a standard point spread function (PSF), the system response to a point source, from multiple microspheres in cardiac tissue. This basic PSF was adapted to each individual sample by scaling to resolution followed by blind deconvolution. In our experience, blockwise deconvolution with such a matched PSF corrected the blurring reasonably well at moderate computational costs. Slice-by-slice removal of the transparency is a simple alternative method for halo removal¹⁶ but does not correct the in-plane blur. A more precise approach would be to inject microspheres of at least two different colors and use these for estimation of the local tissue properties. 17 From this, the local PSFs for the cast material, which differs in excitation/emission

wavelength, could be extrapolated. While feasible, this approach comes at higher computational costs and possibly overfitting.

After correction of the imaging artifacts, segmentation of the arterial network formed the next integral challenge. The simplest form of image segmentation, thresholding, previously provided good reconstructions of large arterial networks but proved insufficient for small animal vasculature. Prior to the actual vessel segmentation, we thus applied multiscale vesselness filtering to enhance the signal of the vessels. While Frangi's method¹⁸ better delineated curvilinear structures, Sato's filter¹⁹ behaved better at junctions, and in view of retaining connectivity we opted for the latter. Sato's filter, however, tended to merge nearby structures such that regions with filled parallel artery—vein pairs could not accurately be automatically segmented. Also, for large arteries (about one millimeter or larger) simple thresholding of the downsampled data set followed by manual inspection to correct for cutting artifacts was superior. By combination with the vesselness result for smaller vessels, we obtained detailed reconstructions of the arterial network at reasonable manual effort.

7.1.3 Improvements of the imaging cryomicrotome

At this time, several of the steps require manual interaction. To improve reproducibility, it would be desirable to automatize the image processing. One major challenge was the discrimination between (especially nearby) arteries and veins. As indicated above, venous filling is difficult to prevent in cases where low viscosity of the casting material is needed. We speculate that intravascular staining could help discrimination in this case. Intravascular staining typically labels the endothelium, for example with fluorescently conjugated isolectin GS-IB4²⁰ or by vessel painting with the lipophilic dye 1,1-Dioctadecyl-3,3,3,3-tetramethy-lindocarbocyanine perchlorate (DiI).²¹ Combination of such staining with a casting material selective for arteries, e.g., undiluted Batson's no. 17, could help arterial versus venous discrimination while reducing the risk of missing collateral vessels. Some DiI dyes furthermore appear to not or only weakly stain veins and venules, ^{22,23} potentially providing a direct means of arterial demarcation. Ideally, molecular markers suitable for perfusion and specific for arterial versus venous endothelial cells would help discrimination.

In addition, molecular markers of active remodeling could aid in the detection of collateral vessels and furthermore provide functional information. We tested three markers, anti-intercellular adhesion molecule-1 (ICAM-1), chemokine (C-X-C

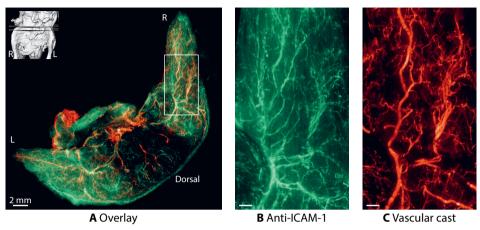


Figure 7.3: Representative example of combined imaging of the molecular marker anti-ICAM-1 with vascular cast in a sham operated mouse. Anti-ICAM-1 was abundantly found throughout the animal, indicating non-specific binding. The images are maximum intensity projection over a slab of 2.6 mm as indicated on the upper left of **(A)**. **(B,C)** Enlargements of the region delineated by the box in **(A)**.

motif) ligand 1 (CXCL1), and Evasin-3, but unfortunately none proved to be both sensitive and specific. Anti-ICAM-1 was abundantly found throughout the entire vasculature (Figure 7.3) indicating non-specific binding, whereas CXCL1 and Evasin-3 were limited to a small region separate from the classical collateral pathways. Altogether, there is still much work to do with respect to combination of the vascular morphology measurements and molecular readouts of endothelial phenotype.

With improvements in computational power, more sophisticated processing methods might become feasible for such large data sets as created by cryomicrotome imaging. Possible improvements include the deblurring of the entire sample volume at once and the use of other segmentation algorithms. While vesselness-based techniques typically perform well,²⁴ they are sensitive to noise and gaps in the vessel casts. This might be improved with sophisticated seed-point based approaches, vessel tracking, or machine learning.^{25,26} Additionally, it would be advisable to validate the entire procedure by comparing the reconstructed network against a known structure. Potentially, fluorescent 3D-printing of computer-generated arterial trees could be of assistance here.

For a better understanding of the interaction of structure and function in collateral development and also of arterial networks in general, hemodynamic simulations can complement structural assessments. For more accurate hemodynamic modeling, future work is needed to incorporate a better representation of the most distal microcirculation, including the capillary and venular network. Could it become possible to image the entire coronary circulation of a human heart at say 1 µm resolution, such that the full capillary bed is covered, and could image reconstructions allow discrimination between arteries and veins based on the availability of the complete connectivity? Compared to the current 30 µm voxel size in the human heart study (Chapter 4), this would require roughly 10 000 times larger datasets, and likely an even much larger scaling in computational efforts for image analysis. Based on Moore's law, stating a doubling of computer power every two years, this might become feasible in 10 to 20 years. While the resolution of the 3D imaging cryomicrotome can be improved and a rise in computational power will enable image analysis of larger data sets, many other issues would remain, e.g., related to the image sensors, fluorescence intensity and distribution as well as associated imaging times. Multi-scale efforts will therefore be needed, based on combinations of imaging technologies with incorporation of high-resolution data that is carefully sampled based on the spatial variation. Moreover, validation of the hemodynamic network models requires independent data. In particular, flow measurements are needed here, and these can be based on intravital microscopy or (molecular) flow tracers in animal studies. We foresee that in iterative work over the coming years, technological progress and improved understanding of vascular network design will help closing the gap between the largest arteries and capillaries in our models combining vascular structure and function.

7.2 Properties of arterial networks

7.2.1 Branching rules

Branching rules have a long history as a base for such models. In Chapter 1, we explained how branching rules are thought to reflect network design. Branching rules are typically formulated as power relations, the so-called scaling laws, with an allometric scaling exponent (α) in the order of 2 (constant cross-sectional area) to 3 (in accordance with but not proving constant wall shear stress). In Chapter 4, we found that the human coronary branching pattern was not uniform but rather changed from asymmetric branching with small α in large coronaries to symmetric bifurcations with larger α in small arterioles. We used network simulation to derive

similar scaling laws for diameter–flow relations, rendering exponents that averaged 2.6 in the major arteries to 3.2 in the arterioles. There was also reasonable agreement between measured flow and flow predicted from a scaling law with $\alpha=2.55$ in mildly diseased human coronary arteries based on angiographic reconstruction (Chapter 6). Our results corroborate the concept of arterial networks stochastically following scaling laws but with considerable spread and monotonically increasing exponents towards the microcirculation, thus rather $E[y] \propto x^{\alpha(d)}$ than $y \propto x^{\alpha}$. In this relation, y and x have to be substituted depending on the specific scaling law. Typical examples include flow–diameter, crown volume – diameter, crown length – crown volume and distal myocardial mass – cross-sectional area relationships.

7.2.2 Application of scaling laws

Scaling laws can be applied wherever network parts are missing and need to be modeled, in particular for simulation of coronary hemodynamics. In Chapter 4, we used extrapolated branching characteristics to simulate the distal microcirculation below the spatial resolution and could thereby apply uniform outlet conditions (capillary pressure). In Chapter 6, a diameter-flow relation was used as outlet boundary condition for computational fluid dynamics (CFD) simulations of coronary bifurcations. Similar concepts could assist in estimating the outflow boundary conditions in patient-specific models for diagnosis. One method that applies such simulation is CT-derived fractional flow reserve (FFR_{CT}), which non-invasively assesses functional stenosis severity. Such noninvasive FFR computations rely on scaling laws for deriving rest myocardial flow from myocardial mass and for estimation of the downstream resistances from outlet diameters, for example.²⁷ We wonder thus how much the stochastic variation in the scaling exponent that we have observed would obfuscate the diagnostic certainty in addition to other assumptions, e.g., with respect to the hyperemic response of the microcirculation. A first study suggests that uncertainty in resistance is of less importance than the uncertainty in geometric reconstruction of the vessels.²⁸ In this study, total hyperemic downstream resistance was adjusted by matching FFR_{CT} to invasively measured FFR, neglecting deviations of the individual downstream networks. Even though this agrees with our observation that intra-patient variation from the patient-specific scaling law of coronary downstream resistance has only limited impact on median pressure (Chapter 4), we expect a higher inter-patient variation from the generalized scaling law. We postulate that the uncertainty (σ) in total resistance (R) of a segment of diameter d and its downstream arterial network roughly scales with

 $\sigma_R \approx R|ln(d)|\sigma_\alpha + \frac{\alpha}{d}\sigma_d$. However, to what extent this uncertainty and deviations associated with microvascular disease influence the FFR prediction still remains to be elucidated.

7.2.3 WSS and structure

Hemodynamic simulation of a reconstructed human heart refuted the paradigm of constant wall shear stress (Chapter 4); the simulated wall shear stress was non-uniform and highly variable. Even though these estimates can strongly be influenced by errors in diameter, it is unlikely that such large dispersion was solely caused by such errors. A multifactorial design might explain non-uniform wall shear stress. Which factors could contribute? In human carotid arteries, we observed a negative correlation between mean wall shear stress and wall thickness after adjustment for systolic blood pressure (Chapter 5). Temporal variation as represented by shear stress pulsatility and proportion of flow reversal, however, were positively correlated with wall thickness. It thus seems that shear stress is a main driver, but that temporal patterns and interaction with pressure effects are involved too, and that both inner diameter and wall thickness should be considered when describing vascular adaptation, ²⁹ not only in these carotid arteries, where the variation is possibly pathological (endothelial dysfunction and initial neo-intima formation) but also in healthy microvascular networks.

The situation is different in the microvascular network, which is not a simple treelike structure. It is well appreciated that control by shear stress alone does not allow maintenance of the loops and collateral connections seen in many vascular beds.³⁰ Since these connections provide robustness for flow maintenance upon progression of local obstructions and since there is a wide individual variation of collateralization, understanding the development, maintenance, and adaptation of these collaterals is highly relevant.

7.3 COLLATERAL VESSELS

The general understanding of collateral vessels is that of natural bypasses connecting two arterial (sub)trees as sketched in Figure 7.4.³¹ These can be either arteriole-to-arteriole or artery-to-artery connections, which remodel into tortuous arteries in response to chronic obstructions that can be detected by X-ray, magnetic resonance and CT angiography. The limited spatial resolution, however, leaves the question as to what extent the increased collateralization seen in chronic obstructive disease is due to formation of new collaterals, outgrowth of existing ones, or merely increased

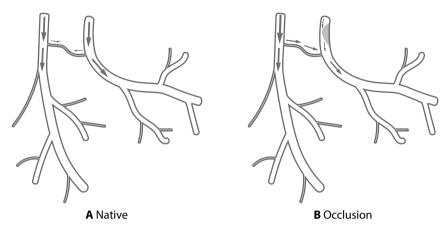


Figure 7.4: A collateral connecting two arterial trees carries little (bidirectional) flow in the native bed **(A)** but provides a backup route in case of an obstruction **(B)**. The arrows indicate flow direction and magnitude.

filling by contrast in the imaging time window due to the higher collateral flow. By high-resolution imaging with the imaging cryomicrotome, we aimed to get a better understanding of the structural adaption of collateral vessels in response to an upstream occlusion.

7.3.1 Characteristics of the gracilis collaterals

In Chapter 3, we stimulated collateral adaptation in rat hindlimbs by femoral artery ligation. The gracilis collaterals typically consisted of two to four main branches connecting the muscular branch of the femoral artery to the saphenous artery. These main branches were interconnected in some animals and frequently gave rise to subloops. The individual topology greatly differed between animals though.

In the native arterial network, the gracilis collaterals tapered towards the midzone and impressed with numerous side branches, corroborating their role as perfusers for the local tissue (Figure 7.5A). These side branches were surprisingly regularly distributed and aligned to each other and also appeared to be maintained during collateral remodeling. In addition to the typical overall increase in arterial diameter and tortuosity with ischemia duration, our data indicated a stronger diameter increase at the re-entry zone, where flow reversed, compared to the stem zone, where flow direction was conserved. Since there was a high heterogeneity in network topologies which complicated inter-animal comparisons, this result should

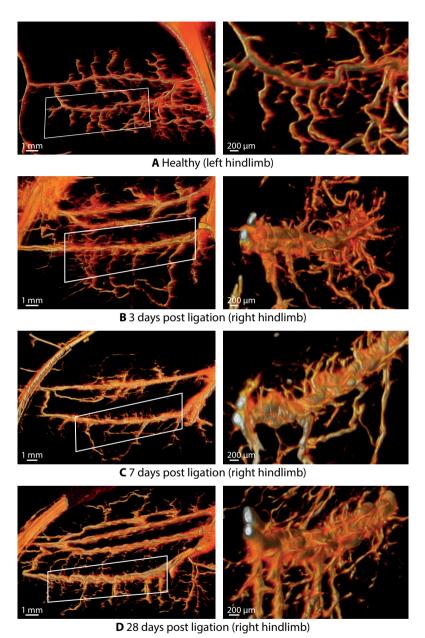


Figure 7.5: Representative examples of gracilis collaterals at different time points after ligation of the femoral artery (different animals). The right column displays enlargements of the regions indicated by the boxes.

be validated by longitudinal studies in the same animal, for example, using optical techniques.

We furthermore noted that the bridging arteries were accompanied by veins, forming intertwined artery–vein bundles (Figure 7.5B–D). In contrast to the arteries, we did not observe a significant change in venous diameter. Venous diameter increased by about 20% at day 3 of remodeling, but this change did not reach statistical significance due to the large inter–animal variability. Together with the proximity of these artery–vein pairs, this observation calls for further investigations of the role of veins during arteriogenesis in future studies.

7.3.2 What is a collateral?

The definition of what constitutes a collateral vessel is not so straightforward. In simple topologies, the differentiation between arterial trees and collateral segments is intuitive (Figure 7.4). But what is a collateral in general? Are there, for example, collaterals in arcading networks? Already for the hindlimb gracilis network, which is classically used in arteriogenesis research, this question becomes non-trivial (see Figure 7.6). As functional backup for the femoral artery, the direct paths between the muscular branch of the femoral artery and the saphenous artery seem most relevant, and these are the vessels commonly denoted as "collaterals". Despite multiple loops and subloops, these are not all just "backup vessels" but form part of the normal perfusing network in the absence of any upstream obstruction. In fact, along each of the three main paths and in each loop, only a single segment carries little or no flow, and one could argue that this is the collateral segment.

Perhaps the most distinguishing characteristic is the low, oscillatory flow at the watershed similar to what we have observed in the gracilis network with vascular filling (Figure 7.2) and for the modeled flow (Figure 7.6). Toriumi et al. noted that at the watershed between the anterior and middle cerebral artery some penetrating arterioles were dually supplied from both sides.³² Even under normal conditions and without significant diameter change, the watershed shifted as reflected by relocations of the dually supplied bifurcation.

Is there, however, anything special in the biology of this segment? These segments are usually small as expected (Figure 7.6), yet, according to a review by some of the leading experts in this field, "it is becoming evident that collaterals differ so much from arteries, capillaries, and veins in phenotypic and functional properties that they might well be considered a third circulation along with the general arterial–venous and lymphatic circulations."³¹, p. 1854 If this were the case, could the special

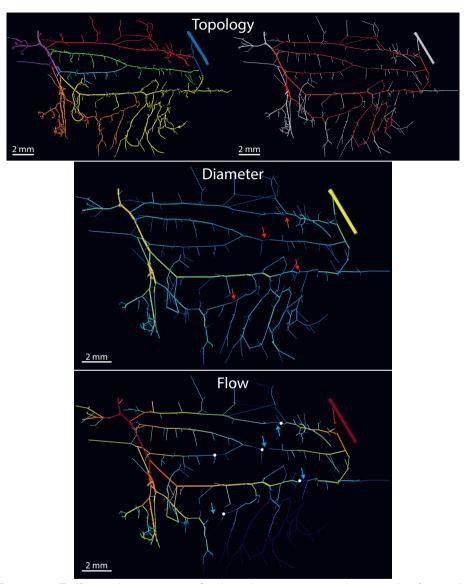
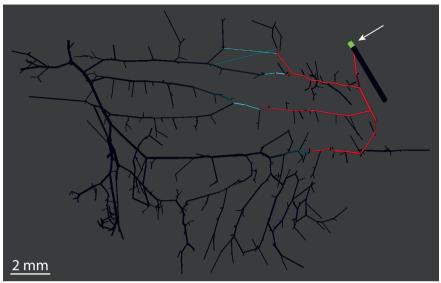


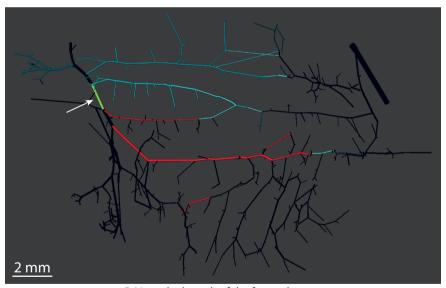
Figure 7.6: Different characteristics of collateral connections on the example of a gracilis arterial network. The network consists of several parts with **(top left)** three anastomoses (red, green, yellow) spanning between the muscular branch (purple) and the saphenous artery (blue) and **(top right)** multiple loops (red). Flow along the main paths is opposing with good agreement between the sites of least flow (blue arrows), flow reversal (white dots) and minimum diameter (red arrows).

properties be exploited for timely stimulation of collateral growth? We thus ponder what is so different and which parts of the anastomoses constitute a "collateral". Data comparing non-functional, i.e., pre-occlusion, collateral arterioles to "normal" arterioles are scarce. There is some evidence for altered phenotypes of the endothelial and smooth muscle cells. Zhang et al. observed more smooth muscle cells, 33 while Chan et al. noted less tone and myogenic responsiveness in pial collaterals compared to nearby arterioles.³⁴ Interestingly, their response to nitric oxide (NO)-dependent interventions was augmented, suggesting higher sensitivity to shear stress-mediated dilation. Zhang et al. also noted fewer primary cilia on the collaterals and a modified gene expression. The endothelial cells of pial collaterals were for the authors surprisingly similar to the nearby "distal-most arterioles" in morphometry and alignment. 33 Yet, to what extent do these observations differ from a similarly sized vessel at a distal part of the arterial tree perfusing only a small territory? Is the biology indeed different or the environment in which they reside? Scholz et al. reported for rabbit hindlimbs that "pre-existing collateral arterioles are morphologically indistinguishable from normal vessels; we could be sure to deal with collateral vessels only after they had become visible."35, p. 259 In our view, the observed gradual tapering and flow decrease towards the midzone in the native gracilis collaterals as well as the similarity between most parts of the anastomoses and an arteriole of comparable size and flow matches the expectation for a normal, perfusing function. We thus tend to agree with the view that there are no (collateral) vessels that are morphologically different from arterioles and arteries in the native arterial network.

An obstruction influences flow and pressure, foremost but, as outlined in Chapter 1, not exclusively, in nearby vessels. All segments of the path that bypasses the obstruction contribute when needed. Clearly, both the network structure and the site of obstruction govern the changes in hemodynamics. Figure 7.7 visualizes the effect on flow for two sites of modeled occlusion in the same gracilis hindlimb network. Flow became unidirectional along the main paths in both cases. Yet, the contribution of the individual segments differed greatly. Such unidirectional flow was, however, not observed when modeling a major acute obstruction in a healthy human coronary circulation. Despite abundant small collateral vessels, there was only a small shift of the watershed, with flow merely reversing in the middle segments of the vasodilated vasculature (Figure 7.8). The high resistance over the small segments impeded further flow reversal, suggesting that the protective effect of such small collaterals may be limited in the acute situation. Yet, the altered level of shear stress most likely would stimulate remodeling, notably of the segment at the watershed but to some extent in the entire network. In our view, the network



A Saphenous artery



B Muscular branch of the femoral artery

Figure 7.7: Effect of a 99%-stenosis on flow for two different sites (green segment, for visibility shown with original diameter), visualizing the profound influence of the obstruction location on the effect on the individual segments. Segments with flow reversal are marked with red. An increase in flow is labeled in cyan.

rather than a special segment responds. Therefore, we consider "collateralization" a network property, with arteriogenesis being part of network adaptation rather than a segment property.

7.3.3 How are innate collateral vessels maintained?

What mechanisms maintain small collateral segments in healthy subjects despite the seemingly adverse environment? Genetic cues certainly play a role as the extent of pre-existing collaterals highly varies between but also within species.³⁶ Guinea pigs and dogs, for example, are known for a plethora of innate collaterals while pigs only have few, small collateral vessels. Already during the development of collaterals during embryogenesis there are large genetic variations.³⁷ There must be additional modulators though, for example epigenetic ones, as there is significant variation in the configuration of the circle of Willis between twins.³⁸

On first sight, the environment at the watershed seems adverse: low flow at relatively high pressure, yet with little pressure gradient. Which mechanisms could contribute to maintaining these segments nonetheless? Temporal mean shear stress hardly seems sufficient. Is flow reversal a cue? Vasomotion and changes in downstream resistance, e.g., due to different metabolic demands, are thought to cause shiftings of the watershed position. Regular but lasting shifts, e.g., due to exercise, could promote sufficient sustained unidirectional flow in alternating segments. This could be augmented by a lowered shear stress set point due to the flow reversal.³⁹ Independently, exercise is well-known to promote collaterals due to the concomitant increase in flow. Whether these cues suffice or whether some form of direct coupling to the neighboring segments (e.g., by electrical communication between endothelial cells) contributes, remains elusive and should be addressed in future studies.

7.4 Conclusion

The imaging cryomicrotome is a versatile technology for studying arterial networks of entire organs down to small arterioles. The resulting 3D data on detailed vascular network patterns together with hemodynamic modeling provide a firm base for a better understanding of network design and adaptation. In this thesis, we have demonstrated its pertinence for quantitative collateral assessment and furthermore established its capacity for combined acquisition of the vascular structure together with co-registered markers of perfusion and remodeling. In morphometric evalua-

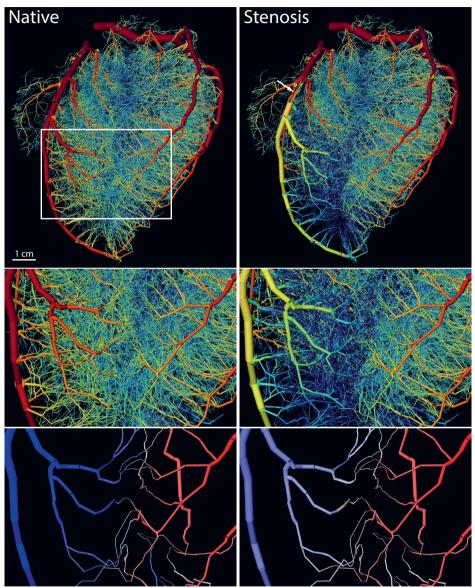


Figure 7.8: Effect of a major stenosis (90% diameter reduction, arrow) on flow in a normal human heart. Downstream flow is greatly reduced and **(bottom row)** the watershed in the collateral vessels only shifts minorly despite numerous native collaterals (blue = flow away from stenosis, red = flow towards stenosis). The second and third row show details of the region indicated by the white box.

tions, we observed stochastic, scale-dependent patterns in contrast to scaling laws that behave identically at all scales.

High-resolution data on human vascular networks are very scarce. We showed the feasibility of obtaining human coronary network data, but clearly more datasets are needed that cover the range of variation in the normal population, as well as relevant pathologies associated with coronary artery disease or myopathies. Even though these will remain difficult to obtain, post-mortem specimens would allow to further pursue a better understanding of the role of collaterals in acute and chronic obstructive diseases of both the heart and the brain.

In addition, we presented two methods for simplified wall shear stress estimation in patients, where wall shear stress pattern could be produced solely based on angiographic data, rendering wall shear stress assessment more accessible to clinical studies.

Altogether, the approaches presented in this thesis provide a promising start for a better understanding of vascular adaptation in chronic conditions such as growing stenoses, extending the current "single vessel knowledge"²⁹ to network adaptation, and generating new hypotheses on the underlying biology that could be experimentally tested. Notably, this could lead to unravelling the factors that dictate the level of collateralization in the network. For example, in acute ischemic stroke care, estimated CT perfusion data and concepts such as "the penumbra" and "collateral score" play dominant roles in decision making, but their correlation with actual network design and local perfusion remains poorly understood. The presented approach could thus add to current initiatives such as INSIST (IN-Silico trials for treatment of acute Ischemic STroke), aiming at better prediction of novel treatment outcomes based on modeling and simulation. ⁴⁰ The ability to combine the post-mortem structure of the adapted network with longitudinal data on local flow or with molecular clues would further strengthen this approach.

REFERENCES

- Ritman, E. L. Current status of developments and applications of micro-CT. Annu Rev Biomed Eng 13, 531–552. doi:10.1146/annurev-bioeng-071910-124717 (2011).
- 2. Du Plessis, A., Broeckhoven, C., Guelpa, A. & le Roux, S. G. Laboratory x-ray micro-computed tomography: a user guideline for biological samples. *Gigascience* 6, 1–11. doi:10.1093/gigascience/gix027 (2017).

- 3. Zhao, J. *et al.* Integration of High-Resolution Optical Mapping and 3-Dimensional Micro-Computed Tomographic Imaging to Resolve the Structural Basis of Atrial Conduction in the Human Heart. *Circ Arrhythm Electrophysiol* **8**, 1514–1517. doi:10.1161/CIRCEP.115.003064 (2015).
- 4. Stephenson, R. S. *et al.* High resolution 3-Dimensional imaging of the human cardiac conduction system from microanatomy to mathematical modeling. *Sci Rep* 7, 7188. doi:10.1038/s41598-017-07694-8 (2017).
- 5. Vasquez, S. X. *et al.* Optimization of microCT imaging and blood vessel diameter quantitation of preclinical specimen vasculature with radiopaque polymer injection medium. *PLoS One* **6**, e19099. doi:10.1371/journal.pone.0019099 (2011).
- 6. Hakimzadeh, N. *et al.* Selective subepicardial localization of monocyte subsets in response to progressive coronary artery constriction. *Am J Physiol Heart Circ Physiol* **311,** H239–H250. doi:10.1152/ajpheart.00187.2016 (2016).
- 7. Van den Wijngaard, J. P. H. M. *et al.* Porcine coronary collateral formation in the absence of a pressure gradient remote of the ischemic border zone. *Am J Physiol Heart Circ Physiol* **300**, H1930–H1937. doi:10.1152/ajpheart.00403.2010 (2011).
- 8. Van Horssen, P., Siebes, M., Spaan, J. A. E., Hoefer, I. E. & van den Wijngaard, J. P. H. M. Innate collateral segments are predominantly present in the subendo-cardium without preferential connectivity within the left ventricular wall. *J Physiol* **592**, 1047–1060. doi:10.1113/jphysiol.2013.258855 (2014).
- 9. Giuvarasteanu, I. Scanning electron microscopy of vascular corrosion casts standard method for studying microvessels. *Rom J Morphol Embryol* **48**, 257–261 (2007).
- 10. Verli, F. D., Rossi-Schneider, T. R., Schneider, F. L., Yurgel, L. S. & de Souza, M. A. Vascular corrosion casting technique steps. *Scanning* **29**, 128–132. doi:10.1002/sca.20051 (2007).
- 11. Levesque, M. J., Cornhill, J. F. & Nerem, R. M. Vascular casting. A new method for the study of the arterial endothelium. *Atherosclerosis* **34**, 457–467. doi:10.1016/0021-9150(79)90070-4 (1979).
- 12. Nopanitaya, W., Aghajanian, J. G. & Gray, L. D. An improved plastic mixture for corrosion casting of the gastrointestinal microvascular system. *Scan Electron Microsc*, 751–755 (1979).
- 13. Hodde, K. C. & Nowell, J. A. SEM of micro-corrosion casts. *Scan Electron Microsc*, 89–106 (1980).
- 14. Van Buskirk, E. M. The ciliary vasculature and its perturbation with drugs and surgery. *Trans Am Ophthalmol Soc* **86**, 794–841 (1988).

- 15. Weiger, T., Lametschwandtner, A. & Stockmayer, P. Technical parameters of plastics (Mercox CL-2B and various methylmethacrylates) used in scanning electron microscopy of vascular corrosion casts. *Scan Electron Microsc*, 243–252 (1986).
- 16. Steyer, G. J., Roy, D., Salvado, O., Stone, M. E. & Wilson, D. L. Removal of out-of-plane fluorescence for single cell visualization and quantification in cryo-imaging. *Ann Biomed Eng* 37, 1613–1628. doi:10.1007/s10439-009-9726-x (2009).
- 17. Goyal, A., van den Wijngaard, J., van Horssen, P., Grau, V., Spaan, J. & Smith, N. Intramural spatial variation of optical tissue properties measured with fluorescence microsphere images of porcine cardiac tissue in 2009 Annual International Conference of the IEEE Engineering in Medicine and Biology Society (2009), 1408–1411. doi:10.1109/IEMBS.2009.5334174.
- Frangi, A. F., Niessen, W. J., Vincken, K. L. & Viergever, M. A. Multiscale vessel enhancement filtering in Medical Image Computing and Computer-Assisted Intervention
 — MICCAI'98 (eds Wells, W. M., Colchester, A. & Delp, S.) (Springer Berlin Heidelberg, Berlin, Heidelberg, 1998), 130–137. doi:10.1007/BFb0056195.
- 19. Sato, Y. *et al.* Three-dimensional multi-scale line filter for segmentation and visualization of curvilinear structures in medical images. *Med Image Anal* **2**, 143–168. doi:10.1016/s1361-8415(98)80009-1 (1998).
- 20. Epah, J. et al. 3D Imaging and Quantitative Analysis of Vascular Networks: A Comparison of Ultramicroscopy and Micro-Computed Tomography. *Theranostics* 8, 2117–2133. doi:10.7150/thno.22610 (2018).
- 21. Ravnic, D. J. *et al.* Vessel painting of the microcirculation using fluorescent lipophilic tracers. *Microvasc Res* **70**, 90–96. doi:10.1016/j.mvr.2005.06.002 (2005).
- 22. Defazio, R. A. *et al.* A protocol for characterizing the impact of collateral flow after distal middle cerebral artery occlusion. *Transl Stroke Res* **2**, 112–127. doi:10.1007/s12975-010-0044-2 (2011).
- 23. Konno, A., Matsumoto, N. & Okazaki, S. Improved vessel painting with carbocyanine dye-liposome solution for visualisation of vasculature. *Sci Rep* 7, 10089. doi:10.1038/s41598-017-09496-4 (2017).
- 24. Rudyanto, R. D. *et al.* Comparing algorithms for automated vessel segmentation in computed tomography scans of the lung: the VESSEL12 study. *Med Image Anal* **18**, 1217–1232. doi:10.1016/j.media.2014.07.003 (2014).
- 25. Moccia, S., De Momi, E., El Hadji, S. & Mattos, L. S. Blood vessel segmentation algorithms Review of methods, datasets and evaluation metrics. *Comput Methods Programs Biomed* **158**, 71–91. doi:10.1016/j.cmpb.2018.02.001 (2018).
- 26. Todorov, M. I. *et al.* Machine learning analysis of whole mouse brain vasculature. *Nat Methods* **17**, 442–449. doi:10.1038/s41592-020-0792-1 (2020).

- 27. Taylor, C. A., Fonte, T. A. & Min, J. K. Computational fluid dynamics applied to cardiac computed tomography for noninvasive quantification of fractional flow reserve: scientific basis. *J Am Coll Cardiol* **61**, 2233–2241. doi:10.1016/j.jacc.2012.11.083 (2013).
- 28. Sankaran, S., Kim, H. J., Choi, G. & Taylor, C. A. Uncertainty quantification in coronary blood flow simulations: Impact of geometry, boundary conditions and blood viscosity. *J Biomech* **49**, 2540–2547. doi:10.1016/j.jbiomech.2016.01.002 (2016).
- 29. VanBavel, E. & Tuna, B. G. Integrative modeling of small artery structure and function uncovers critical parameters for diameter regulation. *PLoS One* **9**, e86901. doi:10.1371/journal.pone.0086901 (2014).
- 30. Hacking, W. J., VanBavel, E. & Spaan, J. A. Shear stress is not sufficient to control growth of vascular networks: a model study. *Am J Physiol Heart Circ Physiol* **270**, H364–H375. doi:10.1152/ajpheart.1996.270.1.H364 (1996).
- 31. Faber, J. E., Chilian, W. M., Deindl, E., van Royen, N. & Simons, M. A brief etymology of the collateral circulation. *Arterioscler Thromb Vasc Biol* **34**, 1854–1859. doi:10.1161/ATVBAHA.114.303929 (2014).
- 32. Toriumi, H., Tatarishvili, J., Tomita, M., Tomita, Y., Unekawa, M. & Suzuki, N. Dually supplied T-junctions in arteriolo-arteriolar anastomosis in mice: key to local hemodynamic homeostasis in normal and ischemic states? *Stroke* **40**, 3378–3383. doi:10.1161/STROKEAHA.109.558577 (2009).
- 33. Zhang, H., Chalothorn, D. & Faber, J. E. Collateral Vessels Have Unique Endothelial and Smooth Muscle Cell Phenotypes. *Int J Mol Sci* **20**, 3608. doi:10.3390/ijms20153608 (2019).
- 34. Chan, S. L., Sweet, J. G., Bishop, N. & Cipolla, M. J. Pial Collateral Reactivity During Hypertension and Aging: Understanding the Function of Collaterals for Stroke Therapy. *Stroke* 47, 1618–1625. doi:10.1161/STROKEAHA.116.013392 (2016).
- 35. Scholz, D. *et al.* Ultrastructure and molecular histology of rabbit hind-limb collateral artery growth (arteriogenesis). *Virchows Arch* **436**, 257–270. doi:10.1007/s004280050039 (2000).
- 36. Mac Gabhann, F. & Peirce, S. M. Collateral capillary arterialization following arteriolar ligation in murine skeletal muscle. *Microcirculation* **17**, 333–347. doi:10.1111/j.1549-8719.2010.00034.x (2010).
- 37. Chalothorn, D. & Faber, J. E. Formation and maturation of the native cerebral collateral circulation. *J Mol Cell Cardiol* **49**, 251–259. doi:10.1016/j.yjmcc.2010.03.014 (2010).

- 38. Forgo, B. *et al.* Are the Variants of the Circle of Willis Determined by Genetic or Environmental Factors? Results of a Twin Study and Review of the Literature. *Twin Res Hum Genet* **21**, 384–393. doi:10.1017/thg.2018.50 (2018).
- 39. Heuslein, J. L., Gorick, C. M., Song, J. & Price, R. J. DNA Methyltransferase 1-Dependent DNA Hypermethylation Constrains Arteriogenesis by Augmenting Shear Stress Set Point. *J Am Heart Assoc* 6, e007673. doi:10.1161/JAHA.117.007673 (2017).
- 40. Konduri, P. R., Marquering, H. A., van Bavel, E. E., Hoekstra, A., Majoie, C. B. L. M. & The INSIST Investigators. In-Silico Trials for Treatment of Acute Ischemic Stroke. *Front Neurol* 11, 558125. doi:10.3389/fneur.2020.558125 (2020).





CHAPTER 8

Summary

English Summary Samenvatting Zusammenfassung

8.1 ARTERIAL NETWORK ADAPTATION AND ENDOTHELIAL SHEAR STRESS. A TALE OF 3D IMAGING AND HEMODYNAMIC MODELING

The overall aim of this thesis was to advance the understanding of arterial network structure and adaptation. For this purpose, the imaging cryomicrotome technique was refined for capturing collateral vessels in small animal ischemia models. The capability of the imaging cryomicrotome for studying arterial network design by yielding high-resolution image stacks of large sample volumes was further demonstrated in a human heart. These structural investigations were complemented by hemodynamic simulations, based on reconstructions of cryomicrotome data as well as on other imaging modalities.

Chapter 1 provides an introduction to vascular network structure and function. Arterial network design is discussed in the context of scaling laws as well as in relation to the most relevant underlying mechanisms with a focus on hemodynamically mediated adjustments. The chapter concludes with an overview of the adaptive processes that shape the network structure.

The first part of this thesis focuses on the structure of arterial networks. Chapter 2 provides an overview of different techniques to image, analyze, and model the structure of whole-organ arterial networks and local perfusion. X-ray angiography, being capable of imaging small arteries, has proven its value in early key studies on the adaptation of coronary collaterals. However, the underlying 2D imaging principle limits its use for 3D reconstructions of arterial networks. Vascular casting enables detailed 3D replications down to the microcirculation but requires a suitable imaging modality for digitization. For visualization of the ultrastructure, small sections of vascular replica can be investigated using scanning electron microscopy. Other options for digitization include the imaging cryomicrotome and micro-CT. Additionally, stand-alone micro-CT can be used for in vivo imaging, achieving a resolution of about 50 µm, albeit over a small sample volume. Challenges of the subsequent image processing include correction for blurring and artifacts and, in particular, the computational costs associated with segmentation of the extensive whole-organ data sets. Tissue perfusion is typically assessed by measuring the fluorescence or radioactivity of labeled microspheres or molecular tracers. With the imaging cryomicrotome, multiple sets of fluorescently labeled microspheres can be located in 3D, co-registered to the arterial network. From the digitized arterial trees, network design patterns can be derived. By imputing the resulting models for the part of the arterial network that cannot be visualized clinically, flow, pressure, and clinical indices such as fractional flow reserve can be predicted for patient-specific diagnosis, albeit with assumptions regarding the physiological response to vasodilators.

In the remainder of this part, the imaging cryomicrotome technique was optimized and applied to the assessment of the murine hindlimb vasculature and the human coronary circulation. Even though vascular filling with Batson's no. 17 had produced good replicas for imaging the coronary circulation of medium and large species, it only incompletely filled the vasculature of small animals. In **Chapter 3**, we addressed this point with the objective of yielding a cast reproducing the in vivo morphology in terms of proper diameter, lengths, and bifurcation angles. Penetration of the cast material depended greatly on viscosity. Lowering the viscosity, either by diluting Batson's no. 17 with methyl methacrylate or by using Mercox, filled an increasing number of small vessels in the hindlimbs of healthy rats while retaining a physiological injection pressure. The volume fraction of vascular cast was about 18-times higher for the 50% dilution compared to the 10% dilution, which was mainly due to an increase in the number of segments rather than segment length. We, however, avoided strong (>50%) dilutions as less pre-polymerized mixtures exhibit more shrinkage and their capillary and venous filling complicates the subsequent image analysis. Dilutions of 25–30% were deemed optimal for filling the arterial network while limiting capillary and venous penetration. Together with multispectral episcopic cryomicrotome imaging, this enabled detailed 3D analysis of collateral adaptation. Both multiple deep collateral pathways and the superficial gracilis collaterals, which appeared as thin anastomoses in healthy legs and became increasingly larger with ischemia duration, could thereby be discerned.

In **Chapter 4**, the left arterial coronary circulation of a normotrophic human heart was reconstructed in great detail, with more than 4000 images at a voxel size of $(30\,\mu\text{m})^3$. From the 3D-reconstruction, morphometric characteristics were determined and extrapolated to the microcirculation below the spatial resolution. The reconstructed left coronary network comprised more than 200 000 segments with diameters ranging from 30 μ m to 4 mm. Most of these segments had a length of 100 μ m to 1 mm. While the smallest segments were also the shortest, median segment length was remarkably similar for diameters between 75 and 200 μ m. Although there was little difference in the distribution of terminal segment diameters, the density of terminal segments strongly increased from the subepicardium to the subendocardium. We furthermore observed a transition from asymmetric branching with small scaling exponents in large coronary arteries to symmetric branching with higher exponents in small arterioles. Also, area growth across bifurcations increased

with decreasing mother diameter and increasing branch symmetry, yet with high variability.

To establish ties with the structural properties, the hemodynamics of this coronary circulation network was modeled. The exponent of the diameter–flow relation increased towards the microcirculation, with 2.6 in the major arteries and 3.2 in the arterioles. Most of the pressure drop occurred in vessels between 200 µm and 1 mm in diameter. Uncertainty in the hemodynamic predictions was tested by stochastic variation of the imputed downstream conductances. Apart from limited added variation to the local flow, neither local pressure nor median local flow predictions were affected. Local perfusion was highly heterogeneous, and also wall shear stress was non-uniform with high variability.

The methods developed in this chapter can be deployed for future hemodynamic modeling studies of whole organs aiming to link arterial network structure and function. In this way, derived branching characteristics could furthermore be employed wherever information on network structure is partially missing and needs to be modeled, especially for simulation of coronary hemodynamics.

In the second part of this thesis, the effect of simplifications of the modeling approach on wall shear stress (WSS) estimates was investigated. In Chapter 5, the wall shear stress estimates of three methods for the common carotid arteries were compared: assuming Poiseuille or Womersley flow models, and as derived from the velocity gradients obtained with magnetic resonance imaging (MRI). Blood flow, axial flow velocity, lumen diameter, and mean wall thickness were measured three times with 3.0-Tesla MRI in 45 subjects. To assess the different shear stress estimates, mean wall shear stress, the amount of pulsatility (shear pulsatility index), and the proportion of flow reversal (oscillatory shear index) of the three modeling methods were compared. All methods exhibited good interscan reproducibility, where the Womersley and Poiseuille based methods tended to have higher intraclass correlation coefficients than the velocity gradient modeling method. The spatial flow velocity profile of the Womersley-based prediction, however, matched the MRI measurements much better than the Poiseuille-based estimate. Correspondingly, the Womersley model predicted flow reversal at the wall, whereas this was only very limitedly reflected in the Poiseuille model.

In general, we observed a negative correlation between mean wall shear stress and wall thickness after adjustment for systolic blood pressure. Temporal variations as represented by the shear pulsatility and the oscillatory shear index, however, were positively correlated with wall thickness. When comparing the three methods, mean WSS and pulsatility indices based on Womersley flow showed equally good

correlations with carotid mean wall thickness as the velocity gradient method. This is in contrast to the Poiseuille flow method that only showed an equally good correlation for mean WSS.

We therefore concluded that for estimation of dynamic WSS in the common carotid artery from flow rate or centerline velocity, Womersley modeling outperforms Poiseuille-based methods. The velocity gradient model differentiates wall regions but requires detailed information on the flow pattern, which is not commonly available. Womersley based methods merely require the measurement of flow rate or centerline velocity and carotid artery diameter, which renders these methods applicable to large clinical studies without the need for complex analyses and computations. Despite their limitations, Womersley-based methods should therefore replace the frequently used Poiseuille-based techniques in future clinical studies.

In **Chapter 6**, a simplification of the boundary conditions for computational fluid dynamics (CFD) simulations was tested for coronary bifurcations, eliminating the necessity for invasive flow measurements. In eight patients undergoing percutaneous coronary intervention, the flow velocity proximal and distal of a mildly diseased coronary bifurcation was measured with intravascular Doppler. The 3D geometry of each bifurcation was reconstructed from angiography, and the computed shear stress of two CFD simulations was compared. The first simulation used the measured flow velocity in defining the boundary conditions, whereas boundary conditions of the second simulation were derived solely from the geometry by assuming diameter flow scaling laws. Reasonable agreement existed between measured flow and flow predicted from a scaling law with exponent 2.55. The absolute WSS estimates, however, were sensitive to the deviations in the predicted from the measured flow values, with partially large differences between the results of the two simulation approaches. The normalized WSS maps, nonetheless, were nearly equivalent. Even though the absolute WSS estimates of simulations exclusively relying on angiographic data should be interpreted with care, the normalized map, by capturing regional differences, can provide a patient-specific distribution of normalized wall shear stress.

In **Chapter 7**, the findings of the work leading to this thesis are appraised. This includes a discussion on several aspects of the vascular casting for cryomicrotome imaging and of the subsequent image analysis. Another focus is on form—function properties of arterial networks, followed by deliberations on the meaning of "collateral vessel" and physiological conditions for their maintenance in vascular networks. Suggestions for improvements and future studies aiming at unraveling the interplay between arterial function and structure conclude this chapter.

8.2 ARTERIËLE NETWERK ADAPTATIE EN ENDOTHELIALE SCHUIFSPANNING. EEN VERHAAL OVER 3D BEELDVORMING EN HEMODYNAMISCHE MODELLERING

Het algemene doel van dit proefschrift was de structuur en aanpassing van arteriële netwerken beter te begrijpen. Hiertoe werd de 'Imaging Cryomicrotome' techniek verfijnd, zodat ook collaterale vaten in ischemie modellen van kleine proefdieren konden worden bestudeerd. De Imaging Cryomicrotome genereert hoge resolutie 3D beelden van complete arteriële netwerken in grote organen. Deze beelden werden gebruikt voor de studie van onder andere de vaatstructuur in het menselijk hart. Dit anatomisch onderzoek werd aangevuld met modelvorming van de hemodynamica, gebaseerd op zowel reconstructies van Cryomicrotome data als op andere beeldvormende modaliteiten.

Hoofdstuk 1 geeft een inleiding over de structuur en functie van vasculaire netwerken. Het ontwerp van arteriële netwerken wordt besproken in de context van schaalwetten en in relatie tot de meest relevante onderliggende mechanismen. Hierbij ligt de focus op de aanpassingen aan hemodynamische omstandigheden. Het hoofdstuk wordt afgesloten met een overzicht van de adaptatieprocessen die de netwerkstructuur vormgeven.

Het eerste deel van dit proefschrift richt zich op de structuur van arteriële netwerken. Hoofdstuk 2 geeft een overzicht van verschillende technieken voor de beeldvorming, analyse en modelvorming van arteriële netwerkstructuur en lokale perfusie in organen. Röntgenangiografie, dat beeldvorming van kleine slagaders mogelijk maakt, heeft zijn waarde bewezen in klassieke studies van de aanpassing van coronaire collateralen. De onderliggende 2D beeldvorming beperkt echter het gebruik ervan voor 3D reconstructies van arteriële netwerken. Plastic afgietsels en vulsels ('casts') van vaten maken gedetailleerde 3D replicaties tot aan de microcirculatie mogelijk, maar vereisen een geschikte beeldvormingsmodaliteit voor digitalisering. Voor de visualisatie van de ultrastructuur kunnen kleine onderdelen van zulke casts met behulp van rasterelektronenmicroscopie worden onderzocht. Andere opties voor digitalisering zijn de Imaging Cryomicrotome en micro-CT. Bovendien kan een stand-alone micro-CT worden gebruikt voor in vivo beeldvorming, waarbij een resolutie van ongeveer 50 µm wordt bereikt, zij het over een klein volume. Uitdagingen in de daaropvolgende beeldverwerking zijn onder meer de correctie voor onscherpte en artefacten. Bovendien vereist segmentatie van de vaatstructuur over de complete organen een zeer grote rekenkracht.

Weefselperfusie wordt vaak bepaald op basis van fluorescerende of radioactief gelabelde kleine partikels, zogenaamde microsferen, of moleculaire tracers. Met de Imaging Cryomicrotome kunnen meerdere sets van zulke fluorescerende microsferen in 3D worden gelokaliseerd, in samenhang met het arteriële netwerk. Uit de gedigitaliseerde arteriële vaatbomen kunnen netwerkpatronen worden afgeleid. Met modellering van dat deel van het arteriële netwerk, dat klinisch niet kan worden gevisualiseerd, kunnen bloedstroom, druk en klinische indices zoals de fractionele flow reserve worden voorspeld ten behoeve van patiënt-specifieke diagnoses. Hierbij moeten wel aannames worden gemaakt over de fysiologische reactie op vaatverwijders.

In de rest van dit eerste deel werd de Imaging Cryomicrotome techniek geoptimaliseerd en toegepast op de vasculatuur in de achterpoot van ratten en de menselijke coronaire circulatie. Hoewel casts met Batson's nr. 17 goede replica's van de coronaire circulatie van middelgrote en grote diersoorten vormden, vulde het de vaten van kleine dieren onvolledig. In Hoofdstuk 3 hebben we dit punt aangepakt met het doel een cast te produceren die de in vivo morfologie correct weergeeft in termen van de diameters, lengtes en bifurcatiehoeken. Penetratie van het casting materiaal hing sterk af van de viscositeit. Met het verlagen van de viscositeit, hetzij door verdunning van Batson's nr. 17 met methylmethacylaat of door gebruik van Mercox, werd met behoud van een fysiologische injectiedruk een toenemend aantal kleine bloedvaten in de achterpoten van gezonde ratten gevuld. De volumefractie van de vasculaire cast was ongeveer 18 keer zo groot voor de verdunning van 50% in vergelijking met de 10% verdunning, wat voornamelijk werd veroorzaakt door een toename van het aantal gevulde segmenten en niet zozeer van de segmentlengte. We vermeden echter sterke (>50%) verdunningen, omdat minder voorgepolymeriseerde mengsels meer krimp vertonen en hun capillaire en veneuze vulling de daaropvolgende beeldanalyse bemoeilijkt. Verdunningen van 25-30% bleken optimaal voor het vullen van het arteriële netwerk met tegelijk beperkte capillaire en veneuze penetratie. Samen met de multispectrale episcopische cryomicrotoombeeldvorming maakte dit een gedetailleerde 3D-analyse van aanpassingen van collaterale vaten mogelijk. Zowel meerdere diepe collaterale paden als de oppervlakkige gracilis collateralen, die als dunne anastomosen in gezonde poten verschenen en met de duur van de ischemie steeds groter werden, konden daardoor worden onderscheiden.

In **Hoofdstuk 4** werd de linker arteriële coronaire circulatie van een normaal menselijk hart tot in groot detail gereconstrueerd, met meer dan 4000 beelden bij een voxelgrootte van $(30 \, \mu m)^3$. Uit de 3D-reconstructie werden morfometrische kenmerken bepaald. Deze werden gebruikt voor extrapolatie van de netwerkstructuur

naar de vaten kleiner dan de beeldresolutie. Het gereconstrueerde linker coronaire netwerk omvatte meer dan 200 000 segmenten met diameters variërend van 30 μm tot 4 mm. De meeste van deze segmenten hadden een lengte tussen 100 μm en 1 mm. Terwijl de kleinste segmenten ook de kortste waren, was de mediane segmentlengte opmerkelijk gelijk voor diameters tussen 75 en 200 μm . Hoewel er weinig verschil was in de verdeling van diameters van de eindsegmenten, nam de dichtheid van eindsegmenten van het subepicard naar het subendocard sterk toe. Verder zagen we een overgang van asymmetrische vertakkingen met kleine allometrische exponenten in de grote kransslagaders naar symmetrische vertakkingen met hogere exponenten in de kleine arteriolen. Ook was de groei van de totale dwarsdoorsnede groter bij bifurcaties met kleinere moederdiameter en toenemende vertakkingssymmetrie, ofschoon met hoge variabiliteit.

Om een verband met de regeling van vaatstructuur te leggen, werd de hemodynamica in dit coronaire circulatienetwerk gemodelleerd. De exponent van de diameter-volumestroom-relatie nam toe van 2,6 in de grote arteriën tot 3,2 in de arteriolen. Het grootste deel van de drukdaling trad op in vaten met een diameter tussen 200 µm en 1 mm. De onzekerheid in de hemodynamische voorspellingen werd getest door stochastische variatie van de gemodelleerde terminale conductanties. Afgezien van beperkte toegevoegde variatie in de lokale stroom, beïnvloedde dit de voorspellingen van de lokale druk en mediane lokale stroom niet. De lokale perfusie was zeer heterogeen, en ook de afschuifspanning op de vaatwand was zeer variabel.

De in dit hoofdstuk ontwikkelde methoden kunnen in de toekomst worden ingezet voor hemodynamische modelvorming van hele organen dat zich richt op het verband tussen de structuur en de functie van het arteriële netwerk. Deze modellen kunnen worden gebruikt wanneer informatie over de netwerkstructuur gedeeltelijk ontbreekt, vooral voor simulatie van coronaire hemodynamica.

In het tweede deel van dit proefschrift werd het effect van vereenvoudiging van hemodynamische modellen op schattingen van de wandschuifspanning (WSS) onderzocht. In **Hoofdstuk 5** werden de schattingen van de WSS in de halsslagader op basis van drie methoden vergeleken: uitgaande van Poiseuille of Womersley stromingsmodellen, en afgeleid van de snelheidsgradiënten verkregen met MRI. Bloedstroom, axiale stroomsnelheid, lumen diameter en gemiddelde wanddikte werden bij 45 proefpersonen drie keer met 3,0-Tesla-MRI gemeten. Om de verschillende schattingen van schuifspanning te beoordelen, werden de gemiddelde wandschuifspanning, de pulsatiliteit (schuifspanning pulsatiliteit index) en de mate van stroomomkering (oscillerende schuifspanningsindex) op basis van de drie me-

thoden vergeleken. Alle methoden vertoonden een goede interscan reproduceerbaarheid, waarbij de Womersley en Poiseuille methoden neigden naar hogere intraclass correlatiecoëfficiënten dan die op basis van de snelheidsgradiënt. Het ruimtelijke stroomsnelheidsprofiel van de Womersley voorspelling kwam echter veel beter overeen met de MRI-metingen dan de schatting op basis van Poiseuille stroming. Hiermee in overeenstemming voorspelde het Womersley model stroomomkering aan de wand, terwijl dit in het Poiseuille-model slechts zeer beperkt optrad.

In het algemeen zagen we een negatieve correlatie tussen de gemiddelde wandschuifspanning en de wanddikte naar correctie voor de systolische bloeddruk. Temporele variaties, zoals weergegeven door de twee schuifspanningsindices, waren echter positief gecorreleerd met wanddikte. De gemiddelde WSS en de pulsatiliteitsindices op basis van de Womersley methode toonden even goede correlaties met de wanddikte als de snelheidsgradiëntmethode. Dit is in tegenstelling tot de Poiseuille methode die alleen voor de gemiddelde WSS een even goede correlatie liet zien.

We concludeerden daarom dat voor de schatting van de dynamische WSS in de halsslagader op basis van de volumestroom of de snelheid in het midden, Womersley modellering beter presteert dan op Poiseuille gebaseerde methoden. Het snelheidsgradiëntmodel onderscheidt wandregio's, maar vereist gedetailleerde informatie over het stromingspatroon, die niet algemeen beschikbaar is. De Womersley methode vereist slechts de meting van de volumestroom of de snelheid in het midden en de diameter van de halsslagader. Hierdoor is deze methode zonder de noodzaak van complexe analyses en berekeningen op grote klinische studies toepasbaar. Ondanks zijn beperkingen zouden in toekomstige klinische studies de op Womersley gebaseerde methoden daarom de veelgebruikte op Poiseuille gebaseerde methoden moeten vervangen.

In **Hoofdstuk 6** werd een vereenvoudiging van de randvoorwaarden voor numerieke vloeistofdynamica (CFD) simulaties op coronaire bifurcaties getest. Met deze aanpassing zouden invasieve stromingsmetingen niet meer nodig zijn. Bij acht patiënten die een percutane coronaire interventie ondergingen, werd de stroomsnelheid proximaal en distaal van een coronaire vertakking met milde atherosclerose gemeten met intravasculaire Doppler. De 3D-geometrie van elke bifurcatie werd uit angiografie gereconstrueerd, en de berekende schuifspanningen van twee CFD simulaties werden vergeleken. De eerste simulatie gebruikte de gemeten stroomsnelheid bij het bepalen van de randvoorwaarden, terwijl de randvoorwaarden van de tweede simulatie werden afgeleid uit de geometrie op basis van schaalwetten voor diameter–volumestroom relaties. Er bestond een redelijke overeenstemming

tussen de gemeten stroming en de stroming die werd voorspeld op basis van een schaalwet met exponent 2,55. De absolute WSS schattingen waren echter gevoelig voor de afwijkingen van de voorspelde van de gemeten volumestroom, met deels grote verschillen tussen de resultaten van de twee simulatiebenaderingen. De genormaliseerde WSS patronen waren niettemin vrijwel gelijkwaardig. De absolute WSS schattingen op basis van uitsluitend de angiografische data dienen voorzichtig te worden geïnterpreteerd. De genormaliseerde patronen geven op basis van de regionale verschillen wel een patiënt-specifieke verdeling van genormaliseerde wandschuifspanning.

In **Hoofdstuk 7** worden de bevindingen van het werk, dat tot dit proefschrift heeft geleid, geëvalueerd. Dit omvat een bespreking van verschillende aspecten van de vasculaire casting voor cryomicrotoom beeldvorming en van de daaropvolgende beeldanalyse. Een tweede focus ligt op de vorm–functie eigenschappen van arteriële netwerken, gevolgd door beschouwingen over de betekenis van "collateraal vaten" en de fysiologische voorwaarden voor hun handhaving in vasculaire netwerken. Suggesties voor verbeteringen en toekomstige studies, gericht op het ontrafelen van het samenspel tussen arteriële functie en structuur, sluiten dit hoofdstuk af.

8.3 ARTERIELLE NETZWERK-ADAPTATION UND ENDOTHELIALE SCHUBSPANNUNG. EINE GESCHICHTE ÜBER 3-D-BILDGEBUNG UND HÄMODYNAMISCHE MODELLIERUNG

Das allgemeine Ziel dieser Dissertation war, zu einem besseren Verständnis der Struktur und Adaption arterieller Netzwerk beizutragen. Zu diesem Zweck wurde die Imaging-Cryomicrotome-Technik, welche hochaufgelöste 3-D Bildstapel von großen Probevolumen und Organen erzeugt, angewandt und für das Studium von Kollateralgefäßen in Kleintier-Ischämiemodellen verfeinert. Die Fähigkeit des Imaging Cryomicrotome, arterielle Netzwerke zu erforschen, wurde ferner an einem menschlichen Herzen demonstriert. Diese anatomischen Studien wurden durch Simulationen der Hämodynamik, welche sowohl auf Rekonstruktionen von Cryomicrotome-Datensätzen als auch auf anderen bildgebenden Verfahren basierten, ergänzt.

Kapitel 1 bietet eine Einführung in den Aufbau und die Funktion von Gefäßnetzwerken. Das Design arterieller Netzwerke wird im Zusammenhang von Skalierungsgesetzen sowie in Bezug auf die relevantesten zugrunde liegenden Mechanismen besprochen. Hierbei liegt der Schwerpunkt auf den Anpassungen an die Hämodynamik. Das Kapitel schließt mit einem Überblick über die adaptiven Prozesse, welche die Netzwerkstruktur prägen.

Der erste Teil dieser Dissertation befasst sich mit dem Aufbau von arteriellen Netzwerken. Kapitel 2 gibt einen Überblick über die verschiedenen Techniken zum Abbilden, Analysieren und Modellieren arterieller Netzwerke vollständiger Organe und deren lokaler Durchblutung. Die Röntgenangiographie, die ermöglicht, kleine Arterien abzubilden, hat sich in klassischen Studien zur Anpassung von koronaren Kollateralgefäßen bewährt. Das zugrunde liegende 2-D-Bildgebungsprinzip schränkt jedoch ihren Nutzen für 3-D-Rekonstruktionen arterieller Netzwerke ein. Gefäßausgüsse und vaskuläres Füllen (Casting) ermöglichen detaillierte 3-D-Replikationen von Blutgefäßen einschließlich der Mikrozirkulation, erfordern allerdings eine geeignete bildgebende Modalität zur Digitalisierung. Zur Visualisierung der Ultrastruktur können kleine Abschnitte der Gefäßausgusspräparate mittels Rasterelektronenmikroskopie untersucht werden. Zu den weiteren Möglichkeiten zur Digitalisierung gehören das Imaging Cryomicrotome und die Mikro-Computertomographie. Darüber hinaus kann eine Stand-alone-Mikro-Computertomographie für eine In-vivo-Bildgebung verwendet werden, wobei eine

Auflösung von etwa 50 µm erreicht wird, wenn auch über ein kleines Probenvolumen. Zu den Herausforderungen der anschließenden Bildverarbeitung gehören die Korrektur von Unschärfe und Artefakten und insbesondere der mit der Segmentierung des Gefäßsystems ganzer Organe verbundene Rechenaufwand.

Die Gewebeperfusion wird typischerweise durch Messung der Fluoreszenz oder Radioaktivität markierter Mikrosphären oder molekularer Tracer bestimmt. Mit dem Imaging Cryomicrotome können gleichzeitig mehrere Sätze fluoreszierender Mikrosphären registriert mit dem arteriellen Netzwerk in 3-D lokalisiert werden. Aus den digitalisierten arteriellen Gefäßbäumen können Netzwerkprinzipien abgeleitet werden. Durch Verwendung der resultierenden Modelle für den Teil des arteriellen Netzwerks, der klinisch nicht visualisiert werden kann, können Blutfluss, Druck und klinische Indizes wie die Fraktionelle Flussreserve für patientenspezifische Diagnosen vorhergesagt werden. Für solche diagnostischen Vorhersagen müssen dabei gleichwohl Annahmen über die physiologische Reaktion auf Vasodilatatoren gemacht werden.

Im weiteren Verlauf dieses Buchteils wurde die Imaging-Cryomicrotome-Technik optimiert und zur Beurteilung des murinen Hinterlaufgefäßsystems und der menschlichen Koronarzirkulation angewendet. Obwohl Casting mit Batson Nr. 17 gute Nachbildungen für die Darstellung der koronaren Zirkulation von mittelgroßen und großen Tierarten hervorgebracht hatte, füllte es das Gefäßsystem von Kleintieren nur unvollständig. In Kapitel 3 haben wir diesen Punkt mit dem Ziel adressiert, ein Präparat zu erzeugen, welches die In-vivo-Morphologie im Sinne der Durchmesser, Längen und Bifurkationswinkel korrekt reproduziert. Die Penetration des Castingmaterials hing stark von der Viskosität ab. Mit Senkung der Viskosität (entweder durch Dilution von Batson Nr. 17 mit Methylmethacrylat oder durch Verwendung von Mercox) wurde unter Beibehaltung eines physiologischen Injektionsdrucks eine zunehmende Menge kleiner Gefäße in den Hinterläufen gesunder Ratten gefüllt. Der Volumenanteil des Gefäßausgusspräparates war bei der Verdünnung von 50 % etwa 18-mal höher als bei der Dilution von 10 %, was hauptsächlich auf eine Zunahme der Anzahl gefüllter Segmente und nicht auf die Segmentlänge zurückzuführen war. Wir haben jedoch starke (>50 %) Verdünnungen vermieden, da weniger vorpolymerisierte Gemische eine ausgeprägtere Schrumpfung aufweisen und das Füllen der Kapillar- und venösen Gefäße zudem die anschließende Bildanalyse erschwert. Dilutionen von 25–30 % wurden als optimal für ein Casting des arteriellen Netzwerks bei gleichzeitiger Begrenzung der kapillaren und venösen Penetration erachtet. Zusammen mit der multispektralen episkopischen Kryomikrotom-Bildgebung ermöglichte dies eine detaillierte 3-D-Analyse der Adaptation der Kollateralgefäße. Sowohl mehrere tief liegende Kollateralwege als auch die oberflächlichen Gracilis-Kollateralgefäße, die in gesunden Beinen als dünne Anastomosen erschienen und mit zunehmender Ischämiedauer immer größer wurden, konnten so erkannt werden.

In **Kapitel 4** wurde die linke arterielle Koronarzirkulation eines normotrophen menschlichen Herzens äußerst detailliert rekonstruiert, mit mehr als 4000 Bildern bei einer Voxelgröße von (30 µm)³. Anhand der 3-D-Rekonstruktion wurden morphometrische Merkmale bestimmt, welche zur Extrapolation für den Teil der Mikrozirkulation, der unterhalb des räumlichen Auflösungsvermögens lag, verwendet wurden. Das rekonstruierte linke Koronarnetzwerk umfasste mehr als 200 000 Segmente mit Durchmessern, welche von 30 µm bis 4 mm reichten. Die meisten dieser Segmente hatten eine Länge zwischen 100 µm und 1 mm. Während die kleinsten Segmente auch die kürzesten waren, war die mediane Segmentlänge der Durchmesser zwischen 75 und 200 µm bemerkenswert ähnlich. Obwohl es kaum Unterschiede in der Verteilung der terminalen Segmentdurchmesser gab, nahm die Dichte der Endsegmente vom Subepikard zum Subendokard stark zu. Darüber hinaus beobachteten wir einen Übergang von asymmetrischen Bifurkationen mit niedrigen Skalierungsexponenten in den großen Koronararterien zu symmetrischen Verzweigungen mit höheren Exponenten in den kleinen Arteriolen. Auch das Flächenwachstum über Bifurkationen nahm mit abnehmendem Mutterdurchmesser und zunehmender Verzweigungssymmetrie zu, jedoch mit beträchtlicher Variabilität.

Um Verbindungen zu den strukturellen Eigenschaften herzustellen, wurde die Hämodynamik dieses Koronarzirkulationsnetzwerkes modelliert. Der Exponent der Durchmesser-Volumenstrom-Beziehung nahm mit einem Wert von 2,6 in den Hauptarterien und 3,2 in den Arteriolen in Richtung der Mikrozirkulation zu. Der größte Teil des Druckabfalls trat in Gefäßen mit einem Durchmesser zwischen 200 µm und 1 mm auf. Die Unsicherheit in den hämodynamischen Schätzungen wurde durch stochastische Variation der modellierten flussabwärtigen Leitfähigkeiten getestet. Abgesehen von einer begrenzten zusätzlichen Variation des lokalen Volumenstromes wurden weder die Vorhersagen des lokalen Drucks noch des mittleren lokalen Volumenstromes beeinflusst. Die lokale Perfusion war sehr heterogen, und auch die Wandschubspannung war äußerst variabel.

Die in diesem Kapitel entwickelten Methoden können für zukünftige hämodynamische Modellierungsstudien ganzer Organe eingesetzt werden, die darauf zielen, den Aufbau und die Funktion arterieller Netzwerke miteinander zu verknüpfen. Die abgeleiteten Verzweigungscharakteristika können überall dort verwendet werden,

wo Informationen zur Netzwerkstruktur teilweise fehlen und modelliert werden müssen, insbesondere bei der Simulation der koronaren Hämodynamik.

Im zweiten Teil dieser Dissertation wurden die Auswirkungen von Vereinfachungen des Modellierungsansatzes auf Schätzungen der Wandschubspannung (WSS) untersucht. In Kapitel 5 wurden die Vorhersagen der Wandschubspannung von drei Methoden für die Arteria carotis communis verglichen: unter Annahme von Poiseuille-, von Womersley-Strömungsmodellen und abgeleitet von den Geschwindigkeitsgradienten, die mithilfe der Magnetresonanztomographie (MRT) bestimmt wurden. Blutfluss, axiale Strömungsgeschwindigkeit, Lumendurchmesser und mittlere Wanddicke wurden bei 45 Probanden dreimal mit einem 3,0-Tesla-MRT gemessen. Zur Bewertung der verschiedenen Schätzungen der Schubspannung wurden die durchschnittliche Wandschubspannung, die Stärke der Pulsatilität (Scherpulsatilitätsindex) und der Anteil der Strömungsumkehr (oszillatorischer Scherindex) der drei Modellierungsmethoden verglichen. Alle Methoden wiesen eine gute Interscan-Reproduzierbarkeit auf, wobei die auf Womersley und Poiseuille basierenden Verfahren tendenziell höhere Intraklassen-Korrelationskoeffizienten hatten als die Geschwindigkeitsgradientenmodellierung. Das räumliche Strömungsgeschwindigkeitsprofil der Womersley-basierten Vorhersage stimmte jedoch viel besser mit den MRT-Messungen überein als die Poiseuille-basierte Schätzung. Dementsprechend sagte das Womersley-Modell eine Strömungsumkehr an der Gefäßwand voraus, während dieses im Poiseuille-Modell nur sehr begrenzt wiedergegeben wurde.

Im Allgemeinen beobachteten wir eine negative Korrelation zwischen mittlerer Wandschubspannung und Wanddicke nach Korrektur für den systolischen Blutdruck. Zeitliche Variationen, wie sie durch Scherpulsatilitäts- und oszillatorischem Scherindex dargestellt werden, waren indessen positiv mit der mittleren Wanddicke korreliert. Beim Vergleich der drei Methoden zeigten die durchschnittliche WSS und die Pulsatilitäts-Indizes auf Basis des Womersley-Flusses ebenso gute Korrelationen mit der Carotis-Wanddicke wie die Geschwindigkeitsgradient-Methode. Dies steht im Gegensatz zur Poiseuille-Fluss-Methode, die nur für die durchschnittliche WSS eine gute Korrelation aufwies.

Wir kamen daher zu dem Schluss, dass die Womersley-Modellierung Poiseuillebasierten Methoden bei der Schätzung der dynamischen WSS auf Basis des Volumenstromes oder der Mittelachsengeschwindigkeit in der Arteria carotis communis überlegen ist. Das Geschwindigkeitsgradientmodell unterscheidet verschiedene Wandbereiche, benötigt allerdings detaillierte Informationen über das Strömungsmuster, das nicht allgemein verfügbar ist. Die Womersley-basierte Methode erfordert lediglich die Messung des Volumenstromes oder der Mittelachsengeschwindigkeit und des Durchmessers der Carotis-Arterie, was diese Technik ohne die Notwendigkeit komplexer Analysen und Berechnungen für große klinische Studien anwendbar macht. Trotz ihrer Einschränkungen sollten Womersley-Verfahren daher die häufig verwendeten Poiseuille-basierten Methoden in zukünftigen klinischen Studien ersetzen.

In **Kapitel 6** wurde eine Vereinfachung der Randbedingungen für numerische Strömungssimulationen (CFD), die die Notwendigkeit für invasive Strömungsmessungen eliminiert, an Bifurkationen der Koronargefäße getestet. Bei acht Patienten, die sich einer perkutanen Koronarintervention unterzogen, wurde die Strömungsgeschwindigkeit proximal und distal einer koronaren Bifurkation mit milder Atherosklerose mit intravaskulärem Doppler gemessen. Die 3-D-Geometrie jeder Verzweigung wurde anhand der Angiographie rekonstruiert, und die berechneten Schubspannungen von zwei CFD-Simulationen wurden miteinander verglichen. Die erste Simulation verwendete die gemessene Strömungsgeschwindigkeit zur Definition der Randbedingungen, während die Randbedingungen der zweiten Simulation ausschließlich von der Geometrie abgeleitet wurden, indem Durchmesser-Volumenstrom-Skalierungsgesetze angenommen wurden. Zwischen gemessenem Blutfluss und Volumenstrom, welcher von einem Skalierungsgesetz mit Exponent 2,55 vorhergesagt wurde, bestand eine passable Übereinstimmung. Die absoluten WSS-Schätzungen reagierten jedoch empfindlich auf die Abweichungen des vorhergesagten vom gemessenen Blutfluss mit teilweise großen Unterschieden zwischen den Ergebnissen der beiden Simulationsansätze. Die normalisierten WSS-Muster waren gleichwohl fast äquivalent. Absolute WSS-Schätzungen von Simulationen, die ausschließlich auf angiographischen Daten beruhen, sollten mit Vorsicht interpretiert werden. Die normalisierten Muster können hingegen durch Erfassung regionaler Unterschiede eine patientenspezifische Verteilung der normalisierten Wandschubspannung liefern.

In Kapitel 7 werden die Ergebnisse der Arbeit, welche zu dieser Dissertation geführt hat, ausgewertet. Dazu gehört eine Diskussion verschiedener Aspekte des vaskulären Castings für die Kryomikrotom-Bildgebung und der anschließenden Bildanalyse. Ein weiterer Schwerpunkt liegt auf den Form-Funktions-Eigenschaften arterieller Netzwerke, gefolgt von Überlegungen zu der Bedeutung des Begriffs "Kollateralgefäß" und physiologischen Bedingungen für dessen Aufrechterhaltung in Gefäßnetzwerken. Verbesserungsvorschläge und Anregungen für zukünftige Studien, die darauf abzielen, das Zusammenspiel von arterieller Funktion und Struktur zu enträtseln, bilden den Abschluss dieses Kapitels.







APPENDIX A

About the PhD Training

Portfolio
List of Publications
Author Contributions
Curriculum Vitae
Acknowledgments

A.1 PhD Portfolio

Name: Janina Caprice Viola Schwarz

PhD Period: 2011–2021

Supervisor: Prof. dr. E. T. van Bavel

Co-supervisor: Dr. ir. M. Siebes

PhD training	Year	Workload (ECTS)
General courses		
The AMC World of Science	2011	0.7
Practical Biostatistics	2012	1.4
Specific courses		
Introduction to Programming on the GPU with CUDA, Delft	2011	0.3
The Macroscopic, Microscopic and Pathological Anatomy of the House Mouse	2012	1.5
Gem4 Summer School: Cellular and molecular mechanics, London, UK	2012	1.5
Summer School on Image Processing (SSIP), Veszprém, Hungary	2013	1.9
Seminars, workshops and master classes		
VPH Workshop on Toolkit Hands-on Training, Sophia-Antipolis, France	2011	0.9
VPH study group on VPH Toolkit, Barcelona	2012	1.4
COMSOL Equation based modeling workshop	2012	0.2
Department seminars	2011–2015	3.0
Ruysch lectures	2011-2016	1.0
Journal Club	2011–2015	5.0

PhD training (cont.)	Year	Workload (ECTS)
(Inter)national conferences		
Cardiac Physiome Workshop, Oxford, UK (poster)	2011	1.0
CTMM annual meeting, Utrecht, The Netherlands (poster)	2011–2014	2.0
Symposium on Microcirculation in Health and Disease, Rotterdam, The Netherlands	2011	0.25
Cardiovascular Research Symposium, Eindhoven, The Netherlands	2011	0.25
IUPS Satellite meeting, Amsterdam, The Netherlands (poster)	2013	0.5
Dutch BME, Egmond aan Zee, The Netherlands (oral)	2015	0.75
Cardiovascular Research Institute symposium, Amsterdam, The Netherlands (poster)	2015	0.5
EMBC, Milano, Italy (poster)	2015	1.5
AHA Scientific Sessions, Orlando, USA (poster)	2015	
Teaching		
BSc thesis, medicine (Anne van Dalen)	2013	1.0
Research practicum physics (2 groups)	2015	0.5
Student demonstrations	2011–2015	0.2
Parameters of Esteem		
Prize for project work (Particle Filter Segmentation), SSIP, Hungary	2013	

A.2 LIST OF PUBLICATIONS

Included in this thesis

- Van den Wijngaard, J. P. H. M., **Schwarz, J. C. V.**, van Horssen, P., van Lier, M. G. J. T. B., Dobbe, J. G. G., Spaan, J. A. E. & Siebes, M. 3D Imaging of vascular networks for biophysical modeling of perfusion distribution within the heart. *J Biomech* **46**, 229–239 (2013).
- Schwarz, J. C. V.*, Duivenvoorden, R.*, Nederveen, A. J., Stroes, E. S. G. & VanBavel, E. Endothelial shear stress estimation in the human carotid artery based on Womersley versus Poiseuille flow. *Int J Cardiovasc Imaging* 31, 585–593 (2015).
- Schrauwen, J. T. C., **Schwarz, J. C. V.**, Wentzel, J. J., van der Steen, A. F. W., Siebes, M. & Gijsen, F. J. H. The impact of scaled boundary conditions on wall shear stress computations in atherosclerotic human coronary bifurcations. *Am J Physiol Heart Circ Physiol* **310**, H1304–H1312 (2016).
- Schwarz, J. C. V., van Lier, M. G. J. T. B., Bakker, E. N. T. P., de Vos, J., Spaan, J. A. E., VanBavel, E. & Siebes, M. Optimization of Vascular Casting for Three-Dimensional Fluorescence Cryo-Imaging of Collateral Vessels in the Ischemic Rat Hindlimb. *Microsc Microanal* 23, 77–87 (2017).
- Schwarz, J. C. V., van Lier, M. G. J. T. B., van den Wijngaard, J. P. H. M., Siebes, M. & VanBavel, E. Topologic and Hemodynamic Characteristics of the Human Coronary Arterial Circulation. *Front Physiol* **10**, 1611 (2020).

Other publications

- Van Dam, A., **Schwarz, J. C. V.**, de Vos, J., Siebes, M., Sijen, T., van Leeuwen, T. G., Aalders, M. C. G. & Lambrechts, S. A. G. Oxidation Monitoring by Fluorescence Spectroscopy Reveals the Age of Fingermarks. *Angew Chem Int Edit* **53**, 6272–6275 (2014).
- Achetib, N., Wilk, L. S., **Schwarz, J. C. V.**, Lambrechts, S. A. G., van Leeuwen, T. G., Aalders, M. C. G. & van Dam, A. Estimating the Time of Deposition of Semen Traces using Fluorescence Protein-Lipid Oxidation Signatures. *Anal Chem* **91**, 3204–3208 (2019).

^{*} Authors have contributed equally

A.3 AUTHOR CONTRIBUTIONS

List of acronyms

- AN Aart J. Nederveen. Department of Radiology, Amsterdam UMC, University of Amsterdam, Amsterdam, The Netherlands
- AvdS Antonius F.W. van der Steen. Department of Biomedical Engineering, Thorax Center, Erasmus Medical Center, Rotterdam, The Netherlands; Department of Imaging Physics, Delft University of Technology, Delft, The Netherlands
- EB Erik N. T. P. Bakker. Department of Biomedical Engineering and Physics, Amsterdam UMC, University of Amsterdam, Amsterdam, The Netherlands
- ES Erik S. G. Stroes. Department of Vascular Medicine, Amsterdam UMC, University of Amsterdam, Amsterdam, The Netherlands
- EvB Ed van Bavel. Department of Biomedical Engineering and Physics, Amsterdam UMC, University of Amsterdam, Amsterdam, The Netherlands
- FG Frank J. H. Gijsen. Department of Biomedical Engineering, Thorax Center, Erasmus Medical Center, Rotterdam, The Netherlands
- JAS Jos A. E. Spaan. Department of Biomedical Engineering and Physics, Amsterdam UMC, University of Amsterdam, Amsterdam, The Netherlands
- JCS Janina C. V. Schwarz. Department of Biomedical Engineering and Physics, Amsterdam UMC, University of Amsterdam, Amsterdam, The Netherlands
- JD Johannes G. G. Dobbe. Department of Biomedical Engineering and Physics, Amsterdam UMC, University of Amsterdam, Amsterdam, The Netherlands
- JdV Judith de Vos. Department of Biomedical Engineering and Physics, Amsterdam UMC, University of Amsterdam, Amsterdam, The Netherlands
- JTS Jelle T. C. Schrauwen. Department of Biomedical Engineering, Thorax Center, Erasmus Medical Center, Rotterdam, The Netherlands
- JvdW Jeroen P. H. M. van den Wijngaard. Department of Biomedical Engineering and Physics, Amsterdam UMC, University of Amsterdam, Amsterdam, The Netherlands
- JW Jolanda J. Wentzel. Department of Biomedical Engineering, Thorax Center, Erasmus Medical Center, Rotterdam, The Netherlands
- MvL Monique G. J. T. B. van Lier. Department of Biomedical Engineering and Physics, Amsterdam UMC, University of Amsterdam, Amsterdam, The Netherlands

- PvH Pepijn van Horssen. Department of Biomedical Engineering and Physics, Amsterdam UMC, University of Amsterdam, Amsterdam, The Netherlands
- MS Maria Siebes. Department of Biomedical Engineering and Physics, Amsterdam UMC, University of Amsterdam, Amsterdam, The Netherlands
- RD Raphaël Duivenvoorden. Department of Vascular Medicine, Amsterdam UMC, University of Amsterdam, Amsterdam, The Netherlands

Chapter 2: 3D Imaging of vascular networks for biophysical modeling of perfusion distribution within the heart

Conception & design: JvdW

Literature review: JvdW, JCS, MS

Figure preparation: JvdW

Manuscript draft: JvdW, MS, JAS

Manuscript revision: JvdW, JCS, PvH, MvL, JD, JAS, MS All authors approved the final version of the manuscript.

Chapter 3: Optimization of Vascular Casting for Three-Dimensional Fluorescence Cryo-Imaging of Collateral Vessels in the Ischemic Rat Hindlimb

Conception & design: JAS, MS, JCS, EvB

Experiments: JCS, MvL, JdV, EB

Data analysis: JCS

Interpretation of results: JCS, MvL, MS, EvB, JAS, EB

Figure preparation: JCS Manuscript draft: JCS

Manuscript revision: JCS, MvL, EB, EvB, MS

All authors approved the final version of the manuscript.

Chapter 4: Topologic and Hemodynamic Characteristics of the Human Coronary Arterial Circulation

Conception & design: EvB, JCS, MvL Methods & software: JCS, JvdW, EvB

Experiments: JCS, MvL, JvdW

Data analysis: JCS, MvL

Interpretation of results: JCS, MvL, EvB, MS

Figure preparation: JCS, MvL Manuscript draft: JCS, MvL, EvB Manuscript revision: JCS, MvL, EvB, MS

All authors approved the final version of the manuscript.

Chapter 5: Endothelial shear stress estimation in the human carotid artery based on Womersley versus Poiseuille flow

Conception & design: EvB, JCS, AN, RD

Methods & software: JCS

Experiments: RD Data analysis: JCS, RD

Interpretation of results: JCS, RD, EvB, AN

Figure preparation: JCS

Manuscript draft: RD, JCS, EvB

Manuscript revision: RD, JCS, EvB, AN, ES

All authors approved the final version of the manuscript.

Chapter 6: The impact of scaled boundary conditions on wall shear stress computations in atherosclerotic human coronary bifurcations

Conception & design: JTS, JW, AvdS, MS, FG

Experiments: JTS

Data analysis: JTS, JCS, MS, FG

Interpretation of results: JTS, JCS, JW, MS, FG

Figure preparation: JTS Manuscript draft: JTS, FG

Manuscript revision: JTS, JCS, JW, AvdS, MS, FG

All authors approved the final version of the manuscript.

A.5 ACKNOWLEDGMENTS

A long, venturous journey is coming to an end, a journey with many delights and also some challenges. Without the support of many, I would not have prevailed through all the difficult moments. A big thanks to everyone who helped in one way or another!

Foremost, I'd like to express my gratitude to my promoter and my co-promoter: Prof. Dr. Ed van Bavel and Dr. Ir. Maria Siebes. Dear Ed, I will not forget our first encounter, now more than 10 years ago. In 2009, you taught a course on the cardiovascular system to physics students. Already starting with an intimate setting of teaching just three students in your office, it soon was clear that I would stay as the only student of the course. Yet, instead of canceling the course, you continued, and the two of us had great discussions on all kinds of physics of the cardiovascular system. This opened a whole new world to me, not knowing that we would pick up similar discussions at a later time point. I very much enjoyed all these discussions, whether it was about physics, vascular network principles, or modeling, and learned a lot at the same time. You were always willing to get to the bottom of the issue, yet without losing the focus. I cannot express enough gratitude that you always kept your trust and faith in me: you gave me a summer project even though it fell in your holidays and never let me down, even when finalizing this thesis took much longer than we both anticipated.

Dear Maria, also you kept supporting me through all rough times. You were always interested in me as a person, not just as a working force. I admire that you never stop asking "How? Why?" with an unequaled catching enthusiasm and energy. I value that you gave me the opportunity of tackling very different fields (experimental, technical, computational, even designing a lab) as well as to explore conferences and courses also beyond the well-established options. I had never envisioned talking about my research in three languages and that not sequentially but all mixed within a sentence!

This thesis would also not have been possible without Professor Emeritus Dr. Ir. Jos Spaan, who offered me to join the cryomicrotome group as a PhD student. Dear Jos, I am very grateful that you gave me this opportunity. Even after your retirement, you were there and helped returning the focus on science whenever we were bogged down in technical details.

To the members of the examination board, Prof. Dr. Daphne Merkus, Prof. Dr. Maurice Aalders, Dr. Ir. Jolanda Wentzel, Prof. Dr. Jan Piek, Prof. Dr. Stephen

Payne, and Prof. Dr. Alfons Hoekstra: thank you very much for your time and effort! I very much appreciate your kind willingness to examine my work.

I would also like to thank all my co-workers for the good teamwork and for everything I have learned from you. Judith and Erik, thank you for your help with surgeries. The experiments would not have been possible without you and the care of the ARIA staff. Angela and Paul, thank you for your aid in the lab and with the cryomicrotome. I would like to extend my thanks to the members of the EMINENCE project for fruitful debates and for the hospitality. Frank Gijsen, Jelle Schrauwen, Aart Nederveen, and Raphaël Duivenvoorden, thanks for your good collaboration during our joint WSS studies.

To everyone at the Biomedical Engineering and Physics department: you make our department special. The vivid, collaborative environment you create is energizing and makes working there easy. Almost never is one alone at the department, no matter what time of the day it is or whether it is weekend or not (okay, there was no-one when I once returned at 12:30 a.m.). In particular I would like to thank all fellow coronary circulation and cryomicrotome group members: Monique, Nazanin, Cristina, Froukje, Elco, Lorena, and Duy. In sharing our experience, successes, and sorrows, we prevailed. You were always there for help and cheer. Days, weeks, and months flew by in your presence.

Pepijn, it is an honor that I could follow your path from a Master project on Elastography to a PhD using the imaging cryomicrotome. It was your enthusiastic introduction to your cryomicrotome work while I was still working on my Master project that attracted me to the field of cryomicrotome imaging. Also after joining the group, you and Jeroen never became tired of explaining the cryomicrotome ins and outs and sharing all your insights. I cherish all our joint efforts in improving the vascular filling and the image processing as well as mastering my data. Martin, we not only shared the entrance to our offices but also an interest for computers as well as many train rides. Your extensive technical knowledge and your hands-on assistance whenever I had yet another computer issue made much of my work possible in the first place.

A special thanks goes to Jetty and Carla, our department fairies. No matter what administrative problem I had (keys, ...), you have solved it.

Ganz herzlich möchte ich mich bei allen Hamburger Freunden bedanken. Wie ihr wisst, waren die letzten beiden Jahre sehr schwer für mich. Ihr habt mir die Kraft gegeben, trotz allem nicht aufzugeben. Danke!

Der allergrößte Dank gebührt meinen Eltern. Ihr wart immer für mich da und habt mich bei allen meinen Schritten mit all eurer Kraft unterstützt. Nichts konnte

uns trennen. Ohne eure Unterstützung und euren Rückhalt wäre ich nie so weit gekommen! Ihr habt mir eine super Schulausbildung ermöglicht und mit dem Austauschjahr in Amerika und dem internationalen Studium in Bremen den Weg in die weite Welt geebnet. Amsterdam und Bussum sind auch für euch zur zweiten Heimat geworden. Auch als nicht alles glatt lief und mein Studium gar nicht mehr zu enden schien, habt ihr mich immer weiter unterstützt und Mut gemacht. Papa, es war unser beider großer Wunsch, meinen Doktor gemeinsam zu feiern. Es schmerzt mich ungemein, dass ich so lange gebraucht habe und du nun nicht mehr dabei sein kannst. Du fehlst, auch wenn du im Herzen immer bei mir sein wirst! Mama, was bin ich froh, dich an meiner Seite zu wissen. Zusammen schaffen wir es!